



*The Identification of the Effect of High Rate  
Deformation on the Microstructure and  
Properties of Titanium Alloys*

By

**Ntovas Michail**

*Department of Design Manufacturing and Engineering Management*

*The University of Strathclyde*

*Thesis submitted for the degree of Engineering Doctorate in Advanced  
Manufacturing:*

*Forging and Forming programme*

**2019**

---

**Statement of Academic Honesty**

I declare that this submission is entirely my own original work.

I declare that, except where fully referenced direct quotations have been included, no aspect of this submission has been copied from any other source.

I declare that all other works cited in this submission have been appropriately referenced.

I declare that I have reviewed this submission through TurnItIn® and it complies with the departmental standards, being the overall similarity figure less than 10 percent and the similarity against any individual source is less than 1 percent.

I understand that any act of Academic Dishonesty such as plagiarism or collusion may result in the non-award of my degree.

Signed ... 

Dated 10/12/2019 .....

‘This thesis is the result of the author’s original research. It has been composed by the author and contains material that has been previously submitted for examination as part of the Engineer Doctorate Program to University of Strathclyde in 2014.’

Signed:



Date:

10/12/2019

---

*The copyright of this thesis belongs to the author under the terms of the United Kingdom Copyright Acts as qualified by the University of Strathclyde Regulation 3.51. Due acknowledgement must always be made of the use of any material contained in, or derived from, this dissertation.*

---

## Abstract

Material forming processes such as forming aerospace components, it is well known that are highly influenced by strain, strain rate and temperature. The effects of these parameters in flow stress and microstructure of titanium alloys are critical. The regime of strain rates where aerospace components such as aerofoil shapes for gas turbine engines are formed are between  $1\text{s}^{-1}$  and  $150\text{ s}^{-1}$ . Conventional testing machines are unable to reach these strain rates and provide accurate information which the manufacturing community is currently interested.

This project focused on the process optimization of a high strain rate forging simulator which is capable for strain rates up to  $200\text{s}^{-1}$ . An equipment bought by the AFRC to deal with the lack of flow data. Data which will be used in the future for simulating high speed forging and extrusion. The experimental optimization was achieved through temperature optimization, sample relevant position to push rod and sample position to induction coil.

Furthermore, the project investigates the high strain rate deformation of Ti6Al4V alloy with two distinct microstructures in terms of strain rate and temperature influence on the microstructure. The flow behaviour of the material were also investigated and modelled. The Hansel-Spittel (H&S) rheological law demonstrates good compliance with the high strain rate deformation of Ti6Al4V.

Last but not least, the data obtained by the high strain rate deformation of the Ti6Al4V was used to create the process and instability maps for the Ti6Al4V. For both microstructures the stable and unstable deformation areas has been identified.

---

# Acknowledgements

I would first like to thank my supervisor, Professor Paul Blackwell. I could not have imagined having a better mentor and supervisor EngD. His knowledge, encouragement and persistence have helped me in accomplishing this milestone. His excellent guidance, support and physical insights have helped me in achieving a better understanding of the scope of process optimisation high strain rate deformation and its applications. He always was there to support me through this journey. His encouragement and support all through this stage of my life cannot be expressed in words.

I would like also to express my sincere gratitude to all the AFRC staff and especially to the material and residual stress team for the support and help during my project.

I would especially like to express my deepest gratitude to my mother who has been a strong pillar of support and sacrifice so many thing so that her children will prosper. Her boundless love and affection shaped my life and make me the person that I am today.

Last but not least I would like to express my deepest gratitude to my partner who support me though all this years. I cannot imagine a better person to share my life. Her strong and supporting character gave me strength during the challenging moments of my life, and give me inspiration to continue trying for a better future.

---

# Table of contents

<b>Abstract</b> .....	<b>III</b>
<b>Acknowledgements</b> .....	<b>IV</b>
<b>Table of contents</b> .....	<b>V</b>
<b>List of Figures</b> .....	<b>IX</b>
<b>List of Tables</b> .....	<b>XIV</b>
<b>1 Introduction</b> .....	<b>1</b>
1.1 General Introduction of Titanium .....	1
1.2 Forging Industry .....	3
1.3 Project Aim, Objectives & Approach.....	5
1.4 Thesis Outline.....	7
<b>2 Literature Survey</b> .....	<b>9</b>
2.1 Titanium Alloys.....	9
2.2 Physical Properties of Titanium .....	13
2.2.1 Titanium Ti-6Al-4V .....	13
2.3 Microstructures and their Property Relationships .....	15
2.3.1 Martensitic Transformation .....	15
2.3.2 Sympathetic Nucleation/Nucleation and Growth.....	16
2.3.3 Microstructural Phases .....	17
2.3.4 $\alpha$ / $\beta$ alloys: representative microstructures .....	20
2.3.5 Microstructure-Property Relationships .....	26
2.4 Deformation Modes.....	27
2.4.1 Deformation by dislocation Slip.....	28
2.4.2 Deformation Twinning .....	31
2.5 Deformed microstructures of Ti-6Al-4V.....	32
2.5.1 The temperature effect on the Ti-6Al-4V flow properties.....	32
2.5.2 The strain rate effect on the Ti-6Al-4V flow properties.....	33
2.6 High Strain Rate Deformation .....	35
2.7 Process map and Instability .....	41

---

2.8 Adiabatic shear bands.....	50
<b>3 High strain rate process optimization .....</b>	<b>57</b>
3.1 Equipment description.....	59
3.2 Experimental optimization.....	61
3.2.1 Temperature control.....	62
3.2.2 Sample position.....	63
3.2.3 Strain rate.....	66
<b>4 Project Methodology .....</b>	<b>69</b>
4.1 Introduction and DoE.....	69
4.2 Material specifications and initial microstructure .....	71
4.3 Sample Geometrical Preparation for Compression .....	74
4.4 Temperature distribution monitoring.....	76
4.5 Hot Isothermal Compression .....	77
4.5.1 Introduction .....	77
4.5.2 Equipment Selection .....	78
4.5.3 Compression setup for HA250 servo-hydraulic machine .....	80
4.5.4 Compression test matrix for HA250 servo-hydraulic machine.....	81
4.5.5 Compression setup for phoenix high strain rate tester .....	82
4.5.6 Compression test matrix for Phoenix high strain rate tester .....	82
4.6 Isothermal hot compression test flow stress analysis .....	84
4.7 Determination of friction .....	85
4.8 Process map and instability criterion.....	87
4.9 Sample Preparation and Investigation.....	88
4.9.1 Sample Preparation route.....	89
4.9.2 Optical microscopy (OM) and Electronic microscopy (SEM, EBSD) .....	91
<b>5 Results and Evaluation of As-Received Microstructure .....</b>	<b>93</b>
5.1 Temperature distribution inside the sample at Phoenix high strain rate Tester.....	93
5.1.1 Results of temperature distribution as a function of temperature .....	93
5.1.2 Evaluation of temperature distribution as a function of temperature.....	95
5.1.3 Temperature distribution versus top die-sample gap .....	96

---

5.1.4 Pyrometer correction based on temperature distribution results .....	97
5.2 Hot isothermal compression tests .....	98
5.3 Ti-6Al-4V flow stress corrections .....	100
5.3.1 Friction correction.....	100
5.3.2 Ringing effect correction.....	100
5.3.3 Machine stiffness correction .....	103
5.3.4 Friction and adiabatic heating correction.....	105
5.4 Modelling of flow curves.....	107
5.5 As-received microstructure.....	112
5.5.1 Flow behaviour at low strain rates .....	112
5.5.2 Flow behaviour at intermediate strain rates .....	116
5.5.3 Flow behaviour at high strain rates .....	120
5.5.4 H&S modelling of flow behaviour .....	126
5.5.5 Strain rate effect .....	138
5.5.6 Temperature effect .....	141
5.5.7 Microstructure evolution during hot isothermal compression .....	142
<b>6 Results and Evaluation Lamellar Microstructure .....</b>	<b>159</b>
6.1 Flow behaviour at high strain rates.....	159
6.2 H&S modelling of flow behaviour .....	163
6.3 Strain rate effect .....	174
6.4 Temperature effect .....	177
6.5 Microstructure evolution during hot isothermal compression .....	179
<b>7 Process map and instability.....</b>	<b>188</b>
7.1 Processing map As-received (equiaxed) microstructure .....	189
7.2 Processing map lamellar microstructure .....	192
<b>8 Further Discussion .....</b>	<b>195</b>
<b>9 CASE STUDY: Comparison Phoenix high strain rate tester with Gleeble 3800200</b>	
<b>10 Summary .....</b>	<b>205</b>
10.1 Further work .....	206
10.2 Industrial benefits .....	207
<b>Appendix A – Temperature distribution experimental photos.....</b>	<b>208</b>

---

<b>Appendix B – Compression test photos .....</b>	<b>209</b>
<b>Appendix C – Strain rate optimization .....</b>	<b>211</b>
<b>Appendix D – True stress vs. True Strain Curves .....</b>	<b>216</b>
<b>Appendix E – Microstructure low strain rates .....</b>	<b>226</b>
<b>Appendix F - Flow patterns .....</b>	<b>231</b>
<b>Reference .....</b>	<b>238</b>

---

# List of Figures

Figure 1.1: Gas turbine engine Material distribution [9] .....	2
Figure 2.1: Crystal structure of hcp ( $\alpha$ phase) left and bcc ( $\beta$ phase) right [6] .....	10
Figure 2.2: Influence of alloying elements to Ti phase diagrams [6] .....	10
Figure 2.3: The five classes of titanium alloys in a $\beta$ -isomorphous phase diagram [26]. .....	12
Figure 2.4: Lamellar microstructure, left obtained by slow cooling rate ( $1^{\circ}\text{C}/\text{min}$ ), right obtained by fast cooling rate ( $100^{\circ}\text{C}/\text{min}$ ) [4].....	21
Figure 2.5: Process route for Lamellar microstructure [4]. .....	22
Figure 2.6: Two alternative bi-modal microstructures created from $\beta$ -phase field by slow (left) and fast (right) cooling rates [4]. .....	23
Figure 2.7: Process route for bi-modal microstructure [4]. .....	24
Figure 2.8: A fully equiaxed microstructure obtained from the bi-modal condition by slow cooling [4]. .....	24
Figure 2.9: Process route for equiaxed microstructure [4].....	26
Figure 2.10: Hexagonal close-packed (hcp) structure slip system [6]. .....	30
Figure 2.11: Flow curves of Ti-6Al-4V at strain rate of $2000\text{s}^{-1}$ [45] .....	33
Figure 2.12: Isothermal flow curves of equiaxed Ti- 6Al-4V deformed in hot compression at strain rates of $0.0003\text{-}100\text{ s}^{-1}$ and temperatures of (a) $850^{\circ}\text{C}$ and (b) $1100^{\circ}\text{C}$ [48] .....	34
Figure 2.13: Strain rate regimes and different techniques[39] .....	37
Figure 2.14: Processing map obtained on Ti-6Al-4C with 1000 ppm oxygen and equiaxed $\alpha+\beta$ preform structure. Contour numbers represent percent efficiency of power dissipation [73]. .	45
Figure 2.15: Process map of Ti-6Al-4V at 0.9 of strain by Aneta et al[77] .....	46
Figure 2.16: Processing maps of Ti-6Al-4V alloy at the strains of: (a) $\epsilon= 0.3$ ; (b) $\epsilon= 0.4$ ; (c) $\epsilon= 0.5$ ; (d) $\epsilon= 0.6$ ; (e) $\epsilon= 0.7$ . Numbers represent efficiency of power dissipation. Shaded areas represent the instability regions[78]. .....	47
Figure 2.17: Processing maps of the Ti-6Al-4V alloy at the strains of (a) 0.3, (b) 0.5, (c) 0.69, and (d) all the strains[79]......	48
Figure 2.18: Processing maps obtained from (a) Prasad's criterion; (b) Malas' criterion; and (c) Murty's criterion[71].....	49
Figure 3.1: Servo-hydraulic forging simulation machine, chamber and interior .....	57
Figure 3.2 Environmental chamber .....	58
Figure 3.3 Interior of the environmental chamber .....	58
Figure 3.4: Software interface supporting the equipment, left: Constant Strain Rate Creator, right: Profile Builder .....	61
Figure 3.5: a) Calibration tool, b) Temperature distribution sample.....	64
Figure 3.6: Optimized strain rate results at $950^{\circ}\text{C}$ .....	67

Figure 4.1 : As-received microstructure of Ti-6Al-4V bar .....	72
Figure 4.2: Ti-6Al-4V microstructure after heat treatment .....	73
Figure 4.3: Heat treatment route of Ti-6Al-4V.....	74
Figure 4.4: Engineering Draw and 3D model of the samples used for compression tests .....	75
Figure 4.5: Engineering Draw and 3D model of the samples used for temperature distribution monitoring .....	75
Figure 4.6: Servo-Hydraulic compression testing system Zwick HA250 [130].....	79
Figure 4.7: Friction calibration curves [131] .....	87
Figure 4.8: Cutting sample direction.....	89
Figure 4.9: Samples after each step of preparation A) step 1- P600 grinding, B) step 2- P1200 grinding, C) Step 3 polishing, D) step 4 polishing, E) step 5 polishing and F) after chemical etching. ....	90
Figure 5.1: Thermocouple radial position in respect to the centre of the sample position inside the T1 sample A) after heating B) initial position .....	95
Figure 5.2: Thermocouple radial position in respect to the centre of the sample inside the T2 sample A) after heating B) initial position .....	95
Figure 5.3 Ringing effect at hot isothermal compression Phoenix equipment .....	102
Figure 5.4 Ringing effect $t$ in tests on Al alloy 5052 at 500 °C [140].....	103
Figure 5.5: Machine stiffness at different temperatures.....	104
Figure 5.6. Effect of friction and adiabatic heating correction on the flow curves at 850°C and 100 s <sup>-1</sup> .....	106
Figure 5.7: Costs association between uncertainty in maximum forging load for a screw press [143].....	110
Figure 5.8: Flow stress behaviour of Ti-6Al-4V at 850°C at strain rates of 0.1s <sup>-1</sup> and 1s <sup>-1</sup> for three strains.....	113
Figure 5.9: Flow stress behaviour of Ti-6Al-4V at 900°C at strain rates of 0.1s <sup>-1</sup> and 1s <sup>-1</sup> for three strains.....	114
Figure 5.10: Flow stress behaviour of Ti-6Al-4V at 950°C at strain rates of 0.1s <sup>-1</sup> and 1s <sup>-1</sup> for three strains .....	115
Figure 5.11: Flow stress behaviour of Ti-6Al-4V at 850°C at 10 s <sup>-1</sup> for two strains.....	117
Figure 5.12: Flow stress behaviour of Ti-6Al-4V at 900°C at 10 s <sup>-1</sup> for two strains.....	118
Figure 5.13: Flow stress behaviour of Ti-6Al-4V at 950°C at 10 s <sup>-1</sup> for two strains.....	119
Figure 5.14: Flow stress at 900°C and 100s <sup>-1</sup> , experimental, with friction correction and adiabatic heating.....	121
Figure 5.15: Flow stress at 900°C and 100s <sup>-1</sup> , after smoothing and fitting with H&S.....	122
Figure 5.16: Flow stress behaviour of Ti-6Al-4V at 50 s <sup>-1</sup> and three temperatures (850°C, 900°C and 950°C).....	123
Figure 5.17: Flow stress behaviour of Ti-6Al-4V at 100 s <sup>-1</sup> and three temperatures (850°C, 900°C and 950°C).....	124

Figure 5.18: Flow stress behaviour of Ti-6Al-4V at 150 s <sup>-1</sup> and three temperatures (850°C, 900°C and 950°C).....	125
Figure 5.19: Experimental and modelled flow curves for 850°C and strain rate 50s <sup>-1</sup> .....	127
Figure 5.20: Experimental and modelled flow curves for 850°C and strain rate 100s <sup>-1</sup> .....	128
Figure 5.21: Experimental and modelled flow curves for 850°C and strain rate 150s <sup>-1</sup> .....	129
Figure 5.22: Experimental and modelled flow curves for 900°C and strain rate 50s <sup>-1</sup> .....	131
Figure 5.23: Experimental and modelled flow curves for 900°C and strain rate 100s <sup>-1</sup> .....	132
Figure 5.24: Experimental and modelled flow curves for 900°C and strain rate 150s <sup>-1</sup> .....	133
Figure 5.25: Experimental and modelled flow curves for 950°C and strain rate 50s <sup>-1</sup> .....	135
Figure 5.26: Experimental and modelled flow curves for 950°C and strain rate 100s <sup>-1</sup> .....	136
Figure 5.27: Experimental and modelled flow curves for 950°C and strain rate 150s <sup>-1</sup> .....	137
Figure 5.28: Influence of strain rate on flow stress at peak stress, at a constant temperature. .....	139
Figure 5.29: Influence of strain rate on flow stress at a constant plastic strain of 0.5, as a function of temperature .....	140
Figure 5.30: Effect of temperature on the peak flow stress at the 3 different strain rates .....	142
Figure 5.31: Flow localization at strain rate of 10s <sup>-1</sup> and three temperatures 850°C, 900°C and 950°C.....	144
Figure 5.32: SEM micrographs at 850°C and strain rate of 50s <sup>-1</sup> .....	146
Figure 5.33: SEM micrographs at 850°C and strain rate of 100s <sup>-1</sup> .....	147
Figure 5.34: SEM micrographs at 850°C and strain rate of 150s <sup>-1</sup> .....	148
Figure 5.35: Volume fraction of beta phase in the centre of the deformed sample at 850°C and strain rates of 50s <sup>-1</sup> , 100s <sup>-1</sup> and 150s <sup>-1</sup> .....	149
Figure 5.36 : SEM micrographs at 900°C and strain rate of 50s <sup>-1</sup> .....	150
Figure 5.37: SEM micrographs at 900°C and strain rate of 100s <sup>-1</sup> .....	151
Figure 5.38: SEM micrographs at 900°C and strain rate of 150s <sup>-1</sup> .....	152
Figure 5.39: Volume fraction of beta phase in the centre of the deformed sample at 900°C and strain rates of 50s <sup>-1</sup> , 100s <sup>-1</sup> and 150s <sup>-1</sup> .....	153
Figure 5.40: SEM micrographs at 950°C and strain rate of 50s <sup>-1</sup> .....	154
Figure 5.41: SEM micrographs at 950°C and strain rate of 100s <sup>-1</sup> .....	155
Figure 5.42: SEM micrographs at 950°C and strain rate of 150s <sup>-1</sup> .....	156
Figure 5.43: Volume fraction of beta phase in the centre of the deformed sample at 950°C and strain rates of 50s <sup>-1</sup> , 100s <sup>-1</sup> and 150s <sup>-1</sup> .....	157
Figure 6.1: Flow stress at 900°C and 100s <sup>-1</sup> , experimental, with friction correction and adiabatic heating. ....	159
Figure 6.2: Flow stress at 900°C and 100s <sup>-1</sup> , after smoothing and fitting with H&S.....	160
Figure 6.3: Flow stress behaviour of Ti-6Al-4V at 50 s <sup>-1</sup> and three temperatures (850°C, 900°C and 950°C).....	161
Figure 6.4: Flow stress behaviour of Ti-6Al-4V at 100 s <sup>-1</sup> and three temperatures (850°C, 900°C and 950°C).....	162

Figure 6.5: Flow stress behaviour of Ti-6Al-4V at 150 s <sup>-1</sup> and three temperatures (850°C, 900°C and 950°C).....	163
Figure 6.6: Experimental and modelled flow curves for 850°C and strain rate 50s <sup>-1</sup> .....	164
Figure 6.7: Experimental and modelled flow curves for 850°C and strain rate 100s <sup>-1</sup> .....	165
Figure 6.8: Experimental and modelled flow curves for 850°C and strain rate 150s <sup>-1</sup> .....	166
Figure 6.9: Experimental and modelled flow curves for 900°C and strain rate 50s <sup>-1</sup> .....	167
Figure 6.10: Experimental and modelled flow curves for 900°C and strain rate 100s <sup>-1</sup> .....	168
Figure 6.11: Experimental and modelled flow curves for 900°C and strain rate 150s <sup>-1</sup> .....	169
Figure 6.12: Experimental and modelled flow curves for 950°C and strain rate 50s <sup>-1</sup> .....	171
Figure 6.13: Experimental and modelled flow curves for 950°C and strain rate 100s <sup>-1</sup> .....	172
Figure 6.14: Experimental and modelled flow curves for 950°C and strain rate 150s <sup>-1</sup> .....	173
Figure 6.15: Influence of strain rate on flow stress at peak stress, as a function of temperature. ....	175
Figure 6.16: Influence of strain rate on flow stress at 0.5 of true stress, as a function of temperature.....	176
Figure 6.17: Effect of temperature on the peak flow stress as a function of strain rate .....	178
Figure 6.18: Schematic illustration representing microstructural evolution during dynamic globularization [159].....	180
Figure 6.19: SEM micrographs at 850°C and strain rate of 50s <sup>-1</sup> (left 500x and right 1000x)....	180
Figure 6.20: SEM micrographs at 850°C and strain rate of 100s <sup>-1</sup> (left 500x and right 1000x)..	181
Figure 6.21: SEM micrographs at 850°C and strain rate of 150s <sup>-1</sup> (left 500x and right 1000x)..	181
Figure 6.22: Volume fraction of alpha phase in the centre of the deformed sample at 850oC and strain rates of 50s <sup>-1</sup> , 100s <sup>-1</sup> and 150s <sup>-1</sup> .....	182
Figure 6.23: SEM micrographs at 900°C and strain rate of 50s <sup>-1</sup> (left 500x and right 1000x)....	183
Figure 6.24: SEM micrographs at 900°C and strain rate of 100s <sup>-1</sup> (left 500x and right 1000x)..	183
Figure 6.25: SEM micrographs at 900°C and strain rate of 150s <sup>-1</sup> (left 1000x and right 2000x)	184
Figure 6.26: Volume fraction of alpha phase in the centre of the deformed sample at 900°C and strain rates of 50s <sup>-1</sup> , 100s <sup>-1</sup> and 150s <sup>-1</sup> .....	185
Figure 6.27: SEM micrographs at 950°C and strain rate of 50s <sup>-1</sup> (left 500x and right 1000x)....	186
Figure 6.28: SEM micrographs at 950°C and strain rate of 100s <sup>-1</sup> magnification 500x .....	186
Figure 6.29: SEM micrographs at 950°C and strain rate of 150s <sup>-1</sup> (left 500x and right 1000x)..	187
Figure 7.1: Processing maps. Ti-6Al-4V. (a) Starting microstructure: equiaxed $\alpha + \beta$ . (b) Starting microstructure: lamellar $\alpha + \beta$ [161].....	188
Figure 7.2: Power dissipation efficiency ( $\eta$ ) contour map, as-received microstructure at 0.5 strain .....	189
Figure 7.3: Instability ( $\xi$ ) map as-received microstructure at 0.5 strain, A, B, C instability regions and D stable region. ....	190
Figure 7.4: Processing map for Ti-6Al-4V as-received microstructure, contour lines represent Power dissipation efficiency ( $\eta$ ) and coloured area the instability ( $\xi$ ).....	190

---

Figure 7.5: Power dissipation efficiency ( $\eta$ ) contour map, lamellar microstructure at 0.5 strain .....	192
Figure 7.6: Flow instability ( $\xi$ ) map for lamellar microstructure at 0.5 strain; A, B, C are instability regions and D a stable region. The area above E would also tend to instability. ....	193
Figure 7.7: Processing map for Ti-6Al-4V lamellar microstructure, contour lines represent Power dissipation efficiency ( $\eta$ ) and coloured area the instability ( $\xi$ ). .....	193
Figure 9.1: A comparisons between Phoenix and Gleeble 3800 at 900°C and strain rates of 50s <sup>-1</sup> and 100s <sup>-1</sup> . .....	201
Figure 9.2: A comparisons between Phoenix and Gleeble 3800 at 950°C and strain rates of 50s <sup>-1</sup> and 100s <sup>-1</sup> . .....	202

---

# List of Tables

Table 2.1: Mechanical properties obtained though different microstructure based on different crystallographic orientations [6].	27
Table 3.1: Strain rate variation	68
Table 4.1: Full factorial DOE for conventional servo-hydraulic Zwick HA250.	70
Table 4.2: Full factorial DOE for prototype high strain rate servo-hydraulic machine.	70
Table 4.3: Full factorial DoE for as-received and heat treated microstructure	71
Table 4.4: Chemical composition of Ti-6Al-4V bar as received.	73
Table 4.5: Test matrix for hot compression tests at HA 250 servo-hydraulic machine.	81
Table 4.6: Test matrix of reference hot isothermal compression tests at Phoenix high strain rate servo-hydraulic machine.	83
Table 4.7: As-received Ti-6Al-4V test matrix.	83
Table 4.8: After heat treatment Ti-6Al-4V	84
Table 4.9: Grinding and Polishing parameters and steps.	91
Table 5.1: Sample T1 temperature distribution.	94
Table 5.2: Sample T2 temperature distribution.	94
Table 5.3: Sample T1 temperature distribution versus die-sample position.	97
Table 5.4: Pyrometer corrected inputs	98
Table 5.5: Examples of microstructural model [143].	108
Table 5.6: Examples of empirical models [143]	109
Table 5.7: H&S material constants and level of confidence for 850°C	130
Table 5.8 H&S material constants and level of confidence for 900°C	133
Table 5.9 H&S material constants and level of confidence for 950°C	138
Table 5.10: Strain rate sensitivity (m) and different temperatures peak stress.	140
Table 6.1: H&S material constants and level of confidence for 850°C	167
Table 6.2: H&S material constants and level of confidence for 900°C	170
Table 6.3: H&S material constants and level of confidence for 950°C	174
Table 6.4: Strain rate sensitivity (m) and different temperatures peak stress.	177
Table 7.1: Flow stress of the isothermally compressed Ti-6Al-4V with equiaxed microstructure at 0.5 true strain.	189
Table 7.2: Flow stress of the isothermally compressed Ti-6Al-4V with lamellar microstructure at 0.5 true strain.	192
Table 8.1: Tendency of the H&S parameters values obtained from the flow curves modelling, correlation with the flow stress at 0.5 of true strain.	196

# 1 Introduction

## 1.1 General Introduction of Titanium

Within the Earth's crust titanium is the ninth most abundant element and the fourth most plentiful metal [1][2]. Titanium can be found in two natural forms, as a mixed oxide with iron  $\text{FeTiO}_3$  (ilmenite) or as an oxide  $\text{TiO}_2$  (rutile) [3][4][5].

The first person to discover Titanium was William Gregor, an amateur mineralogist in 1791. Gregor discovered titanium in dark, magnetic iron sand (ilmenite) in Cornwall (UK). In 1795, Klaproth, a German scientist, identified an oxide of an unknown element, which was the same Gregor earlier had discovered. The element was named by Klaproth "titanium" in reference to the Titans of Greek mythology, the powerful sons of Earth, who symbolised strength and power. Nevertheless, titanium was not used before the Kroll process was at commercialised in 1950. The process makes titanium more readily recoverable from the ores. The process until now remains unchanged and is the principal process for titanium production today [4] [5] [6].

In comparison to other conventional engineered materials such as steel or aluminium, titanium is regarded as expensive, because of the production cost; however, the combination of unique and useful properties such as superior strength-to-weight ratio, fatigue and corrosion resistance at elevated temperatures justifies the higher cost. Furthermore, titanium and its alloys show

superior lifetime and high durability with minimum maintenance demands in comparison with steel. It was these properties that make titanium and its alloys cost effective and led them to extensive use in aerospace applications and especially in aircraft turbines engines as the material of choice for many of gas turbine components.

The continuous growth of the aerospace industry in the last 30 years has resulted in a demand for new titanium alloys for challenging aerospace applications [7]. Owing to these demands the research and development of titanium alloys has run parallel to the development of the aircraft engines. Titanium was introduced to gas turbines for the first time in 1952, when Pratt and Whitney used titanium in compressor blades and discs in the J57 engine [8]. Today titanium alloys compose almost the 30 per cent of the weight of modern aerospace-engines Figure 1.1[9]. This extensive use of titanium generates the need for a lot of different alloys. One of the most important is Ti-6Al-4V.

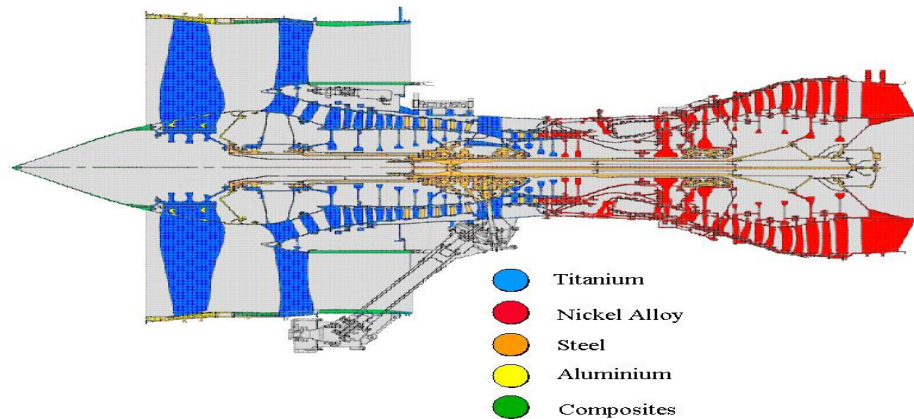


Figure 1.1: Gas turbine engine Material distribution [9]

## 1.2 Forging Industry

The global forging market was capitalised at 57.42 billion dollars in 2015 and anticipated to cross 86.90 billion dollars in 2021 with 8% annual growth rate [10]. In the UK manufacturing makes up to 11% of Gross value added (GVA), 44% of total UK exports, 70% of business R&D and directly employs 2.6 million people. The UK is the eighth largest manufacturing nation in the world. The main sectors in UK manufacture are the automotive, aerospace and Oil & Gas. Based on that need the University of Strathclyde and Boeing, Rolls Royce and Timet have created the Advanced Forming Research Centre (AFRC) part of the CATAPULT in High Value Manufacturing to address the challenges of future forming and forging. The research reported herein is part of the AFRC's developing of forging and forming technologies to support the development of high integrity components for automotive, aerospace, medical and oil and gas sectors.

In modern manufacturing the need for process optimization is becoming more and more important due to the need to drive down costs and increase production rate [11]. In the past high strain rate forging processes were often used to manufacture parts that were oversize and which required final machining to shape. More recently there has been a move to forge parts close to net shape to minimize the need for such final machining. In addition, there is a requirement to ensure close control of microstructure to guarantee final properties. A principle tool in

supporting process optimization is the use of Finite Element (FE) simulation [12][13].

A number of factors need to be in place to ensure that process models are robust; these include a large database of materials properties and a representation of the boundary conditions relevant to the process. These boundary conditions may include such factors as the heat transfer [14][15][16] and friction coefficient [11][17][18][19]. Both of these factors are difficult to determine since they are each affected by a range of secondary factors e.g. lubrication thickness and type, forging loads and tool condition.

The most widely used method for collecting material data to simulate forging processes are literature-models, static or dynamic tests and from material databases which are included in many commercial FE software packages. Software such as DEFORM-3D®, QFORM® and FORGE®NxT provide users with material databases and have the facility to incorporate various material models which researchers can use. In addition, software which works with material models like that of Hensel & Spittel (see section 5.4) require material constant and coefficients as an input from the user [20]. That has as a consequence the need for accurate material data which will be incorporated in the simulations to achieve optimum results.

Taking under consideration the significance of the accuracy in the material data which is required for forging process optimization only mechanical tests under

quasi-static and dynamic loading can provide the material flow behaviour. A fundamental principle of the materials science discipline is that any changes in the mechanical properties are entirely determined by the metallurgical structure of a metal and that any differences in these properties are the direct consequence of changes in that microstructure. Usually materials behaviour is expressed by three major factors, the way that structure evolves with strain, temperature and how flow stress interacts at a constant strain rate [21].

Due to the nature of the forging process, material data from conventional mechanical tests are not enough to provide the full flow behaviour. Most of the forging processes take place at strain rates higher than conventional testing equipment can operate. For that reason special modified equipment is required to achieve strain rates from  $10\text{s}^{-1}$  up to  $200\text{s}^{-1}$  where forging processes are taking place and material data are extremely important for process optimization.

### 1.3 Project Aim, Objectives & Approach

The general aim of this work is to establish and optimise an experimental procedure for a new high strain rate servo-hydraulic forging simulator capable for strain rates up to  $150\text{s}^{-1}$  with final goal to obtain material data for Ti-6Al-4V. The material data will be used in the Advanced Forming Research Centre (AFRC) for future forging process optimization to address the challenges of future forging and enhance the capabilities of UK manufacture industry.

The necessity for this project comes from the manufacturing community. The need for experimental data for new and established titanium alloys for the development of new Finite Element models to simulate forging operations is essential for the future of the manufacturing industry.

For this work conventional and special modified servo hydraulic testing machines will be used which are capable of achieving strain rates up to  $200\text{s}^{-1}$ . Previous studies conducted in the field of high strain rate deformation of titanium alloys most commonly use split Hopkinson pressure bar (also known as Kolsky bar) or Taylor impact [22]. Split Hopkinson pressure bar can achieve strain rates up to  $10^5\text{s}^{-1}$  and the Taylor impact testing method can achieve strain rates up to  $10^7\text{s}^{-1}$  [23]. The strain rates which are achieved by these methods exceed the strain rates that occur in high speed forging of titanium alloys and that makes the use of special modified hydraulic testing machines preferable for the accurate study of deformation phenomenon in the region of  $1\text{s}^{-1}$  to  $200\text{s}^{-1}$  where high speed forging occurs.

The study will be focused on examining the effects of strain rate and temperature during high strain rate deformation of Ti-6Al-4V and determine how these parameters affect the flow stress and microstructure.

The objectives of this project can be summarised as follow:

- A. To identify the experimental parameters and understand the level of influence during the high strain rate deformation.

- B. Process optimize through modification of each parameter (temperature control, position of the sample control and heating temperature uniformity control) and all together and propose an experimental procedure with aim to minimize the experimental variance.
- C. To develop a framework for analysis for the results which will tackle the challenge of the dynamic regime where high strain deformation occurs, taking under consideration all the corrections needed for the experimental results to represent the actual flow behaviour of the material.
- D. Investigate the flow behaviour of Ti-6Al-4V with two different microstructures during isothermal high strain rate compression test and correlate the results with the microstructure.
- E. Investigate the formability of the Ti-6Al-4V in terms of processing map and flow instability.

#### 1.4 Thesis Outline

The thesis comprised by ten chapters:

The first chapter is the introduction to the thesis including the projects objectives and approach.

The second chapter is the literature survey about titanium alloys and particular Ti-6Al-4V. The deformation modes and deformed microstructures also included in this chapter.

In the third chapter the methodology for the process optimization of the high strain rate deformation simulator is presented.

The project methodology is presented in chapter four. The methodology proposed includes mechanical testing, flow behaviour, process mapping and process optimisation methodologies.

Chapter five and six shows the results and evaluation of the as-received (equiaxed) and lamellar microstructures respectively. The strain rate and the temperature effect on the deformation behaviour of the Ti-6Al-4V are discussed.

Chapter seven is about the process map of the examined material as well as the flow instability. Both microstructures were investigated.

Chapter eight is a discussion about the results of chapter five, six and seven. The chapter presents the comparison between the two microstructures.

Chapter nine is a case study, comparing results between the high strain rate simulator (Phoenix) and Gleeble 3800 high strain rate deformation equipment.

Finally, chapter 10 is a summary of the research as well as future recommendations.

The next chapter provides an overview of Ti-6Al-4V alloy and its properties. Furthermore, previous research on titanium alloy under thermo-mechanical processes on different strain rates and temperatures were presented. Also the concept of flow instability during deformation is examined.

## 2 Literature Survey

Ti-6Al-4V is comprised of 90 weight per cent titanium (Ti), 6 weight per cent aluminium (Al) and 4 weight per cent vanadium (V) [24]. This chapter covers a summary of titanium alloys microstructures, properties and deformation mechanisms.

### 2.1 Titanium Alloys

Pure titanium has two allotropic forms. At low temperatures it has a hexagonal close-packed (hcp) structure, known as  $\alpha$  phase and at elevated temperatures (above  $\beta$ -transus) a body-centred cubic (bcc) structure, known as  $\beta$  phase. The atomic unit cells of  $\alpha$  and  $\beta$  phase are schematically shown in Figure 2.1. The allotropic phase transformation occurs at 882°C which is known as the  $\beta$  transus. At temperature under the  $\beta$ -transus pure titanium is stable in the  $\alpha$  phase and above the  $\beta$  transus is stable in the  $\beta$  phase until its melting point of 1678°C. These two allotropic forms are one of the main reasons why titanium properties show large variation [4][6][25].

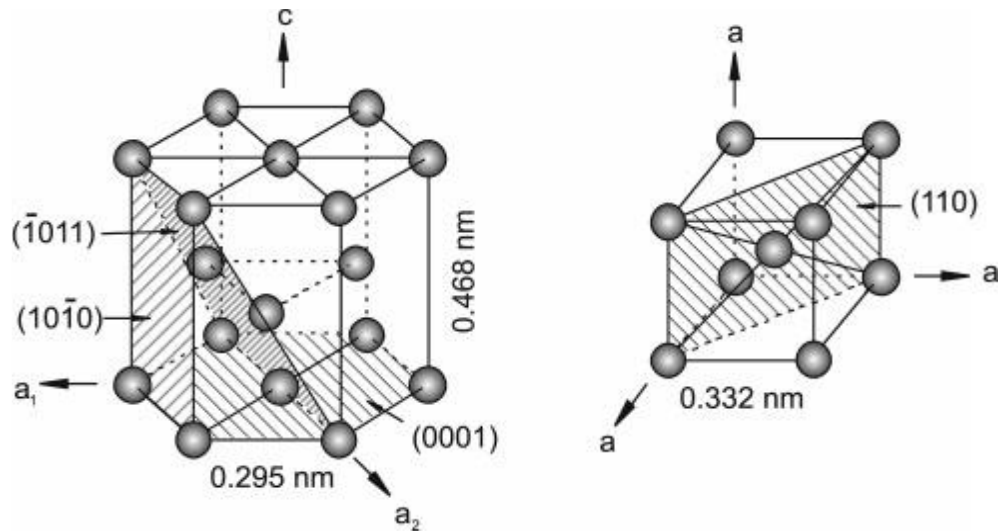


Figure 2.1: Crystal structure of hcp ( $\alpha$  phase) left and bcc ( $\beta$  phase) right [6]

The microstructure and phase equilibrium of titanium alloy heavily depend on a variety of alloying additions. In Figure 2.2, these elements are classified as neutral,  $\alpha$ -stabilisers or  $\beta$ -stabilisers by which allotropic form they thermodynamically stabilise. The  $\alpha$ -stabilisers extend the  $\alpha$  phase to higher temperatures, while the  $\beta$ -stabilisers move the  $\beta$  phase field to lower temperatures. Neutral elements such as zirconium (Zn) and tin (Sn) do not affect  $\beta$ -transus temperature [5][6].

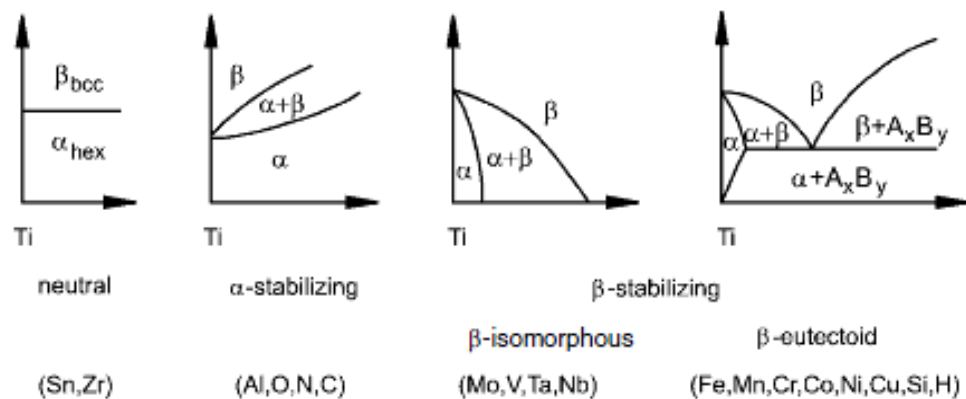


Figure 2.2: Influence of alloying elements to Ti phase diagrams [6]

The  $\alpha$ -stabilisers are oxygen (O), nitrogen (N), carbon (C) and aluminium (Al). Aluminium is an important element within titanium alloys. As already stated due to  $\alpha$ -stabilisers the  $\alpha$  phase field may be extended to higher temperatures, in addition  $\alpha$ -stabilisers are responsible for the development of a two phase field ( $\alpha+\beta$ ) [2].

The  $\beta$ -stabilisers are subdivided in two types; the  $\beta$ -isomorphous and the  $\beta$ -eutectoid. The most significant  $\beta$ -isomorphous elements are niobium (Nb), molybdenum (Mo) and vanadium (V) due to their high solubility to titanium. Copper (Cu), chromium (Cr), magnesium (Mn) and iron (Fe) are the  $\beta$ -eutectoid elements. The  $\beta$ -isomorphous and  $\beta$ -eutectoid elements can lower the  $\beta$ -transus temperature. The reduction of the  $\beta$ -transus temperature will carry on until an eutectoid reaction occurs [26].

The alloy elements (neutral,  $\alpha$ -stabilisers or  $\beta$ -stabilisers) and a combination of thermo-mechanical processing (TMP) steps are the main mechanisms behind the microstructure evolution in titanium alloys. Through the manipulation of thermo-mechanical processing routes and alloying, a great number of new and advanced titanium alloys has been created with unique and different mechanical properties. These titanium alloys can be divided in five classes; (i)  $\alpha$ , (ii)  $\beta$ , (iii)  $\alpha+\beta$ , (iv) near- $\alpha$ , (v) near- $\beta$ . These five classes can be displayed on a pseudo binary  $\beta$ -isomorphous phase diagram; Figure 2.3, which also comprises the start/ finish martensitic line (Ms/Mf). From Figure 2.3 we can observe that the appearance of  $\alpha$ -phase will be the result of cooling below the  $\beta$ -transus where a phase

transformation takes place through a martensitic reaction (diffusionless shear), or by nucleation and growth of the  $\alpha$ -phase. If the cooling process is through the start/ finish martensitic line, then a percentage of the  $\beta$ -phase will be retained only if the process is quick enough to suppress the nucleation and growth of the  $\alpha$ -phase.

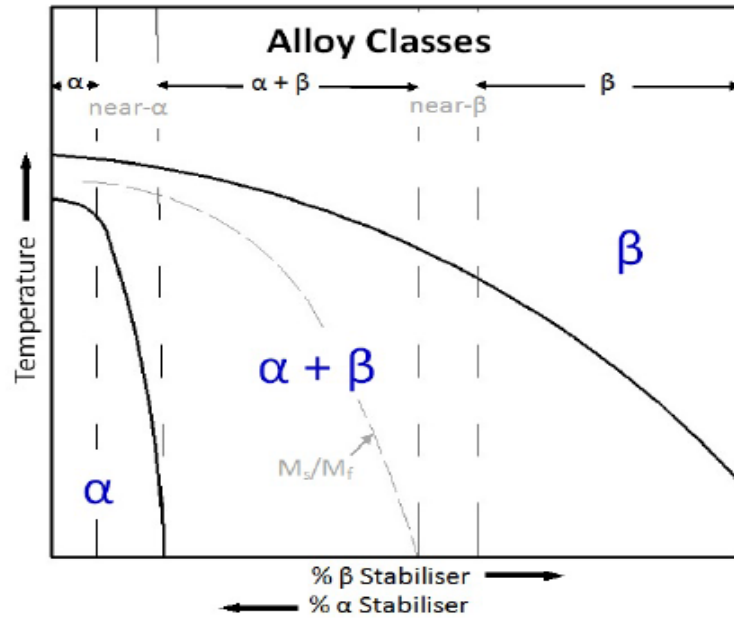


Figure 2.3: The five classes of titanium alloys in a  $\beta$ -isomorphous phase diagram [26].

The  $\alpha$ -phase range is limited to compositions where it is not possible to form the  $\beta$ -phase. Unlike  $\alpha$  alloys, near- $\alpha$  alloys through heat treatment in the  $\alpha + \beta$  region can lead to production of retained  $\beta$  in a metastable form at room temperature. This can only happen when the composition is to the right of the start/ finish martensitic line. The  $\alpha + \beta$  composition range continues to the start/ finish martensitic line at room temperature while past this complete retention of  $\beta$ -phase

is possible. To the right of the start/ finish martensitic line the alloy composition is defined as near-beta. The retained  $\beta$ -phase in this case is extremely metastable. Furthermore, the transformation of  $\beta$  alloys can be achieved inside the equilibrium  $\alpha + \beta$  field by precipitation reactions [26].

## 2.2 Physical Properties of Titanium

Titanium is a transition element with an atomic number of 33 and atomic weight of 47.90. Titanium's position in the periodic table gives it unique physical and electronic properties which make it suitable material to produce a broad spectrum, of alloys.

### 2.2.1 Titanium Ti-6Al-4V

Ti-6Al-4V is an  $\alpha + \beta$  titanium alloy that is among the most widely used titanium alloys in the world [27]. This versatile alloy accounts for approximately 45% of the total titanium production. Ti-6Al-4V was first introduced in 1954 and is considered to be a "general purpose titanium alloy" or "workhorse of the industry" [28]. Ti-6Al-4V is an  $\alpha$ -rich  $\alpha+\beta$  alloy and is available in powder, casting and semi-wrought forms. In addition to being lightweight, this alloy possesses high strength along with excellent corrosion resistance, stiffness and fracture toughness. These properties make it an attractive and feasible choice for aerospace, military and bio-engineering applications [27].

Ti-6Al-4V is usually used for applications with temperatures from -210°C to 400°C. The density of Ti-6Al-4V is 4,43g/cm<sup>3</sup>, which is 56% of that of steel. The melting point ranges from 1630°C-1650°C.

#### *2.2.1.1 Aluminium Alloying Element*

Ti-6Al-4V alloy is 6% aluminium, which stabilizes the  $\alpha$  phase and 4% vanadium, which stabilizes the  $\beta$  phase. The addition of aluminium increases the allotropic transformation temperature, the percentage of aluminium defines the value of the temperature. The 6% content is enough to strengthen the  $\alpha$  phase by solid solution, but yet, it is insufficient to cause embrittlement [29].

#### *2.2.1.2 Vanadium Alloying Element*

Vanadium is a  $\beta$  phase stabilizing additive that solid-solution strengthens the  $\beta$  phase to refine the microstructure and strengthen the alloy [30]. It is believed that the main mechanism which controls the transformation from the  $\beta$  phase to the  $\alpha$  phase is diffusional redistribution of vanadium between  $\alpha$  phase and  $\beta$  phase. The  $\alpha$  plates formed at faster cooling are thinner than those obtained at slower cooling rates due to shorter periods of diffusion [31].

Katzarov et al. [31] developed a computer program based on a predictive mathematical model designed for numerical simulation in the Ti-6Al-4V alloy of the nucleation and growth processes of the  $\alpha$  plates during  $\beta \rightarrow \alpha$  transformation. Furthermore, the authors described a numerical procedure that used vanadium concentration and temperature as variables in random nucleation simulations.

Using computer program packages, they simulated the effects of different heat treatments on the morphology of microstructural evolution. Their detailed findings are beyond the scope of this dissertation, but their model can be used to predict the morphology of the actual application of the  $\beta \rightarrow \alpha$  phase transformation in Ti-6Al-4V.

## 2.3 Microstructures and their Property Relationships

According to Lütjering [4] the titanium microstructure is determined by the composition and the thermo-mechanical treatment history and consists of different phases the most significant of which are described in section 2.3.3. These phases can be produced through diffusion control and diffusionless transformations [32]. Titanium alloys are in single-phase  $\beta$  when they are heat treated above the  $\beta$  transus temperature. On cooling, through the  $\beta$  transus temperature,  $\beta$  can undergo transformation to different equilibrium or non-equilibrium phases [33]. Different mechanical properties in the final designed product can be achieved through the manipulation of the microstructure.

### 2.3.1 Martensitic Transformation

Beta phase can transform to martensite during rapid cooling, such as oil or water quenching. Rapid cooling eliminates transformation to the alpha phase. Martensite transformation is referred to as “diffusionless,” “displacive,” and “shear-like” [34]. Martensite transformation involves the movement of atoms via a shear type reaction which produces homogeneous transformation of the bcc into

the hcp lattice over a defined volume. For the majority of titanium alloys the transformed morphology of the transformed phase is often disk shaped or plate shaped [4].

The martensitic structure can take one of two forms:  $\alpha'$  (alpha prime) is a hexagonal crystallographic structure whereas  $\alpha''$  (alpha double prime) is an orthorhombic crystallographic structure. On subsequent aging, these martensitic structures will decompose to precipitate fine  $\beta$ , which gives useful increments in strength. The type and amount of  $\alpha'$  or  $\alpha''$  that forms with quenching is dependent on the chemistry of the beta phase prior to quenching. Those alloys with increasing beta stabilizing elements have a higher tendency to form  $\alpha''$  instead of  $\alpha'$ .

### 2.3.2 Sympathetic Nucleation/Nucleation and Growth

According to Menon and Aaronson [35] sympathetic nucleation is “the nucleation of a precipitate crystal, the composition of which differs from that of the matrix, at the interphase boundary of another crystal of the same phase.” There are two primary components to the recrystallization: the nucleation phase and growth of new grains. Recrystallization is “the formation of a new grain structure in a deformed material by the formation and migration of high angle grain boundaries driven by the stored energy of deformation” [36] .

During recrystallization, the microstructure of the alloy is mainly influenced by the cooling rate from the  $\beta$  region when a thermo-mechanical process/step or heat

treatment is applied in the  $\beta$  phase field. Once the alloy is cooled gradually below the  $\beta$  transus temperature from the  $\beta$  phase field into the  $\alpha + \beta$  phase field, the  $\alpha$  phase initially will preferentially nucleate and form a continuous  $\alpha$  layer along the  $\beta$  grain boundaries. The final lamellar structure, which is known as  $\beta$  processed, is “platelike” [4].

As cooling continues, the  $\alpha$  plates will nucleate at one of two locations: along the  $\beta$  grain boundary or at the crossing point of the continuous  $\alpha$  layer. They will grow and extend into the  $\beta$  grain interior as parallel plates belonging to the same variant/morphology. They will stop growing into the  $\beta$  grain interior only when they encounter other  $\alpha$  colonies (of a different variant) that had previously nucleated at other grain boundary locations on the  $\beta$  grain. The process which is described above is known as sympathetic nucleation [4].

The retained  $\beta$  matrix remains as a thin layer separating the individual plates within the  $\alpha$  colonies. Eventually, colonies that underwent nucleation at the  $\beta$  grain boundaries can no longer fill the entire interior of the grain so they begin to nucleate on the boundaries of other colonies. As a result the total elastic strain is minimized; the new  $\alpha$  plates nucleate and grow in a nearly perpendicular orientation to the existing plane [4].

### 2.3.3 Microstructural Phases

Diffusionless transformations and diffusion-controlled transformations are the most common mechanism with which different phases can be generated within

the microstructure of titanium alloys. Taking in consideration that titanium alloys microstructure heavily depends on the thermo-mechanical processing history and composition. The manipulation of microstructure can offer a variety of different final mechanical properties in the final product. These manipulations are widely used in industry for product optimisation. The most common microstructures are described in section 2.3.4. The microstructure effect on final mechanical properties will be discussed in section 2.3.5.

#### *2.3.3.1 Primary $\alpha$*

The primary  $\alpha$  phase appears in two morphologies, lamellar [4] or equiaxed. The origin of the primary  $\alpha$  phase is not the transformation of  $\beta$  phase through nucleation and growth but it is an untransformed state as suggested by the G. Lütjering, [37]. The volume fraction, of the primary  $\alpha$  phase decreases with temperature as indicated by the phase diagram until the structure becomes fully  $\beta$  at the  $\beta$ -transus. Given an adequate amount of time, at temperatures lower than  $\beta$ -transus an equilibrium volume fraction of alpha/beta phase will develop. This phase balance is the outcome of a diffusion controlled  $\alpha \leftrightarrow \beta$  phase transformation. The primary  $\alpha$  phase is the portion that has not transformed.

#### *2.3.3.2 Transformed $\beta$*

The transformed  $\beta$  phase appears when the  $\beta$  phase is transformed into  $\alpha$  phase upon cooling through the  $\beta$  transus temperature. At  $\beta$  grain boundaries the transformed  $\beta$  phase nucleates and grows quickly during very slow cooling. At

the same time into the  $\beta$  matrix a slower diffusional growth of  $\alpha$  lamellae takes place. These  $\alpha$  lamellae are separated by an area of retained  $\beta$  as a result of solute partitioning of the alloy stabilizers. These areas of  $\alpha$  lamellae and retained  $\beta$  form colonies of individual plates. These colonies of individual plates act as larger microstructural units. Because of very small angle misorientation between these individual plates dislocation slip across the interface of the plate occurs easily [37].

#### *2.3.3.3 $\alpha$ prime ( $\alpha'$ )*

The  $\alpha'$  phase has an hcp crystal structure similar to the  $\alpha$  phase. The formation of  $\alpha'$  phase takes place at high cooling rates when martensitic or diffusionless transformation of  $\beta$  phase is combined with a low concentration of  $\beta$  stabilizers. The final microstructure is colonies of parallel sided plates or lathes, lamellar microstructure, with substructures enclosing a significant number of stacking faults and dislocations [37].

#### *2.3.3.4 Double alpha prime ( $\alpha''$ )*

Double alpha prime ( $\alpha''$ ) is a phase that occurs from the formation of a second martensitic form. The second martensitic form occurs when an alloy is quenched from a lower starting temperature and retains an increased  $\beta$  stabilizing content that will lead to a reduction of the martensitic start ( $M_s$ ) and martensitic finish ( $M_f$ ) temperatures [38].

### *2.3.3.5 Metastable $\beta$*

The rapid cooling of an alloy that has sufficient quantities of  $\beta$  stabilizers in the composition depresses the martensitic start ( $M_s$ ) and martensitic finish ( $M_f$ ) temperatures, can lead to the formation of the metastable  $\beta$  phase. The decomposition of the retained metastable  $\beta$  phase with heat treatment can create high strength alloys[38].

### *2.3.4 $\alpha / \beta$ alloys: representative microstructures*

The typical microstructure of a titanium alloy usually contains a variation of the phases mentioned above. Depending on heat treatment and cooling rate different microstructures can form: fully lamellar, bi-modal (duplex) and fully equiaxed. These microstructures are not restricted only to  $\alpha + \beta$  alloys but also can be present in other classes of titanium alloys. The different microstructures have a vast effect on the titanium alloys mechanical behaviour. Fine-scale microstructures can have a higher ductility and strength [2].

#### *2.3.4.1 Fully Lamellar Microstructure*

The full lamellar microstructure also called “ $\beta$  annealed” can be obtained by an annealing treatment in the  $\beta$  phase during the final steps of processing. The morphology depicted in Figure 2.4 shows large prior  $\beta$  grains consisting of alternating  $\alpha$  and  $\beta$  phases. The  $\alpha$  phase is placed at the grain boundary which is typical for the lamellar structure. The final microstructure is determined by the

cooling rate from the  $\beta$  phase field. An increased cooling rate results in decreased width of the  $\alpha$  layer at the grain boundary, thickness of the  $\alpha$  lamellae and size of the  $\alpha$  colonies [2].

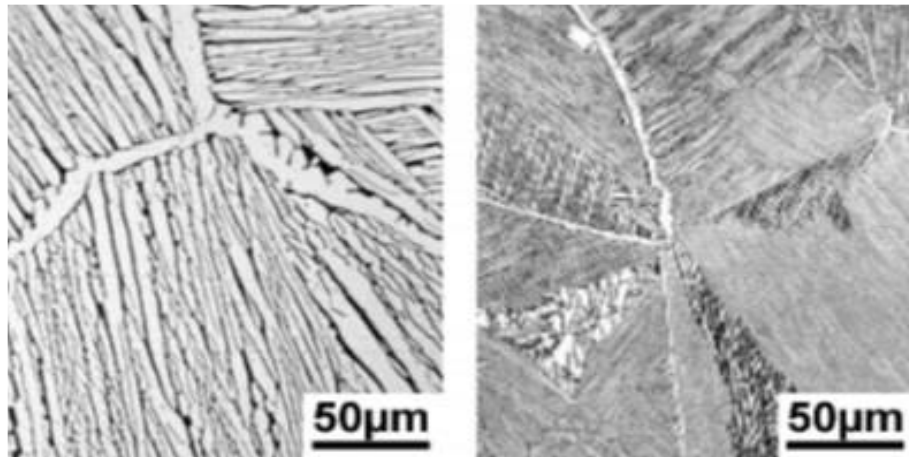


Figure 2.4: Lamellar microstructure, left obtained by slow cooling rate (1°C/min), right obtained by fast cooling rate (100°C/min) [4]

The thermo-mechanical processing route to achieve the lamellar microstructure is shown in Figure 2.5. During the first step the material is homogenized in the  $\beta$  phase field because of the lower flow stress in comparison with the alpha or alpha / beta phase field. In the second step additional deformation in the alpha / beta phase field occurs to avoid large  $\beta$  grain sizes. In the next step, at a temperature within 50°C of the  $\beta$ -transus, recrystallization of the microstructure takes place in the  $\beta$  phase field. Finally, in step four the time is not so significant as the temperature due to the fact that the temperature defines if age hardening of the  $\alpha$  phase by  $Ti_3Al$  particles takes place or not [2]. The martensitic microstructure is rarely presented in  $\alpha + \beta$  alloys due to the need of high cooling rates. In the case

that a martensitic microstructure is formed the transformation to lamellar  $\alpha + \beta$  is possible through annealing in the temperature region of about 700-850°C [4].

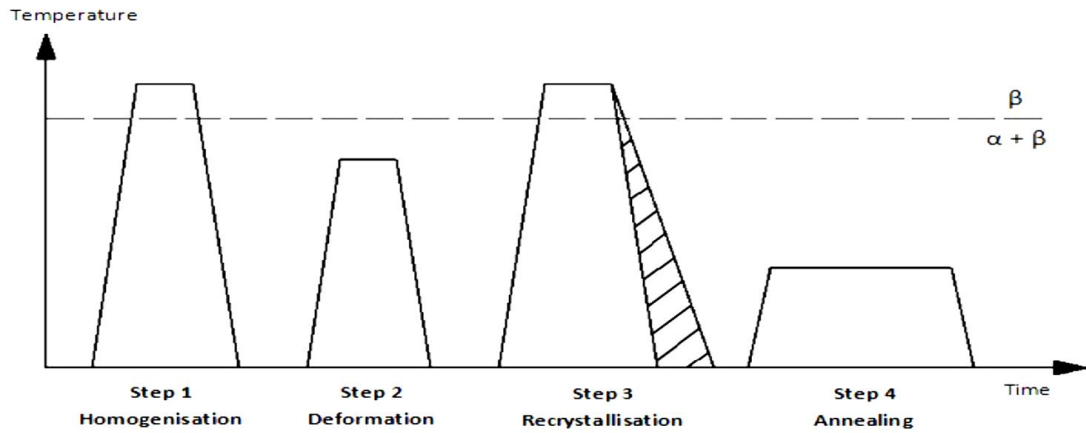


Figure 2.5: Process route for Lamellar microstructure [4].

#### 2.3.4.2 Bi-modal

The bi-modal microstructure is comprised by a matrix of alternating lamellae of  $\alpha$  and  $\beta$  plates and primary  $\alpha$  grains within this matrix. The formation of this microstructure is achieved in industry in the first step of the homogenisation process where the width of the  $\alpha$  lamellae is defined by the cooling rate from the  $\beta$  phase field. The cooling rate plays a vital role in the development of the final microstructure and mechanical properties. In Figure 2.6 the microstructures from two alternative cooling rates are presented showing the effects of fast and slow cooling rates. In the next step, the deformation of these lamellae takes place, and after that a recrystallization in the alpha / beta phase field occurs to create the bi-modal microstructure.

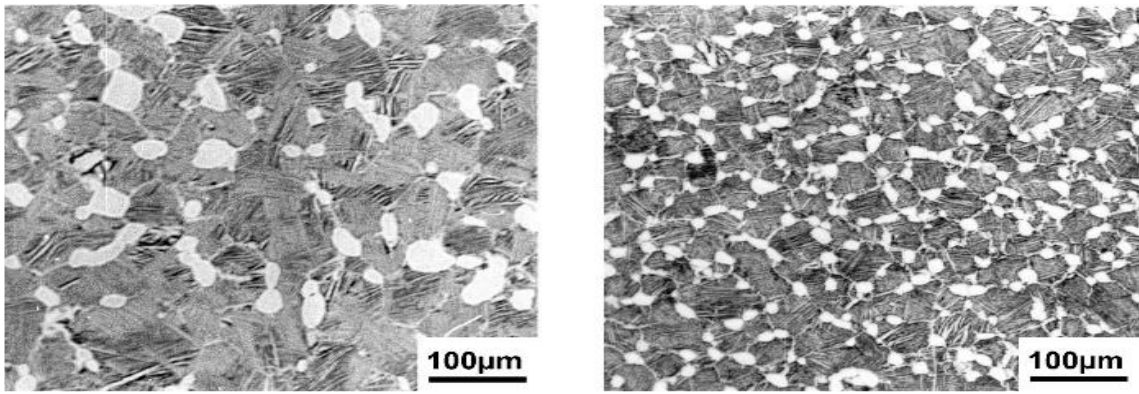


Figure 2.6: Two alternative bi-modal microstructures created from  $\beta$ -phase field by slow (left) and fast (right) cooling rates [4].

On first observation the process route to obtain the bi-modal microstructure Figure 2.7, looks similar to the process route for obtaining a fully lamellar microstructure. However, between these process routes there exists a significant difference. In the third step during the recrystallization the temperature is not set in the  $\beta$  phase field, but in the  $\alpha$  /  $\beta$  phase field. The recrystallization can be achieved only if the plastic deformation in step two is sufficient to introduce a high enough dislocation density. With the increased dislocation density eventually some of the local differences in dislocation density become large enough to overcome the capillary term to allow the formation of new grains. In step three the  $\beta$  grain size is determined through the size of the  $\alpha$  grains and the volume fraction of recrystallized equiaxed primary  $\alpha$  grains. The final volume fraction of recrystallized equiaxed primary  $\alpha$  grains is determined by the temperature. The  $\alpha$  lamellae width, strongly depends on the cooling rate from the recrystallization temperature. The grain size of the  $\beta$ , in this case, defines the length of the layers and the  $\alpha$  colony size at the  $\beta$  grain boundaries [2].

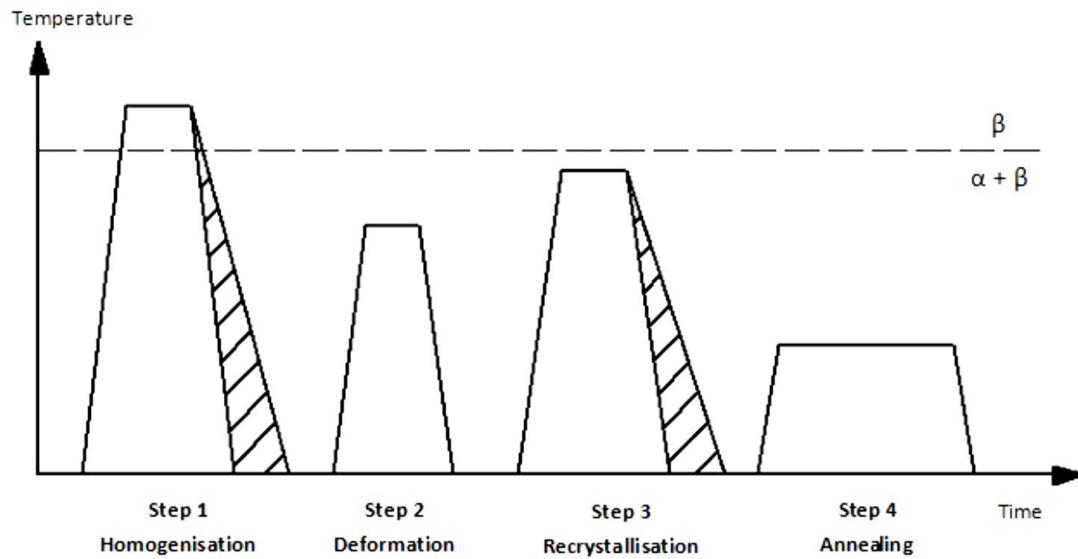


Figure 2.7: Process route for bi-modal microstructure [4].

#### 2.3.4.3 Fully Equiaxed

The process route to produce a fully equiaxed structure, as shown in Figure 2.8, is similar to the bi-modal route but with a small alteration in the recrystallization step, which can take two different routes as shown in Figure 2.9.

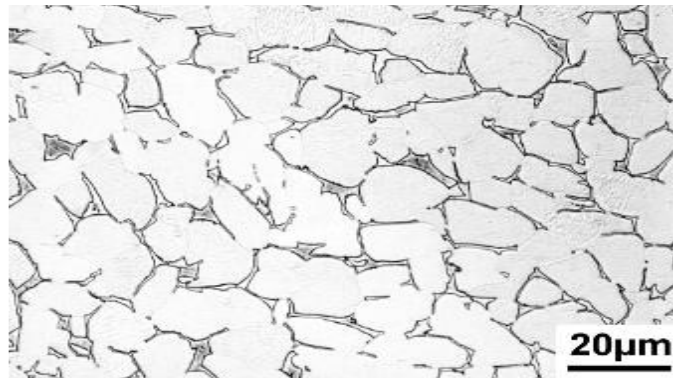


Figure 2.8: A fully equiaxed microstructure obtained from the bi-modal condition by slow cooling [4].

The reduction of the cooling rate from the recrystallization temperature is the first option that leads to no  $\alpha$  lamellae structure within the  $\beta$  grain, with the equilibrium volume fraction of  $\beta$  phase located at the “triple-points” of the  $\alpha$  grains. The result of this process is an equiaxed structure. The equiaxed microstructure can be also obtained from the deformed lamellar structure during stage three of the processing route, at such a low temperature that volume fraction of  $\alpha$  is significant enough. The mechanism followed is that the  $\alpha$  phase penetrates along  $\beta/\beta$  grain boundaries into the recrystallized  $\beta$  lamellae causing separation of the  $\beta$  grains in the final microstructure. Additional to this, during the first step of the processing route a fast cooling rate is required from the  $\beta$  phase field (step I) is a necessity to obtain fully equiaxed microstructures with small  $\alpha$  grain sizes via the low recrystallization annealing temperature route [4]. Both methods have the same result; a fully equiaxed  $\alpha$  phase with the equilibrium volume fraction of  $\beta$  phase between the  $\alpha$  grains at the “triple-point”.

The fully equiaxed microstructure can change to a bi-modal structure and vice versa. The transformation can occur by heating the material to an elevated temperature within the  $\alpha + \beta$  phase field and after that cooling it quickly for  $\alpha$  lamellar structure to form within the  $\beta$  phase. The volume fraction of primary  $\alpha$  will be the result of the exact temperature in the  $\alpha + \beta$  phase field. In the same way, the temperature must increase for the transformation from bi-modal to equiaxed so that all lamellar structures in the  $\beta$  grains dissolve followed by a slow cool to

prompt the growth of the primary  $\alpha$  phase. Significant is the fact that after each heat treatment the grain size of both  $\alpha$  and  $\beta$  grains increases.

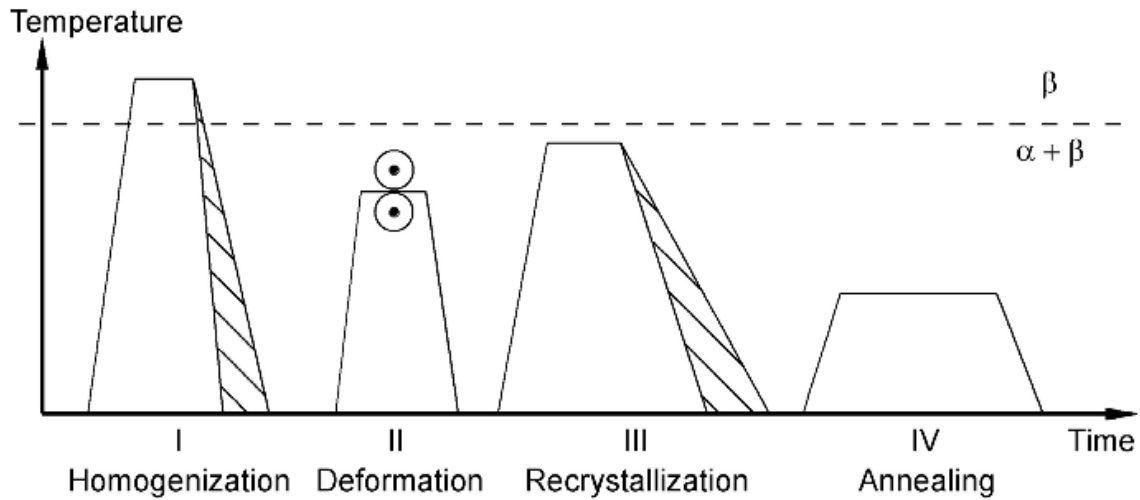


Figure 2.9: Process route for equiaxed microstructure [4].

### 2.3.5 Microstructure-Property Relationships

The mechanical properties of a material are an important factor when choosing materials for an application. These mechanical properties must fulfil all the necessary criteria required by the design and the conditions otherwise a catastrophic failure may occur during operation. One of the most demanding sectors is the aerospace industry, where applications are more challenging and high mechanical properties in intense conditions are required. In order to meet these needs the microstructure of the materials must be manipulated and controlled to high standards.

As previously discussed, the microstructure has a profound effect on the final mechanical properties. These effects are summarized in Table 2.1 where different microstructures enhance or decrease different mechanical properties. In particular, lamellar  $\alpha$  in large prior  $\beta$  grains has as a result a titanium alloy with high creep, fatigue and fracture toughness properties. These superior properties are the outcome of difficult paths encountered upon initiation of cracks[39]. Furthermore, a fine equiaxed  $\alpha$  bi-modal microstructure can give properties like crack initiation resistance, improved strength and more ductility.

**Table 2.1: Mechanical properties obtained through different microstructure based on different crystallographic orientations [6].**

Property	Fine Grain	Coarse Grain	Lamellar	Equiaxed
Elastic Modulus	0	0	0	+ / - *
Strength	+	-	-	+
Ductility	+	-	-	+
Fatigue Crack Initiation	+	-	-	+
Fatigue Crack Propagation	-	+	+	-
Fracture Toughness	-	+	+	-
Creep Strength	-	+	+	-
Superplasticity	+	-	-	+
Oxidation Behaviour	+	-	+	-

## 2.4 Deformation Modes

Plastic deformation of crystalline metals may occur by different mechanisms, dislocation slip, twinning, diffusion and phase transformations [40]. Plastic deformation is usually not restricted to a single isolated mechanism. Several mechanisms acting simultaneously are more likely. All these deformation mechanisms are however competing mechanisms that are activated under specific deformation conditions. Furthermore, their activation criterion is affected

differently by temperature and strain rate. For example, large stacking fault energy makes cross slip difficult and gliding dislocations are therefore restricted in motion which may build up large plastic stresses and activate twinning. At lower temperature and higher strain rates, then slip requires a larger stress. Then it may turn out that twinning may occur more readily than slip.

A deep understanding of titanium crystal lattice structure is essential in advance for the better comprehension of deformation modes. As has been previously mentioned titanium exists in two structures; hexagonal close-packed (HCP) structure and a body-centred cubic (BCC) structure. The two distinct structures are explained in section 2.1 and illustrated in Figure 2.1. These two structures are the main reason why titanium alloys demonstrate a high variation of mechanical properties. Furthermore, diffusion rate and plastic deformation are mainly influenced by the corresponding crystal structure. Particularly, in the hexagonal close-packed structure the Young's modulus for elasticity changes from 100GPa (stress axis perpendicular to c-axis) to 145GPa (stress axis parallel to c-axis) (0001) due to the anisotropy.

#### 2.4.1 Deformation by dislocation Slip

The plastic deformation of a crystal mainly depends on the lattice structure. For example, a lattice structure such as a hexagonal close-packed structure has a restricted plastic deformability in comparison to a body-centred cubic structure. Furthermore, the body-centred cubic structure is less deformable than the face

centred cubic structure which is among the most common in other metals. The number of slip systems which are presented in a lattice structure can be considered as one of the most important factors which influence the difference. For body-centred cubic (BCC) structure there are twelve slip systems while for the hexagonal close-packed (HCP) structure there are only three slip systems [6].

A slip system is basically a chance for a crystallographic defect to 'slip' or glide inside a crystal structure. The number of slip systems can be defined by two factors. The first factor is the number of the slip planes in which movement is likely and the second factor is the number of the directions in which movement is possible. The total number of slip systems comes from the multiplication of these two factors. The directions and planes which are most densely packed are preferential for plastic deformation [6].

A crystallographic defect prefers a path with as short length of slip as possible but also with as dense slip plane as possible. For instance hexagonal close-packed (HCP) structure has denser slip plane compare to body-centred cubic (BCC) structure. The hcp has 91% packing density and the bcc has 83% packing density. But the BCC structure possesses a shorter minimum slip path than HCP structure (BCC slip path  $b_{\min} = 1 \cdot a$ , HCP slip path  $b_{\min} = 0.78 \cdot a$ ) which has as a result the fact that BCC structures are preferred for deformation (by dislocation move) over HCP structures [6].

The HCP titanium has three basal plane slip systems and three prism plane slip systems. Nevertheless, only four independent slip systems can be acknowledged due to the lack of freedom [6]. Furthermore, the slip system on the pyramid plane cannot be entailed to be independent either, due to the fact that is composed of a prism and a basal component. As a result, in hcp titanium only three slip systems are active, Figure 2.10. Additionally, the von-Mises criterion for homogeneous deformation of metals prescribes the poor deformability of hcp  $\alpha$ -titanium by stating that is essential than there are at least five independent slip systems active. The deformation on secondary slip systems and the mechanical twinning are the main sources for the limited ductility [6].

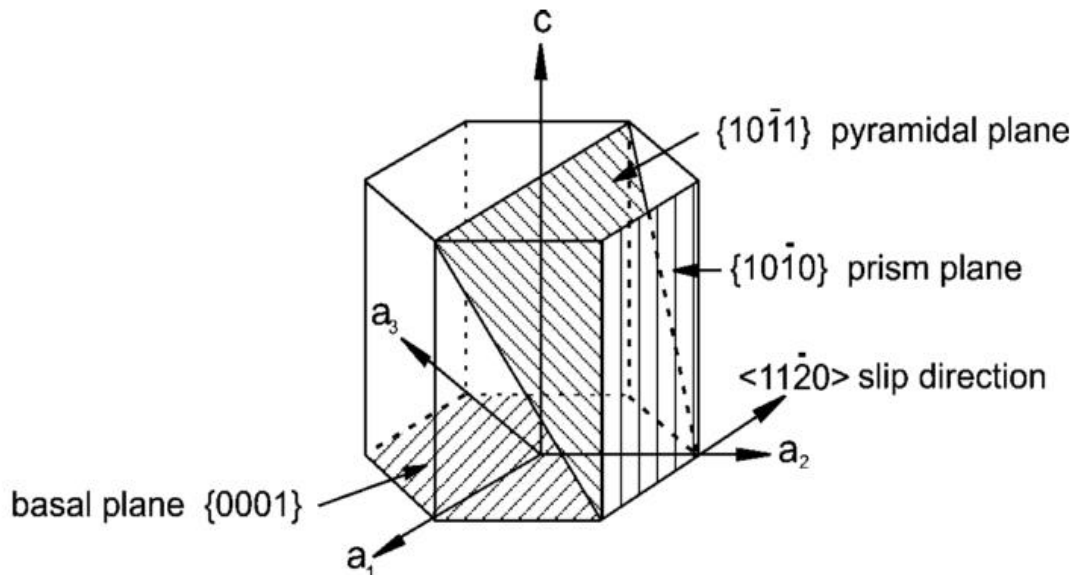


Figure 2.10: Hexagonal close-packed (hcp) structure slip system [6].

### 2.4.2 Deformation Twinning

Deformation twinning is a deformation mechanism where a portion of the original crystal will take up a new orientation under shearing. The twin portion will in the simplest cases produce a mirror image of the parent crystal [41]. The applied shear stress is the driving force. The movements of the individual atoms are small and the resulting plastic deformation which is accommodated by twinning is comparably small compared to slip. The contribution to the macroscopic strain depends on the volume fraction of the twins. However, deformation by twin formation is more pronounced when the slip systems are restricted to accommodate the imposed strain. Furthermore, metals with low stacking fault energy are known to have restricted ability to cross slip and that restricts the plastic deformation that can be accommodated by slip alone [41].

Twinning is a nucleation and growth process where the nucleation is the most critical part [42]. Growth can occur at stresses far below the nucleating stress. When the critical stress is reached, twins nucleate and continue to grow until the saturated thickness of the twin is reached which is related to the critical twin nucleus size [43]. A compilation of different results in Meyers et al. [42] showed that the critical twinning stress increases with the stacking fault energy. Furthermore the twinning density was shown to further increase when subjected to stresses beyond the critical stress for nucleation. However, twins may not only be formed during plastic deformation, they may also be formed during solid state

phase transformation or annealing. An annealing twin structure may be formed e.g. during recovery, primary recrystallization or during grain growth [44].

The plastic deformation is restricted to only three slip systems in hcp titanium and also twinning, as mentioned previously. When the stress axis is parallel to the c-axis at low temperatures the twinning mechanism is very important for plastic deformation, due to the fact that the dislocations with a basal Burgers vector are not able to move because of the orientation. The main mechanism for the activation of twinning in different planes is either compression or tension leading to a contraction or extension of the c-axis [4] [45].

## 2.5 Deformed microstructures of Ti-6Al-4V

The microstructural evolution during deformation of Ti-6Al-4V has been extensively investigated to identify the influence of strain rate and temperature on the flow stress properties under hot conditions for Ti-6Al-4V. Most of the works have been conducted by the use of mechanical testing and split Hopkinson Bar. Mechanical testing in the form of simple uniaxial compression / tension is typically used to generate results below strain rates of  $10\text{s}^{-1}$ , while the split Hopkinson Bar is used above  $10^3\text{s}^{-1}$ . As a result a significant gap within the material data is exists.

### 2.5.1 The temperature effect on the Ti-6Al-4V flow properties

Research conducted by Lee et al. deforming Ti-6Al-4V at temperatures ranging from 25 to 1100°C and high strain rate of  $2000\text{ s}^{-1}$  clearly show that increased

deformation temperature has as a result the decrease of the flow stress as demonstrated in Figure 2.11. This flow stress decrease is connected to the activation energy through the increased temperature, due to dislocations at elevated temperatures being able to emit or absorb vacancies and overcome obstacles within their path[46][47][48].

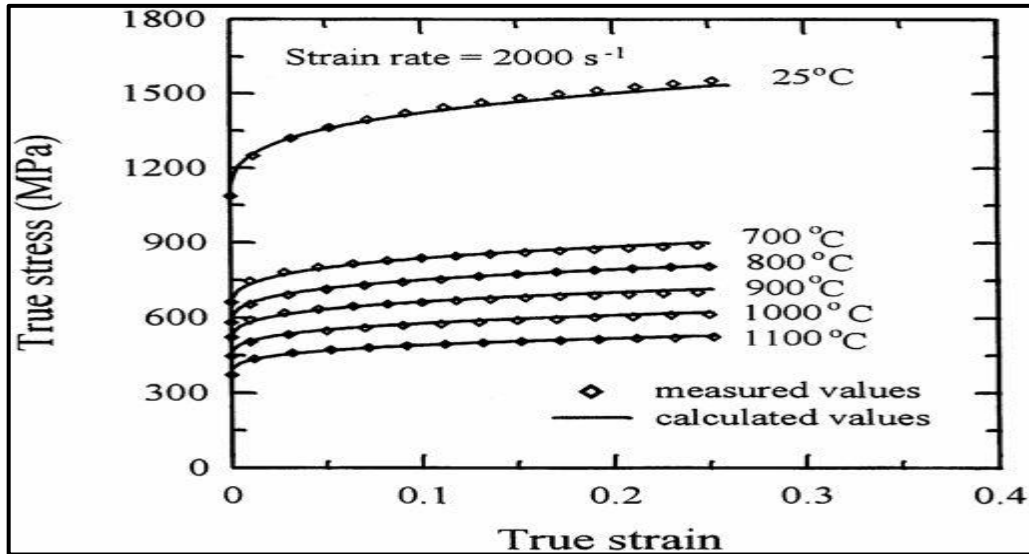


Figure 2.11: Flow curves of Ti-6Al-4V at strain rate of  $2000\text{s}^{-1}$ [46]

From a microstructural perspective Lee et al. observed that the dislocation density decreases linearly with temperature. Moreover, the dislocation cell size increases with temperature, but decreases with dislocation density [46].

### 2.5.2 The strain rate effect on the Ti-6Al-4V flow properties

At different strain rates and temperatures Sechacharyulu et al. investigated the flow behaviour of an equiaxed Ti-6Al-4V under isothermal conditions and

identified characteristic features of the flow curves [49]. Three regions are presented in the flow curves, starting with work hardening as a result of dislocation pile-ups due to the movement of dislocations being inhibited by the  $\alpha$  and  $\beta$  grain boundaries and the presence of other dislocations. A peak stress ( $\sigma_p$ ) in the stress-strain curve can be observed in Figure 2.12 as a result of the work hardening. The third region is detected after the critical peak where flow-softening takes place and can be attributed to dynamic recrystallization, adiabatic shear bands, dynamic recovery or micro-cracking[49].

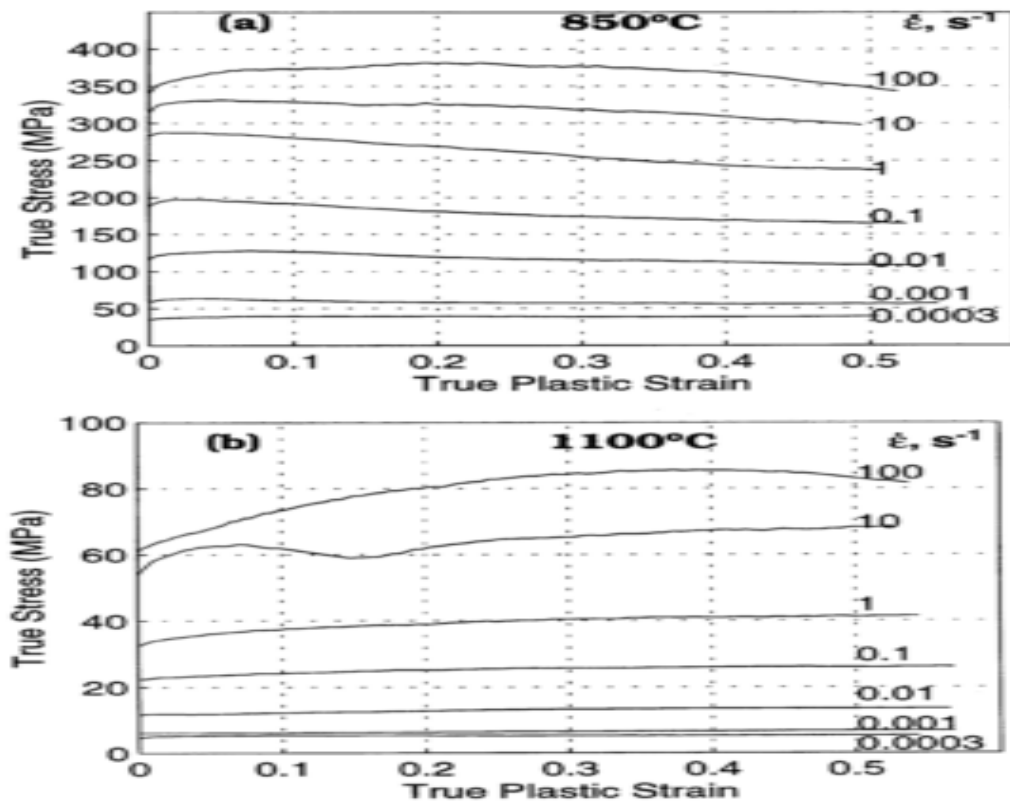


Figure 2.12: Isothermal flow curves of equiaxed Ti- 6Al-4V deformed in hot compression at strain rates of 0.0003-100 s<sup>-1</sup> and temperatures of (a) 850 °C and (b) 1100 °C[49]

At high strain and strain rates lower than  $0.1 \text{ s}^{-1}$ , at temperatures in the  $(\alpha+\beta)$  field the flow stress reaches a steady state. This takes place when work hardening and dynamic softening reach equilibrium. During deformation, the dislocation density increases, so does the driving force for dynamic recovery (DRV). Recovery takes the form of dislocations cross-slipping, or rearranging themselves by climb or annihilating each other to generate lower energy configurations. A microstructure of low angle grain boundaries and sub-grains is subsequently formed [50][44]. Provided that the dislocation density reaches a critical value, the stored energy will be large enough to facilitate dynamic recrystallization (DRX) after DRV. DRX involves high angle grain boundary migration, producing new strain-free grains with a low density of dislocations. The progressively lower density of dislocations during DRX softens the Ti-6Al-4V until reaching a steady state flow stress and grain size.

## 2.6 High Strain Rate Deformation

High strain rate deformation response is critical for a wide number of structural materials under different process conditions. Typical material processing operations, in which high strain rate deformation is observed, include material cutting, numerous forming and forging operations for automobile and aerospace applications.

Experimental tests have been conducted on a wide variety of metals and alloys in order to characterize the material responses to different strain rates and

temperatures. The results have in the majority revealed a significant different behaviour between low rate deformation and high rate deformation. The mechanical properties of materials under various strain rates can be measured by several different experimental techniques (Figure 2.13).

During titanium deformation the strain rate increases and other deformation modes set in motion due to the increased stress required to move dislocations through the metal. The most significant deformation modes are: a) deformation twinning, where deformation take place over a volume (rather than on a plane as in slip) and, b) adiabatic shear, where deformation is narrowed to a small volume of material at a locally high temperature [51]. Adiabatic shear deformation mode is frequently detected in high-speed metal forming and fabrication, ballistic impacts and explosive fragmentation and has vital effects in terms of loading conditions. It is widely believed that thermally-induced plastic instability, which suppresses work hardening in the deformed region, is the reason for the formation of adiabatic shear bands [52]. The phenomenon arises when the rate at which heat is created as a result of local plastic flow exceeds that at which it is dissipated to the surrounding material (temperature rises at a rate proportional to the plastic flow rate).

Strain Rate, s <sup>-1</sup>	Common Testing Methods	Dynamic Considerations	
10 <sup>7</sup>	<b>High Velocity Impact</b> - Explosives - Normal plate impact - Pulsed laser - Exploding foil - Incl. plate impact (pressure shear)	Shock Wave Propagation	Inertial Forces Important
10 <sup>6</sup>		Shear-Wave Propagation	
10 <sup>5</sup>		Plastic-Wave Propagation	
10 <sup>4</sup>	<b>Dynamic High</b> - Taylor anvil tests - Hopkinson Bar - Expanding ring	Mechanical Resonance in Specimen and Machine is Important	
10 <sup>3</sup>			
10 <sup>2</sup>	<b>Dynamic Low</b> High-velocity hydraulic, or pneumatic machines; cam plastometer		
10 <sup>1</sup>			
10 <sup>0</sup>	<b>Quasi-Static</b> Hydraulic, servo-hydraulic or screw-driven testing machines	Tests with Constant Cross-Head Velocity Stress the Same Throughout Length of Specimen	Inertial Forces Negligible
10 <sup>-1</sup>			
10 <sup>-2</sup>			
10 <sup>-3</sup>			
10 <sup>-4</sup>	<b>Creep and Stress-Relaxation</b>  - Conventional testing machines  - Creep testers	Visco-Plastic Response of Metals	
10 <sup>-5</sup>			
10 <sup>-6</sup>			
10 <sup>-7</sup>			
10 <sup>-8</sup>			
10 <sup>-9</sup>			

Figure 2.13: Strain rate regimes and different techniques[40]

Over the last 40 years several studies have been published aiming to explore high strain rate deformation mechanisms in metals. In the next paragraphs some of the most important studies are presented.

In 1964 Lindholm [53] published his work on strain rate dependence in copper, aluminium and lead. Lindholm used a split Hopkinson pressure bar to examine three FCC metals at strain rates up to  $10^3\text{s}^{-1}$ . The researcher concluded that a single activated mechanism was predominant, proposing that one possible mechanism of this type is the intersection of glide and forest dislocations.

Marchand and Duffy [54] used a torsional Kolsky bar to study the formation of adiabatic shear bands (ASB) at high strain rates in a structural steel. Even though their work was mainly aiming to explore the formation of ASBs they provide significant findings about the stress-strain behaviour at high strain rates. Another work from Yadav and Ramesh [55] also explore the high strain rate behaviour and mechanical properties of tungsten-based composites. In the research they reported significant differences in the failure mechanisms between the composites, on the other hand during the dynamic deformation the flow stress was similar.

The effect of high strain rate in Ti-6Al-4V was investigated by Lee and Lin [56] in terms of the compressive deformation behaviour and temperature relationship. They reported that the flow stress was affected slightly by the strain rate from  $0.02 - 1.00\text{s}^{-1}$ . Another study from Da Silva and Ramesh [57] in Ti-6Al-4V investigated the localization and deformation dependence of strain rate. The study was conducted in porous and non-porous Ti-6Al-4V at low and high strain rates ( $10^{-4}\text{s}^{-1}$ ). Research on high strain rate deformation in Ti-6Al-4V was published by Lee and Lin [46], they evaluated the deformation behaviour under a constant strain

rate of  $2 \times 10^3 \text{s}^{-1}$  at high temperatures. Lee and Lin [58] also investigated the stress-strain, temperature and possible deformation mechanisms under high strain rates ( $5 \times 10^2 \text{s}^{-1}$  and  $3 \times 10^3 \text{s}^{-1}$ ). The results show that flow stress, material constants and work hardening coefficient are sensitive to strain rate and temperature. Evaluation of temperature effects shows that temperature sensitivity increases with the increase of temperature, but is independent of strain rate.

Alpha-titanium response to high strain rate deformation was examined from Chichili et al. [59] in terms of underlying deformation mechanisms. They observed that in high strain rates the strain-hardening is greater than in low strain rates. Furthermore, they reported an increase in twin' density with the increase of strain rate. Beta-titanium alloys were investigated by Weiss and Semiatin [60] as part of the thermo-mechanical processing review they published. They summarised the final mechanical properties and high temperature deformation mechanisms of several beta-titanium alloys at low and high strain rates. Deformation mechanisms and mechanical properties in pure titanium were investigated by Nemat-Nasser et al. [61] at high strain rate. They reported that the flow stress is highly dependent on strain rate and temperature.

Ti-6Al-4V with an equiaxed alpha-beta microstructure was studied by Sechacharyulu et al. (Seshacharyulu et al. 2000a) at low and high strain rate ( $10^3 \text{s}^{-1}$  -  $100 \text{s}^{-1}$ ). They used hot compression tests at different strain rates and temperatures to achieve microstructural control and obtain processing windows during hot working. They reported that at strain rates higher than  $1 \text{s}^{-1}$  (high strain

rate) the material exhibits flow instabilities. The flow instability at high strain rates was also reported for a lamellar microstructure by Sechacharyulu et al. (Seshacharyulu et al. 2002b).

Titanium undergoing ballistic impact and penetration was investigated by Meyer and Kleponis [63] in term of high strain rate behaviour and modelling. They conducted high strain rate experiments (up to  $2000\text{s}^{-1}$ ) in Ti-6Al-4V to generate constants for the Zerilli-Armstrong (ZA) and Johnson-Cook (JC) models and compared the two models with the experimental results. The JC model did not perform as well as the ZA model, where the ZA model better represented the ballistic behaviour in the velocity range between 1200 m/s and 2000m/s.

Bruschi et al. [64] carried out hot compression tests at high strain rates aiming to investigate the workability of Ti-6Al-4V. They used a constitutive equation to calculate the flow stress and obtain the material behaviour for forging process simulation. They identify that the plastic flow is stable, in the investigated range ( $880^{\circ}\text{C}$  and  $950^{\circ}\text{C}$ ), only for temperatures between  $940^{\circ}\text{C}$  and  $950^{\circ}\text{C}$  and strain rate lower than  $15\text{ s}^{-1}$ . These values correspond to a stable deformation zone and represent the optimal conditions for hot working of the Ti-6Al-4V alloy.

In 2007 Khan et al. [65] conducted a series of multi-axial loading experiments on Ti-6Al-4V at high strain rates in order to study the material behaviour under deformation. They used the Khan-Huang-Liang (KHL) model [66] to predict and

to observe the material response. They concluded that the model was reacting well and was able to predict the material's behaviour.

The shear behaviour of Ti-6Al-4V under high strain rate deformation was investigated by Peirs et al. [67]. They used hat-shape specimens and a compression split Hopkinson bar to analyse and understand the mechanisms underlying shear behaviour. Results show micro-cracks and micro-voids were initiated at different places along the shear band where a low hydrostatic pressure exists and they follow the same orientation of the grains. Large cracks were formed by a process of void growth and coalescence

In 2012 Gray [21] published a review in high strain rate deformation of materials. He summarises the deformation twinning in BCC, FCC and HCP metals under high strain deformation as well as the point defect production, the dynamic recovery and shock-induced phase transformations.

## 2.7 Process map and Instability

During the manufacture of engineering components the mechanical processing is a vital step because it is used not only to obtain the required shape, but also to achieve the required microstructure and properties. During the manufacturing process the key task is the selection of the controlling process parameters which will reach the part quality as well as the desirable physical and mechanical characteristics. These process parameters are a sequence and number of

material deformation operations; where temperature, rate of deformation, strain all have a significant influence, and also heat treating operations[68].

During the manufacturing process workability problems may arise due to deformation localisation. This flow localisation can lead to failure during the service of the component because of different properties and structure in the region of the localisation. In the absence of chilling effects frictional flow localisation may occur during hot deformation. The result will be flow softening. The reasons behind flow softening are structural instabilities such as adiabatic heating, dynamic recrystallization, spheroidisation or grain coarsening. The understanding of the material workability (process map) is essential for the development of successful manufacturing processes[68].

The processing map was first proposed by Ray [69] and further developed by Prasad et al. [70] based on the dynamic material modelling (DMM). Such process maps have been developed and used to optimize the hot manufacture processes and control the final microstructure of the engineering part[71].

With the process maps the plastic instability criteria also emerge. The “safe” and “unsafe” regions during hot working are determined by the plastic instability criteria which are very important during hot working and a number of criteria have been proposed in the past 30 years [72]. Some of these criterial will be presented in this section.

One of the most popular criteria was proposed by Prasad et al for evaluating the flow instability. The criterion is based on the principles of irreversible thermodynamics as applied to large plastic flow, and the authors suggested that flow instability will occur during hot deformation if:

$$\xi(\dot{\epsilon}) = \frac{\partial \ln \left( \frac{m}{m+1} \right)}{\partial \ln \dot{\epsilon}} + m < 0$$

Where  $m$  is the strain rate sensitivity of the flow stress,  $\dot{\epsilon}$  is strain rate, and  $\xi(\dot{\epsilon})$  is the instability parameter [70][71][71]. This instability criterion was questioned by some scholars because of the assumption that strain rate sensitivity was constant.

Because of that reason Murty et al. proposed a more strict plastic instability criteria based on the second law of thermodynamics theory and the Liapunov equation. The assumption for this instability criterion was that the strain rate sensitivity  $m$  is not constant, and the power dissipation efficiency ( $\eta$ ) was derived from J co-content (according to DMM):

$$\eta = \frac{J}{J_{max}} = 2 \left( 1 - \frac{1}{\bar{\sigma} \dot{\epsilon}} \int \bar{\sigma} d\dot{\epsilon} \right)$$

Where  $J_{max}$  is the maximum of co-content and for unstable material flow  $2m < \eta < 0$  [73][68][71][74].

Semiatin et al. proposed a phenomenological criterion that correlates the flow softening with the materials properties, such as the normalized flow softening rate ( $\gamma$ ) and the strain rate sensitivity ( $m$ ), by a parameter  $\alpha = -\gamma / m$ , where  $\alpha$  is an

instability parameter, for plain strain compression. Based on experimental results on titanium and its alloys, they have recommended a condition of  $\alpha > 5$  for flow localization or fracture to occur during hot deformation[75][76].

Malas and Seetharaman also proposed an instability criterion by considering that  $\eta$  is the same as the strain rate sensitivity[77]. The four conditions proposed for stable material flow are:

$$\begin{aligned} 0 < m < 1 & \qquad \frac{\partial m}{\partial \ln \dot{\epsilon}} < 0 \\ \frac{\partial s}{\partial \ln \dot{\epsilon}} < 0 & \qquad s \geq 1 \end{aligned}$$

Where  $s$  is the temperature sensitivity.

Ti-6Al-4V has been investigated by many researchers in terms of process mapping and instability. First was Prasad et al. who presented the process map of an ELI grade Ti-6Al-4V with transformed (Widmanstätten) preform microstructure, the map was for strain rate  $0.001\text{s}^{-1}$  to  $100\text{s}^{-1}$  and temperature from  $750^{\circ}\text{C}$  to  $1100^{\circ}\text{C}$ [74].

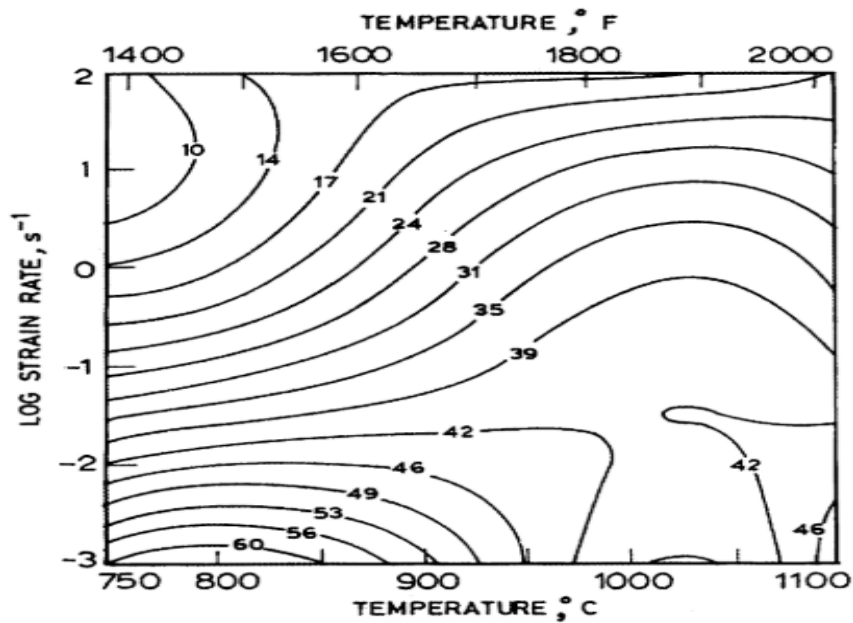


Figure 2.14: Processing map obtained on Ti-6Al-4V with 1000 ppm oxygen and equiaxed  $\alpha+\beta$  preform structure. Contour numbers represent percent efficiency of power dissipation [74].

Based on the map for the specific material Prasad et al. identified two instability areas: in the  $\alpha+\beta$  range (lower than 800°C and above  $0.1\text{ s}^{-1}$ ) as well as in the  $\beta$  range (above 1050°C and  $10\text{ s}^{-1}$ ). These areas were investigated through optical microscopy and were identified as adiabatic shear bands (ASBs) and flow inhomogeneity of  $\beta$ , respectively. The microstructure of the specimen deformed at 750°C and  $100\text{ s}^{-1}$  exhibiting adiabatic shear bands at an angle  $45^\circ$  to the compression axis[74].

Another work presented by Aneta et al. on Ti-6Al-4V where test was carried out in a wide range of temperatures (800°C–1100°C) and strain rates ( $0.01\text{ s}^{-1}$ – $100\text{ s}^{-1}$ ), up to the constant final true strain value of 0.9 (Figure 2.15)[78].

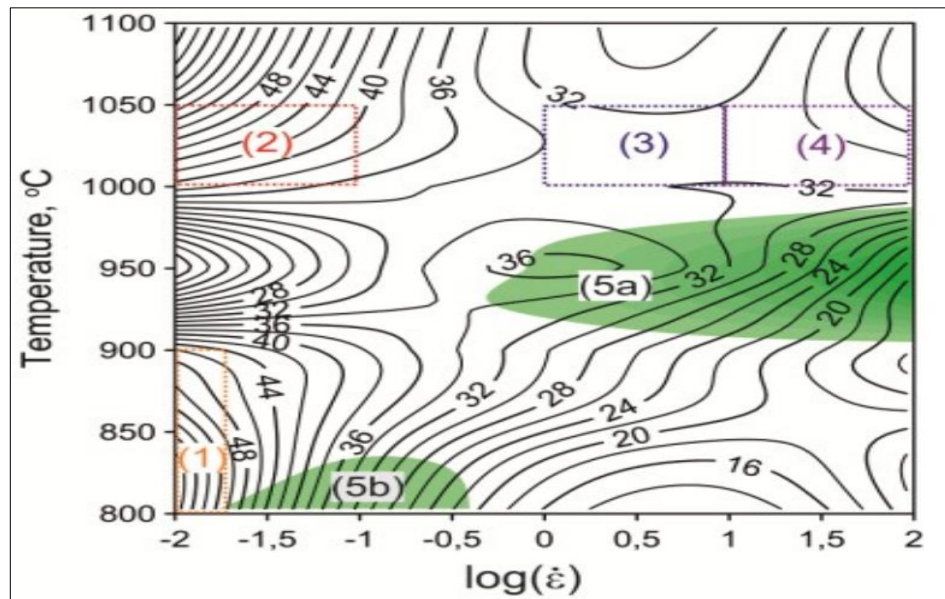
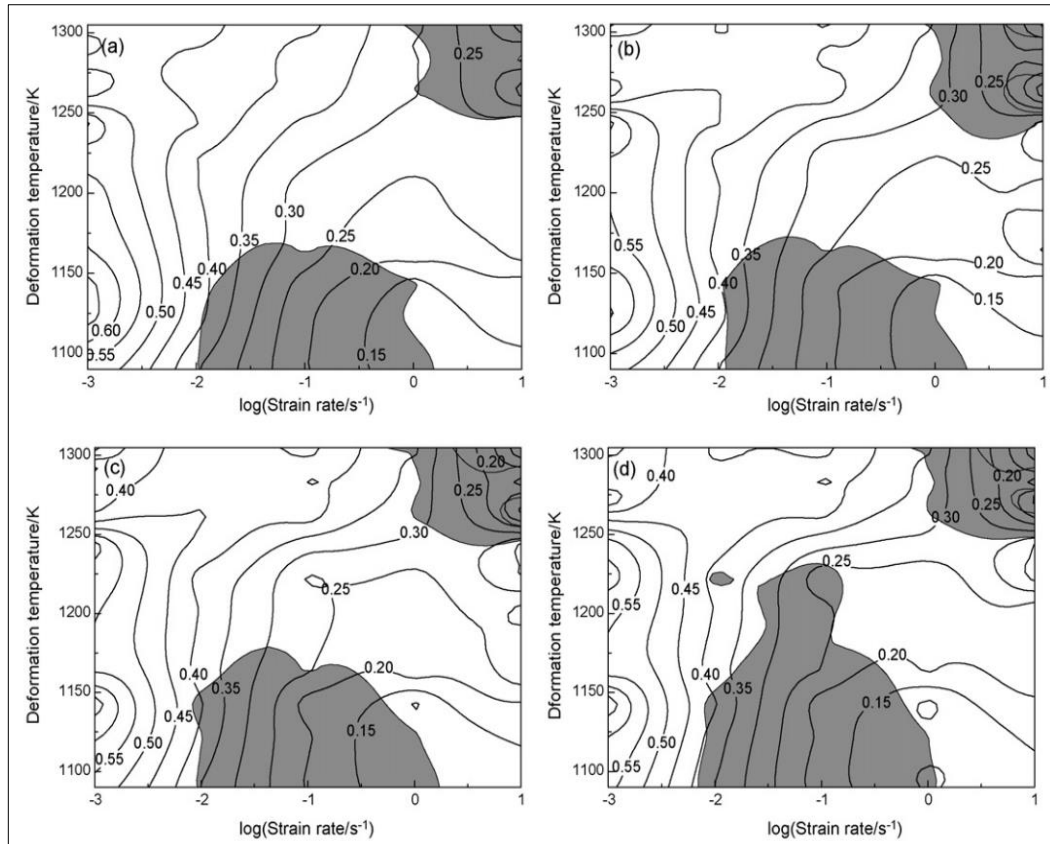


Figure 2.15: Process map of Ti-6Al-4V at 0.9 of strain by Aneta et al.[78]

Two instability regions were reported by the authors' area 5a and 5b, marked by green colour in the process map (see Figure 2.15), although the authors were not specific about mechanisms. Also Luo et al. [79] investigate Ti-6Al-4V in terms of the effect of strain at the process map. The research was conducted in a wide range of temperatures (820°C–130°C) and strain rates (0.001s<sup>-1</sup>–10s<sup>-1</sup>) (see Figure 2.16). They concluded that the final grain size of primary  $\alpha$  phase of Ti-6Al-4V alloy varies significantly with increasing strain due to the combined action and competition one another of several different mechanisms in high temperature deformation. Furthermore, the strain significantly affects the efficiency of power dissipation of Ti-6Al-4V alloy at the strain rates of 0.001s<sup>-1</sup> and 10.0s<sup>-1</sup>, however at a strain rate of 0.1s<sup>-1</sup> in the  $\beta$  single-phase region the effect of strain on the efficiency of power dissipation is slight. And finally, the instability parameter of Ti-6Al-4V alloy varies significantly with strain at each strain rate and deformation

temperature. The unstable flow of Ti-6Al-4V alloy easily occurs at a strain rate of  $0.1\text{s}^{-1}$  in the  $\alpha+\beta$  two-phase region and a strain rate of  $10.0\text{s}^{-1}$  in the  $\beta$  single-phase region.



**Figure 2.16: Processing maps of Ti-6Al-4V alloy at the strains of: (a)  $\epsilon=0.3$ ; (b)  $\epsilon=0.4$ ; (c)  $\epsilon=0.5$ ; (d)  $\epsilon=0.6$ ; (e)  $\epsilon=0.7$ . Numbers represent efficiency of power dissipation. Shaded areas represent the instability regions[79].**

The process map of a full lamellar microstructure was investigated by Zhang et al. [80] by conducting isothermal hot compression tests at three strains 0.3, 0.5 and 0.69, at temperature of  $700\text{--}1000^\circ\text{C}$  and strain rates of  $0.001\text{--}10\text{s}^{-1}$  (see Figure 2.17).

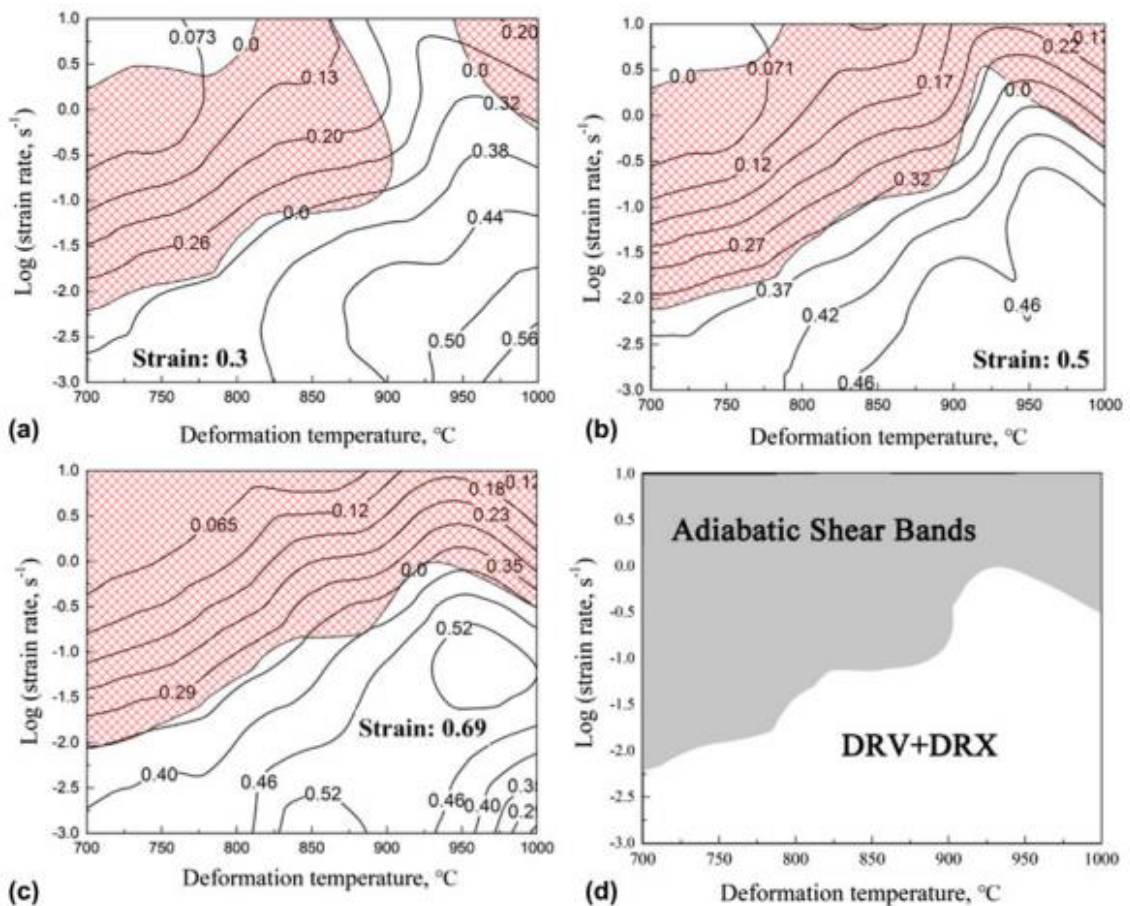
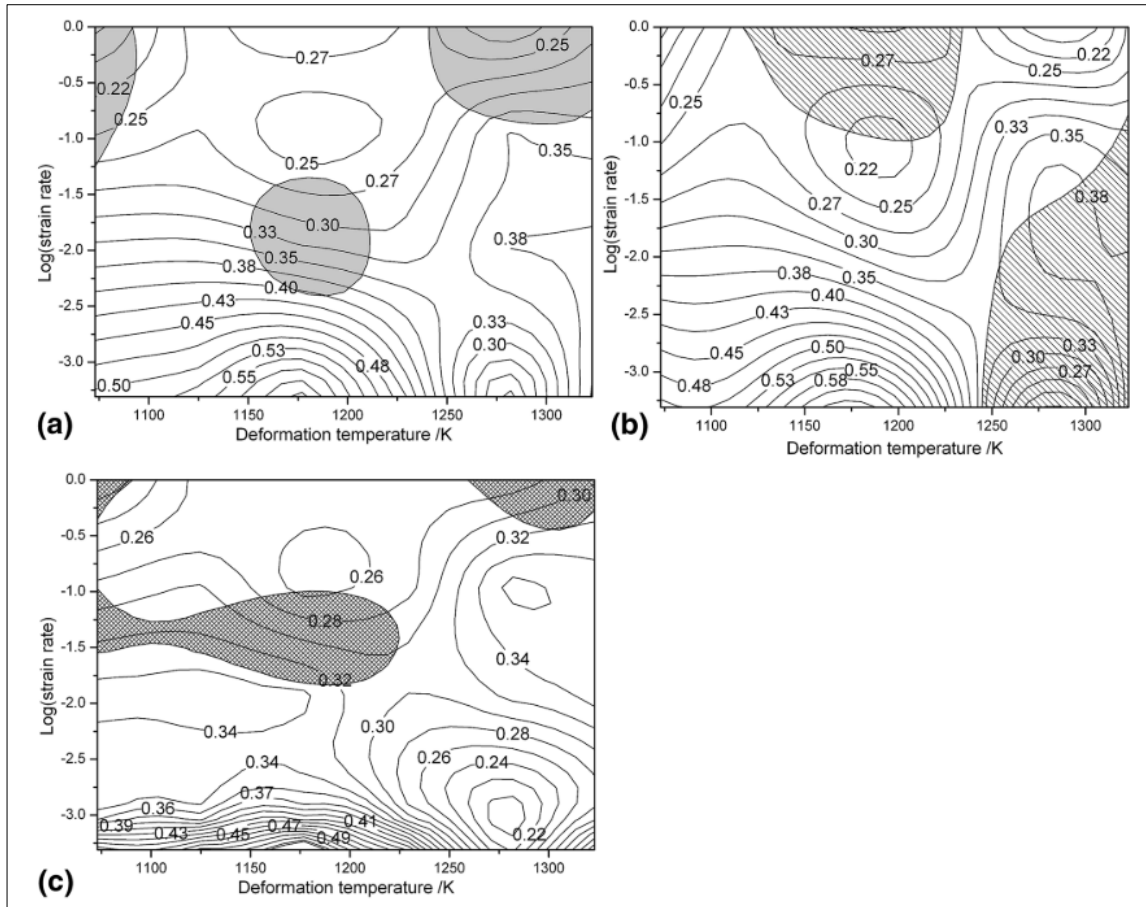


Figure 2.17: Processing maps of the Ti-6Al-4V alloy at the strains of (a) 0.3, (b) 0.5, (c) 0.69, and (d) all the strains[80].

Based on their observation they report that the instability domain increased with increasing strain and it mainly located in the low temperature and high strain rate range. Furthermore, the unstable flow was mainly attributed to the presence of adiabatic shear bands, and the main dynamic softening mechanism has been confirmed as DRX together with DRV.

Various instability criteria for the development of a Ti-6Al-4V process map were investigated by Cai et al. by hot isothermal compression tests in the strain rate of

$0.0005\text{s}^{-1}$  and temperature range of  $800\text{-}1050^\circ\text{C}$ . They developed a process map based on the instability criteria of Prasad, Malas and Murty's (see Figure 2.18).



**Figure 2.18:** Processing maps obtained from (a) Prasad's criterion; (b) Malas' criterion; and (c) Murty's criterion[72]

The authors' presented results that reflected similar trends to the predicted instability areas using Prasad's and Murty's criteria. The peak efficiency of power dissipation, corresponding to the optimal deformation conditions, was located on power dissipation maps with the deformation temperature of  $1173\text{K}$  and the strain rate of  $0.005\text{s}^{-1}$ , which indicates that both criteria can be used to determine the optimal deformation domain for Ti-6Al-4V alloy. The instability domains in the

processing maps obtained from Prasad's criterion, Malas' criterion, and Murty's criterion showed significant differences. Overall, the processing map that was developed using Murty's criterion was determined to be more accurate (through microstructure observations) than those developed using other criteria.

## 2.8 Adiabatic shear bands

Lee and Lin [81] describe the adiabatic shear banding as “a localized plastic instability phenomenon resulted from dynamic impact and high speed loading”. In 1941 Trent was the first to describe the adiabatic shear phenomenon, and in 1944 the phenomenon was observed for the first time by Zener and Hollomon [81]. Rogers [82] was the first that classified the adiabatic shear bands into two types “transformed” and “deformed”. When metals are subjected to large plastic deformations, it is possible to cause localization of plastic flow due to the localized heating. The phenomenon is usually catastrophic; leading to fracture by localized shearing [83].

During high strain rate deformation of titanium alloys, adiabatic shear bands are frequently formed; these bands are narrow zones of highly localized flow. This deformation mode is detected in high-speed metal forming and fabrication, ballistic impacts and explosive fragmentation and has vital effects in terms of loading conditions. It is widely believed that a thermally-induced plastic instability effect, which suppresses work hardening in the deformed region, is the reason for the formation of adiabatic shear bands [52]. This phenomenon is concentrated in

narrow bands close to the plane of maximum shear stress due to elevated material temperature [51]. The phenomenon arises when the rate at which heat is created as a result of local plastic flow exceeds that at which it is dissipated to the surrounding material (temperature rises at a rate proportional to the plastic flow rate).

A number of studies have been carried out to identify the mechanisms that lie behind the formation of adiabatic shear bands. Me-Bar and Shechtman [84] investigated Ti-6Al-4V under various heat treatment and strain rates as ballistic targets. They observed that at shear bands the high rise in temperature can cause transformation from alpha phase to beta phase. Furthermore, they observed that micro cracks are formed within the bands due to tensile stress vertical to the shear surface. Timothy and Hutchings [85] also investigated the different structure of ASB in Ti-6Al-4V after ballistic impact. They concluded that the ASB consisted of regions of high shearing distortion of the original microstructure. A critical review from Timothy [86] about the structure of adiabatic shear bands in metals summarises the results of several researchers for “transformed” and “deformed” shear bands for steel, aluminium and titanium alloys.

Marchand and Duffy [54] examined a low alloy structural steel in terms of local strain and temperature during the formation of an adiabatic shear band. They revealed that the shear bands propagate in the material with a speed of 510m/sec and the plastic deformation follows a three stage process in which the final stage is the formation of fine shear bands due to localisation of the strain distribution. In

1993 Shahan and Taheri [87] published a review about the modes of fracture, mechanical properties, microstructure and formation of adiabatic shear bands in titanium alloys summarising four decades of research.

Grady [88] performed a critical path analysis to calculate the shear band toughness for a number of different metals. He reports that the magnitude of shear band toughness had a correlation to the corresponding fracture toughness of every metal he studied.

The shear band formation in alpha-hcp titanium has been studied by Meyers et al. [89] by compression testing with a Kolsky bar in hat shape specimens. They have reported that the formation of shear bands takes place in two phases. In the first phase is instability, produced by thermal softening and the enhancement of the thermal assistance in the motion of dislocations; the second step is localization, which requires softening due to major microstructural changes in the material. Furthermore, they have observed that the shear band region consists of a mixture of elongated sub-grains and equiaxed micro-grains. Zhou et al. [90] investigated the initiation and propagation of shear bands in C-300 steel and Ti-6Al-4V. They have observed that shear bands are more diffused in Ti-6Al-4V and at the same time Ti-6Al-4V presents a stronger resistance to shear banding. In the same year Yang et al. [91] with the use of OM, SEM and TEM presented research about the microstructure of adiabatic shear bands in pure Titanium. They revealed that the microstructure in adiabatic shear bands consisted of a very fine equiaxed grains with a low dislocation density.

In 1997 Molinari [92] used analytical methods to characterise the spacing between adiabatic shear bands. He has proposed explicit solutions for materials with no strain hardening. In addition, he has achieved results for strain hardening materials by using asymptotic developments. Another significant piece of research in adiabatic shear banding had been conducted by Liao and Duffy [93]. They investigated the initiation and formation of ASB in Ti-6Al-4V by dynamic torsional experiments. They reported that during the localization of intense shear strain in the shear band area, the temperature in that area increased very fast. Additionally, inside the ASB the microstructure consists of fine and high elongated grains parallel to the shear direction.

The propagation and microstructure of ASB was investigated by Li et al. [94] in terms of simulations by using the mesh-free Galerkin approximation in two and three dimensions. They concluded that the use of mesh-free interpolations is efficient to avoid mesh alignment sensitivity and it can relieve mesh-distortion. Furthermore, they reported that the use of multi-physics models permits the simulation of dynamic shear band propagation and it predicts the thermo-mechanical instability that takes place inside the ASB. Another investigation of the propagation of ASBs was conducted by Bonnet-Lebouvier et al. [95] based on research of Marchand and Duffy. Based on their research they introduced the concept of “process zones” which they define them as “a region propagating with the shear band tip, where an intense stress softening is produced by thermo-mechanical coupling”.

Molinari et al. [96] have investigated Ti-6Al-4V in terms of formation of ASBs during high speed machining. Their study primarily aimed to analyse the evolution of the cutting force in the terms of ASB development and cutting speed. Burnes and Davies [97] also investigated the formation of ASB during high speed machining. Their research focused on the comparison of the formation of repeated ASB formation during high speed machining and the well-known single shear band formation. Xue et al. [98] investigated the evolution of multiple ASB in Ti-6Al-4V and pure titanium. They observed that the evolution of ASBs patterns shows a self-organization character during deformation. Furthermore, they discovered that the number of ASBs in Ti-6Al-4V was less than in pure titanium but the propagation velocity is almost three times higher.

Pure titanium and Ti-6Al-4V are not the only materials prone to the formation of ASBs. Researchers like Qiang et al. [99] and Meyers et al. [100] investigated the evolution and formation of ASBs also in other materials. Qiang et al. studied the Ti17 alloy and Meyers et al. with the use of the collapse of a thick-walled cylinder and compression Kolsky-Hopkinsons bar investigated AISI 304L stainless steel. Furthermore, Wei et al. [101] explored the formation of ASB in ultrafine grained (UGF) Fe during severe plastic deformation and Lins et al. [102] investigated the microstructure of ASB in a interstitial free steel. In 2006 Yang and Wang [103] studied the micro-texture and microstructure of ASB in alpha-titanium. The result of their investigations points to the fact that dynamic recrystallization occurs inside adiabatic shear bands.

Wang [104] researched Ti-6Al-4V ASB formation and focused on the calculation of local shear deformation. He observed that the decrease of flow shear stress, beyond the occurrence of adiabatic shear bands, is slower than the local plastic deformation inside the ASBs; leading to shear localisation increasing. Because ASBs formation is considered as one of the failure modes. Teng et al. [105] studied the ASBs in terms of fracture initiation and propagation through numerical simulations. Ranc et al. [106] studied the initiation and propagation of ASBs through temperature heterogeneities and proposed an experimental device to measure the temperature in ASBs.

In 2009 Liu et al. (Liu et al. 2009a) presented their work in Ti-6Al-4V and the impact of strain rate and microstructure on the ASBs. In the same year another two works were presented for Ti-6Al-4V; the first from Murr et al. [108] studied the ASB failure due to microstructure evolution and the second from Liu et al. (Liu et al. 2009b) correlated ASB formation with fracture.

In last five years several works have been published about the adiabatic shear bands in titanium alloys. Beta-Ti alloys have been investigated by Yang, Jiang et al. [110] and Yang, Li et al. [111] in terms of microstructural evolution and microstructure effects respectively. Even though, several Ti alloys have been introduced the last years, Ti-6Al-4V continues to maintain a strong position in the aerospace industry. As a result the most recent works published for ASBs referred to Ti-6Al-4V. Two of them examine the formation of ASBs in machining; Wan et al. [112] studied the microstructural evolution and Ye et al. [113] modelling the

evolution of ASBs. ASBs formation in Ti-6Al-4V was investigated in terms of microstructure by Peirs et al. [114], microstructural effects by Osovski et al. [115] and fracture by Zhang et al. [116].

The majority of the research which is presented in this chapter were conducted with compression or torsion Kolsky-Hopkinsons bar or Taylor impact tests which are very accurate in ultra-high strain rates (above  $1000\text{s}^{-1}$ ). For strain rates in the area of  $1\text{-}300\text{ s}^{-1}$  where forming and forging occur, a significant gap arises due to the range of equipment available for this strain rate range and lack of accuracy of the existing equipment. The need for experimental results at the range of  $1\text{-}300\text{ s}^{-1}$  have created the need for new dedicated equipment able to produce accurate experimental results. Such results may be used to simulate more accurate future forming and forming procedures aiming to reduce the cost and achieve improved microstructure and mechanical properties.

Based on the need for dedicated equipment for simulating the forming and forging range of strain rates, in the next chapter were presented a bespoke servo-hydraulic equipment owned by the AFRC and used in this research. The challenges and the process optimization and verification of the equipment is presented also.

### 3 High strain rate process optimization

The servo-hydraulic forging simulator (Phoenix), was manufactured by Phoenix Calibration & Service Limited under the Advanced Forming Research Centre (AFRC) directions and specifications; Figure 3.1, is a state of the art forging simulator based on a bespoke design able to reach strain rates up to  $300\text{s}^{-1}$  [117]. Since the equipment is unique, the experimental challenges will be highlighted, and discussed. The route of experimental process optimization is described in the chapter.



**Figure 3.1:** Servo-hydraulic forging simulation a) machine, b) chamber and c) interior

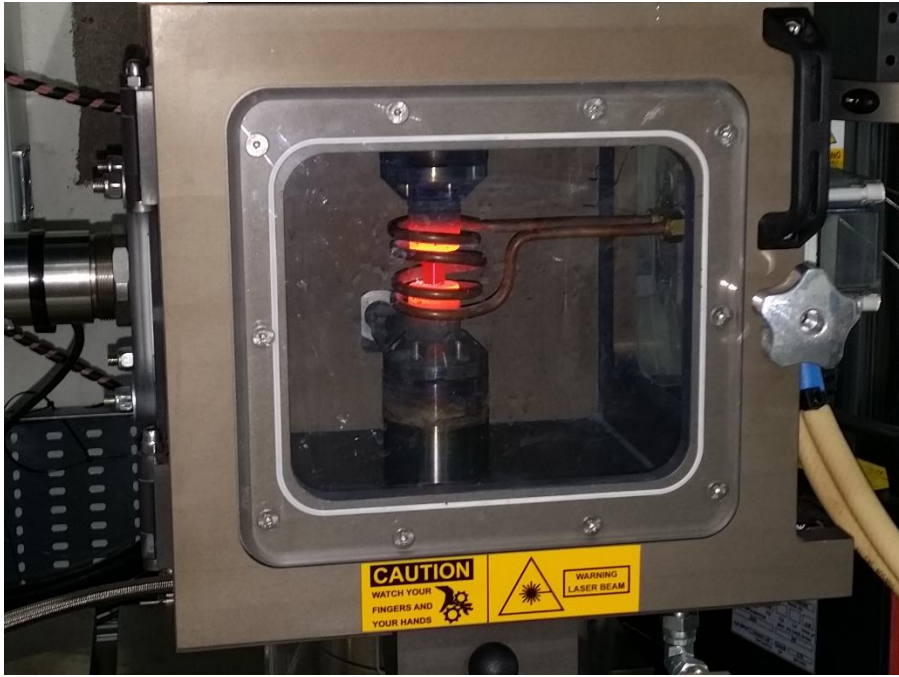


Figure 3.2 Environmental chamber

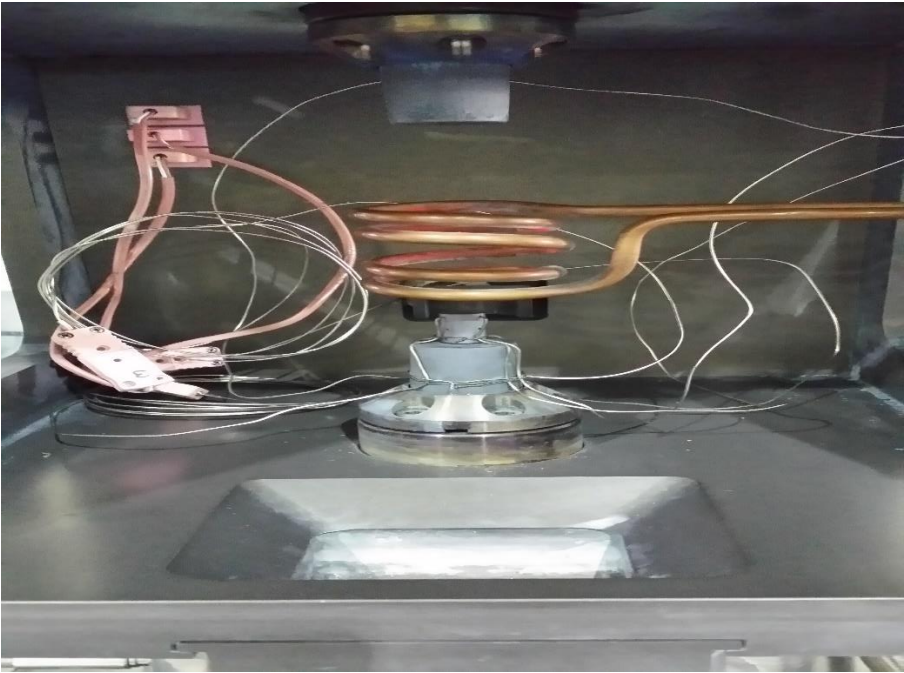


Figure 3.3 Interior of the environmental chamber

### 3.1 Equipment description

The servo-hydraulic forging simulator (Phoenix) is capable of conducting experiments (under strain rate control) in the range of “medium” strain rates up to maximum of  $300\text{s}^{-1}$ , and is equipped with 2 load cells; the first is 100KN and the second 500KN. The current set-up is adjusted for compression tests, accommodating samples with dimensions of 12mm diameter and 18mm long, the specimens dimensions conform to NPL code for practice for hot compression testing [118]. The multi-functional design provides the capability for other geometries also. Furthermore, the machine is capable for tensile and fatigue tests. An unusual and at the same time unique characteristic is that both platens move during the compression test in contrast with conventional equipment where only one of the platen will move. Furthermore, each platen can be controlled independently from the other which confers considerable freedom in setting up complex displacement regimes.

The system is also equipped with an environmental chamber and argon supply system which allows experiments to be carried out in a neutral (non-oxidizing) environment and at the same time prevents the corrosion of the tungsten carbide platens. Additionally, an automatic quenching system is installed in the chamber which makes possible fast quenching (within less than 5 sec from the end of the experiment).

For high temperature experiments an induction heating system is used capable of generating temperature up to 1300°C, the system has been designed to be very flexible in terms of coils geometry (different coils can be used based on the material being tested) and heating ramps. The temperature may be controlled either using a pyrometer attached in the environmental chamber or by thermocouples (up to eight thermocouples can be used simultaneously to monitor the temperature).

Two software packages support the equipment with distinct functions; Figure 3.4. The first software “Constant Strain Rate Profile Creator” is specially designed software dedicated for forging or compression tests. The input parameters for the experiment are; the strain rate, the true final strain, the acceleration gap, the profile duration, overshoot period and the PID (Proportional-Integral-Derivative controller). The second software is the “Profile Builder” which is dedicated to create a multistep forging profile.

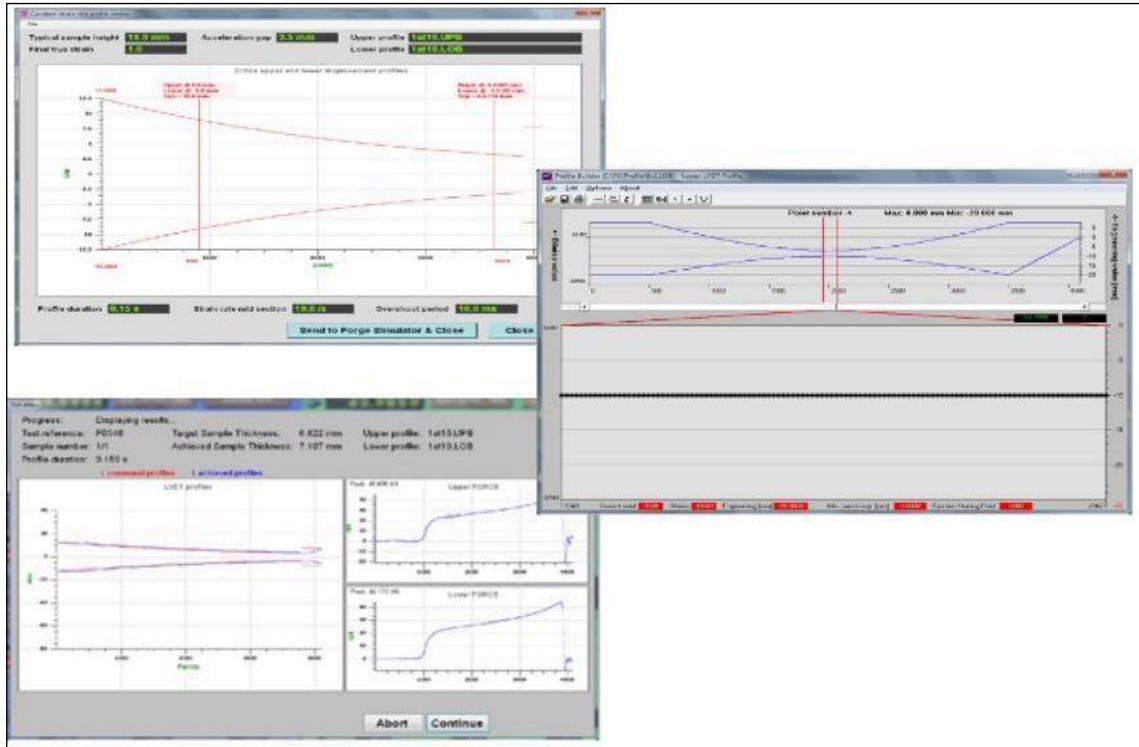


Figure 3.4: Software interface supporting the equipment, left: Constant Strain Rate Creator, right: Profile Builder

### 3.2 Experimental optimization

Optimizing an experimental procedure is always challenging and becomes more challenging when the equipment is new and no previous method is in place. The most significant step in the optimization procedure is to define the parameters that influence the experiment and then minimize them to achieve a solid, repeatable and accurate experiment. Due to similarities with the hot isothermal compression test the protocols and the standards used worldwide to describe the experimental procedure has been used as a baseline for the experiments [119].

Six main parameters have been identified that influence the experimental procedure. The first is the temperature control, the second is the sample position,

and the third is the strain rate variation which is linked to the acceleration gap, the profile duration, overshoot period and the PID values. Two factors are important with regard to the sample position; it's location on the platens i.e. is it central, and the platens position in the coil.

### 3.2.1 Temperature control

During the experiment an accurate and precise temperature control has been identified as critical to achieving a solid, repeatable and useful experiment. The system is supplied with an induction heating arrangement which is controlled by a pyrometer. The ASTM standard, E209-18 [120], designates that the uniformity of temperature within the specimen gage length should be within  $+5.5^{\circ}\text{C}$  and  $-11^{\circ}\text{C}$  of the nominal test temperature up to and including  $538^{\circ}\text{C}$  and within  $+1\%$  and  $-2\%$  of the nominal temperature above  $538^{\circ}\text{C}$  [121]. Due to changes in emissivity and the volume of the heated platens the pyrometer which is used to control the temperature lacks the accuracy for the precise temperature control required by the standard, for that reason also thermocouples were used. The thermocouple measurement where used to correct and drive the pyrometer input and control of the heating. Experimental results have shown that even small differences (2% of nominal temperature) in the temperature during high strain rate compression tests can have a significant influence at the results.

To optimize the temperature control in conjunction with the pyrometer a very fine, rapid response and minimum size thermocouple have been used (Type-K

0.25mm). The small diameter of the thermocouple has been selected to avoid any failure due to thermocouple thermal expansion. The thermocouple is carefully spot welded to the sample and the temperature is recorded throughout the heating phase. The combination of two measuring/monitoring methods minimizes the actual temperature variation between experiments. The results of the temperature optimization are presented in chapter 5, section 5.1.4. The optimisation study has taken the best stringing practice from E209-18 and NPL guide to create a new AFRC operation procedure.

### 3.2.2 Sample position

The sample positioning is crucial due to the nature of the heating system which is used (induction heating). An incorrect sample position inside the induction heating coil generates a lack of temperature uniformity within the sample and as a result non-uniform deformation would be obtained. There are two factors which influence the sample position and hence temperature uniformity; the sample position on the platens and the platen position within the coil. Any off-axis positioning, either vertical or horizontally, will tend to create a non-uniform electromagnetic field within the sample. To address that factor a calibration tool. Figure 3.5, was designed and manufactured. The tool uses the platen shape and a constant point in the chamber to identify the correct position of the sample.



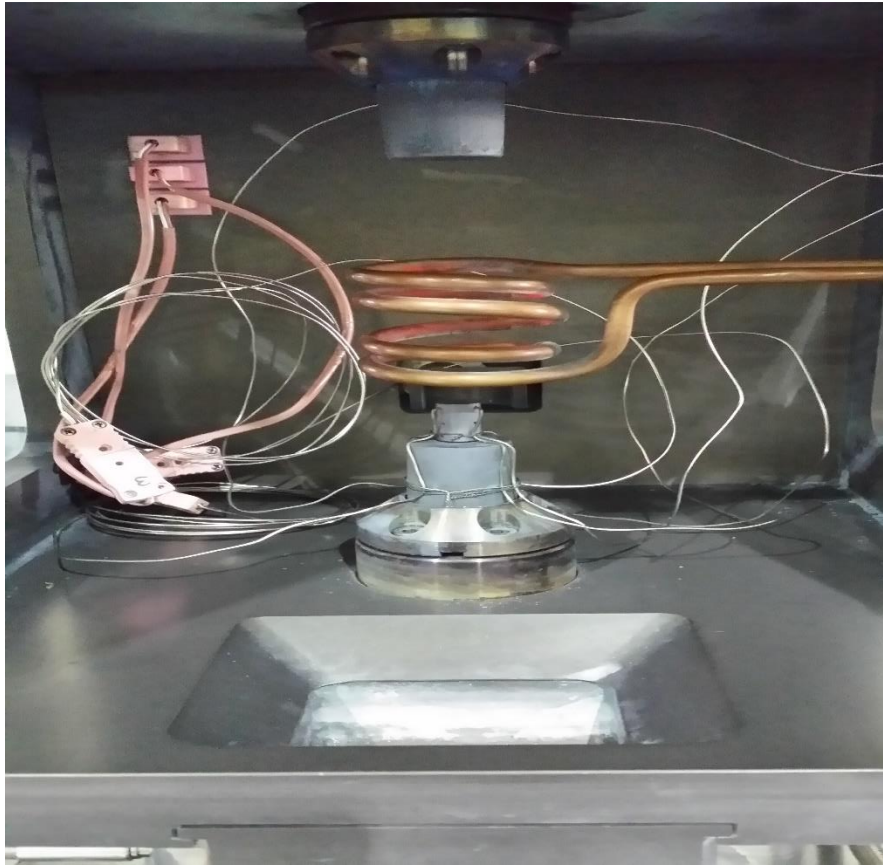


**Figure 3.6 Experimental set-up for temperature validation and uniformity**

The experimental set-up is illustrated in Figure 3.6. The sample was inserted inside the coil and heated to 500°C and the temperature monitored and recorded. The platen position was adjusted until the temperature distribution satisfied the ASTM standard E209-00 specifications [122]. The trial was repeated for a number of temperatures starting from 500°C up to 700°C with a step of 100°C and then up to 950°C with a 50°C step. The experimental set-up is demonstrated in Appendix A. The results of the temperature distribution inside the sample and the sample position with the platens are presented in chapter 5 and sections 5.1

### 3.2.3 Strain rate

Having obtained the necessary temperature control, the next stage in experimental optimization is to then consider the control of the strain rate. Tests at these high speeds may take as little as 0.1sec. In the case of this particular equipment the input parameters are; the acceleration gap, the strain rate, the final true strain, the profile duration and the overshoot period. With regard to the acceleration gap, given the high speeds required to obtain these strain rates, it is necessary to have an initial gap between the specimen and the top platen to allow the upper actuator to reach full speed prior to impacting the sample. The magnitude of the acceleration gap effects the initial phase of the test and needs to be optimized to ensure that the top actuator hits the sample in the right speed. The profile duration is the parameter responsible for the data sampling period of the experiment. The software records up to 4096 values during the test. The third parameter is the overshoot period which works as a counter for the recording delay between the software and the hardware.

To achieve a minimum strain rate variation a number of trials were run to determine the optimum values for the three parameters. For all the strain rates that were optimized the true final strain was kept constant at 0.5. The strain rate optimization was conducted for a number of strain rates and temperatures. Samples from the same Ti6Al4V rod were used to avoid inputting any variance in the tests. A number of the optimized strain rates conducted at 950<sup>o</sup>C are presented in Figure 3.7 and the average strain rate and standard deviation are

shown in Table 3.1: Strain rate variation. Examples of strain rate optimization experiments are presented in Appendix C.

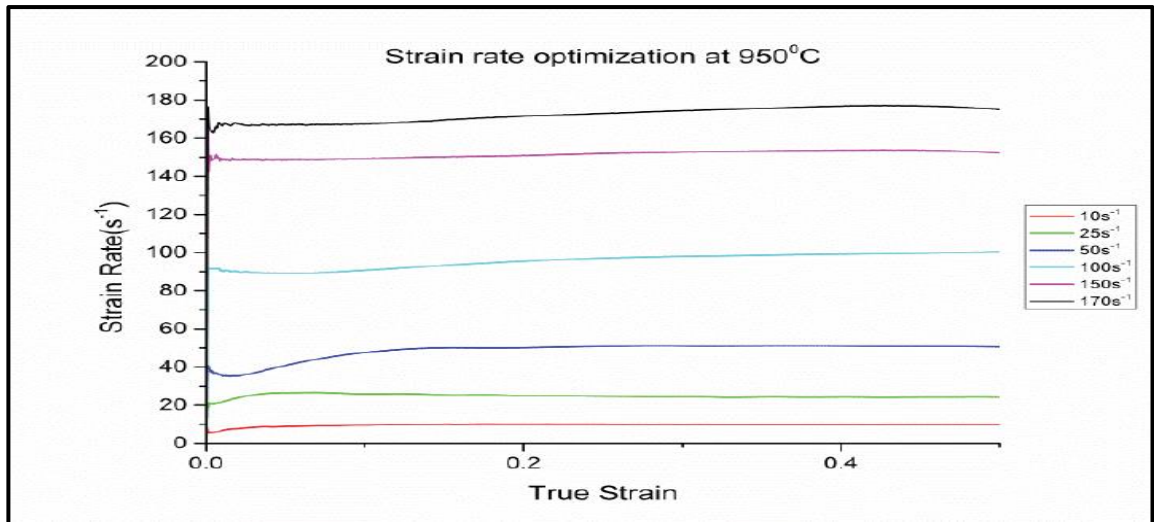


Figure 3.7: Optimized strain rate results at 950°C

Table 3.1: Strain rate variation

	Average Strain rate	Standard Deviation
$10 \text{ s}^{-1}$	$9.60\text{s}^{-1}$	0.80
$25 \text{ s}^{-1}$	$24.75\text{s}^{-1}$	1.01
$50 \text{ s}^{-1}$	$48.38\text{s}^{-1}$	4.68
$100 \text{ s}^{-1}$	$98.34\text{s}^{-1}$	4.07
$150 \text{ s}^{-1}$	$151.50\text{s}^{-1}$	1.92
$170 \text{ s}^{-1}$	$172.28\text{s}^{-1}$	3.75

## 4 Project Methodology

### 4.1 Introduction and DoE

This chapter describes the details of the methodology for the hot isothermal compression test at low and high strain rates, and the metallurgical work which will identify the effect of strain rate on the properties and microstructure of the selected material. The selection of temperatures and strain rates was performed based on the high speed industrial forging operation after consultation with industrial partners of the AFRC.

For the design of experiment (DOE) the author explored several different methods to avoid the “One-Variable-At-a-Time (OVAT) approach. Antony [123] proposes the classic DOE, Plackett and Burman (P-B) design, Taguchi’s orthogonal array, Shainin’s and the full factorial design that can provide superior and more comprehensive results [124]. The author by comparing all these powerful tools and investigating in the literature [125][126][127][128] for potential applications in the present field of research concluded that the use of a full factorial design should be the best solution due to the fact that is the only methodology that combines all the interactions of the variables to identify the effect of strain rate on the properties of the material.

For this research three full factorial design of experiments were used. The first two full factorial design of experiments were referred to hot isothermal compression tests with a conventional servo-hydraulic machine (low strain rates) and the bespoke high strain tester (high strain rates) for strain rates  $0.1 \text{ s}^{-1}$ ,  $1 \text{ s}^{-1}$  and  $10 \text{ s}^{-1}$  to establish a base line of the flow behaviour for the as-received material. The third full factorial DoE was the main target of this work for strain rates  $50 \text{ s}^{-1}$ ,  $100 \text{ s}^{-1}$  and  $150 \text{ s}^{-1}$ . For both designs of experiment three variables were selected, strain, strain rate and temperature during deformation. For the

base-line tests using the conventional servo-hydraulic machine (Zwick HA250), strain and temperature was investigated in three levels and strain rate at two levels as demonstrated at Table 4.1. For the high strain rate servo-hydraulic machine the strain was investigated at two levels due to the machine's limitations at this point, strain rate at one level and temperature at three levels as demonstrated in Table 4.2. Both full factorial designs of experiment have been designed to allow the final results to be combined and evaluated together.

**Table 4.1: Full factorial DOE for conventional servo-hydraulic Zwick HA250**

Variable	Levels	Level 1 (minimum)	Level 2	Level 3 (maximum)
Strain	3	25%	40%	55%
Strain Rate	2	$10^{-1} \text{ s}^{-1}$		$1 \text{ s}^{-1}$
Temperature	3	850°C	900°C	950°C

**Table 4.2: Full factorial DOE for prototype high strain rate servo-hydraulic machine**

Variable	Levels	Level 1 (minimum)	Level 2	Level 3 (maximum)
Strain	2	40%	40%	55%
Strain Rate	1	$1 \text{ s}^{-1}$		
Temperature	3	850°C	900°C	950°C

The third design of experiments was used for the as-received condition and heat treated (details of the heat treatment are given in the next section). Three temperatures (850°C, 900°C and 950°C), three strain rates ( $50 \text{ s}^{-1}$ ,  $100 \text{ s}^{-1}$  and  $150 \text{ s}^{-1}$ ) and one strain (55%) were investigated and the DoE presented in Table 4.3.

**Table 4.3: Full factorial DoE for as-received and heat treated microstructure**

Variable	Levels	Level 1 (minimum)	Level 2	Level 3 (maximum)
Strain	2	55%		
Strain Rate	1	50 s <sup>-1</sup>	100 s <sup>-1</sup>	150 s <sup>-1</sup>
Temperature	3	850°C	900°C	950°C

The research methodology has been divided into six phases. The first phase was the sample preparation. The second phase was the temperature distribution inside the sample for correcting the pyrometer settings. The third phase was the hot isothermal compression tests. The fourth phase was the analysis of the results. The fifth phase was the material preparation for microscopic observation. The sixth phase was the microscopic observation for flow patterns and adiabatic shear band formation.

#### 4.2 Material specifications and initial microstructure

The material under investigation was Ti-6Al-4V whose initial chemical composition is shown in Table 4.4. The material's initial dimension was 12.7 mm diameter and 2500 mm length and it conformed to the AMS 4928 standard [129]. The material was supplied by AirCraftMaterials UK as well as the certificate. The reported UTS was 1051.6 MPa and the beta transus as determined by DTA (Differential Thermal Analysis) was 995°C. The initial microstructure was elongated alpha-phase following the direction of the rolling axis and the ASTM grain size was 8.3. Figure 4.1 illustrates the initial microstructure, all the pictures have been taken with the rolling direction from left to right. The same material was also investigated after heat treatment at 1050 °C for 60 minutes and cool down at 5°C per minute in vacuum to achieve a lamellar microstructure (see Figure 4.3).

The final microstructure after heat treatment is presented at Figure 4.2 with an average lath length of 36  $\mu\text{m}$  and thickness of 3  $\mu\text{m}$  Figure 4.2.

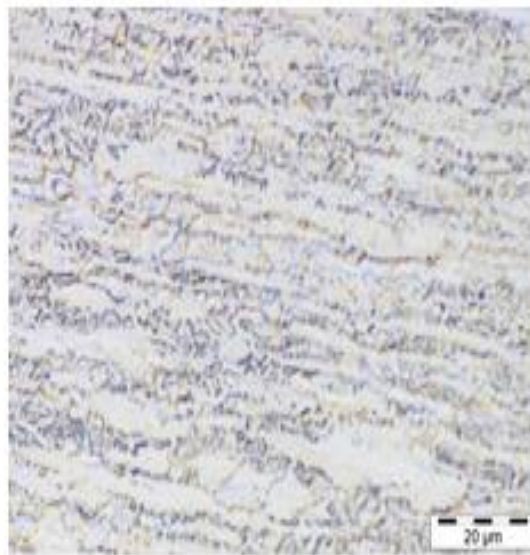
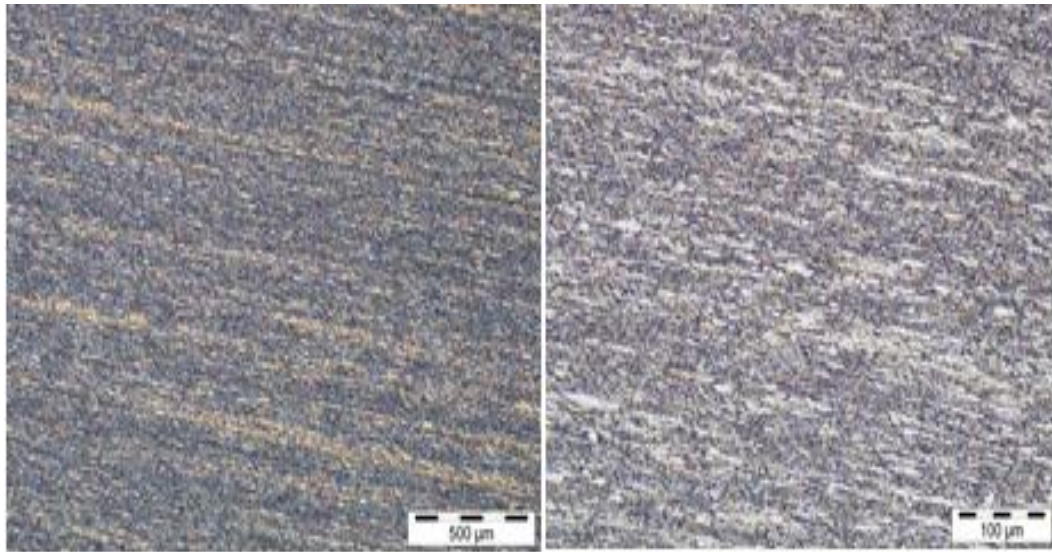


Figure 4.1 : As-received microstructure of Ti-6Al-4V bar

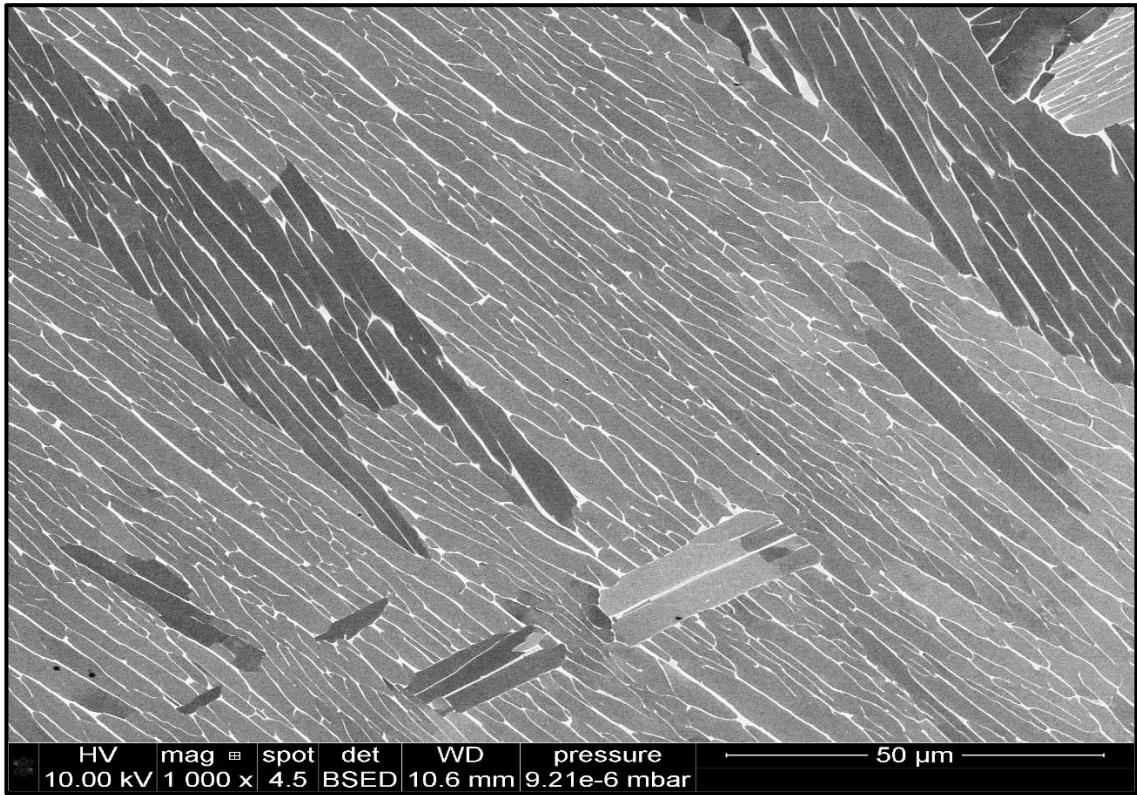


Figure 4.2: Ti-6Al-4V microstructure after heat treatment

Table 4.4: Chemical composition of Ti-6Al-4V bar as received

Element	Ti	Al	V	Fe	C	O	N	H
Weight %	balance	6.22	4.15	0.15	0.012	0.18	0.009	0.0026

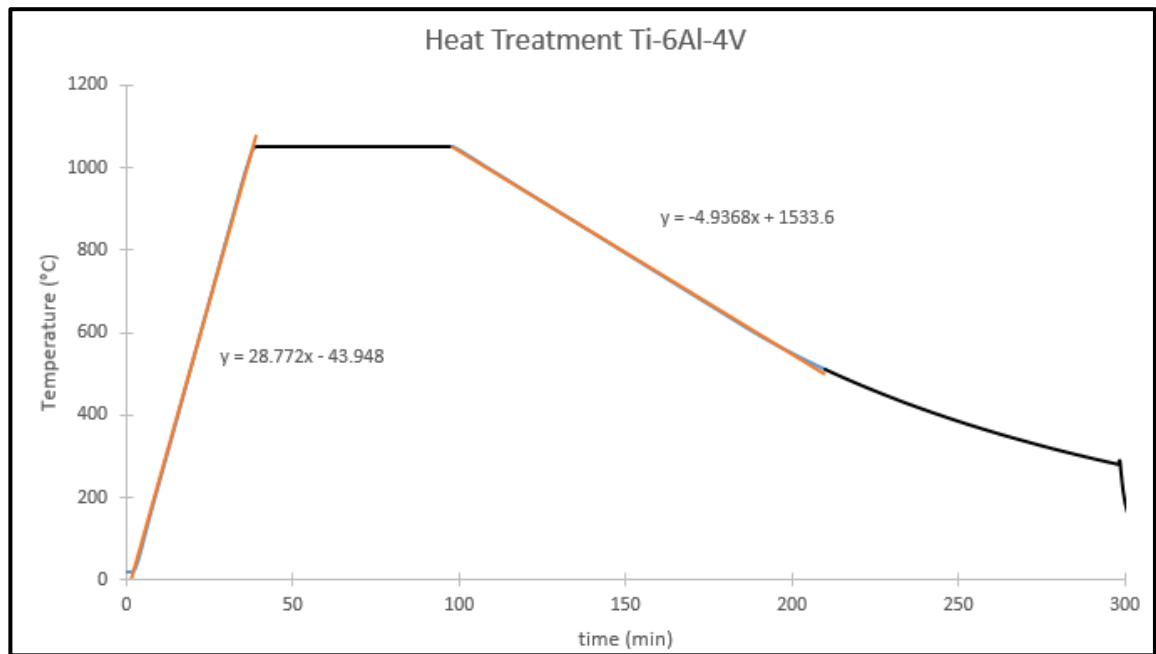


Figure 4.3: Heat treatment route of Ti-6Al-4V to achieve lamellar microstructure

### 4.3 Sample Geometrical Preparation for Compression

The samples were prepared by machining the initial Ti-6Al-4V bars and reducing the diameter from 12.7 mm to 12 mm with 0.1 mm tolerance. Then the bar had been cut in samples of 12 mm diameter and 18 mm height with 0.1 mm tolerance. All the equipment used for the measurements of the samples such as calipers and micrometres were calibrated and UKAS certified. The compression samples conformed to the ASTM E209-18 standard and the NPL guide No3 based on the work from Roebuck et.al. [130]. The Figure 4.4 demonstrates the dimensions and the 3D model of the samples which were used for the compression tests.

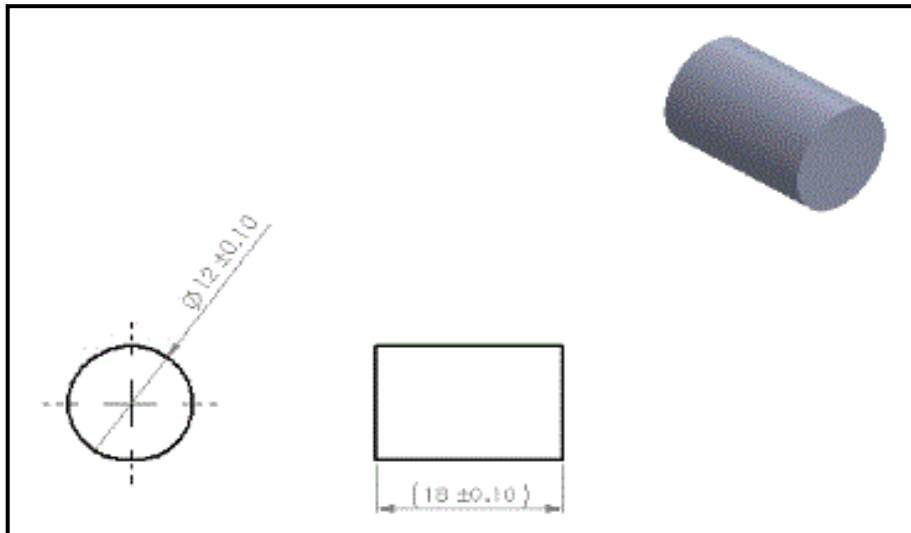


Figure 4.4: Engineering Draw and 3D model of the samples used for compression tests

For the temperature distribution mapping two samples were machined with the same dimensions as the samples which were used for compression tests ASTM E209-18 [120]. The samples were drilled at six positions with 1 mm holes. Two holes were placed at 2 mm from the top of the sample, two holes at 2 mm from the bottom of the sample and 2 holes at the middle of the sample. All the holes penetrated the entire diameter. The sample engineering draw and 3D model demonstrated in Figure 4.5.

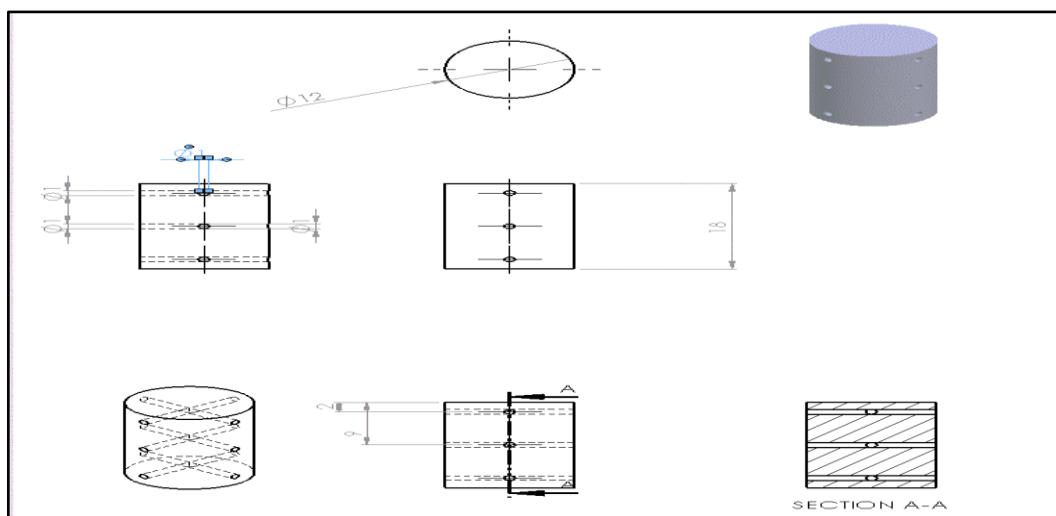


Figure 4.5: Engineering Draw and 3D model of the samples used for temperature distribution monitoring

#### 4.4 Temperature distribution monitoring

For the temperature distribution mapping two samples and the Phoenix machine was used as demonstrated in Figure 4.5. Several temperatures ranges were examined from 500°C to 950°C. At lower temperatures a step of 100°C was used and from 700°C until 950°C a step of 50°C was used. Furthermore, at 950°C the temperature distribution was also investigated in correlation with the distance of the upper die and the sample top surface (see section 3.2.2, 3.2.3 and Appendix A). For all the temperatures the distance between the upper die and the sample was 2 mm. A 0.3 mm gap between the upper die and the sample and no gap with the upper die were investigated at 950°C to identify the best heating position. The position of the upper die has significant effect on the magnetic field created by the induction heating system and the temperature distribution inside the sample.

Six K-type 1 mm thermocouples were used to monitor the temperature inside the sample. Three thermocouples were placed 6mm inside the sample to monitor the centre of the sample at 2 mm of the top of the sample, 2 mm of the bottom of the sample and at the middle. The other three thermocouples were placed 10mm inside the sample to monitor the temperature 2 mm of the surface also at the same distances of the top, bottom and middle (Figure 4.5). The positioning of the thermocouples were based on the stability and keeping the same position during the heating. The thermal expansion of the thermocouple prevent the spot welding to the sample because that could cause movement of the sample.

Both tests were conducted under the same conditions, six new calibrated thermocouples were used and the temperature was monitored by a TC-08 Thermocouple Data Logger suitable for temperature from -270°C to +1820°C with 20bits resolution and sample rate of 10 samples/sec. The built in pyrometer was used to control the induction heating system and monitor the temperature at the surface of the sample. Photos taken during the experimental procedure are presented in Appendix A. The test was split in three phases. The first phase was

the heating of the sample at the required temperature, which was controlled by the pyrometer. After the sample reached the temperature the second phase took place where the temperature was maintained stable for five minutes. The third stage was the recording of the temperatures from the thermocouples and the pyrometer.

The results of the temperature distribution and thermocouple position set up inside the sample was used to identify the best position of the sample in connection with the top die position and to correct the pyrometer input to achieve the right temperature for the compression tests. The experimental procedure, results and utilisation of them to achieve optimal heating position are presented in section 5.1.

## 4.5 Hot Isothermal Compression

For simulating deformation processes such as extrusion or forging the compression test is the most suitable in comparison with the tension test, due to similar mode of stress, smaller specimen and better controlled procedure [131].

### 4.5.1 Introduction

The compression test at elevated temperatures has to deal with some difficult problems. The first problem that arises is how to control and maintain uniform temperature during the experiment. As the test must be isothermal this is very important. Another problem is the uniform lubrication of the dies. Furthermore, hot working plastic instabilities can be developed in the compression test due to thermo-mechanical processes such as recrystallization and dynamic recovery. The first type is associated with a maximum in the true stress-strain curve and the second type concerns inhomogeneous deformation and shear band formation. Finally, at elevated temperatures metals may become more strain rate sensitive which makes the strain rate control an important parameter for the test [131] [68].

To overcome the problems occurring in a hot compression test the experimental compression method was split into four stages. The first stage was the selection of the appropriate equipment for the experimental parameters. The second stage was the experimental setup, which includes the selection of suitable lubrication for the dies and the quench timing. All the individual elements were essential to eliminate any variations during the test and allow the third and fourth stage to run as effectively as possible. The third stage was the temperature and strain rate control which was critical for the test. The final stage was the performance of the hot isothermal compression test.

The tests were conducted by the author and an experienced technician at the AFRC. Photos taken during the experimental procedure are presented in Appendix B.

#### 4.5.2 Equipment Selection

The equipment was selected based on the experimental parameters. The capability of the equipment to conduct the tests at the requested strain rates was the main characteristic. For the tests with strain rates  $0.1 \text{ s}^{-1}$  and  $1 \text{ s}^{-1}$  a Zwick – HA 250 servo hydraulic press was selected, capable of 250KN load with an attached furnace capable of produce temperatures up to  $1100^{\circ}\text{C}$ . A schematic of the compression-testing machine is shown in Figure 4.6.

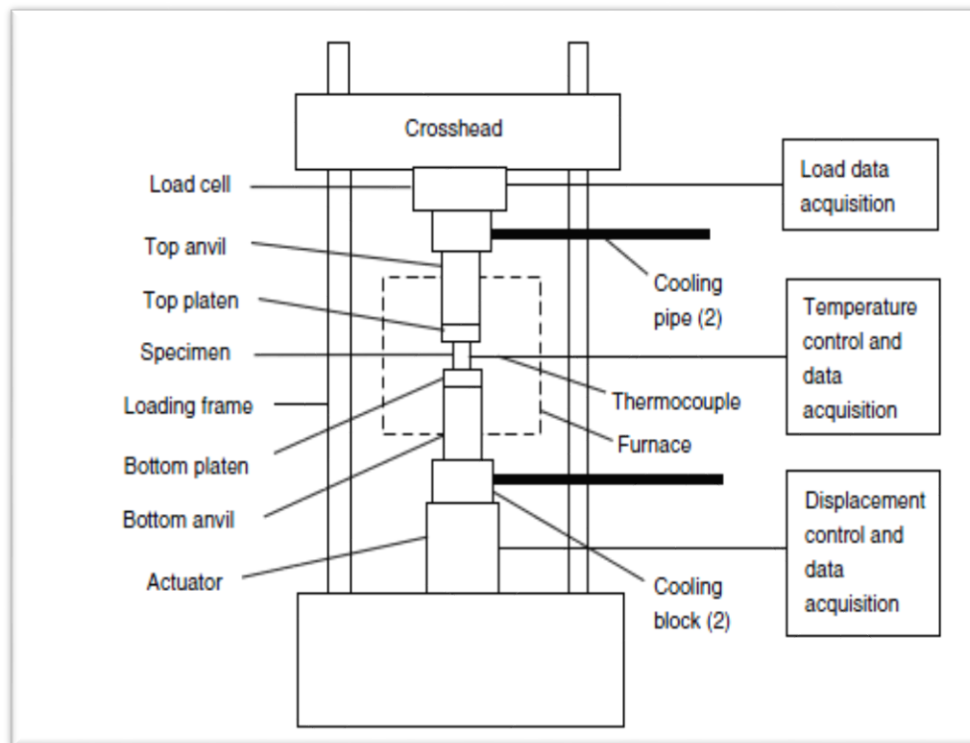


Figure 4.6: Servo-Hydraulic compression testing system Zwick HA250 (image [132])

For strain rates greater than  $5 \text{ s}^{-1}$  most common servo-hydraulic machines are not capable ensuring a constant strain rate. For that reason AFRC procured a bespoke servo-hydraulic machine with the capability to conduct hot isothermal compression tests at strain rates from  $1 \text{ s}^{-1}$  to  $200 \text{ s}^{-1}$ . The Phoenix high strain rate tester is a specially modified servo-hydraulic machine capable of conducting compression tests at strain rates that commonly available servo-hydraulic machines are not able to support and maintain a stable strain rate during the compression test. It is equipped with a closed chamber that is filled with a non-reactive gas. Inside the chamber is installed an induction heating coil linked to a power system adjacent to the press which is capable of rapid heating the test piece and tooling to temperature of circa  $1300^\circ\text{C}$ . Furthermore, the machine is equipped with an automatic system for water quenching in under 5 seconds.

#### 4.5.3 Compression setup for HA250 servo-hydraulic machine

The experimental setup which is described in this section was followed for all the samples to ensure the repeatability of the tests and to eliminate any external parameters which would affect the final outcome.

Following machining all samples were washed with ethanol to ensure that they were free of foreign particles on their surface. The clean surface was required for the next step where the samples were coated with standard glass coating provided by the AFRC. The chemical composition and details for the coating is not available as the coating is AFRC's intellectual property. The coating provides lubrication between the sample and the die and minimises the friction occurring during the test and at the same time works as thermal barrier reduce the heat loss.

The flat surface of dies is essential for the test. Both of the dies are made of CMSX-4; a nickel super-alloy. The dies were incrementally ground by using three different grinding papers P240, P600 and P1200 with water suspension. After the grinding the surface was cleaned and coated with a Boron Nitride solution which ensures lower friction between the dies and the sample and enhance the life of the dies.

The dies were mounted on the push rods in the Zwick HA 250 servo-hydraulic machine. The push rods were manufactured from Inconel 100, U720 super alloy and Stainless Steel 316. The sample was mounted on the bottom die and placed in the middle of the die.

To achieve the temperature needed for the tests a Severn Thermal Solutions SF 2113 clamshell furnace was used to heat the sample and the push rods. The temperature was increased from room temperature to the target temperature based on the experimental matrix which is described below at a rate of 12°C/minute, a total of 80 minutes to achieve 950°C plus 15 minutes of soak

time. The temperature was controlled by a controller which was connected with six N-type thermocouples. Three thermocouples were connected to three different areas of the furnace and the other three were at the top and bottom die and one at the surface between the bottom die and the sample. The six point control of the temperature was essential for the accurate monitoring of the temperature before and during the test. The required temperature was reached and maintained at least for 15 minutes before the test started.

The final stage of the test was the quench. The Zwick HA 250 and the control software allow a small move of the push rods after the end of the test. The small move of the push rod allows the user to remove the sample with the help of a tongs tool and quench it. The average time between the end of the test and the quench was kept at five seconds to allow investigation of the microstructure after the hot compression.

#### 4.5.4 Compression test matrix for HA250 servo-hydraulic machine

The parameters and the levels are detailed in Table 4.1 and they are the result of a full factorial design of experiments. The compression tests which were conducted on HA 250 conventional servo-hydraulic machine given in Table 4.5. As already mentioned the procedure was randomized and the sample reference number used in the table does not indicate the order of the experiments.

**Table 4.5: Test matrix for hot compression tests at HA 250 servo-hydraulic machine**

Sample Ref. Number	Strain (%)	Strain Rate( $s^{-1}$ )	Temperature( $^{\circ}C$ )
1	25	0,1	850
2	25	0,1	900
3	25	0,1	950
4	25	1	850
5	25	1	900
6	25	1	950
7	40	0,1	850
8	40	0,1	900

9	40	0,1	950
10	40	1	850
11	40	1	900
12	40	1	950
13	55	0,1	850
14	55	0,1	900
15	55	0,1	950
16	55	1	850
17	55	1	900
18	55	1	950

#### 4.5.5 Compression setup for phoenix high strain rate tester

Samples preparation was as described above – machining followed by cleaning and lubrication using the glass lubricant referred to.

The dies of the Phoenix are made of tungsten carbide. The surface was cleaned and coated with a Boron Nitride solution which ensures lower friction between the dies and the sample and enhance the life of the dies.

The dies and the sample were shielded inside an insulated chamber which was filled with non-reactive gas (Argon) to eliminate the corrosion of the dies and to inhibit the formation of alpha case on the titanium [133]. The sample was carefully located at the centre of the induction heating coil. The heating of the sample was controlled by a pyrometer at a rate of 10°C/sec and at the same time with a K-type 0.25 mm diameter thermocouple spot welded to the surface of the sample.

#### 4.5.6 Compression test matrix for Phoenix high strain rate tester

The design of experiment parameters and the levels had been discussed and illustrated in Table 4.2 and Table 4.3. The compression tests which were conducted on the Phoenix special modified servo-hydraulic machine were divided in three sets; the first set was the baseline tests, the second was the as-received

condition of the Ti-6Al-4V and third the heat treated condition. The complete test matrices are illustrated in Table 4.6, Table 4.7 and Table 4.8 respectively.

**Table 4.6: Test matrix of reference hot isothermal compression tests at Phoenix high strain rate servo-hydraulic machine**

Sample Ref. Number	Strain (%)	Strain Rate (s <sup>-1</sup> )	Temperature(°C)
P4	40	10	850
P5	40	10	900
P6	40	10	950
P7	55	10	850
P8	55	10	900
P9	55	10	950

**Table 4.7: As-received Ti-6Al-4V test matrix**

Sample Ref. Number	Strain (%)	Strain Rate(s <sup>-1</sup> )	Temperature(°C)
EQ 1	55	50	850
EQ 2	55	50	850
EQ 3	55	100	850
EQ 4	55	100	850
EQ 5	55	150	850
EQ 6	55	150	850
EQ 7	55	50	900
EQ 8	55	50	900
EQ 9	55	100	900
EQ 10	55	100	900
EQ 11	55	150	900
EQ 12	55	150	900
EQ 13	55	50	950
EQ 14	55	50	950

Project Methodology

EQ 15	55	100	950
EQ 16	55	100	950
EQ 17	55	150	950
EQ 18	55	150	950

Table 4.8: After heat treatment Ti-6Al-4V

Sample Ref. Number	Strain (%)	Strain Rate(s <sup>-1</sup> )	Temperature(°C)
LH 1	55	50	850
LH 2	55	50	850
LH 3	55	100	850
LH 4	55	100	850
LH 5	55	150	850
LH 6	55	150	850
LH 7	55	50	900
LH 8	55	50	900
LH 9	55	100	900
LH 10	55	100	900
LH 11	55	150	900
LH 12	55	150	900
LH 13	55	50	950
LH 14	55	50	950
LH 15	55	100	950
LH 16	55	100	950
LH 17	55	150	950
LH 18	55	150	950

#### 4.6 Isothermal hot compression test flow stress analysis

The data obtained from a conventional compression test are the load  $F$  from the load cell and the displacement  $\Delta H$  (mm) from the Linear Variable Differential Transformer (LVDT). In the case of the Phoenix high strain rate tester the data obtained are the load  $F$  from both the load cells (load cell A is more accurate at forces above 300 KN and load cell B below 300 KN) and the displacement  $\Delta H$  (mm) from the two LVDTs placed at the end in both push rods. The final value of the displacement is calculated from the deduction of stroke B from stroke A. The

displacement is corrected for compliance based on the compliance curve obtained for each temperature [118].

The true stress is defined as the load  $F$  divided by the instantaneous cross-section area of the sample (in our case a cylinder) with diameter  $D_i$ . During an isothermal compression test the cylinder with initial height  $H_0$  is deformed to an instantaneous height  $H_i$ , the result is the expansion of the initial diameter  $D_0$  following the law of volume conservation:

$$D_0^2 H_0 = D_i^2 H_i$$

The flow stress  $\sigma$ , assuming frictionless conditions, can be calculated in association with the deformation force  $F$  by:

$$\sigma = \frac{F}{A_i} = \frac{4F}{\pi D_i^2} = \frac{4F}{\pi D_0^2 H_0}$$

Furthermore, the true strain can be calculated as a function of the sample's (cylinder) instantaneous height  $H_i$  by:

$$\varepsilon = \ln\left(\frac{H_i}{H_0}\right) = \ln\left(\frac{H_0 - \Delta H}{H_0}\right) = \ln\left(1 - \frac{\Delta H}{H_0}\right)$$

Finally, during the compression testing the true strain rate  $\dot{\varepsilon}$  can be expressed in terms of the instantaneous height  $H_i$ , and the instantaneous crosshead velocity  $V_i$  by [131]:

$$\dot{\varepsilon} = \frac{d\varepsilon}{dt} = \frac{d\left(\ln\frac{H_i}{H_0}\right)}{dt} = \frac{1}{H_i} \frac{dH_i}{dt} = \frac{V_i}{H_i}$$

#### 4.7 Determination of friction

During compression testing and metal forming processes, the material shape is changing because of the contact with the dies forcing it to flow under load. The workpiece and die (platen) move relative to each other under force, as a result

friction forces are generated in the interface. The frictional forces resist the relative movement, this influencing the deformation load and causing energy losses [134]. The friction in the interface can be controlled by applying the appropriate lubricant. The system of sample, die and lubricant can be characterised in terms of a coefficient ( $\mu$ ). The value of the coefficient lies between 1 (sticking conditions) and 0 (frictionless conditions).

The standard method to determine the friction conditions is the ring test. The method was developed by Kunogi [135] and improved by Male and Cockcroft [136] and gained wide acceptance around the world for the quantitative evaluation of the friction. The method is simple and involves a flat ring shaped sample which is deformed to a known axial reduction. The information on the friction coefficient at the sample-die interface is provided by the change in the inner diameter of the ring specimen. If the friction is high the internal diameter decreases indicating poor lubricant performance; whereas if the friction is low the internal diameter increases demonstrating good lubrication. To obtain the friction factor, the internal diameter of the deformed ring must be compared with the value predicted by using various friction coefficients,  $\mu$ . As demonstrated in Figure 4.7 the friction coefficient  $\mu$  is plotted against the reduction in height of the ring for a range of friction values.

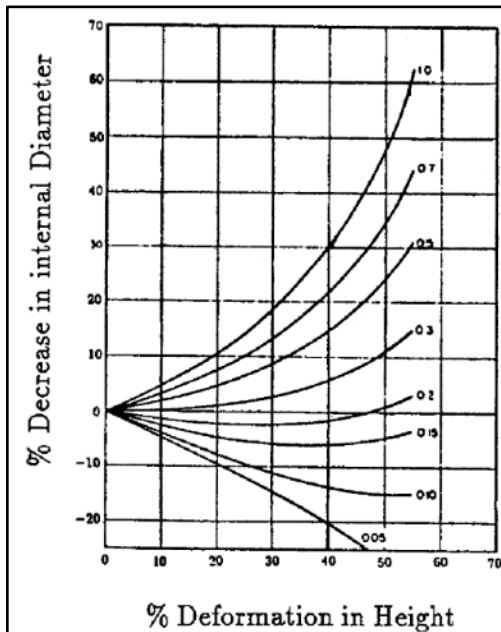


Figure 4.7: Friction calibration curves [134]

Force measurement is not a requirement of the ring compression test, making it one of the biggest advantages of the technique. Furthermore, the test can take place for large-scale deformations such involved in forming and forging.

#### 4.8 Process map and instability criterion

‘As has been mentioned in section 2.7 for the development of process maps many instability criteria are available. For this research Prasad’s instability criterion was selected as it has been extensively accepted and used. The approach is based on the Dynamic Material Model (DMM). In this model, the sample subjected to hot deformation is assumed to be a non-linear dissipator of power. The energy transactions occurring in the sample consist of two types: a temperature rise and described by the component (G) and a microstructural change (J). The total input power is partitioned between these two as decided by the strain rate sensitivity of flow stress ( $m$ )[74].

$$P = \sigma * \dot{\epsilon} = \dot{G} + J$$

$$G = \int_0^{\dot{\varepsilon}} \sigma d\dot{\varepsilon}$$

$$J = \int_0^{\sigma} \dot{\varepsilon} d\sigma$$

The processing maps were composed of parameter  $\eta$ , which represents the efficiency of the power dissipation and the parameter  $\xi$ :

$$\eta = \frac{J}{J_{max}} = \frac{2m}{m+1}$$

$$\xi(\dot{\varepsilon}) = \frac{\partial \ln\left(\frac{m}{m+1}\right)}{\partial \ln \dot{\varepsilon}} + m < 0$$

Where  $\dot{\varepsilon}$  is the applied strain rate. The variation of dimensionless parameter  $\xi(\dot{\varepsilon})$  with temperature and strain rate constitutes an instability map. If parameter  $\eta$  has a negative value, microstructural flow instabilities, such as adiabatic shear bands (ASBs), localization of deformation, or cracks, may occur. On a processing map, such a region is considered as unsafe[137].

#### 4.9 Sample Preparation and Investigation

Except for the compression tests the microstructure investigation and identification were also one of the crucial aims of the project. The intent was to compare the effect of the different process parameters on the microstructural development. Standard metallographic procedure involving grinding and polishing of the samples were used. Due to the microstructure and thermo-mechanical history of the samples the process route of grinding and polishing was changed incrementally to provide the best final result. The chemical etching of the prepared samples was the last stage which revealed the microstructure and allowed metallographic examination.

#### 4.9.1 Sample Preparation route

The samples after the compression test were all cleaned and cut in the vertical direction of the compression axis along the centreline as is shown in Figure 4.8. In order to cut the samples the author used the Isomet 5000 cutting machine. In some cases where the samples were too big for the isomet they were cut by an EDM (Electrical Discharge Machining). The EDM cutting was conducted by an experienced technician at the AFRC. All the samples were inspected for rough edges before mounting with any being removed by using loose grinding papers.

The cut samples were mounted using an automatic SimpliMet 3000 mounting press from Buehler. As a consequence of the samples' dimension the 40mm diameter case was selected as the most suitable. The PhenoCure thermoplastic powder was used to fill the case. The settings was set to 290 bar pressure and temperature of 150°C to melt the powder for 110 sec followed by 270 seconds cooling before the removal of the sample.

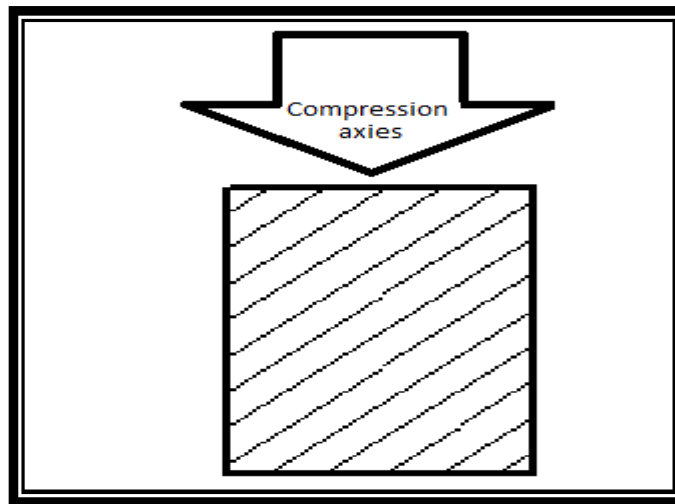


Figure 4.8: Cutting sample direction

The next step was the grinding and polishing. All the samples were subjected to the grinding and polishing process as detailed in Table 4.9. For the grinding and polishing an Ecoment 300Pro grinding and polishing machine was used with an

AutoMet 300 power head. The process route of grinding and polishing which is proposed was the result of many trials and alterations to the process due to the material behaviour. The author can speculate that the problem occurred because the samples deformed under different conditions have different volume fractions of alpha and beta phase changing the general surface hardness of the material from area to area and sample to sample. The surface hardness has a significant effect on the rate of grinding and polishing. All the parameters selected for each stage of the process are detailed at the Table 4.9 and the finish which was achieved after each step is illustrated at Figure 4.9.

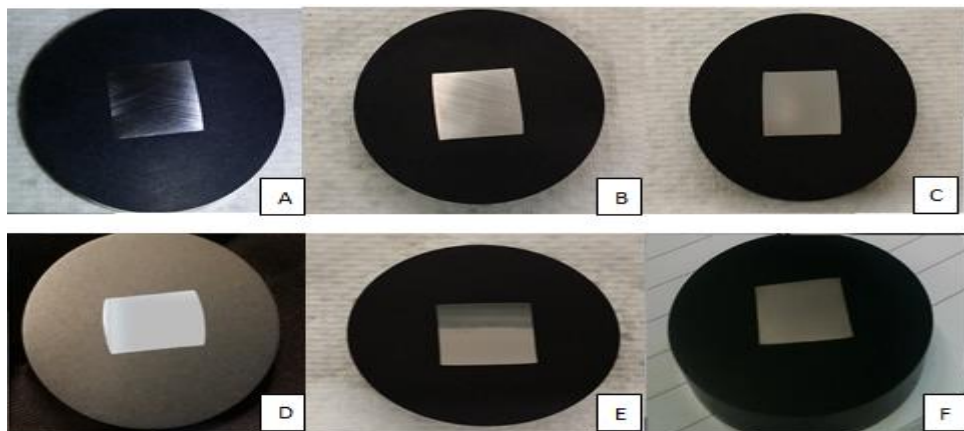


Figure 4.9: Samples after each step of preparation A) step 1- P600 grinding, B) step 2- P1200 grinding, C) Step 3 polishing, D) step 4 polishing, E) step 5 polishing and F) after chemical etching.

The final stage of the material preparation for microstructure observation was the chemical etching. After the polishing, chemical etching is a necessity to reveal the microstructure. The Kroll's method was used for all the samples. Due to health and safety regulations the process was conducted by an experienced AFRC technician. A solution of 1% HF (Hydrofluoric acid) and 99% H<sub>2</sub>O was used, the sample was immersed for 15-30 seconds to reveal the microstructure. To ensure over etching did not occur, regular inspections were conducted during the etching operation. Finally, the sample washed with water after etching.

Table 4.9: Grinding and Polishing parameters and steps.

	<i>Step 1</i>	<i>Step 2</i>	<i>Step 3</i>	<i>Step 4</i>	<i>Step 5</i>
<i>Description</i>	<i>Grinding</i>	<i>Grinding</i>	<i>Polishing</i>	<i>Polishing</i>	<i>Polishing</i>
<i>Pad</i>	<i>P600</i>	<i>P1200</i>	<i>Texmet P 9<math>\mu</math>m</i>	<i>Chemo met</i>	<i>Chemo met</i>
<i>Particle size</i>	<i>25.8 <math>\mu</math>m</i>	<i>15.3 <math>\mu</math>m</i>	<i>9 <math>\mu</math>m</i>	<i>0.02 <math>\mu</math>m</i>	<i>0.02 <math>\mu</math>m</i>
<i>Lubrication</i>	<i>Water</i>	<i>Water</i>	<i>Meta-Di Fluid</i>	<i>None</i>	<i>None</i>
<i>Suspension</i>	<i>N/A</i>	<i>N/A</i>	<i>Meta-Di 9 <math>\mu</math>m Polycrystalline Diamond</i>	<i>Master Met 2 0.02 <math>\mu</math>m Colloidal Silica</i>	<i>Master Met 2 0.02 <math>\mu</math>m Colloidal Silica</i>
<i>Rotation type</i>	<i>Compli</i>	<i>Contra</i>	<i>Contra</i>	<i>Contra</i>	<i>Contra</i>
<i>Plate speed</i>	<i>150 RPM</i>	<i>150 RPM</i>	<i>150 RPM</i>	<i>150 RPM</i>	<i>150 RPM</i>
<i>Plate head</i>	<i>60 RPM</i>	<i>60 RPM</i>	<i>60 RPM</i>	<i>60 RPM</i>	<i>60 RPM</i>
<i>Force</i>	<i>25 N</i>	<i>25 N</i>	<i>25 N</i>	<i>20 N</i>	<i>15 N</i>
<i>Time</i>	<i>3-5 minutes</i>	<i>1 minute</i>	<i>6 minutes</i>	<i>6 minutes</i>	<i>6 minutes</i>
<i>Finish</i>	<i>Scratched</i>	<i>Less Scratched</i>	<i>Dull Shine</i>	<i>Bright Shine</i>	<i>Mirror finish</i>

#### 4.9.2 Optical microscopy (OM) and Electronic microscopy (SEM, EBSD)

The microstructure observation and investigation was conducted on the initial and deformed samples. An Olympus GX51 and a Leica DM12000M optical microscope with five different optical lenses which gave magnifications of X5,

X10, X20, X50 and X100 was used for microstructure observation . Furthermore, the optical microscope was equipped with a lambda filter suitable for the author's investigation. Both software (Olympus IAS and Leica LAS) were capable of 2560 x 1920 pixel analysis. For the analysis of the images the author used the image analysis software from Leica (Grain Expert) with automatic grain size analysis (ASTM-112-13) [138] when this was applicable. For grain size analysis when the automatic procedure was not suitable, because of the grain boundary quality and the software limitations to properly identify them, a Mathcad routine based on the intercept line method that has been developed in-house was used.

The flow patterns and the ASBs were investigated by the Leica S6 D stereo microscope. The stereo microscope was capable of magnification of X0.64 minimum to X2 maximum. Furthermore, the stereo microscope was equipped with a full high definition camera. Video and snapshot images were taken by the author to capture the flow patterns and ASBs in the samples which were deformed to 55%.

In this study a FEI/Oxford Instruments Quanta 250 FEG SEM has also been used to capture micrographs. For SEM images, the acceleration voltage was 20kV, the spot size 4.5  $\mu\text{m}$  and the working distance 10mm. A range of magnifications were used to reveal the microstructure.

In the following chapter the results for the temperature distribution during the optimization of the Phoenix high strain tester are presented and discussed. The chapter will be mainly focused on the results from the equiaxed microstructure (as-received) in terms of mechanical testing, modelling the flow behaviour, identifying the strain rate effect and the temperature effect as well as microstructure observations.

## 5 Results and Evaluation of As-Received Microstructure

Based on the methodology described in the previous chapter the results and a brief evaluation of every step will be presented in this chapter. Further discussion and comments will be presented in chapter 6.

### 5.1 Temperature distribution inside the sample at Phoenix high strain rate Tester

The temperature distribution inside the sample was a critical factor because the compression test was intended to be isothermal. The induction heating system was influenced by many parameters such as the position of the sample inside the coils, the geometry of the coils, the number of coils and the frequency of the electric current. Furthermore, the pyrometer which controls the heating system measured the surface temperature of the sample which was not always the real temperature inside the sample.

#### 5.1.1 Results of temperature distribution as a function of temperature

Two samples were investigated as has been described in the previous chapter (section 4.4). The results of sample T1 are presented in Table 5.1 and the results of sample T2 are presented in Table 5.2. Furthermore, to validate the results given by the thermocouples the sample position after heating was measured to ensure that it had not moved. The measurement conducted with the designed tool presented in Figure 3.5. The reason for this is that thermocouples usually expand and can change the position of the sample when heated at high temperatures. The radial position of the thermocouples with respect to the centre of the sample after heating in comparison with the initial position in the sample T1 is presented in Figure 5.1 and for sample T2 in Figure 5.2.

Results and Evaluation of As-Received Microstructure

**Table 5.1: Sample T1 temperature distribution**

Sample T1		Pyrometer Temperature							
		500°C	600°C	700°C	750°C	800°C	850°C	900°C	950°C
Thermocouples Temperature	Top Centre	582	672	737	773	824	888	929	986
	Top Edge	580	670	735	770	822	884	925	982
	Middle Centre	578	669	733	768	818	878	917	971
	Middle Edge	585	678	740	774	824	884	925	982
	Bottom Centre	569	667	735	774	824	883	920	976
	Bottom Edge	585	679	744	780	832	892	931	988
	Average	579	672	737	773	824	884.83	924	980
	Standard Dev.	6	5	4	4	5	5	5	6

**Table 5.2: Sample T2 temperature distribution**

Sample T2		Pyrometer Temperature							
		500°C	600°C	700°C	750°C	800°C	850°C	900°C	950°C
Thermocouples Temperature	Top Centre	580	658	697	752	817	869	901	948
	Top Edge	598	676	711	763	830	883	916	962
	Middle Centre	599	676	713	765	831	884	918	966
	Middle Edge	603	679	715	767	833	888	922	971
	Bottom Centre	593	671	711	767	835	887	920	969
	Bottom Edge	599	676	716	772	840	893	927	976
	Average	595	672	710	764	831	884	917	965
	Standard Dev.	8	7	7	7	7	8	9	10

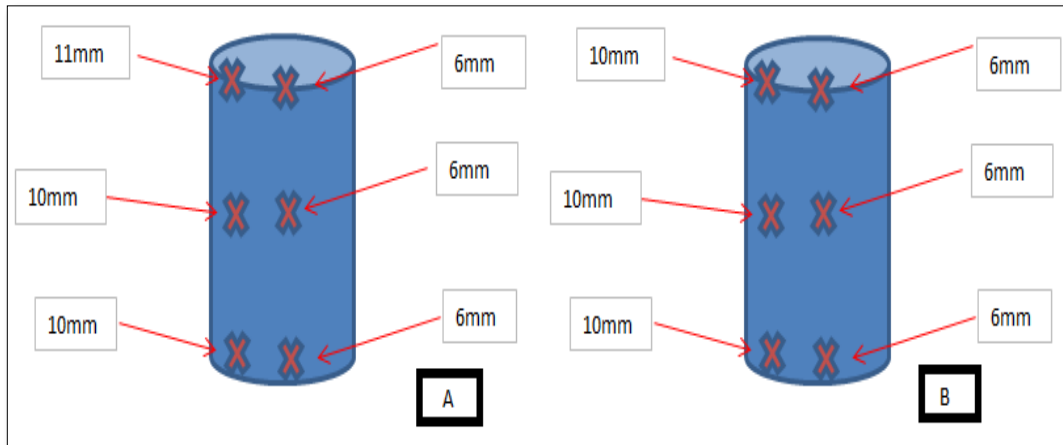


Figure 5.1: Thermocouple radial position in respect to the centre of the sample position inside the T1 sample A) after heating B) initial position

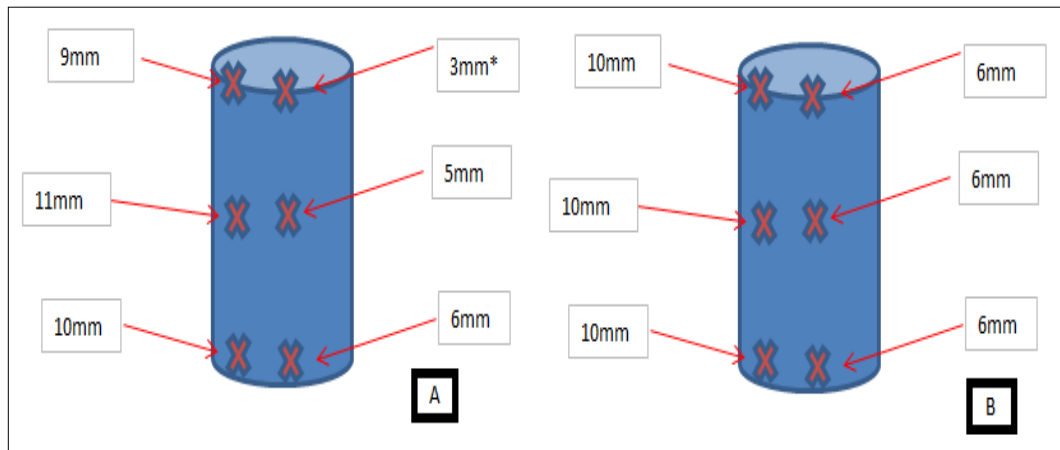


Figure 5.2: Thermocouple radial position in respect to the centre of the sample inside the T2 sample A) after heating B) initial position

### 5.1.2 Evaluation of temperature distribution as a function of temperature

The temperature distribution test shows that the temperature inside the samples is different from the pyrometers readings. The average difference between the pyrometer and the thermocouple varied from 14°C to 95°C. This may be because the difference between the thermocouple and the pyrometer had its' origin in the fact that the platen size was several times bigger than the sample and the

emission originating from the surface of the platens had influenced the temperature readings at lower temperatures. The fluctuation of the temperature inside the sample was between 9.70°C to  $\approx$ 4.00°C in relationship with the average temperature of the sample.

After taking under consideration the final position of the thermocouples the results from sample T2 are questionable. Due to the expansion of the thermocouples the temperature readings were not reliable. Sample T1 however fulfilled all the conditions which are required in order to be valid. The small displacement which was noted at in the thermocouple located on the top edge would not affect the results.

The results of temperature distribution inside the sample T1 show that the temperature required for the experiments can be corrected based on the average temperature inside the sample. The results indicate a 95% possibility that the temperature inside the sample is the required one for the experiment with an error of  $\pm 6^\circ\text{C}$ , values that conform to the ASTM E209-19 standard for rapid heating [139].

### 5.1.3 Temperature distribution versus top die-sample gap

The temperature distribution compared to the relative position of the upper platen and the top surface of the sample was investigated in three positions 2 mm, 0.3 mm and in contact, at 950°C. Due to the final position of the thermocouples only the results of sample T1 are considered as valid. The results of Sample T1 are presented in Table 5.3.

Table 5.3: Sample T1 temperature distribution versus die-sample position

Distance		2mm	0.3mm	Contact
Pyrometer Temperature		950°C	950°C	950°C
Thermocouples Temperature	Top Centre	986	994	1000
	Top Edge	982	990	994
	Middle Centre	971	974	974
	Middle Edge	982	985	984
	Bottom Centre	976	977	976
	Bottom Edge	988	988	986
	Average	980	984	985
	Standard Dev.	6	7	10

The average temperature inside the sample shows a very small change in relationship with the relative position of the top die to the sample. On the other hand, the fluctuation of the temperature increases is significant when the distance between the sample and the die decreases. The fluctuation of the temperature inside the sample, in relationship with the average temperature when the sample is closer to the die, goes beyond the  $\pm 6^\circ\text{C}$  which has been set as the error target for the compression experiments. The results clearly show that the 2 mm distance between the sample and the die is the best position for the compression tests.

#### 5.1.4 Pyrometer correction based on temperature distribution results

After taking all the above results under consideration the pyrometer input temperature has been corrected based on the average temperature distribution on sample T1. The corrected temperatures, used for the compression experiments, are presented in Table 5.4. The final temperature inside the sample

will be the required one with a possibility of 95% of an error within  $\pm 6^{\circ}\text{C}$ , which is acceptable.

**Table 5.4: Pyrometer corrected inputs**

Experiment temperature	Correction	Pyrometer input temperature	Error	Confidence
850°C	-35°C	815°C	$\pm 6^{\circ}\text{C}$	95%
900°C	-25°C	875°C	$\pm 6^{\circ}\text{C}$	95%
950°C	-31°C	919°C	$\pm 6^{\circ}\text{C}$	95%

## 5.2 Hot isothermal compression tests

In manufacturing industry, a significant amount of the production parts are produced with conventional hot working processes such as forging and extrusion. One of the most critical aspects of the metal forming process, is the determination of forming energy and forces; which requires deep knowledge of the flow behaviour of the formed material. The understanding of the flow behaviour during hot forming processes is complex due to the influence of many parameters such as starting microstructure, temperature, strain and strain rate [140]. Strain rate and temperature also have a significant effect on softening and hardening mechanisms, and a direct influence on the final mechanical properties.

The optimization of manufacturing routes and achievement of cost reduction with optimal mechanical properties of the final part is important for the manufacturing industry. Consequently, the study of the flow behaviour at different conditions

(strain rate, temperature, strain), is necessary to quantify the constitutive behaviour of the formed material. Even though a significant amount of research has been conducted to determine the deformation behaviour of two phase alloys (especially Ti-6Al-4V) [140], a comprehensive understanding of these materials does not exist. Significant work has been presented by Seshacharyulu et al. [49] for the hot deformation behaviour of Ti-6Al-4V with initial equiaxed microstructure at elevated temperatures and a wide range of strain rates. A process map based on flow behaviour is presented in this work and the flow instabilities at high strain rates are highlighted and attributed to adiabatic shear banding. Also, Seshacharyulu et al. [62] investigated the evolution of the deformed microstructure of Ti-6Al-4V with an initial lamellar microstructure. The experimental work was similar to Seshacharyulu et al. [49] creating a microstructural deformation mechanism map. Also, the flow stress behaviour of Ti-6Al-4V with a lamellar colony structure during hot working has been investigated by Semiatin et al. [141] and correlated to microstructure evolution. Semiatin et al. [142] also investigated the flow softening behaviour of Ti-6Al-4V and concluded that the underlying mechanism responsible is the microstructural evolution and the deformation heating. Further, Bruschi et al. [64] investigated the workability of Ti-6Al-4V at high temperatures and strain rates and correlate the flow behaviour to microstructure characteristics.

In order to optimize the manufacturing process routes, and achieve microstructural and property control of the final part it is mandatory to understand the constitutive behaviour of the material. Although, a significant amount of research has been conducted globally to investigate the flow behaviour of Ti-6Al-4V and the material's dependence on the initial microstructure, a significant data gap exists especially at strain rates above  $50 \text{ s}^{-1}$  which are important for high strain rate forging or extrusion. It is therefore pertinent that the correlation of strain, strain rate and temperature with flow behaviour is investigated in order to enhance process models.

## 5.3 Ti-6Al-4V flow stress corrections

### 5.3.1 Friction correction

A friction coefficient equal to 0.1 was used for all samples and has been suggested by the author's supervisor from previous ring compression test experiments (see description in section 4.7) which had been conducted at the AFRC [143]. The ring compression tests as well as the experiments were conducted with the same lubricant (AFRC IP), which was uniformly applied to the sample with the use of a small brush. The friction correction was based on the slab analysis presented in "Mechanical Metallurgy" by G.E. Dieter [144], as implied in its name, the slab method is based on the assumption that the deformation on the sample can be approximated with the deformation of a series of slabs, the slabs shape can be either flat or cylindrical in this case cylindrical, which is not changing during the deformation process.

### 5.3.2 Ringing effect correction

At high strain rates the test frame or the test piece vibrate. The transducers attached to the machine to measure load and displacement frequently register their vibration superimposed on the true signal. This is called ringing [118]. The ringing effect depends on the elastic characteristics of the material, the deformation rate, and the components measuring the load and the displacement. Roebuck et al. [145] have proposed a methodology to subtract the ringing effect from the flow curve by filtering the flow curve with the moving average method.

In this study, because of the unique layout of the attached sensors (two LVDT and two Load cells) the ringing effect is less strong (see Figure 5.3) in comparison with other equipment that has been reported in the literature [145] (see Figure 5.4).

The author exploring the signal filtering methodologies, concluded that running average smoothing was not giving a sufficiently smoothed curve. The reason behind that is the form of the ringing; a wave oscillation that is subject to the degradation as a function of the time that can be better addressed through a non-linear filter that takes under consideration the signal amplitude. The filtering of the curves was applied from strain rates higher than  $10 \text{ s}^{-1}$  up to  $100 \text{ s}^{-1}$ . Roebuck et al. [146] have demonstrate that the ringing effect increases with the increase of strain rate and became significant for strain rates above  $10 \text{ s}^{-1}$ . For higher strain rates the time of the experiment is so small that the ringing effect is not embedded in the flow curves.

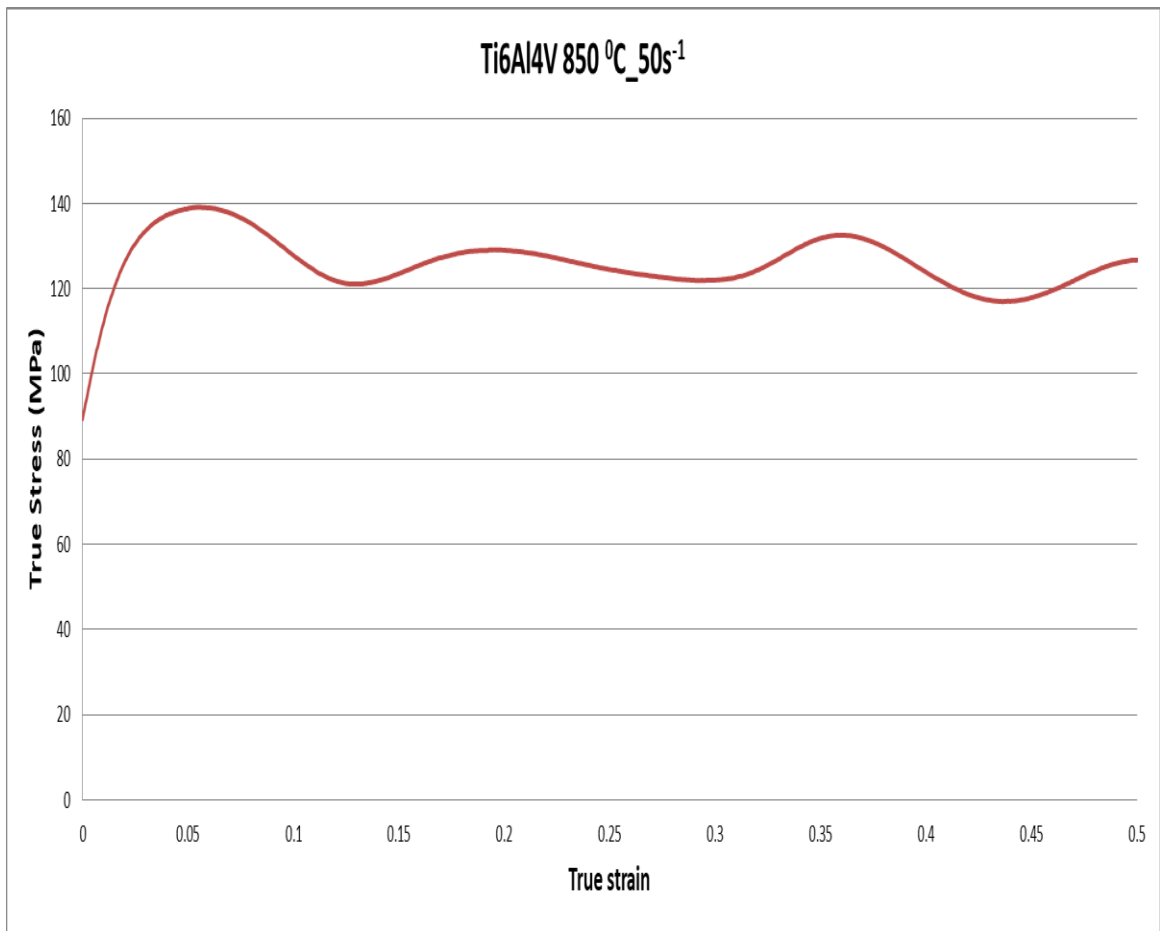


Figure 5.3 Ringing effect at hot isothermal compression Phoenix equipment

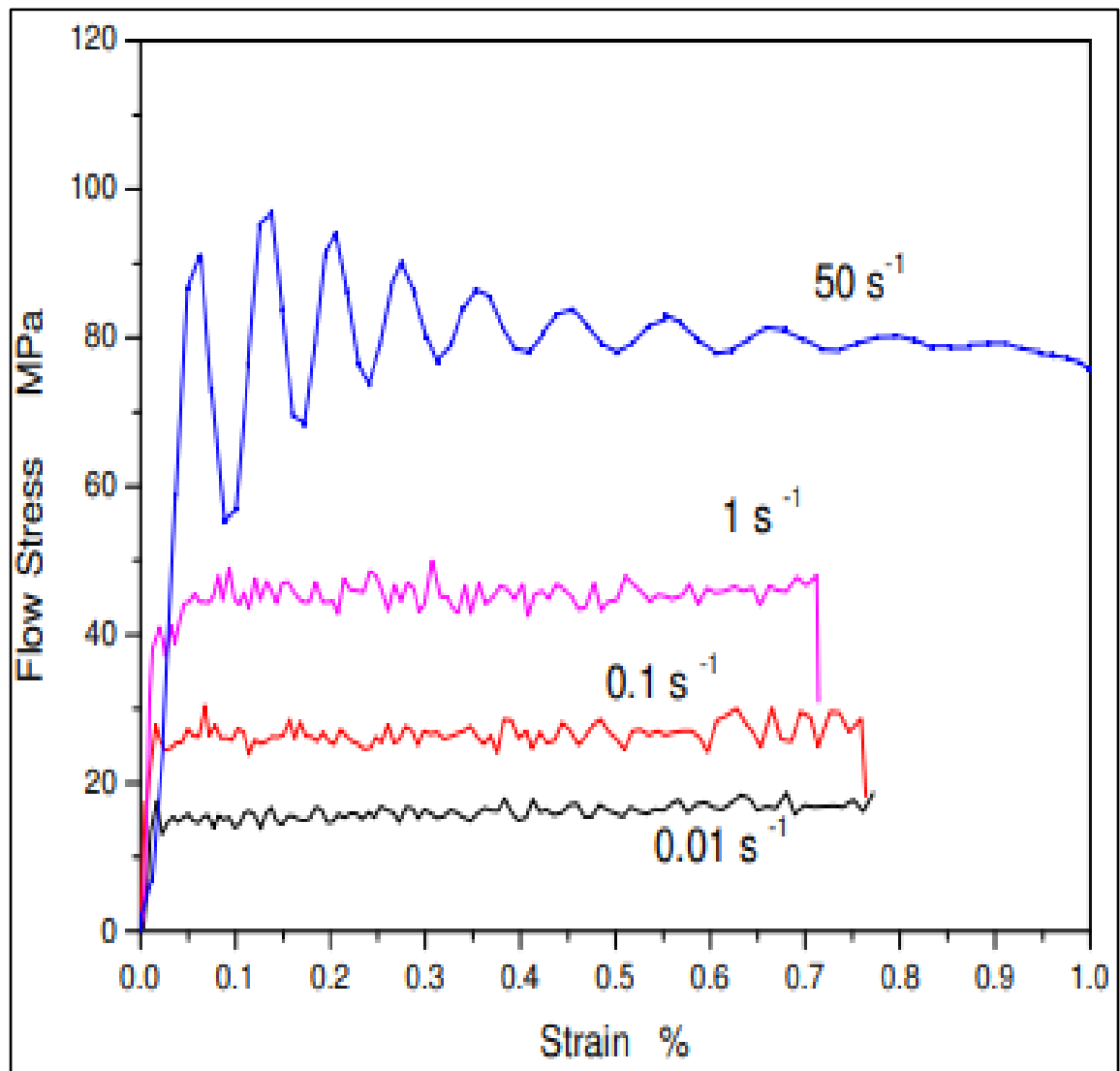


Figure 5.4 Ringing effect in tests on Al alloy 5052 at 500 °C [145]

### 5.3.3 Machine stiffness correction

The calculation of the machine's stiffness was conducted by standard procedures. The results of the machine's stiffness are presented in Figure 5.5 and the values which were used to correct the displacement are shown in Table 5.1.

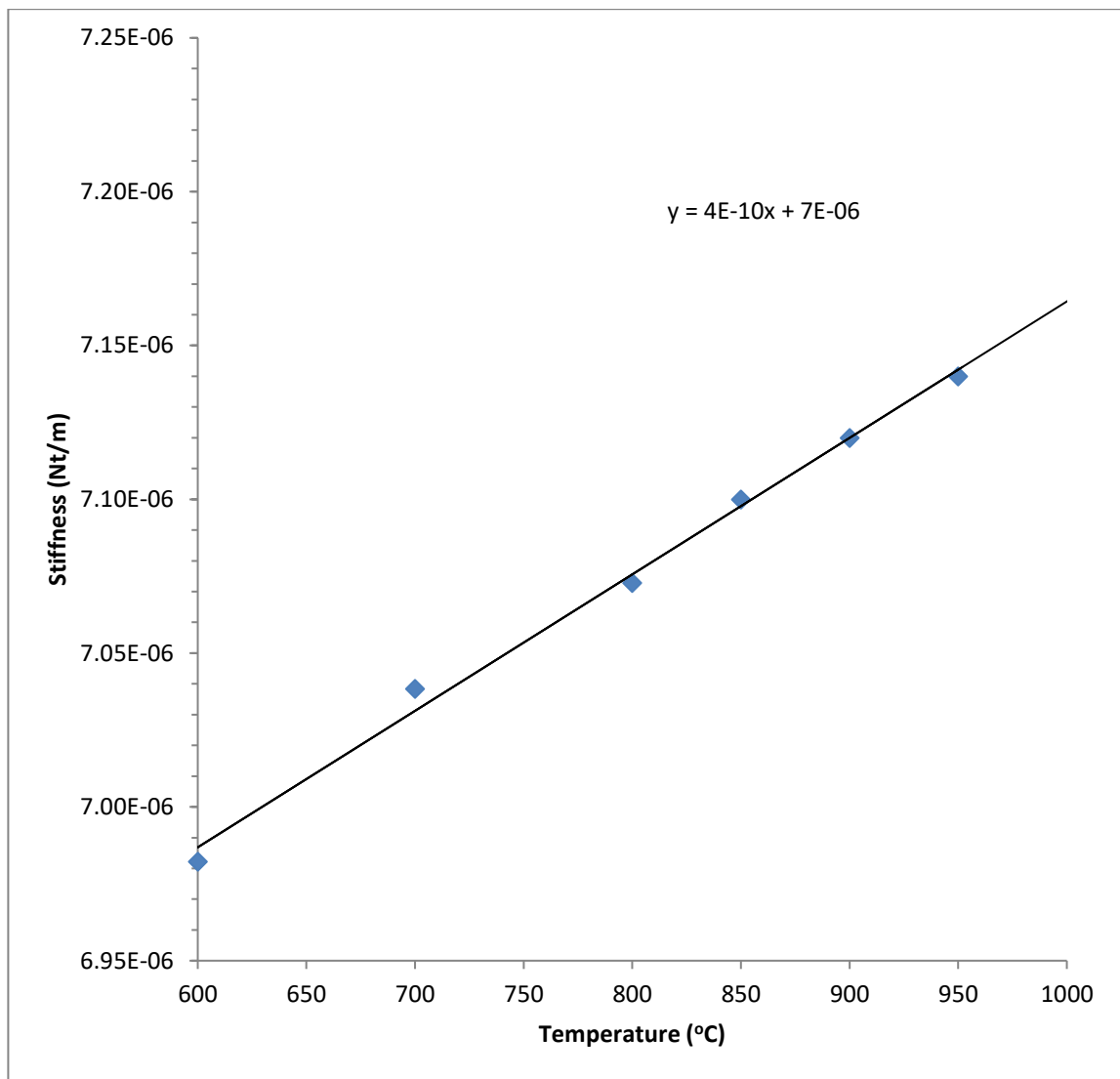


Figure 5.5: Machine stiffness at different temperatures

Table 5.1: Stiffness values from correction curves

Temperature (°C)	Stiffness (N/m)
850	0,00000710
900	0,00000712
950	0,00000714

For the high strain rate test the compliance correction was obtained through a unique experimental procedure after the isothermal compression test. The build in software base on the experimental temperature and max load during the test, executes a heating cycle and loads the platens for a small time period with the same load to obtain the compliance correction which presented in form of a five order polynomial.

#### 5.3.4 Friction and adiabatic heating correction

The stress-strain curves (flow curves) obtained from the hot isothermal tests are not representative of the true material behaviour. Friction and adiabatic heating are two factors contributing to the measured values and must be compensated for.

In this work, the correction for friction and adiabatic heating due to deformation was based on the slab analysis proposed by Dieter [144], and performed through a MathCAD routine [147]. Both corrections were conducted together within the routine. The friction coefficient is introduced to the routine with the uncorrected data, the adiabatic heat is calculated from the energy under the flow stress curve, taking under consideration the conduction heat losses from the ends and subtracts them; when the remaining energy is converted to temperature rise. Then a linear temperature sensitivity is assumed based on the flow stress data and the final temperature correction is applied to the flow stress.

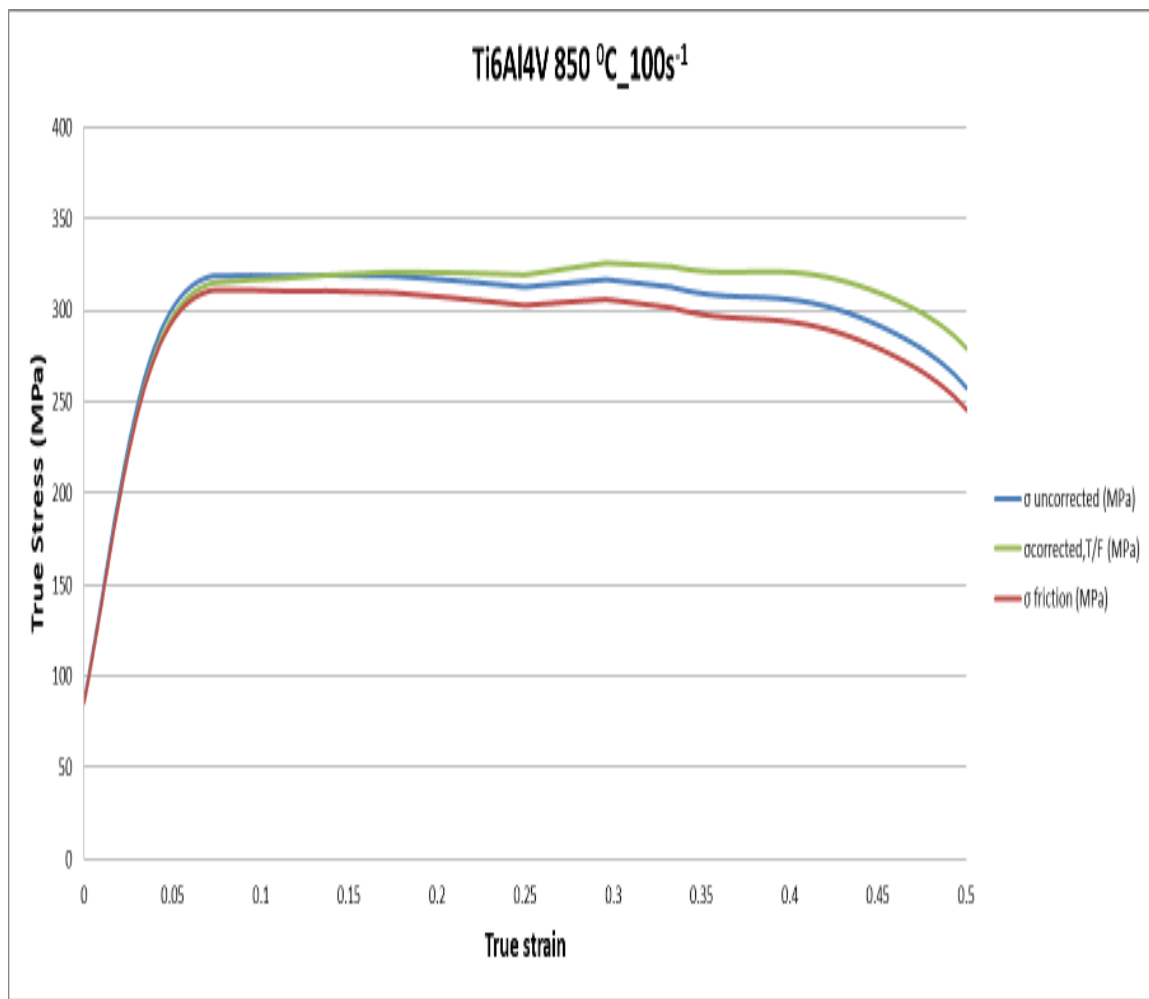


**Figure 5.6. Effect of friction and adiabatic heating correction on the flow curves at 850°C and 100 s<sup>-1</sup>**

The effect of the friction and adiabatic corrections of Ti-6Al-4V, at 850°C compressed at 100 s<sup>-1</sup>, to the flow curve is presented in Figure 5.6. From the curves the significant effect of the adiabatic heating is clearly demonstrated and can be spot it on the difference of the flow curve and the increased values of strain.

When metal is deformed at high strain rates, a significant amount of the applied energy is converted to heat, the phenomenon is amplified especially in regions of high localized deformations. The heat generation can lead to significant increase of the temperature inside the metal, since there is no time to conduct the heat to the environment [148]. The increased temperature inside the metal leads to the

reduction of the flow stress. Therefore, all the hot isothermal compression results have been corrected for machine compliance, friction and adiabatic heating.

#### 5.4 Modelling of flow curves

As forging moves to a new era of virtual forging operation instead of trial and error, accurate material behaviour becomes more and more important. Reliable and versatile simulations become necessity to predict process routes parameters and accurate final parts [149].

The complexity of materials flow behaviour during hot forging processes is well-known. The underlining mechanisms such as softening and hardening are both significantly influenced by many factors such as temperature, strain and strain rate. During hot deformation conditions, the understanding of metal and alloy flow behaviour plays important role for designing forging processes because of its active part on metal flow kinetics and patterns [140].

The flow properties of the metals are often described through predictive models (empirical-analytical or microstructural), empirical-analytical models using empirically derived equations to calculate the flow stress as a function of the process parameters. Microstructural models may also be used to describe the material response (during and post-deformation) in terms of microstructure parameters. Some examples of microstructural and empirical-analytical models are presented in Table 5.5 and Table 5.6.

The idea behind modelling for metals should be to accurately describe the material's flow behaviour to include forming temperature, strain rate dependence, and strain and work hardening. However, a single model which includes all these phenomena is a very difficult task. Therefore, always some limitations will apply to each model and must be carefully used.

Table 5.5: Examples of microstructural model [149]

MICROSTRUCTURAL MODELS		FEATURES
A	$D = D_0 - C_0 \cdot \varepsilon \cdot \dot{\varepsilon}^{C_1}$	Evolution of grain size $D$ during hardening and dynamic recovery $D_0$ = initial grain size
B	$\varepsilon_c = a \cdot \varepsilon_p$ $\varepsilon_c = K \cdot D_0^n \cdot Z^m$	$\varepsilon_c$ =critical deformation for the onset of dynamic recrystallization $\varepsilon_p$ = peak strain $Z$ = Zener-Hollomon parameter
C	$X = 1 - \exp\left(-\alpha \cdot (t/t_{0.5})^k\right)$ where $t_{0.5} = k_1 \cdot D_0 \cdot \dot{\varepsilon}^{n_1} \cdot \exp(Q/R \cdot T)$	Dynamic recrystallised fraction evolution $t_{0.5}$ = time to reach 50% recrystallization
D	$D_{0i+1} = X_i^{4/3} \cdot D_d + (1 - X_i)^2 \cdot D_{0i}$ $D_d = K_d \cdot (Z/A)^{m_d}$	Dynamic recrystallised grain size evolution
E	$X = 1 - \exp\left(-\alpha_s \cdot (t/t_{0.5})^{k_s}\right)$ $t_{0.5} = k_2 \cdot \varepsilon^{-n} \cdot D_0^m \cdot Z^p \cdot \exp(Q_{stat}/R \cdot T)$	Static recrystallisation fraction evolution
F	$D_{0i+1} = X_i^{4/3} \cdot D_{stat} + (1 - X_i)^2 \cdot D_{0i}$ $D_{stat} = K_{stat} \cdot \varepsilon^{-n} \cdot D_0^m$	Static recrystallised grain size evolution
G	$X = 1 - \exp\left(-\alpha_m \cdot (t/t_{0.5})^{k_m}\right)$ $t_{0.5} = k_3 \cdot Z^{p'} \cdot \exp(Q_{met}/R \cdot T)$	Metadynamic recrystallisation fraction evolution
H	$D_{0i+1} = X_i^{4/3} \cdot D_{met} + (1 - X_i)^2 \cdot D_{0i}$ $D_{met} = K_{met} \cdot Z^{p''}$	Metadynamic recrystallised grain size evolution
I	$D^{4.5} = D_{statormet}^{4.5} + B \cdot (t - t_{0.95}) \cdot \exp(Q_{growth}/R \cdot T)$	Grain growth $t_{0.95}$ = time to reach 95% recrystallization
J	$\zeta(t) = 1 - \exp(-k \cdot t^n)$	Phase transformation kinetics $\xi$ = volume fraction at the growing phase at time $t$
<p><math>\varepsilon</math> : equivalent strain <math>\dot{\varepsilon}</math> : equivalent strain rate <math>T</math> : temperature  <math>D_0</math> : initial grain size <math>D</math> : average grain size <math>\varepsilon_c</math> : critical deformation  <math>\varepsilon_p</math> : peak strain <math>Z</math> : Zener-Hollomon parameter <math>X</math> : recrystallised fraction  <math>t</math> : time <math>Q</math> : activation energy <math>R</math> : universal gas constant  <math>t_{0.5}</math> : time to reach 50% recrystallization <math>t_{0.95}</math> : time to reach 95% recrystallization <math>\zeta</math> : volume fraction</p>		

Table 5.6: Examples of empirical models [149]

EMPIRICAL MODELS		FEATURES
A	$\sigma = k\varepsilon^n$ [47]	Strain hardening
B	$\sigma = A - (A - B)\exp\left(-\frac{\varepsilon}{\varepsilon_0}\right)$ [48]	Strain hardening and dynamic recovery at large strains
C	$\sigma = k\varepsilon^n \dot{\varepsilon}^m \exp\left(\frac{\beta}{T}\right)$ [46]	Simultaneous dependence on equivalent strain, strain rate and temperature
D	$\sigma = A \exp(m_1 T) T^{m_2} \varepsilon^{m_3} \exp\left(\frac{m_4}{\varepsilon}\right)$ $(1 + \varepsilon)^{m_5 T} \exp(m_7 \varepsilon) \dot{\varepsilon}^{m_3} \varepsilon^{m_6 T}$	Accurate representation of the flow curve in hot deformation conditions
E	$\sigma = \sigma_{ecr} (1 - W) + \sigma_{sat} W$ $\sigma_{ecr} = A(\dot{\varepsilon}, T) (\varepsilon + \varepsilon_0)^{B(\dot{\varepsilon}, T)}$ $\sigma_{sat} = C_0 \exp(-C_1 T) \dot{\varepsilon}^{(C_2 + C_3 T)}$ $W = 1 - \exp(-R\varepsilon^{-s})$ [46]	Accurate representation of the flow curve in hot deformation conditions
F	$Z = \dot{\varepsilon} \exp\left(\frac{Q}{RT}\right) = A[\sinh(\alpha\sigma)]^{n'}$ [42]	Neglects the effects of strain
G	$\sigma = \frac{1}{\alpha} \sinh^{-1} \left[ \frac{\dot{\varepsilon} \exp\left(\frac{Q}{RT}\right)}{A} \right]^{\frac{1}{n'}}$ [43]	Accurate representation of the flow curve in hot deformation conditions
H	$\sigma = \left( A + B\varepsilon^n \right) \left( 1 + C \ln\left(\frac{\dot{\varepsilon}}{\dot{\varepsilon}_0}\right) \right) \left( 1 - \left( \frac{T - T_0}{T_m - T_0} \right)^m \right)$ [49]	Accurate representation of the flow curve at high strain rate
I	$\sigma = \left[ \left( \frac{\dot{\varepsilon}}{\dot{\varepsilon}_{st}} \right)^m \sigma_{st} + B \right] \exp \left[ -p \left( \frac{\dot{\varepsilon}}{\dot{\varepsilon}_{st}} \right)^q (T - T_{st}) \right]$ [50]	Deformation history taken into account when no recrystallization occurs
$\sigma$ : equivalent stress; $\varepsilon$ : equivalent strain $\dot{\varepsilon}$ : equivalent strain rate $T$ : temperature $Z$ : Zener-Hollomon parameter $Q$ : activation energy $T_0$ : initial temperature $T_m$ : melting temperature		

Many researchers have used different models to address the material behaviour under various conditions. Zhao et al. [150] have used the Johnson Cook(JC) model [151] and the KHL model [66] to describe the deformation behaviour of Ti-6Al-4V under dynamic compression. To predict the flow stress of severely deformed pure titanium at high temperature Sajadifar et al. [152] used the constitutive equation proposed by Zener and Hollomon [153]. The common

features of all these approaches is that the models take into consideration the strain, strain rate and temperature to describe the flow behaviour of metals.

This study is driven from a specific objective; to establish and enhance the capabilities of the AFRC to test and properly describe the material behaviour under high strain rates, with the final aim to offer the forming and forging UK manufacturing industry more reliable material data which will be used to FE simulations for more accurate and cost effective process optimization. As the material response contributes to the prediction of energy use and maximum load, this, together with the strain and temperature inside the formed or forged part plays a significant part in the final process optimization and design.

As the Holy Grail of the modern manufacturing industry is cost reduction, significant work is carried out to avoid uncertainties in the maximum forging load which can lead to extra costs [154]. An example is presented in Figure 5.7; Baniani et al. [155] investigated the cost associated with uncertainty in maximum forging load for a screw press. They concluded that 30% uncertainty in evaluation of forging load can lead to an extra cost of 5-9% for the forged material and a potential extra capital cost for equipment acquisition of up to 90% [149].

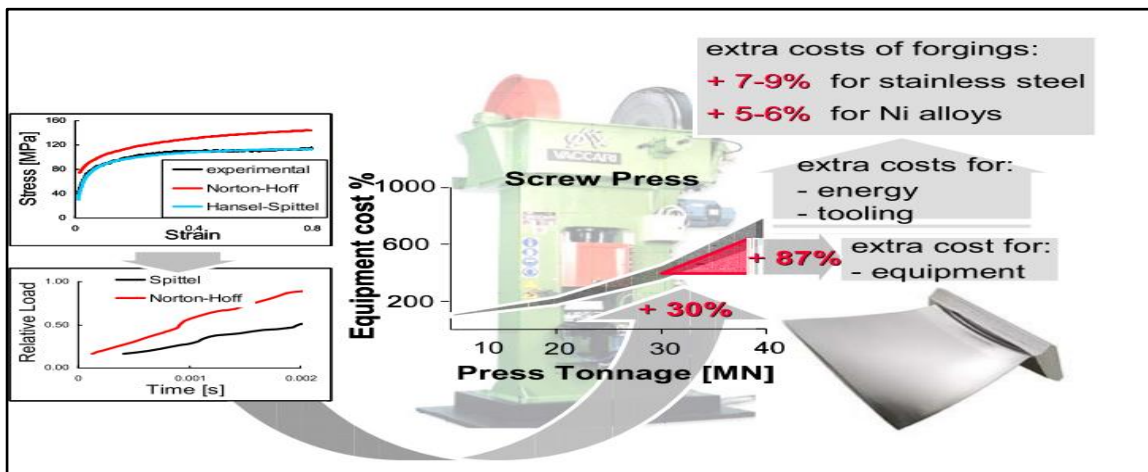


Figure 5.7: Costs association between uncertainty in maximum forging load for a screw press [149]

In this work the flow curves were modelled by the Hansel-Spittel (H&S) rheological law [156]. The constitutive equation was selected because it can adequately incorporate the strain, strain rate and temperature effects at high temperatures. Furthermore, much of the commercial high speed forging modelling is implemented by the finite element software Forge® and Deform® and the Hansel-Spittel (H&S) rheological law is widely used in this software [157].

The full form of the law is presented below:

$$\sigma_f = A e^{m_1 T} \varepsilon^{m_2} \dot{\varepsilon}^{m_3} e^{\frac{m_4}{\varepsilon}} (1 + \varepsilon)^{m_5 T} e^{m_7 \varepsilon} \dot{\varepsilon}^{m_8 T} T^{m_9}$$

Where  $\sigma_f, \varepsilon, \dot{\varepsilon}$  are respectively stress, strain and strain rate and T is the temperature given in Celsius,  $m_1$  and  $m_9$  define the material's sensitivity to temperature,  $m_5$  defines the coupling of temperature and strain,  $m_7$  defines the coupling of temperature and strain rate, the  $m_8$  term coupling temperature and strain rate,  $m_2, m_4$  and  $m_7$  define the material's sensitivity to strain and  $m_3$  depends on the material's sensitivity to strain rate. Usually, constants  $m_8$  and  $m_9$  are taken as zero [158] as well as  $m_7$ , it was assumed that, at a given strain (or at steady state), the stress exponent  $n = 1/(m_3 + m_7 T)$  should be temperature independent, i.e.,  $m_7 = 0$  [159]. A more simplified version of the equation is presented below:

$$\sigma_f = A e^{m_1 T} \varepsilon^{m_2} \dot{\varepsilon}^{m_3} e^{\frac{m_4}{\varepsilon}}$$

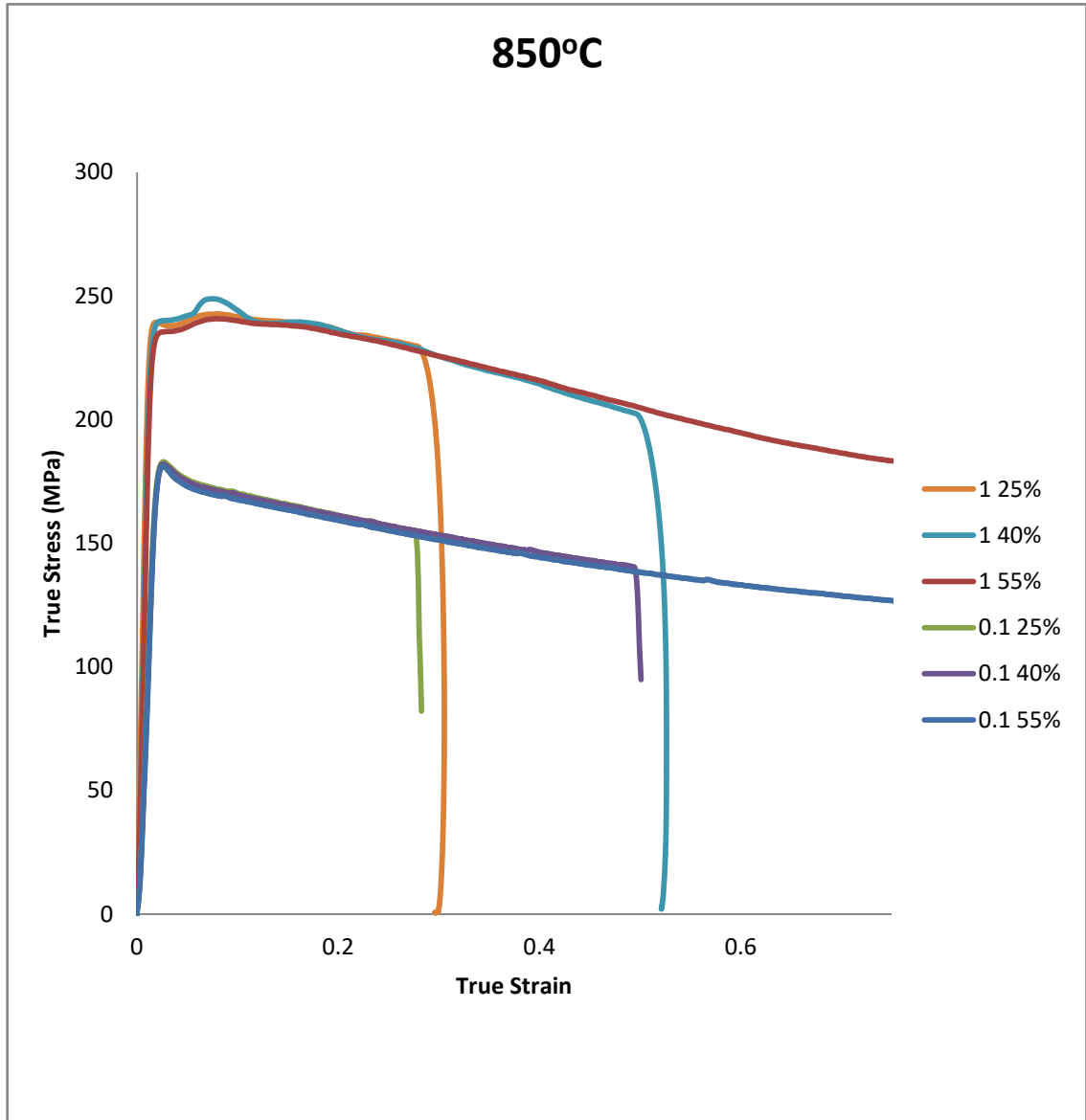
The simplified version of the equation was used to avoid over-parameterisation of the flow behaviour. A non-linear approach was used to fit the model for all conditions separately and globally. The materials constants were calculated using non-linear regression after the correction of the flow curves for friction and adiabatic heating.

## 5.5 As-received microstructure

### 5.5.1 Flow behaviour at low strain rates

According to the experimental plan (presented in chapter 4, section 4.5.4 and Table 4.5), the flow curves of Ti-4Al-4V with as-received microstructure derived from hot isothermal compression tests at two strain rates ( $0.1\text{s}^{-1}$  and  $1\text{s}^{-1}$ ), three strain levels (25%, 40% and 55%) and three temperatures (850°C, 900°C and 950°C) are presented in Figure 5.8, Figure 5.9 and Figure 5.10.

Figure 5.8: Flow stress behaviour of Ti-6Al-4V at 850°C at strain rates of  $0.1s^{-1}$  and  $1s^{-1}$  for three strains



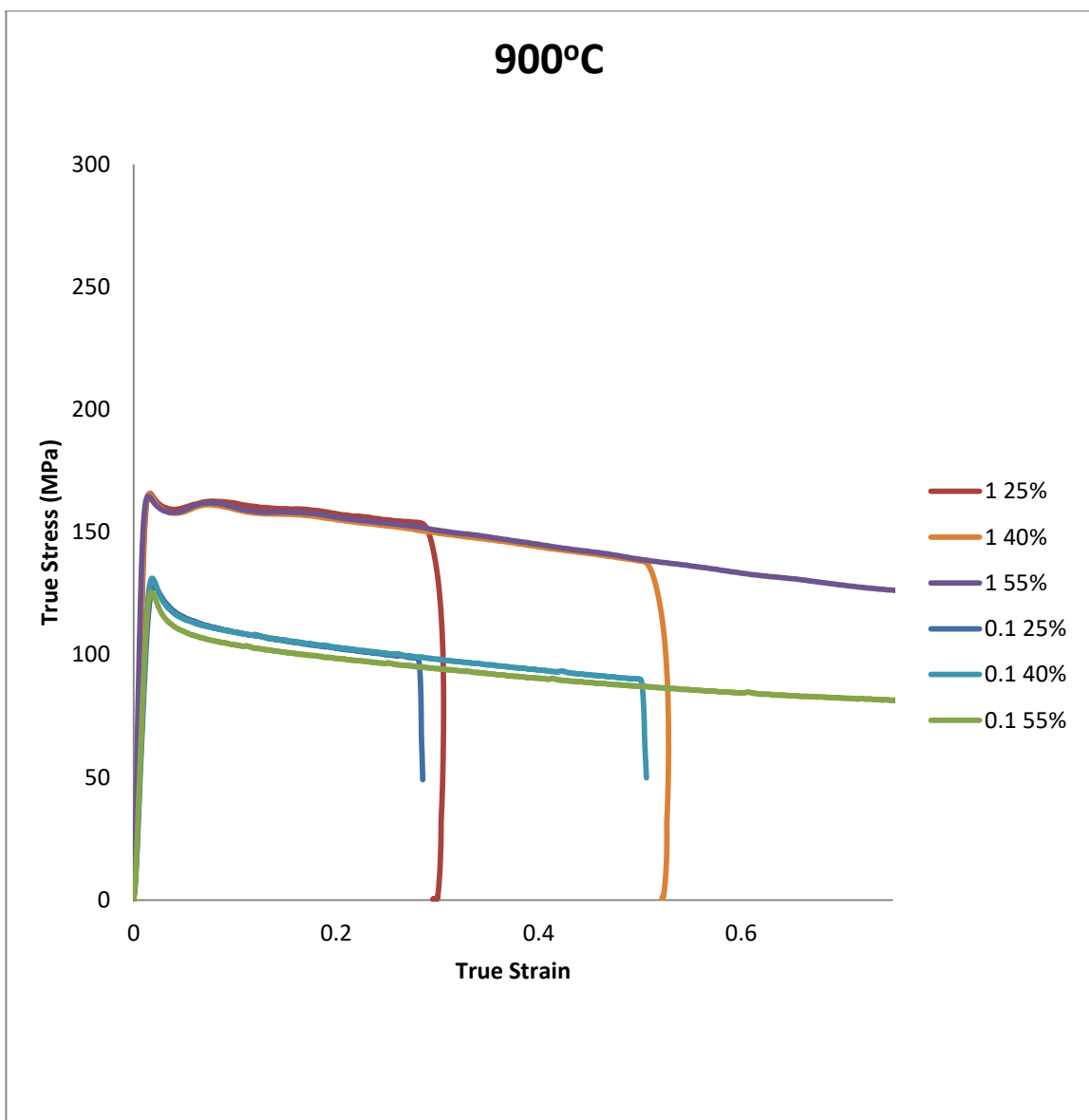


Figure 5.9: Flow stress behaviour of Ti-6Al-4V at 900°C at strain rates of 0.1s<sup>-1</sup> and 1s<sup>-1</sup> for three strains

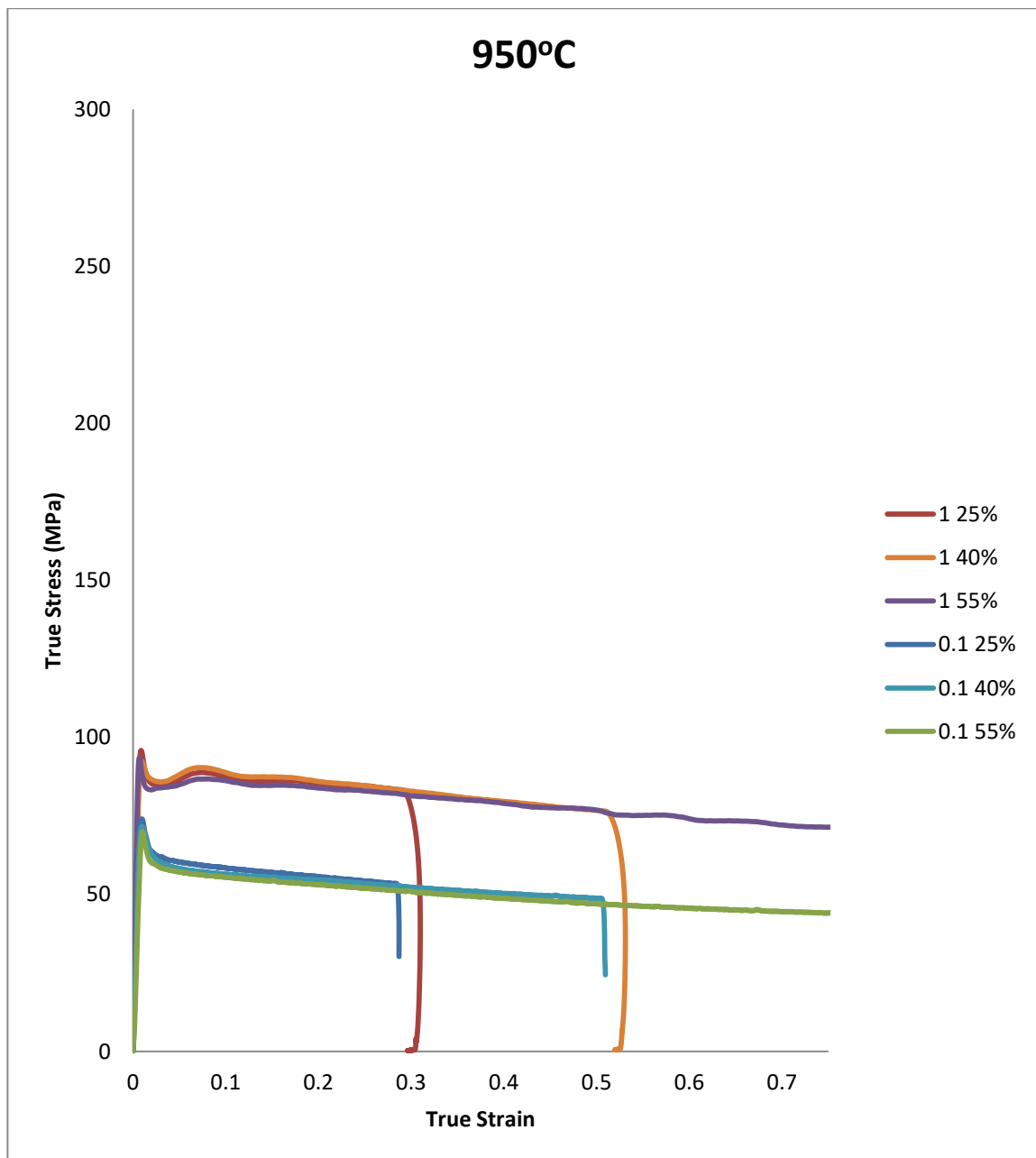


Figure 5.10: Flow stress behaviour of Ti-6Al-4V at 950°C at strain rates of 0.1s<sup>-1</sup> and 1s<sup>-1</sup> for three strains

The flow behaviour of the curves for the three temperatures strongly depended on the strain rate. All the curves initially present strain hardening with a small peak at all strain rates, followed by moderate flow softening. This type of flow behaviour is well documented in the literature for similar microstructures [49] [50]. The flow

softening behaviour can be attributed at the adiabatic heating, which increases the temperature inside the sample and at the same time the proportion of the soft  $\beta$  phase.

#### 5.5.2 Flow behaviour at intermediate strain rates

Following the low strain rate hot isothermal compression tests, the intermediate strain rate test results (see section 4.5.6 and Table 4.6 ) are presented in this section. The flow curves of Ti-4Al-4V with the as-received microstructure derived from hot isothermal compression tests at strain rate of  $10\text{s}^{-1}$ , two stain levels( 40% and 55%) and three temperatures (850°C, 900°C and 950°C) are presented in Figure 5.11, Figure 5.12 and Figure 5.13.

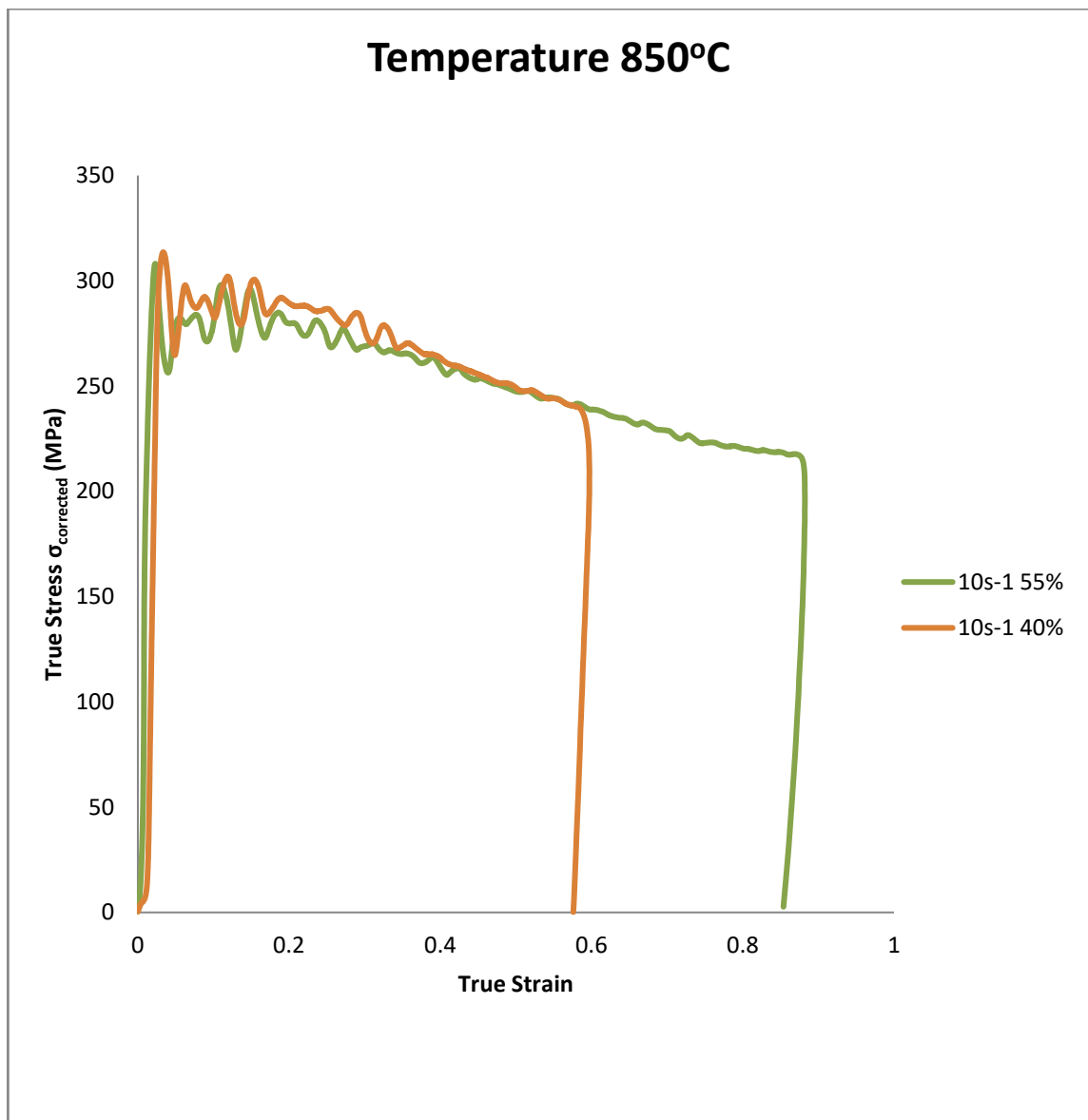


Figure 5.11: Flow stress behaviour of Ti-6Al-4V at 850°C at 10 s<sup>-1</sup> for two strains

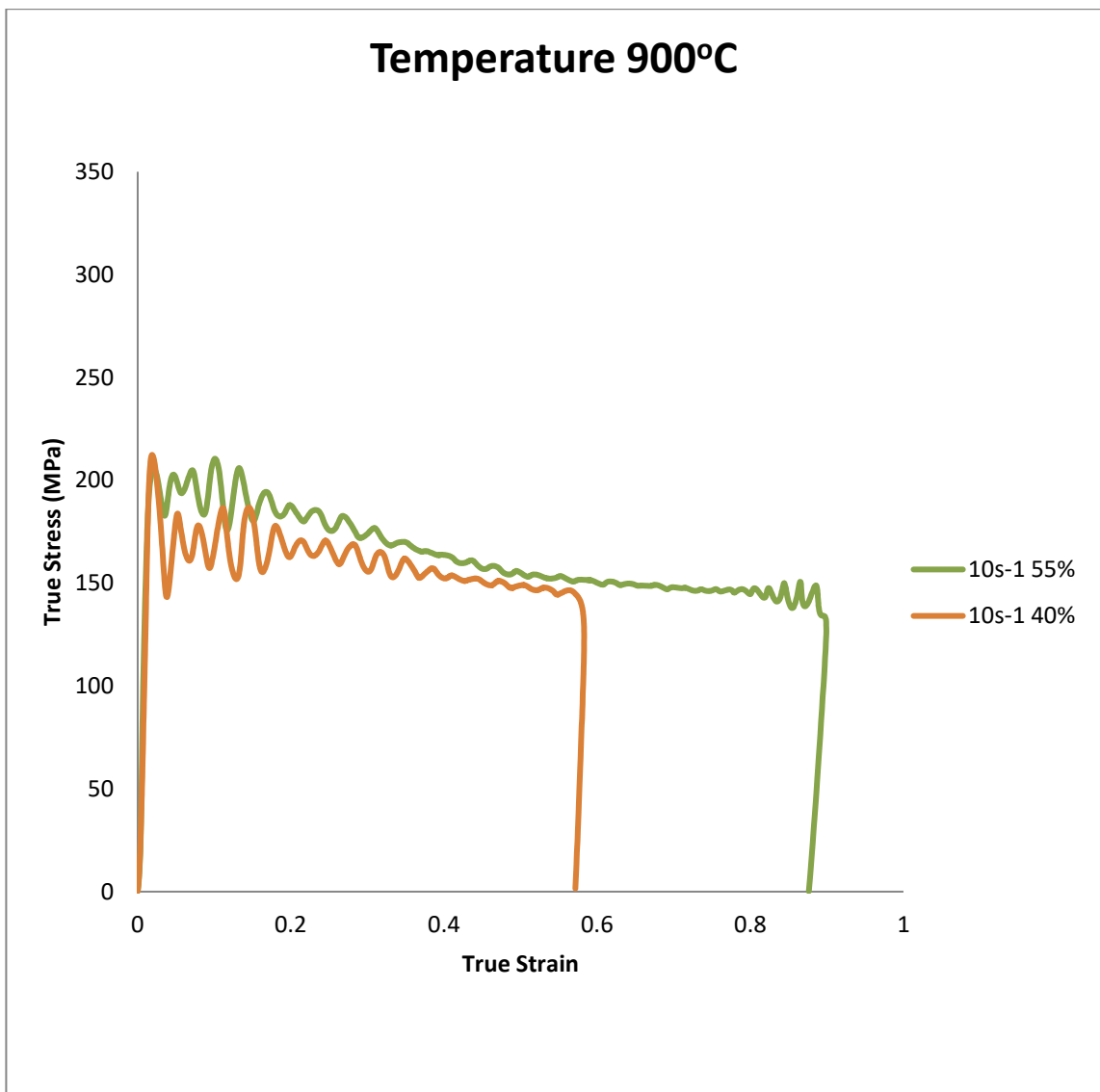


Figure 5.12: Flow stress behaviour of Ti-6Al-4V at 900°C at 10 s<sup>-1</sup> for two strains

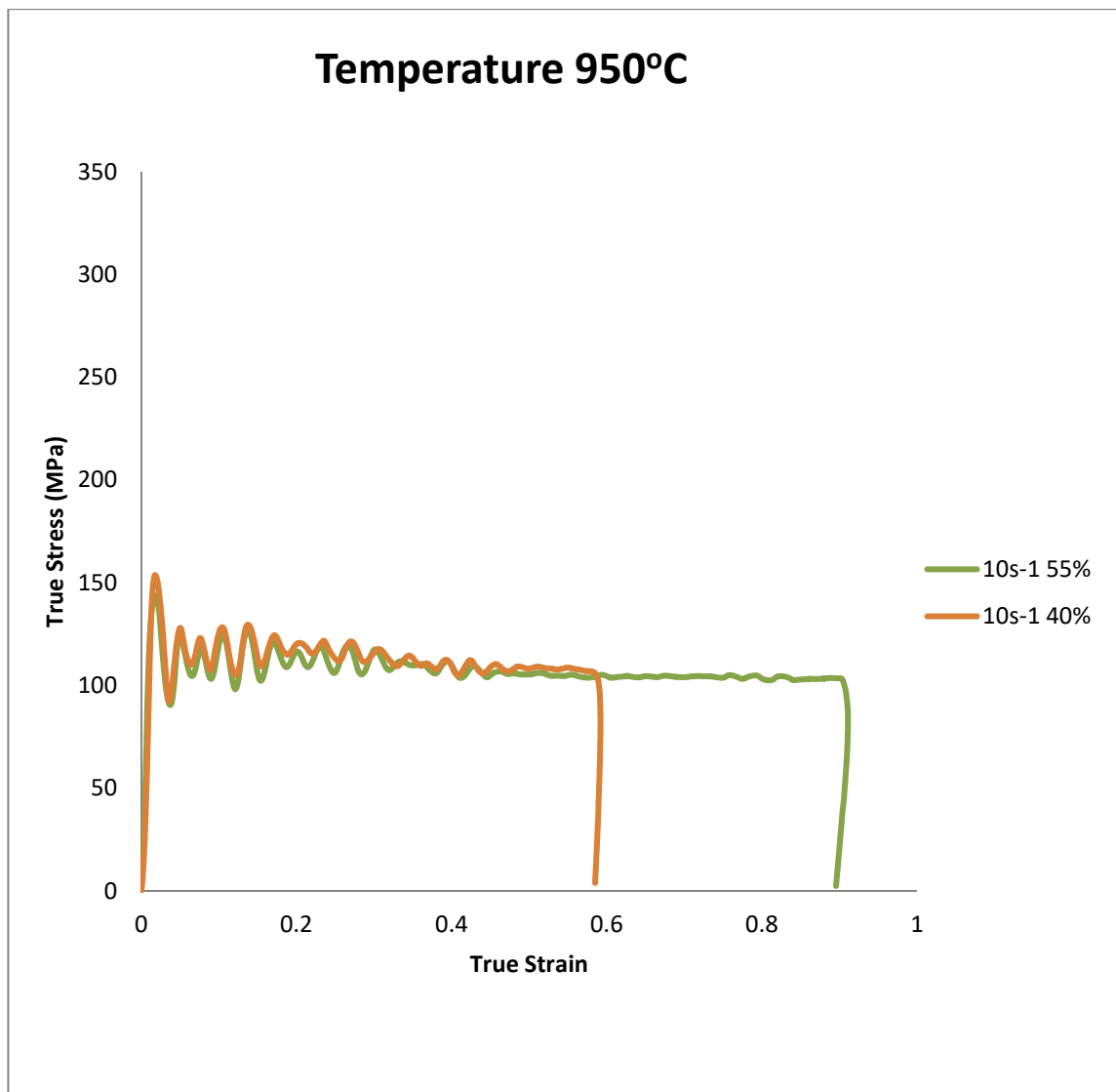


Figure 5.13: Flow stress behaviour of Ti-6Al-4V at 950°C at 10 s<sup>-1</sup> for two strains

The flow behaviour for the strain rate of 10 s<sup>-1</sup> and the temperature of 850°C and 900°C is similar to 1 s<sup>-1</sup> strain rate, with initial peak due to strain hardening followed by flow softening. For both temperatures after the initial peak, a flow instability is presented with multiple peaks, indicating dynamic recrystallization (DRX) or flow localization [49]. As been discussed in section 5.5.7 the phenomenon is due to flow localization. Similar behaviour at higher temperatures

(in  $\beta$  range) have been presented in the literature [49], in this case the phenomenon may arise because the actual temperature have risen due to adiabatic heating or flow localization. At a temperature of 950°C, the flow behaviour after the strain hardening in the beginning presents an immediate steady state condition which is characteristic of a discontinuous dynamic recrystallization (DDRX)[160]. The possibility that the flow softening is absorbed in the unstable region of the flow, may explain the DDRX behaviour and not the DRX that is expected [49].

### 5.5.3 Flow behaviour at high strain rates

The high strain rate flow stress behaviour of Ti-6Al-4V was explored based on the experimental plan detailed in chapter 4 and presented in Table 4.7. The results of the 18 isothermal compression tests are presented in Appendix D. An example of the flow curve and the corrected curves for friction and adiabatic heating, as well as the flow curve fitted with the H&S rheological law for both the experiments conducted at 900°C and strain rate of 100s<sup>-1</sup> is presented in Figure 5.14 and Figure 5.15.

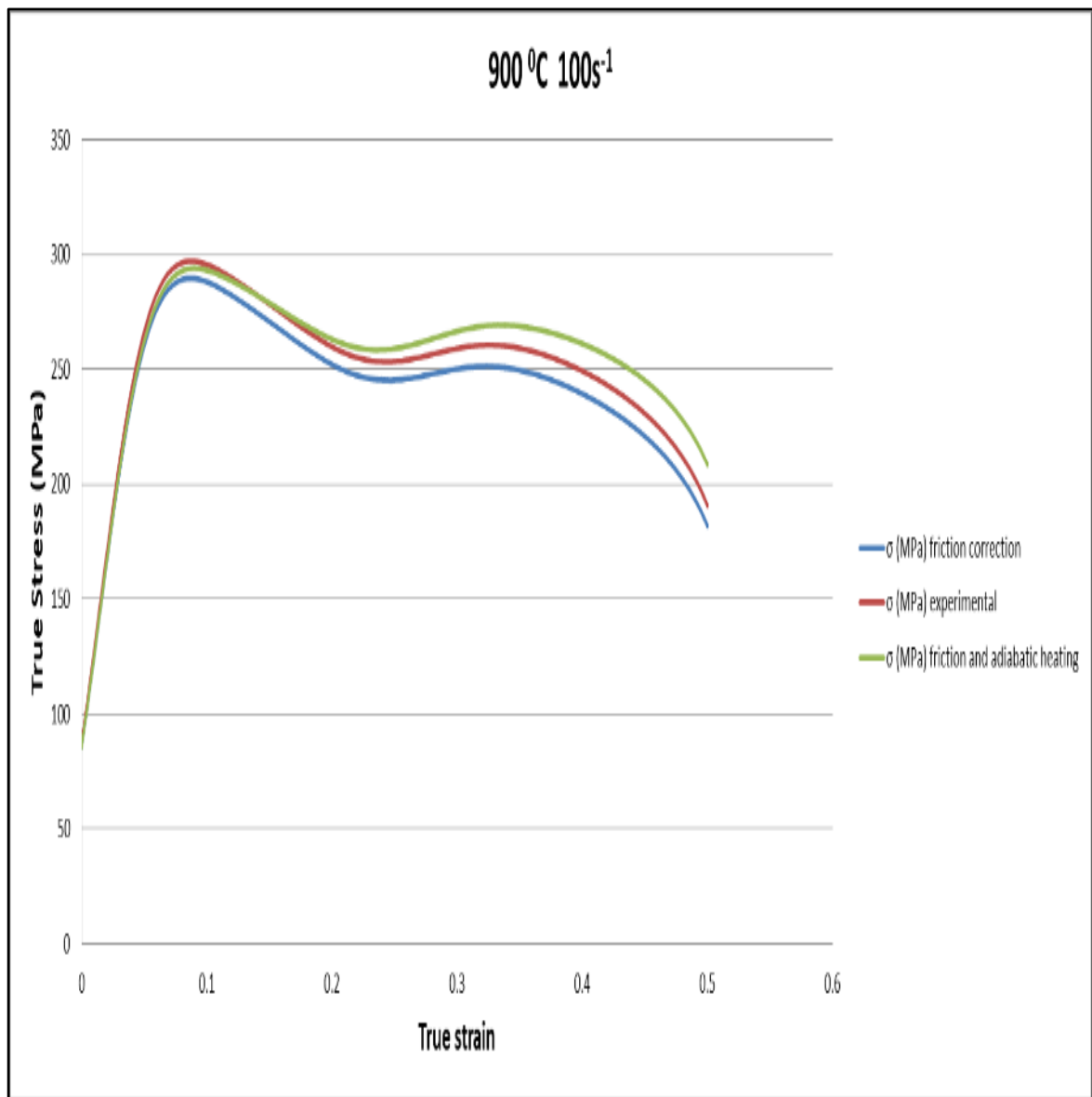


Figure 5.14: Flow stress at 900°C and 100s<sup>-1</sup>, experimental, with friction correction and adiabatic heating.

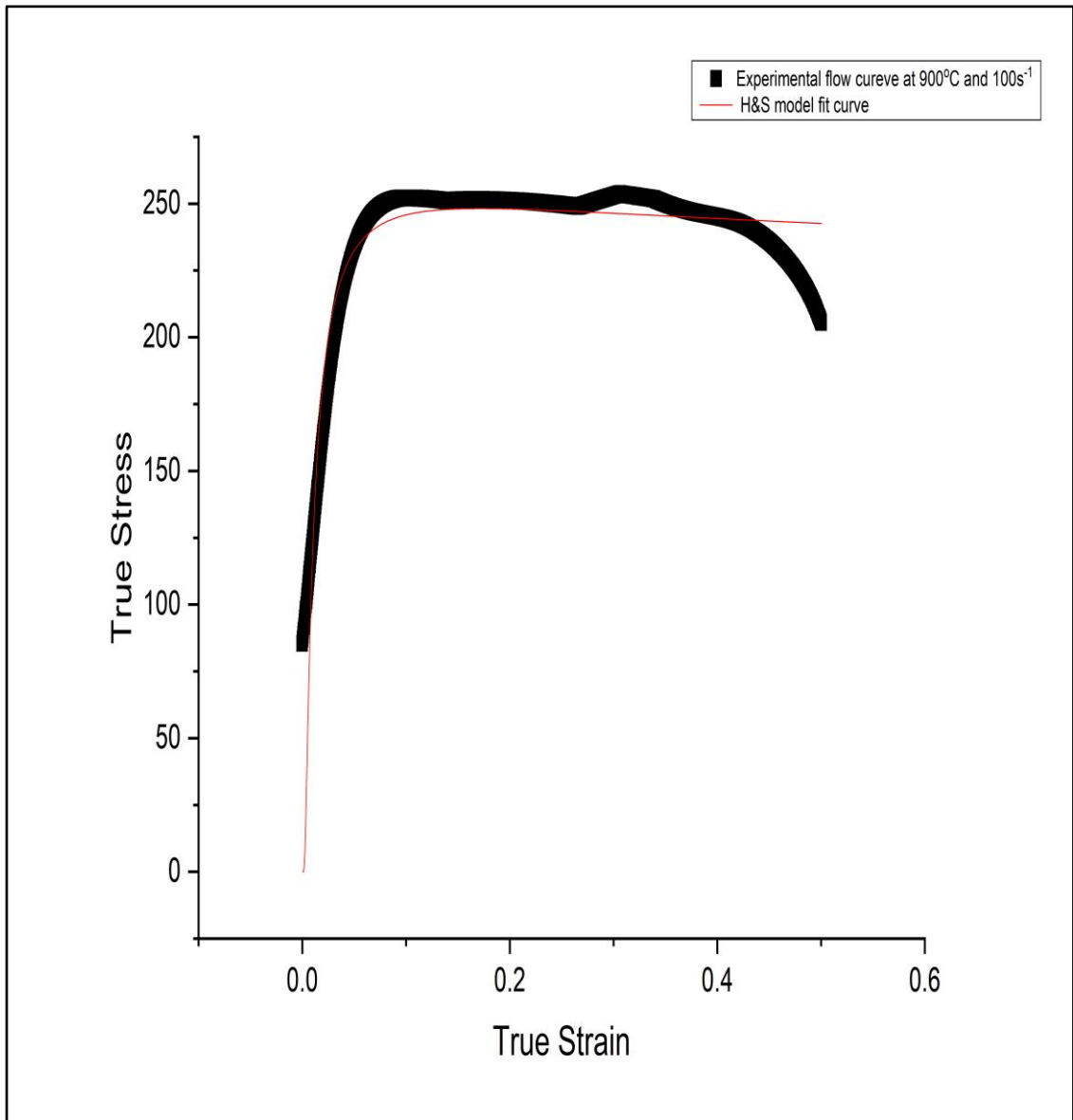


Figure 5.15: Flow stress at 900°C and 100s<sup>-1</sup>, after smoothing and fitting with H&S

The curves for the as received microstructure derived from hot isothermal compression tests at three strain rates (50s<sup>-1</sup>, 100s<sup>-1</sup> and 150s<sup>-1</sup>), at a strain level of 55% and three temperatures (850°C, 900°C and 950°C) are presented in Figure 5.16, Figure 5.17 and Figure 5.18. The curves were corrected for friction and adiabatic heating. Furthermore, they were smoothed and fitted with H&S model.

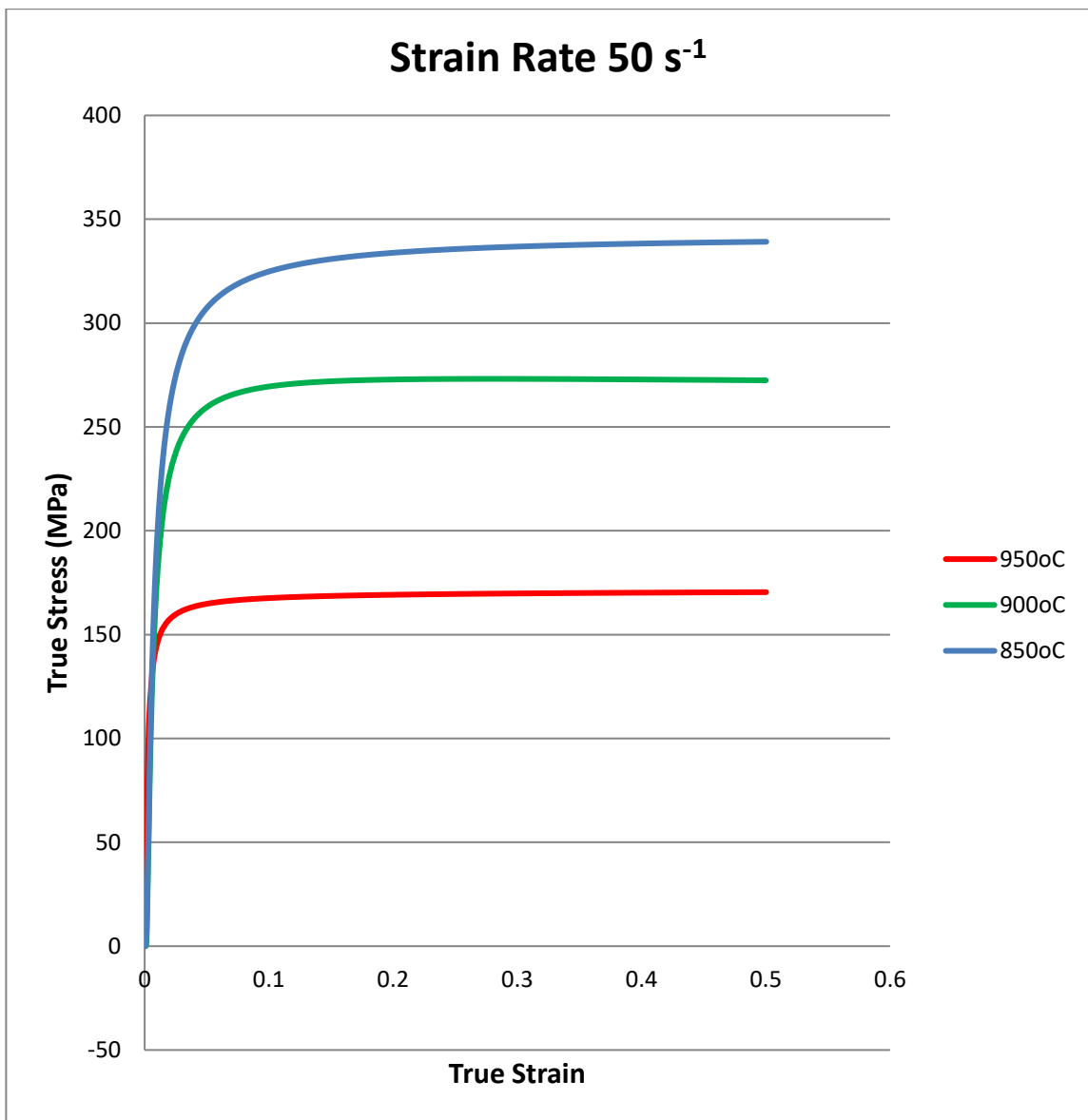


Figure 5.16: Flow stress behaviour of Ti-6Al-4V at 50 s<sup>-1</sup> and three temperatures (850°C, 900°C and 950°C)

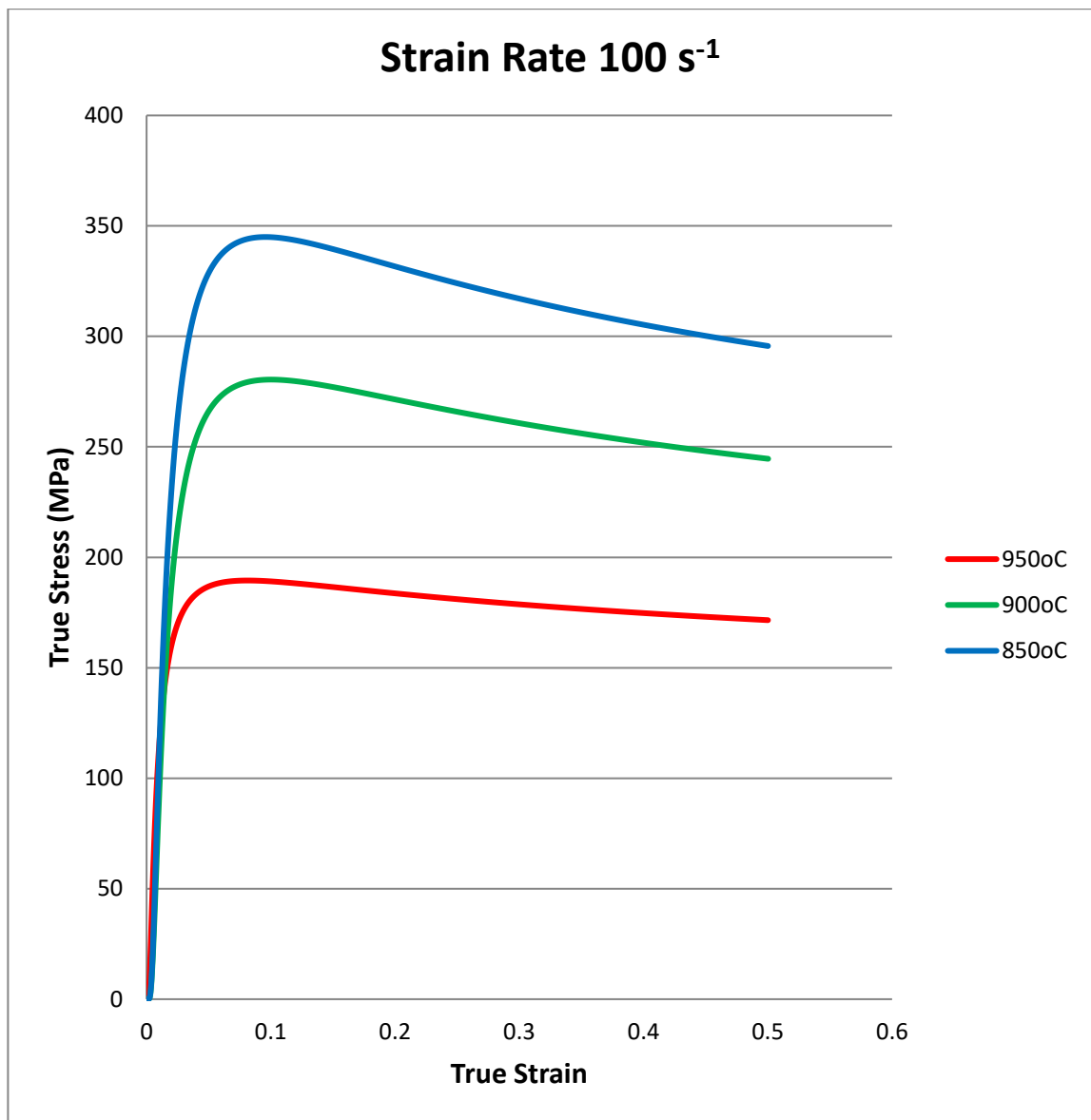


Figure 5.17: Flow stress behaviour of Ti-6Al-4V at 100 s<sup>-1</sup> and three temperatures (850°C, 900°C and 950°C)

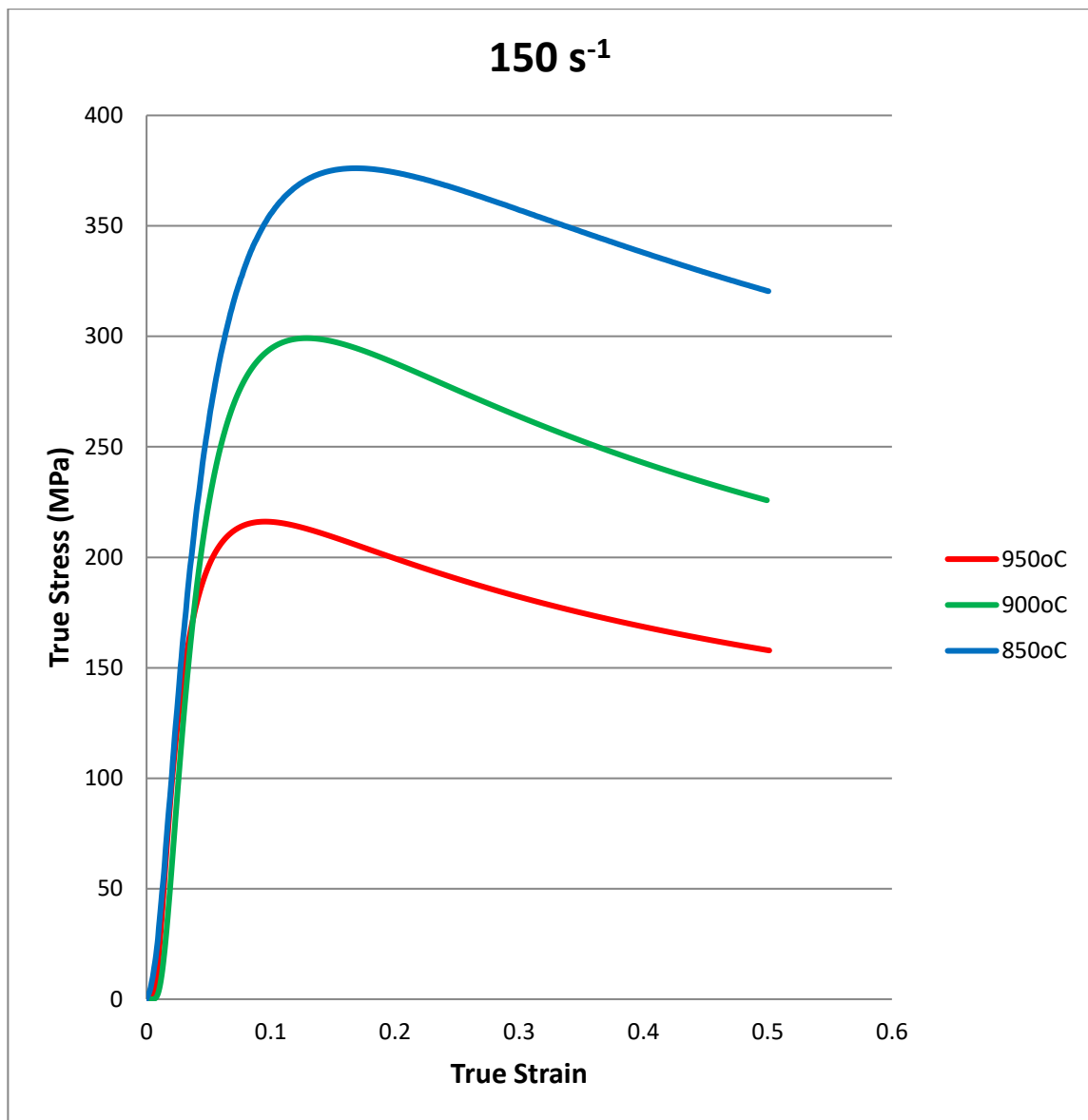


Figure 5.18: Flow stress behaviour of Ti-6Al-4V at 150 s<sup>-1</sup> and three temperatures (850°C, 900°C and 950°C)

The flow behaviour of the curves for the three strain rates are strongly dependent on the temperature. The flow stress curves initially show strain hardening with a peak at all strain rates and temperatures, followed by moderate flow softening except at a strain rate of 50 s<sup>-1</sup> for all temperatures (850°C, 900°C and 950°C). This type of flow behaviour is expected for strain rates of 50 s<sup>-1</sup> and 100 s<sup>-1</sup>; that

is documented in the literature [49][64]. For strain rates of  $150 \text{ s}^{-1}$  there is no comparable experimental data in the literature. The steady state behaviour at a strain rate of  $50 \text{ s}^{-1}$  and temperatures of  $850^\circ\text{C}$  and  $900^\circ\text{C}$ , follow the behaviour monitored at  $950^\circ\text{C}$  and a strain rate of  $1 \text{ s}^{-1}$ , indicating DRX or dynamic recovery was in operation [50][161].

#### 5.5.4 H&S modelling of flow behaviour

As has been mentioned in section 5.4 the flow behaviour of the as-received microstructure has been modelled with the H&S rheological law. The flow curves and the material constants, as well as the percentage of confidence for the three temperatures and three strain rates are presented in this section.

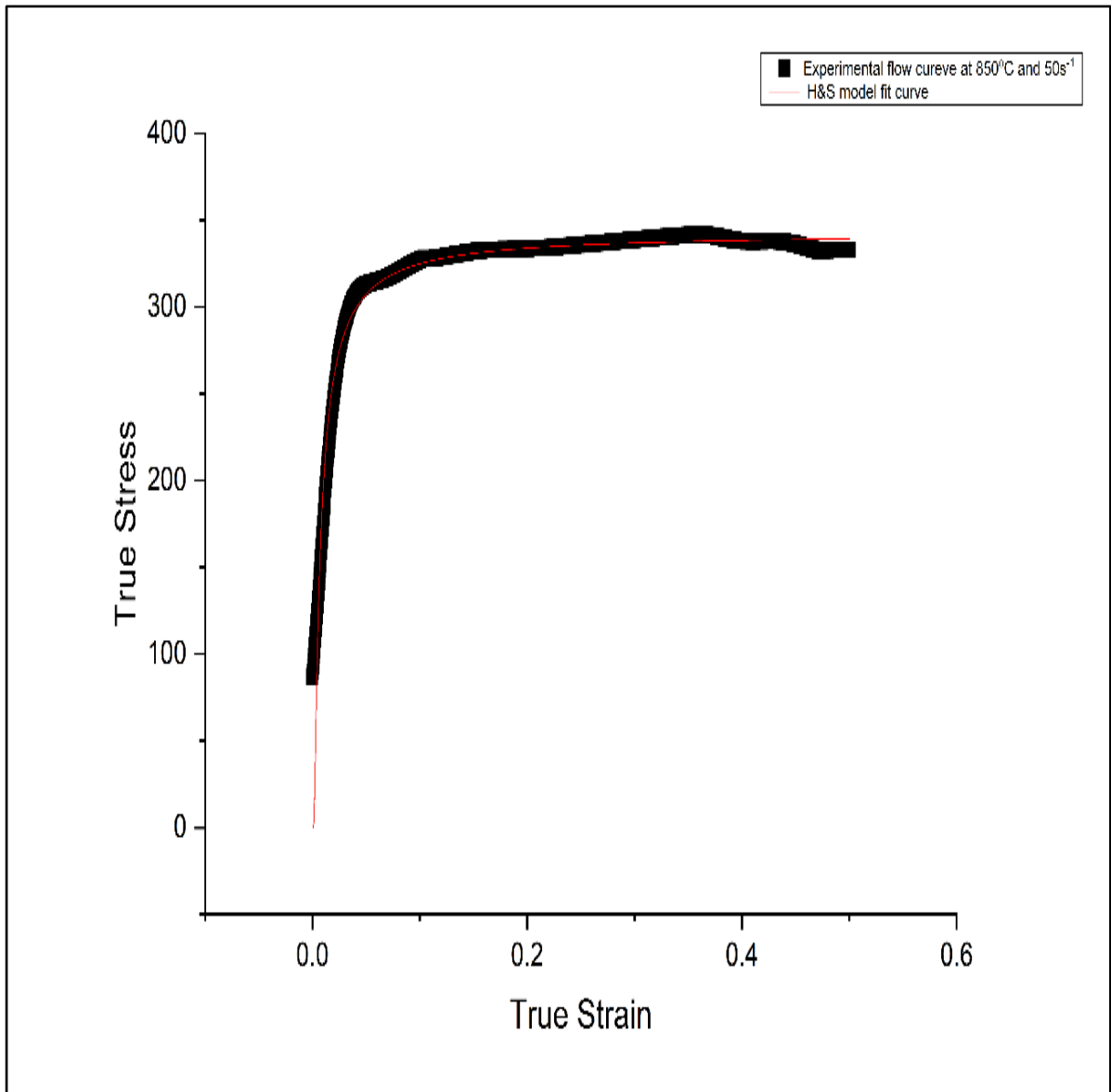


Figure 5.19: Experimental and modelled flow curves for 850°C and strain rate 50s<sup>-1</sup>

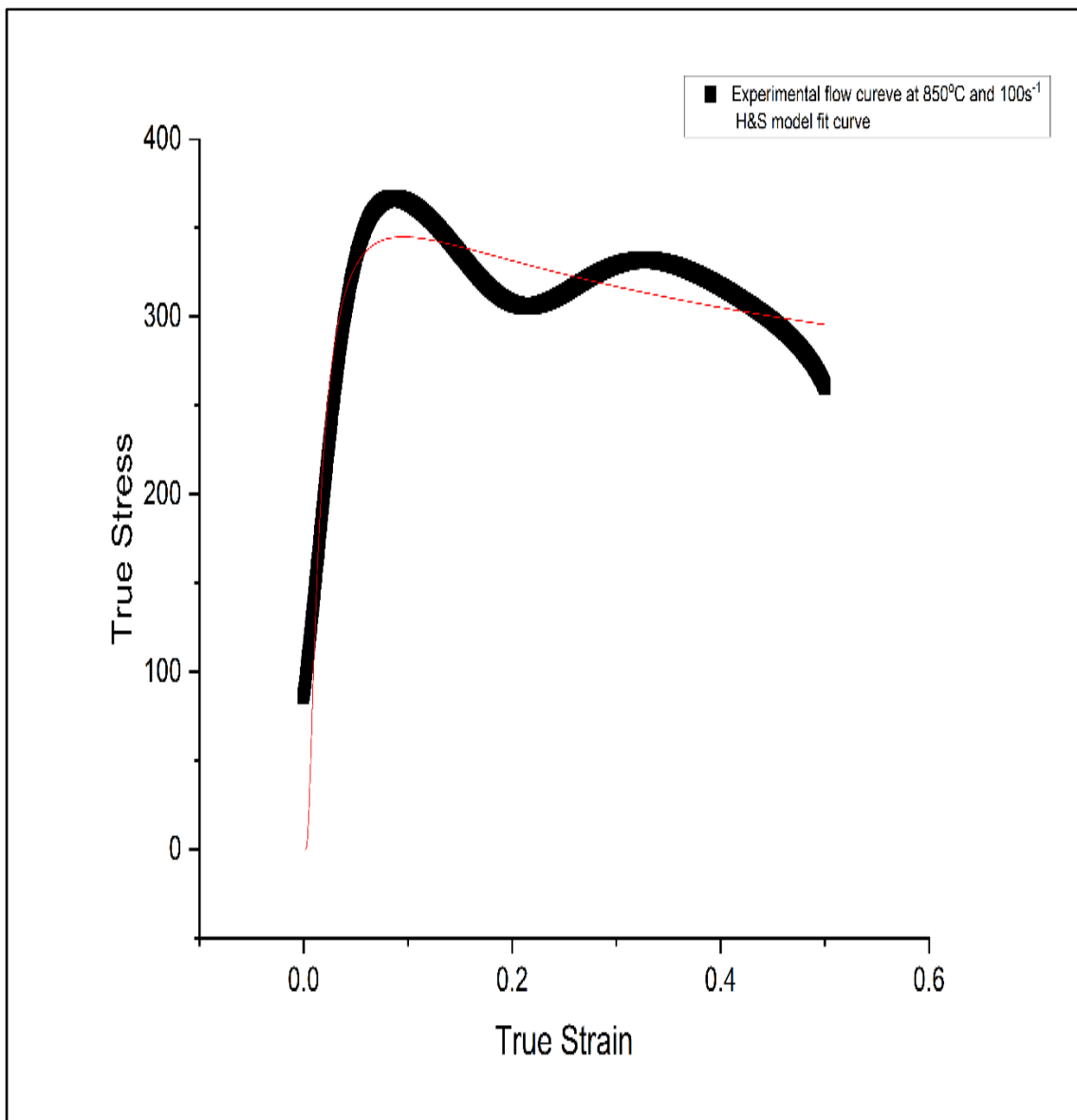


Figure 5.20: Experimental and modelled flow curves for 850°C and strain rate 100s<sup>-1</sup>

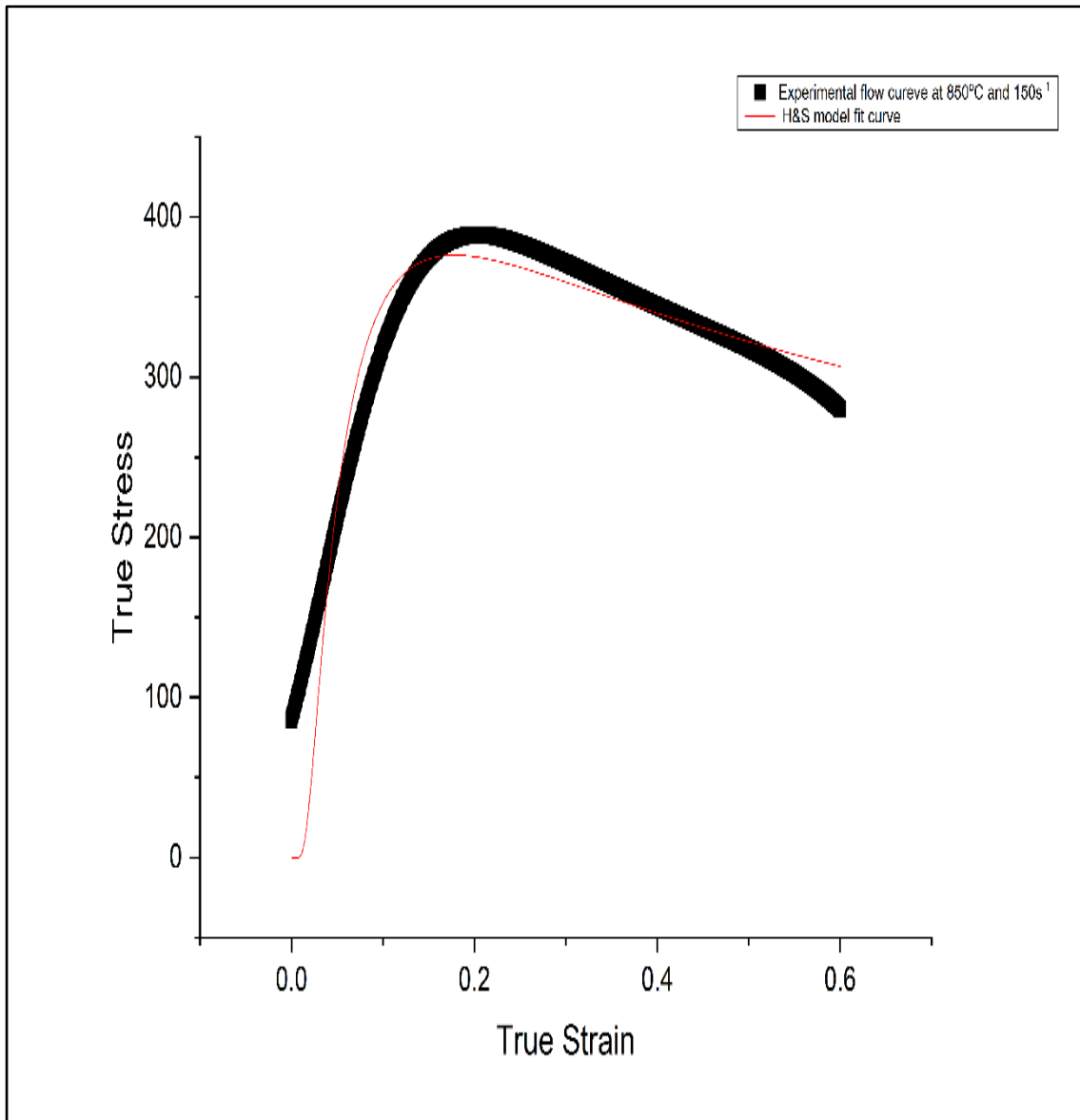


Figure 5.21: Experimental and modelled flow curves for 850°C and strain rate 150s<sup>-1</sup>

For the temperature of 850°C the confidence level and the H&S material constants are presented in Table 5.7. From the results it is clear that the model demonstrated a very good response and the reduced values of the confidence are determined from the initial part (low strain) of the flow curve.

## Results and Evaluation of As-Received Microstructure

**Table 5.7: H&S material constants and level of confidence for 850°C**

Strain rate (s <sup>-1</sup> )	A	m1	m2	m3	m4	Confidence (%)
50	18783.4	-0.00234	-0.00125	-0.51287	-0.00565	94.4
100	17328.4	-0.00235	-0.18255	-0.48688	-0.01746	82.7
150	135135.7	0.001	-0.40049	1.3526	-0.07155	85.0

For the temperature of 900°C the flow curves, the fitted curve, the confidence level and the H&S material constants are presented below.

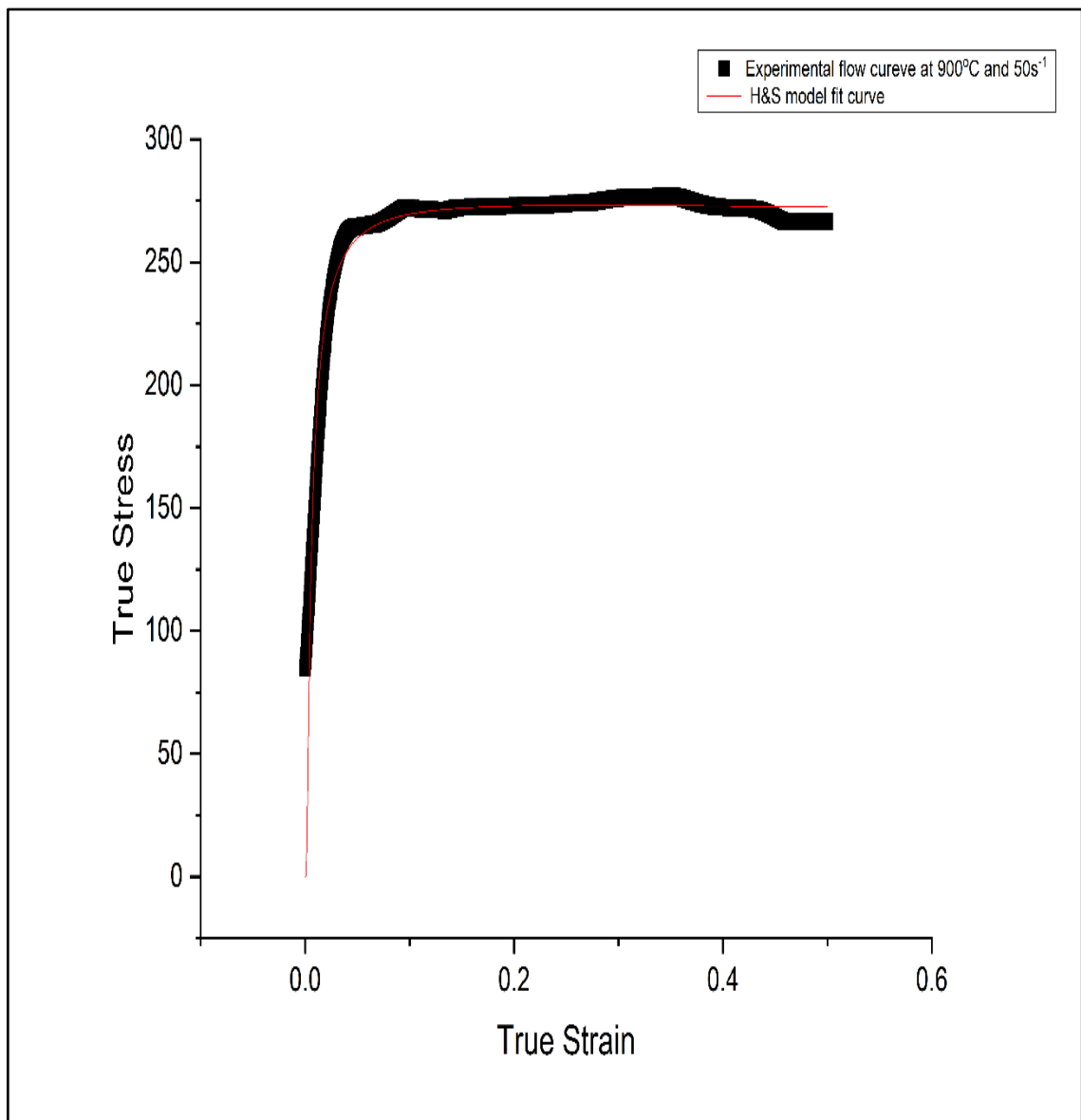


Figure 5.22: Experimental and modelled flow curves for 900°C and strain rate 50s<sup>-1</sup>

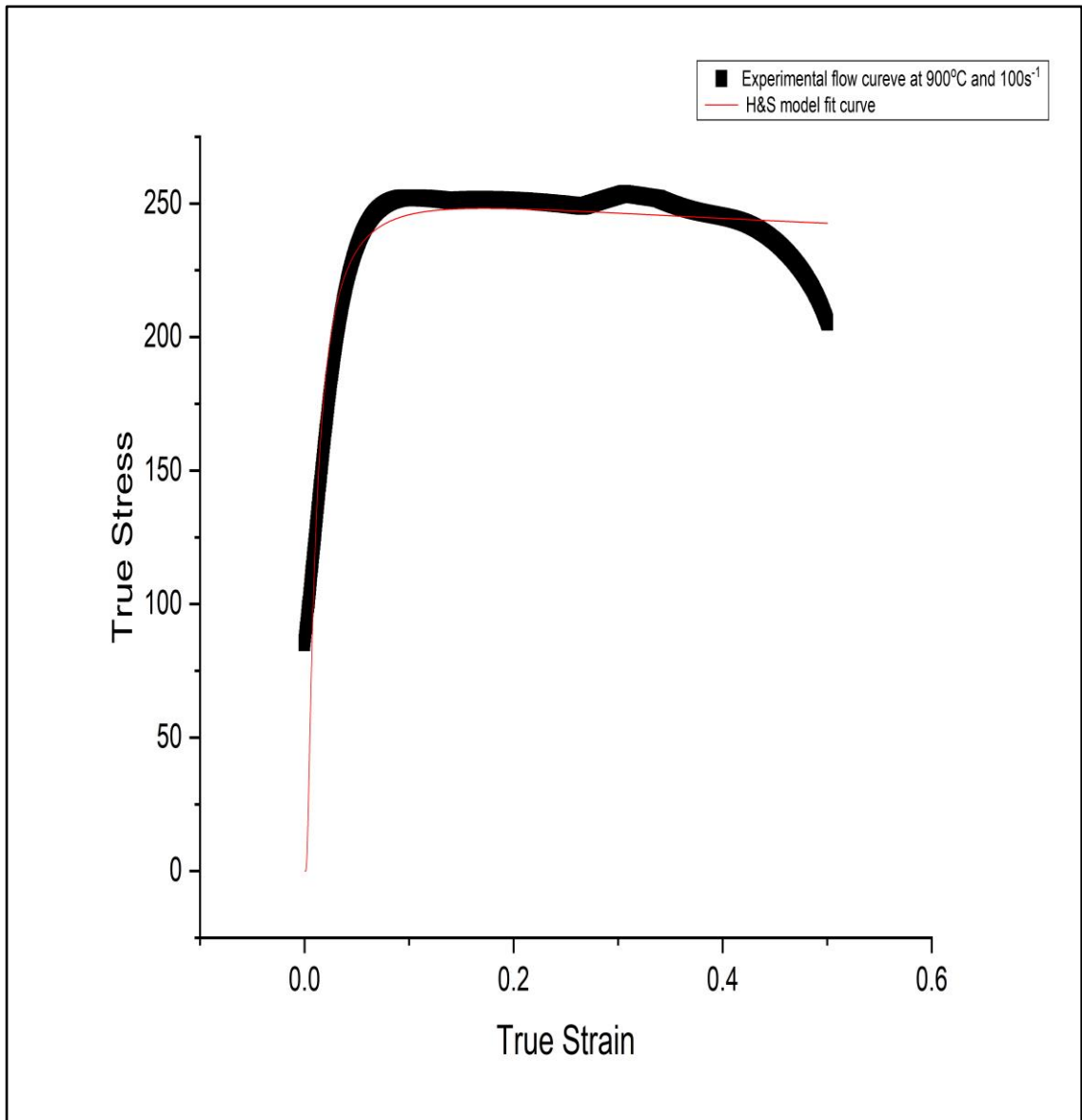


Figure 5.23: Experimental and modelled flow curves for 900°C and strain rate 100s<sup>-1</sup>

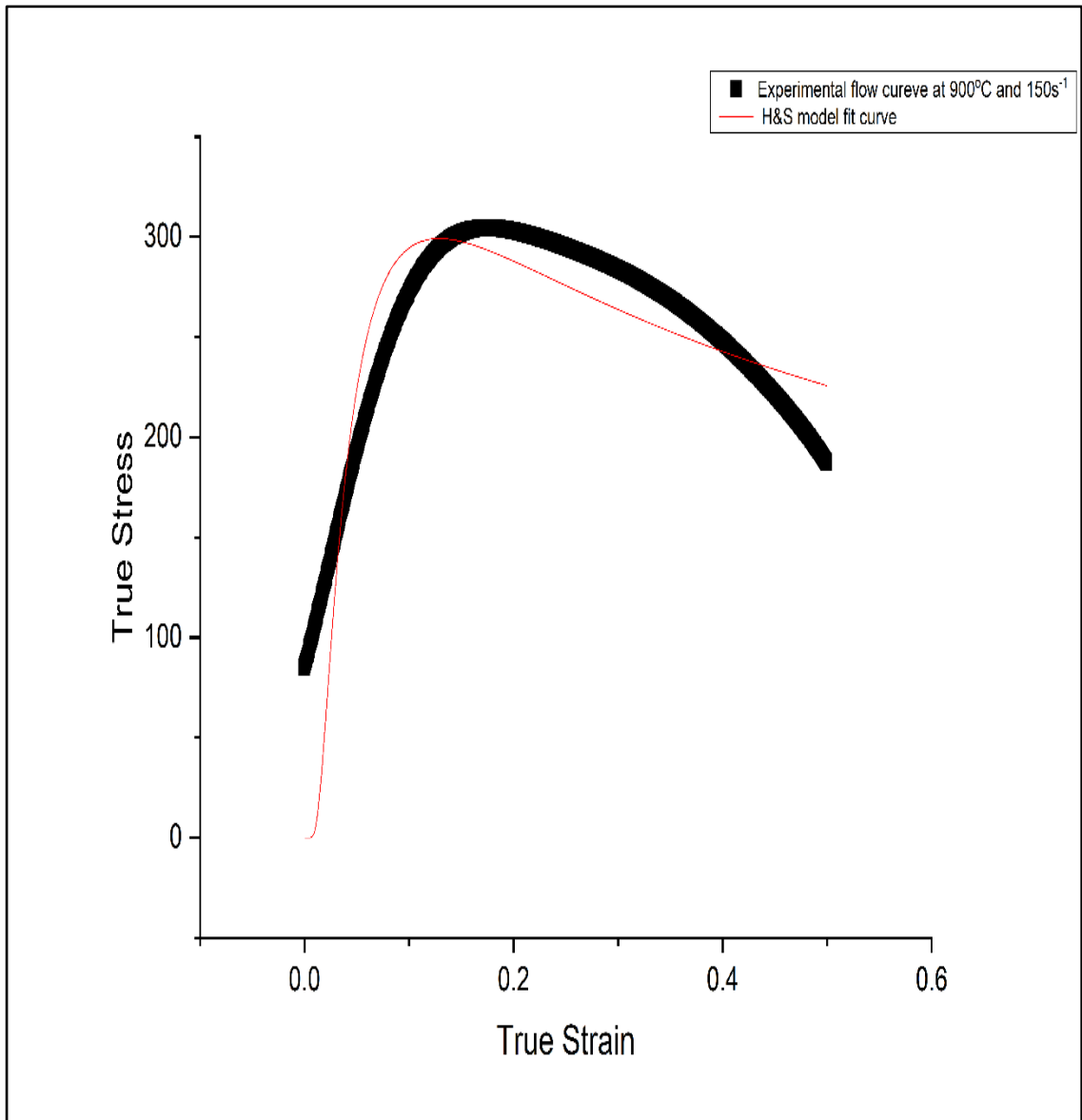


Figure 5.24: Experimental and modelled flow curves for 900°C and strain rate 150s<sup>-1</sup>

Table 5.8 H&S material constants and level of confidence for 900°C

Strain rate (s <sup>-1</sup> )	A	m1	m2	m3	m4	Confidence (%)
50	17204.8	-0.00223	-0.01777	-0.54683	-0.00493	90.8
100	15615.3	-0.00239	-0.16921	-0.46547	-0.01696	80.0
150	0.13675	-0.00635	-0.45927	2.51148	-0.05918	69.7

From the results the percentage of confidence is reduced with the increase of temperature. This can be explained due to high degree of flow softening and also because of the dynamic phenomena; dynamic recovery and dynamic recrystallization, creating a shift of the flow stress curve to the right and also the dynamic response of the equipment where the measurement are shifting from the quasi-static to dynamic mechanical testing.

The flow modelling curves and material constants at temperature of 950°C and the three strain rates is presented below.

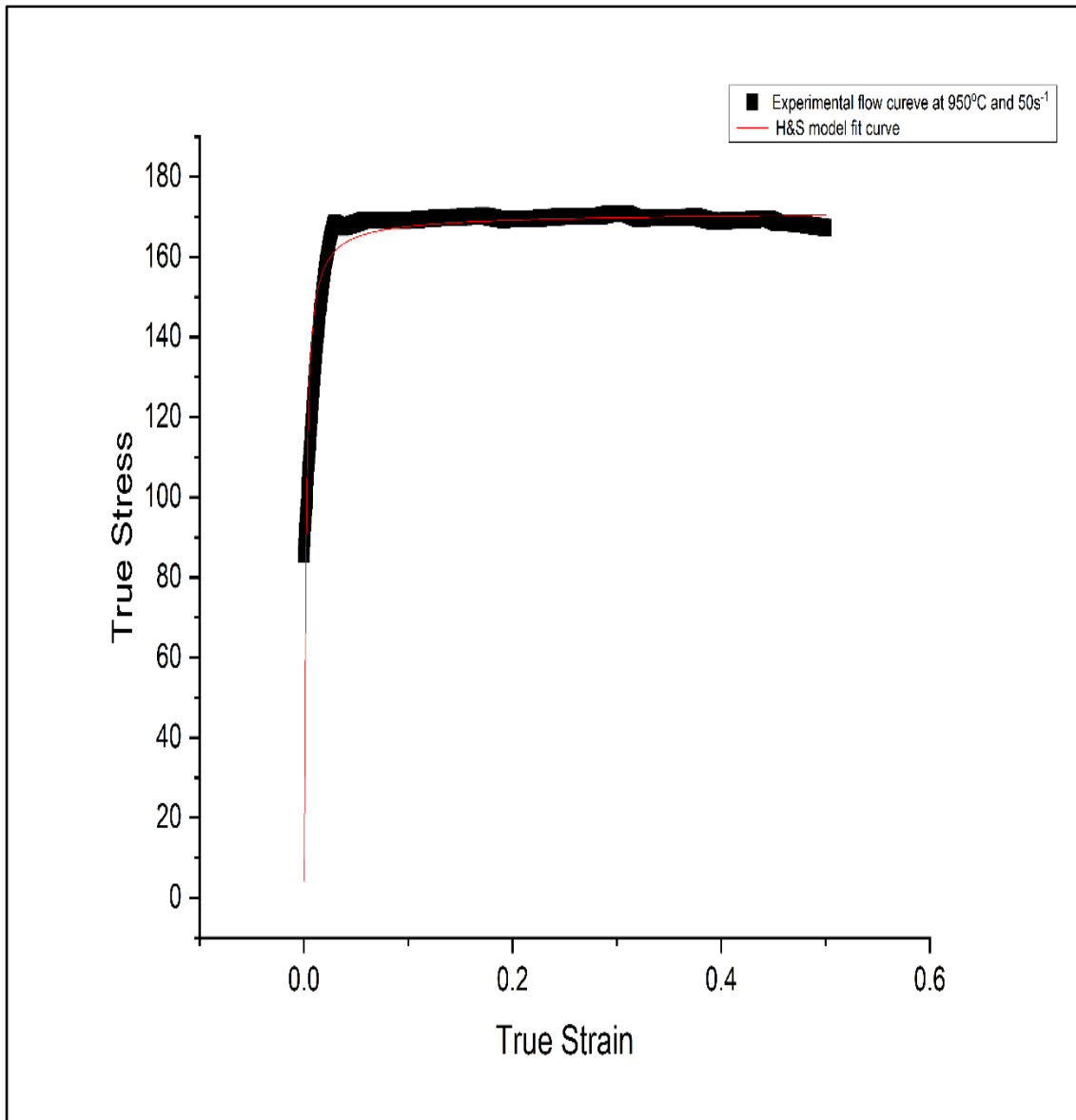


Figure 5.25: Experimental and modelled flow curves for 950°C and strain rate 50s<sup>-1</sup>

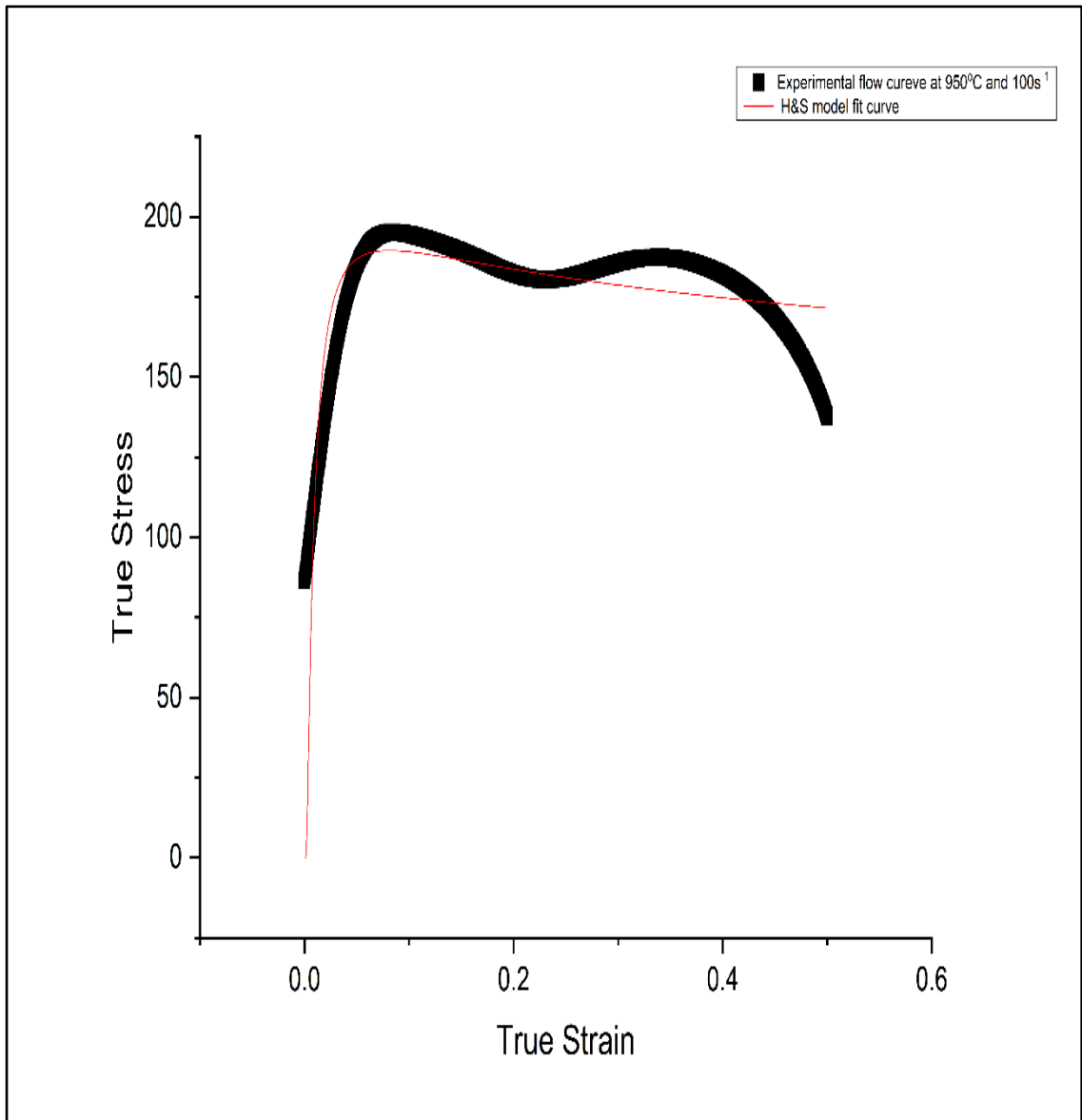


Figure 5.26: Experimental and modelled flow curves for 950°C and strain rate 100s<sup>-1</sup>

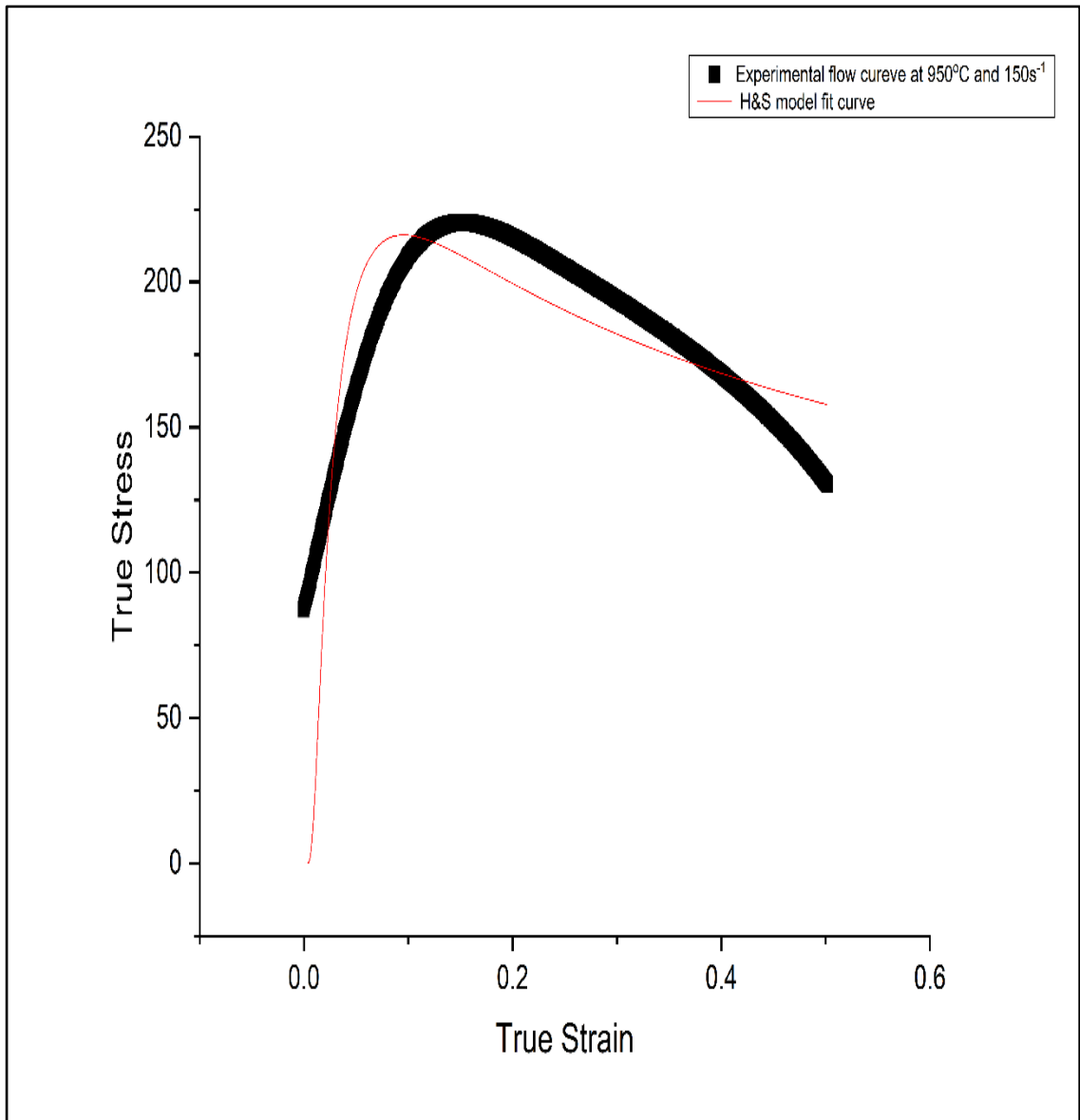


Figure 5.27: Experimental and modelled flow curves for 950°C and strain rate 150s<sup>-1</sup>

Table 5.9 presents the confidence level and the H&S material constants for 950°C.

Table 5.9 H&amp;S material constants and level of confidence for 950°C

Strain rate (s <sup>-1</sup> )	A	m1	m2	m3	m4	Confidence (%)
50	14484.80727	-0.00232	0.0034	-0.56495	-0.00141	73.8
100	16219.62002	-0.00415	-0.10159	-0.14514	-0.00826	57.8
150	0.60564	-0.00494	0.37064	1.93987	-0.03541	55.3

As has been seen for 900°C, at 950°C, the confidence level is reduced with the increase of strain rate. Even though, the values of confidence are reduced significantly in comparison with the values at 850°C. The decrease in confidence can be associated to extreme flow softening at high strain rates, and the dynamic phenomena (dynamic recovery and dynamic recrystallization) responsible for the shift of the flow curve to the right at low strains.

#### 5.5.5 Strain rate effect

The effect of strain rate on flow stress is demonstrated in Figure 5.28 at 0.5 of strain in Figure 5.29, which presents the variations of flow stress at three different temperatures with the logarithm of the strain rate. For each tested temperature, the strain rate sensitivity, as defined by the slope of the log flow stress versus the log strain rate relationship, is minor increased linear for the 850°C to 900°C; and significant higher increase for 950°C. However, as seen in the comparison of temperature ranges, the flow stress is quite sensitive to temperature but relatively less sensitive to strain rate. Typically, the macroscopic flow stress  $\sigma$  (compared at constant strain  $\dot{\epsilon}$ ) varies linearly with strain rate, meaning that a thermally activated mechanism controls the deformation process [58].

The strain rate sensitivity ( $m$ ) quantifies the effect of strain rate on the flow stress of a material.

$$m = \log(\sigma_2/\sigma_1)/\log(\dot{\epsilon}_2/\dot{\epsilon}_1)$$

At a given temperature and plastic strain it gives a measure of the stress required to generate a certain increase in strain rate. All the values of the equation correspond to the same strain value. The strain rate sensitivity ( $m$ ) values determined by the hot isothermal compression test are presented in Table 5.10 for the peak stress.

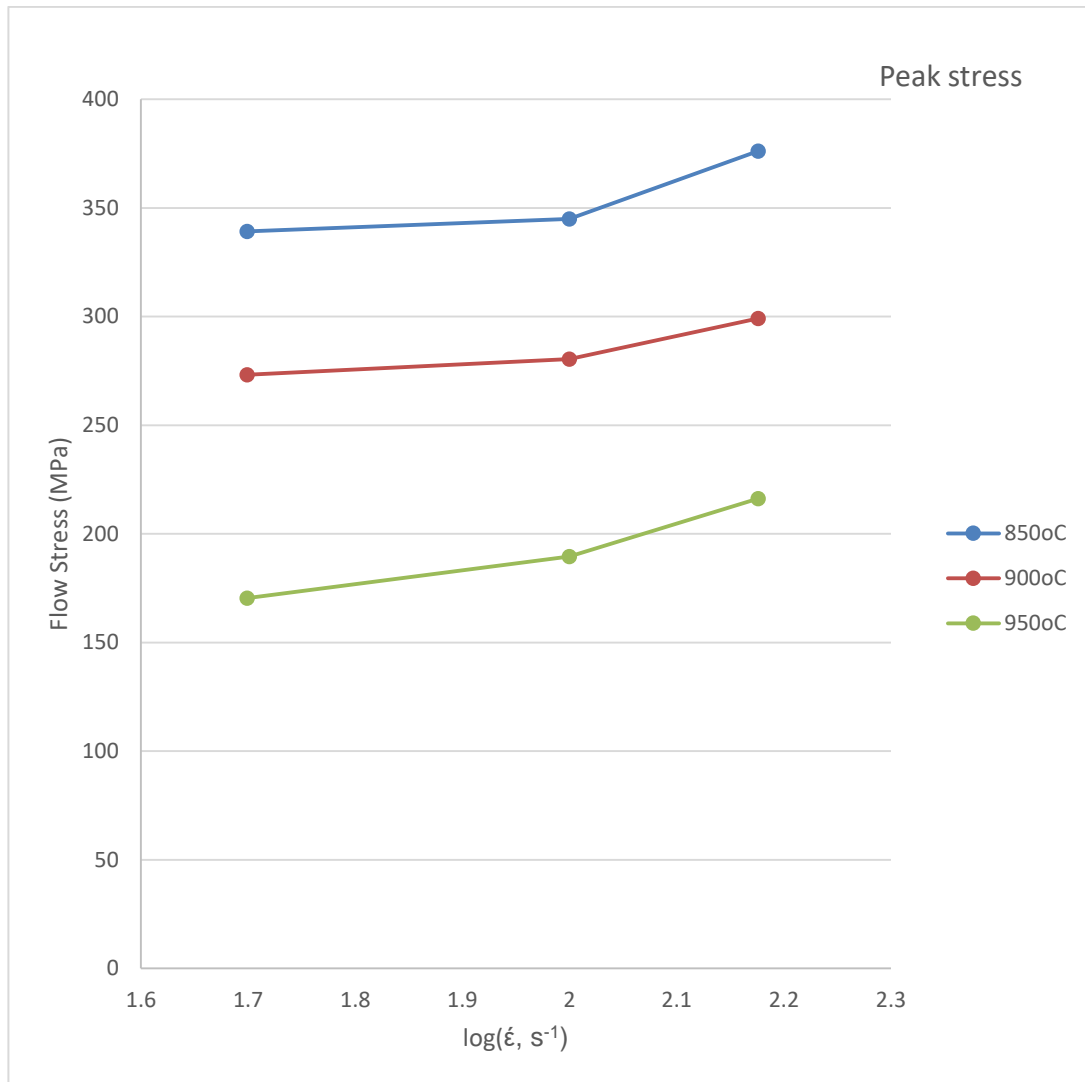


Figure 5.28: Influence of strain rate on flow stress at peak stress, at a constant temperature.

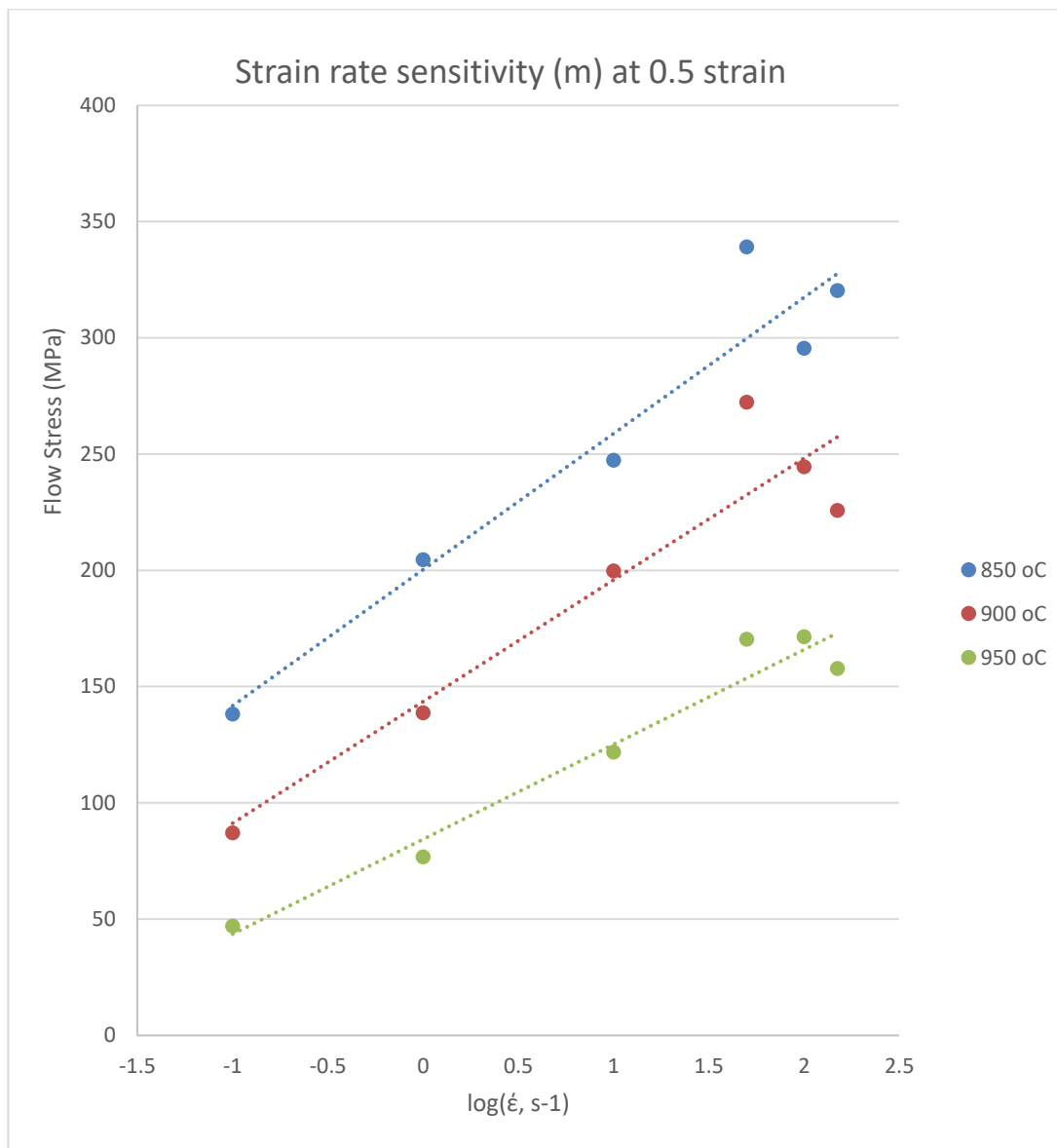


Figure 5.29: Influence of strain rate on flow stress at a constant plastic strain of 0.5, as a function of temperature

Table 5.10: Strain rate sensitivity (m) and different temperatures peak stress.

Temperature	Strain rate sensitivity (m) peak stress	Strain rate sensitivity (m) true strain of 0.5
850°C	0.08	0.11
900°C	0.08	0.14
950°C	0.2	0.18

The calculated  $m$  values of the three hot isothermal compression tests at peak stress reveals a small increase from 850°C to 900°C. In contrast, at 950°C the value of strain rate sensitivity  $m$  presents a significant increase. At a strain of 0.5 the increase of strain rate sensitivity is clear with the increase of temperature. Previous studies have been reported that the strain rate sensitivity has a clear dependence on temperature, microstructure and strain rate [162][142]. The strain rate sensitivity values are below the value of 0.3 which indicates that the deformation is controlled by a dislocation glide process [163].

#### 5.5.6 Temperature effect

The temperature effect on the flow behaviour of Ti-6Al-4V is illustrated in Figure 5.30; the plot of the peak flow stress as a function of the temperature for the three strain rates demonstrates the influence of temperature on deformation stress of Ti-6Al-4V.

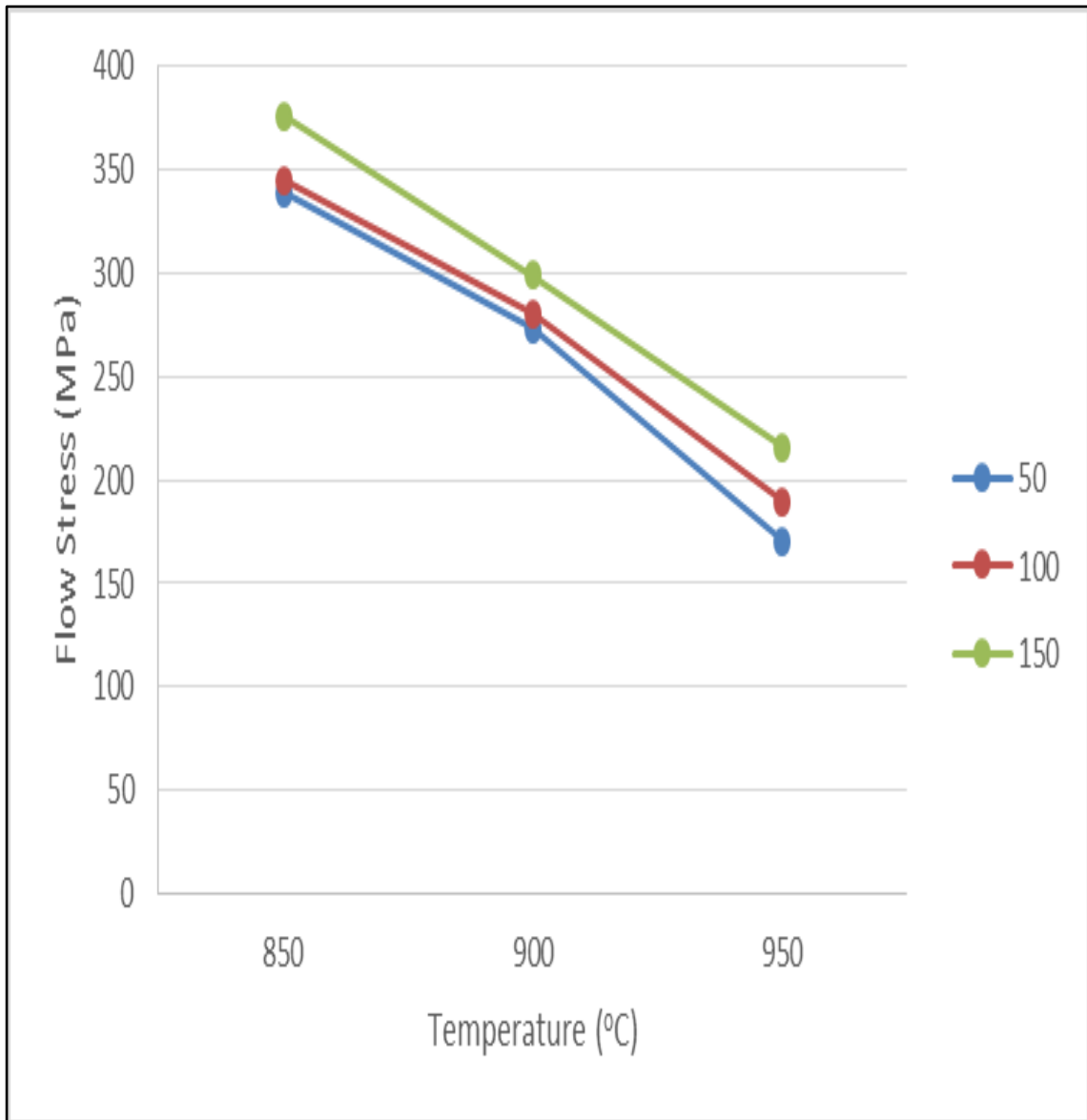


Figure 5.30: Effect of temperature on the peak flow stress at the 3 different strain rates

From the plot the influence of the temperature for all strain rates can be seen; the increased temperature has as a result a linear decrease of the peak flow stress for all strain rates. The temperature effect is almost identical for all the strain rates.

#### 5.5.7 Microstructure evolution during hot isothermal compression

This section presents and discusses the evolution and changes in the as-received microstructure due to hot isothermal compression under a range of temperatures and strain rates. In particular, the volume fraction of beta-phase in association with hot working parameters such as temperature and strain rate is considered.

At an intermediate strain rate of  $10 \text{ s}^{-1}$  and the temperatures of  $850^\circ\text{C}$ ,  $900^\circ\text{C}$  and  $950^\circ\text{C}$  an initial peak due to strain hardening followed by flow softening is presented. For all temperatures after the initial peak, a flow instability is presented with multiple peaks, indicating dynamic recrystallization (DRX) or flow localization. In Figure 5.31 we can see that the flow instability occurs due to flow localization and formation of adiabatic shear bands.

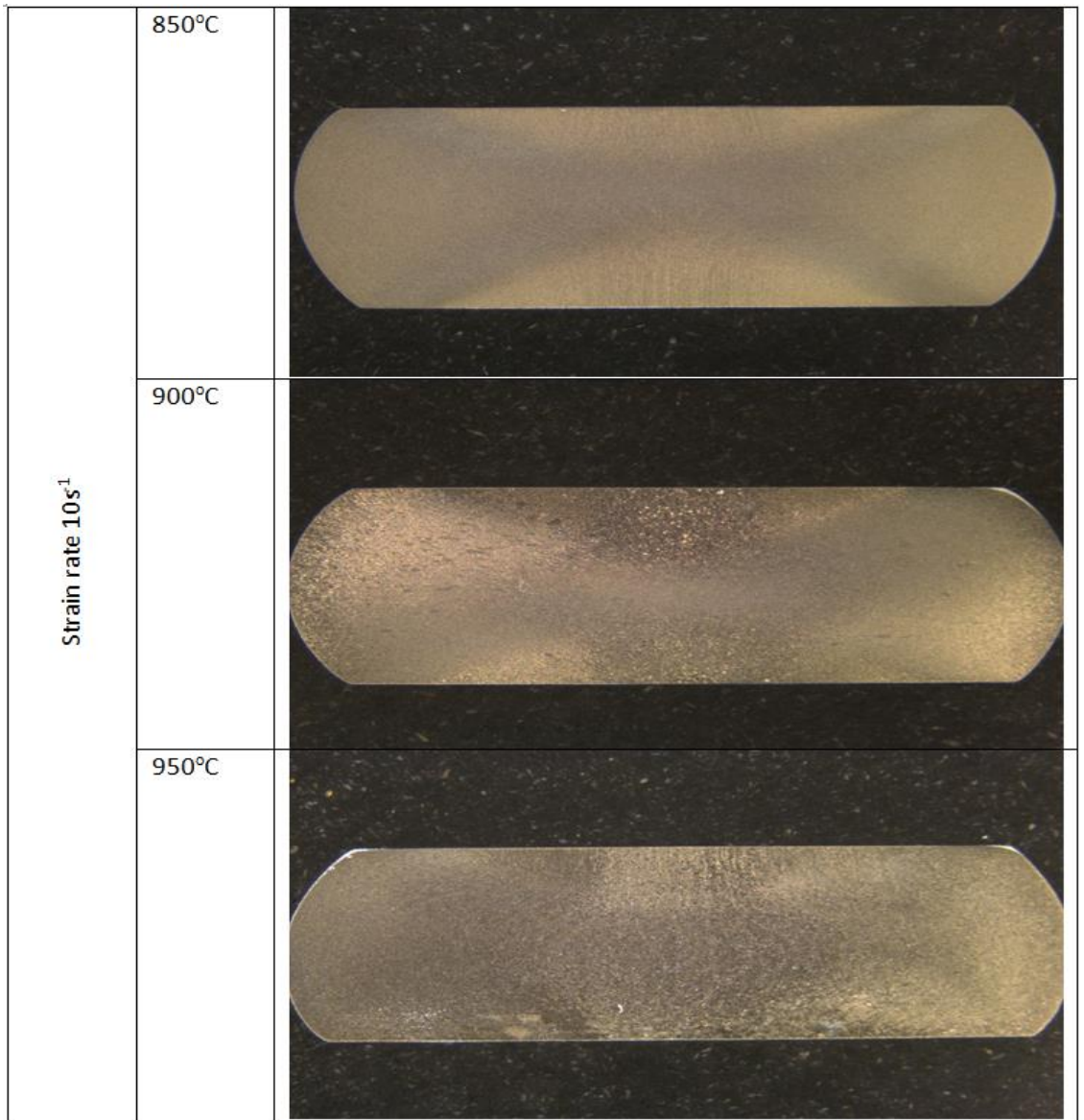


Figure 5.31: Flow localization at strain rate of  $10s^{-1}$  and three temperatures 850°C, 900°C and 950°C

It is imperative to understand the flow behaviour of the titanium alloys, to control the final properties through manipulation of the final microstructure. Hardening, steady state flow and, most common for titanium alloys, softening, are the three behaviours that have been encountered in this study. It is well acknowledged that flow softening occurs at high strain rates and low temperatures due to adiabatic heating or changes to microstructure morphology [164]. Because in this study the

effect of adiabatic heating on the flow behaviour was corrected, consequently, the flow softening must be related to microstructure's morphological changes.

The as-received microstructure was alpha-phase (Figure 4.1), following the direction of the rolling axis, and a beta-phase matrix. The micrographs obtained with SEM for 850°C hot isothermal compression tests are presented in Figure 5.32, Figure 5.33, Figure 5.34. The magnification was 2000, 4000, and 6000 from left to right and top to bottom respectively for all micrographs.

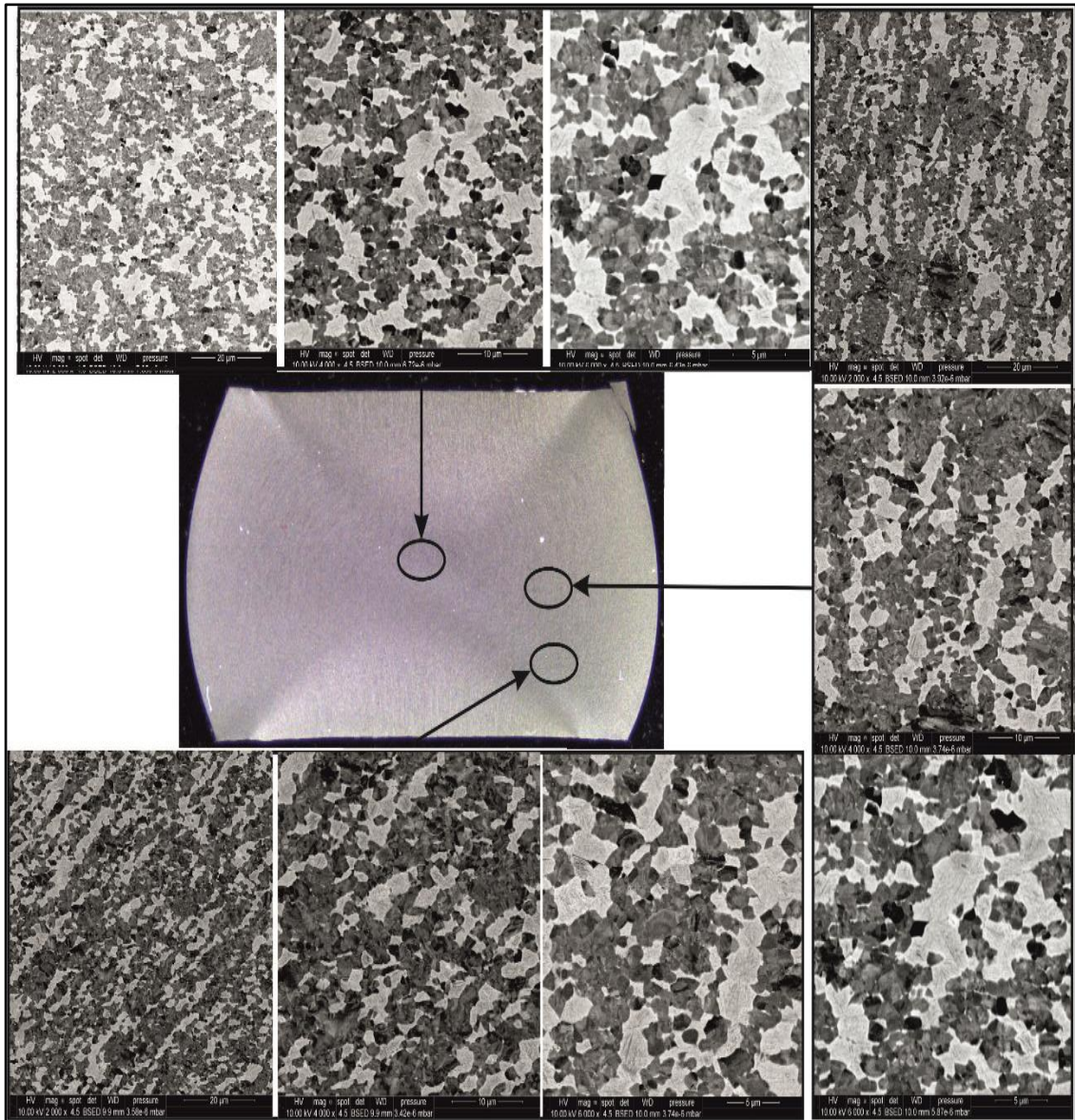


Figure 5.32: SEM micrographs at 850°C and strain rate of 50s<sup>-1</sup>

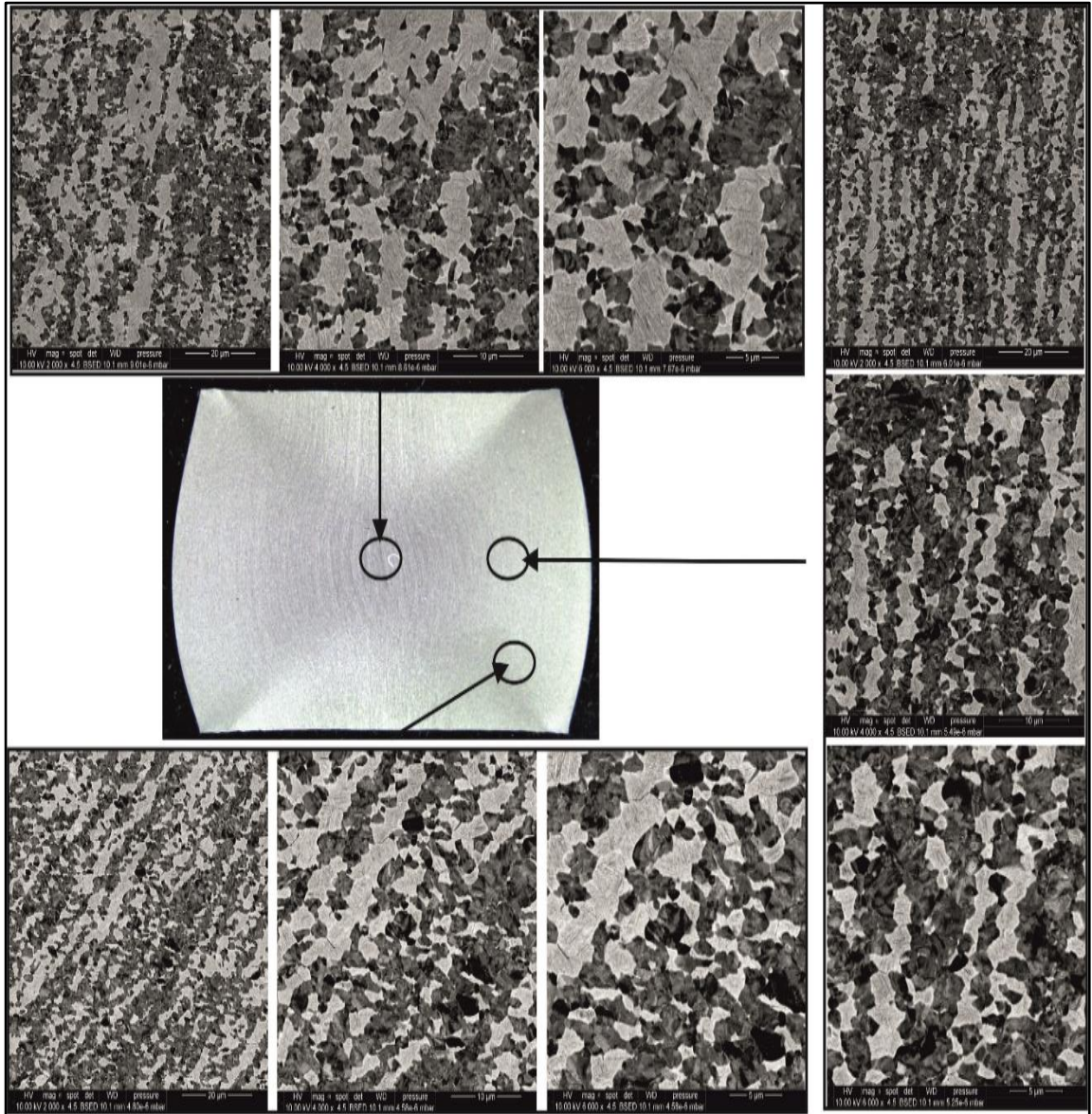


Figure 5.33: SEM micrographs at 850°C and strain rate of  $100s^{-1}$

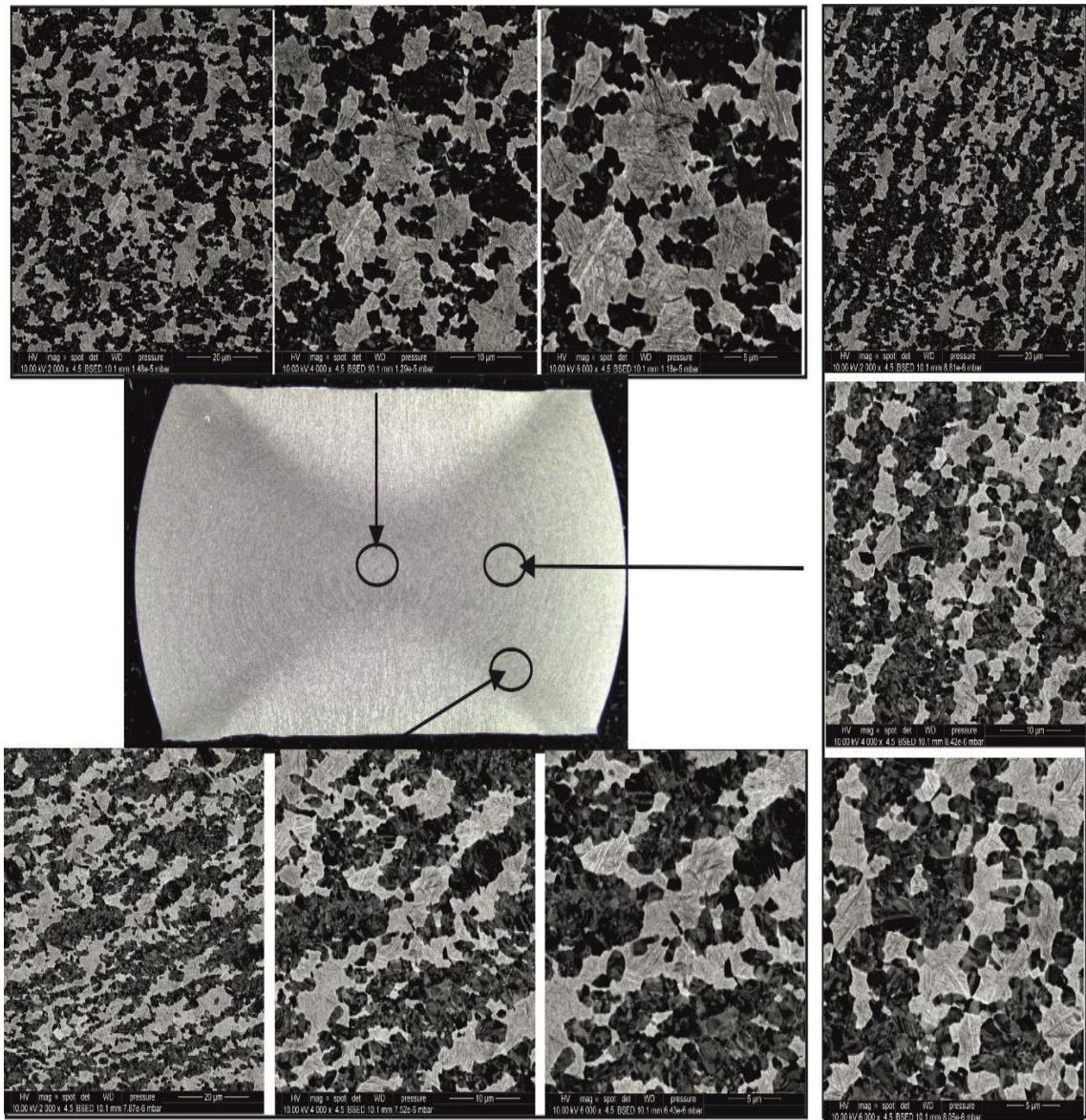
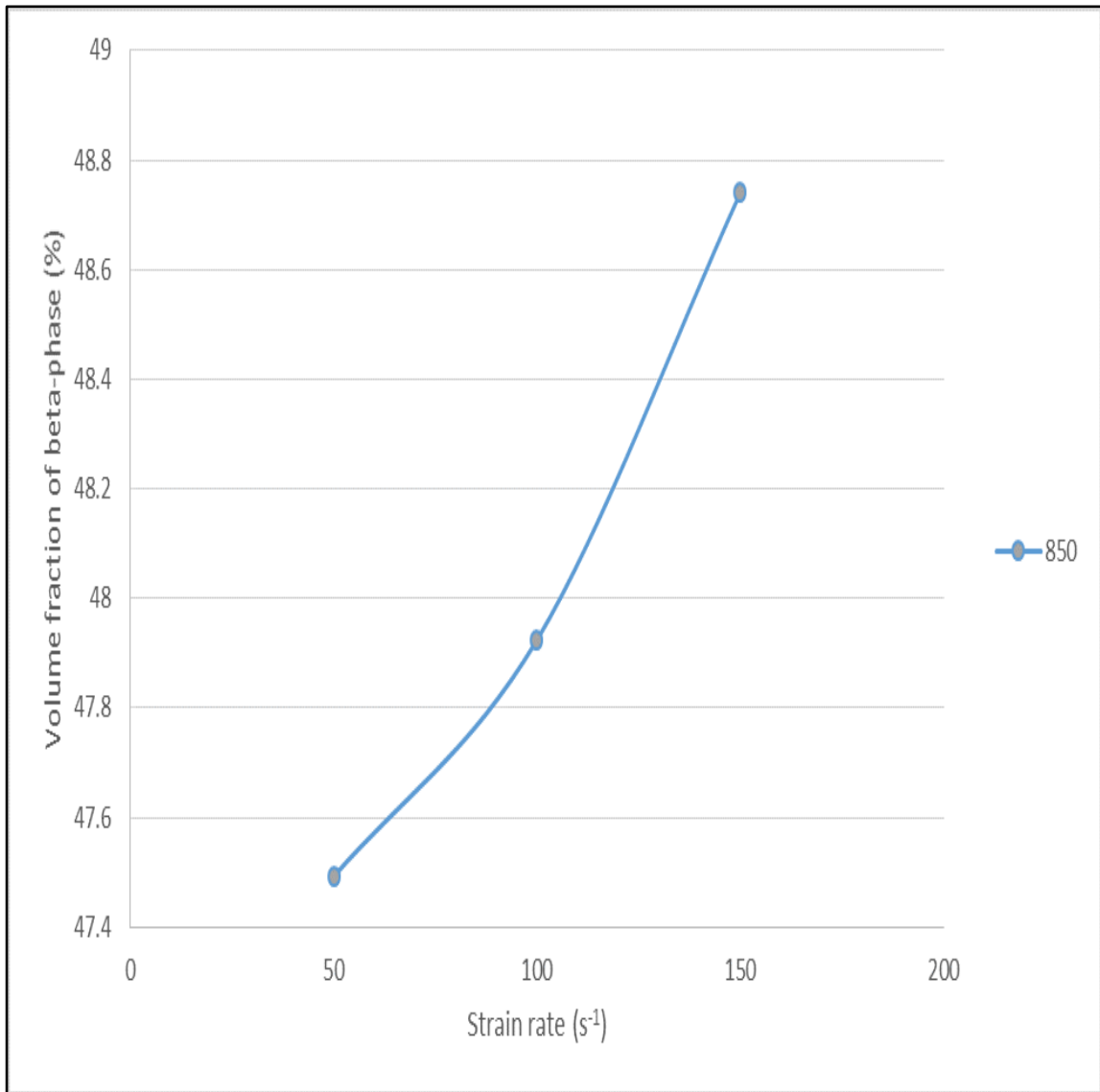


Figure 5.34: SEM micrographs at 850°C and strain rate of 150s<sup>-1</sup>

The microstructure of the deformed samples for all strain rates for the temperature of 850°C is bi-modal, consisting of primary alpha grains ( $\alpha_p$ -dark),  $\alpha$  laths between the grains ( $\alpha$ -dark), and martensitic  $\beta$  matrix in between (light). The analysis of the volume fraction of beta phase in the centre of the samples where corresponds to the strain presented in the flow curves is presented in Figure 5.35.



**Figure 5.35: Volume fraction of beta phase in the centre of the deformed sample at 850°C and strain rates of 50s<sup>-1</sup>, 100s<sup>-1</sup> and 150s<sup>-1</sup>**

The increase of the volume fraction of the beta phase is following an approximately linear trend, but is not significant at this temperature. The volume fraction is only increased by 1.2% from strain rate of 50 s<sup>-1</sup> to a strain rate of 150 s<sup>-1</sup>. The morphology of the microstructure for the given temperature was not presenting a significant change, which may explain the similar flow behaviour (initial hardening followed by steady state) and at this temperature.

Figure 5.36, Figure 5.37 and Figure 5.38 present the micrographs obtained with SEM for 900°C hot isothermal compression tests.

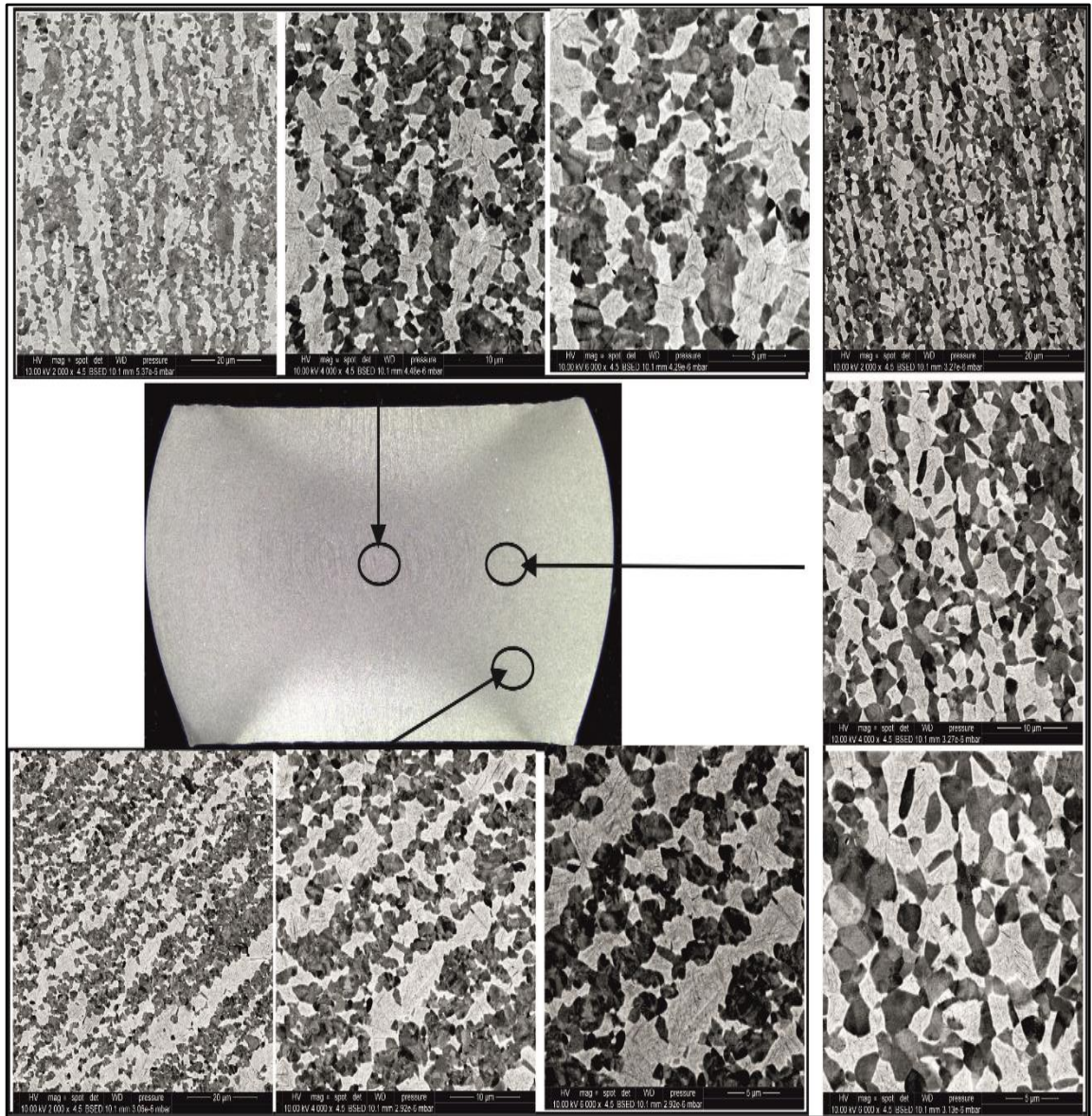


Figure 5.36 : SEM micrographs at 900°C and strain rate of 50s<sup>-1</sup>

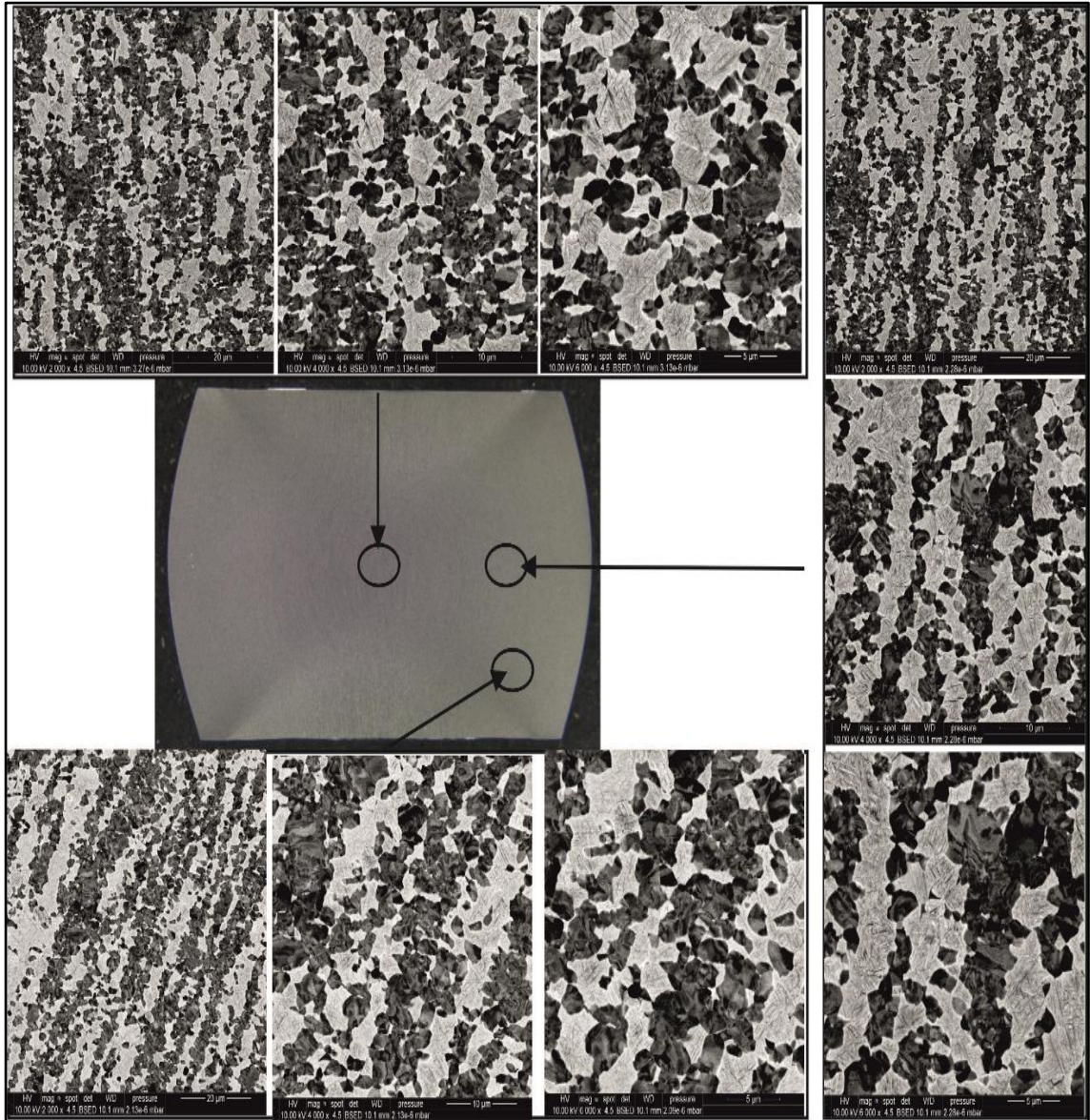


Figure 5.37: SEM micrographs at 900°C and strain rate of 100s<sup>-1</sup>

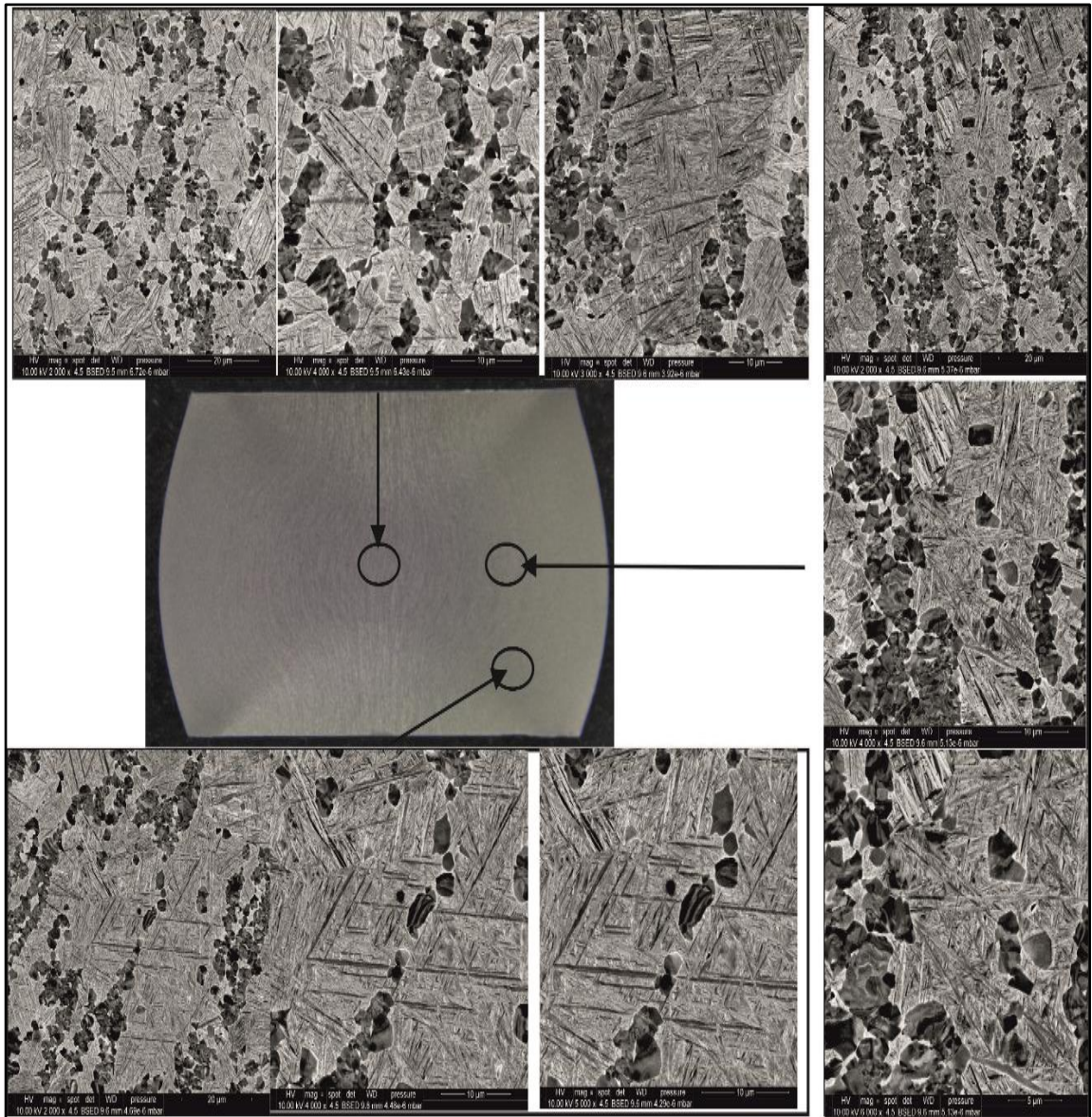
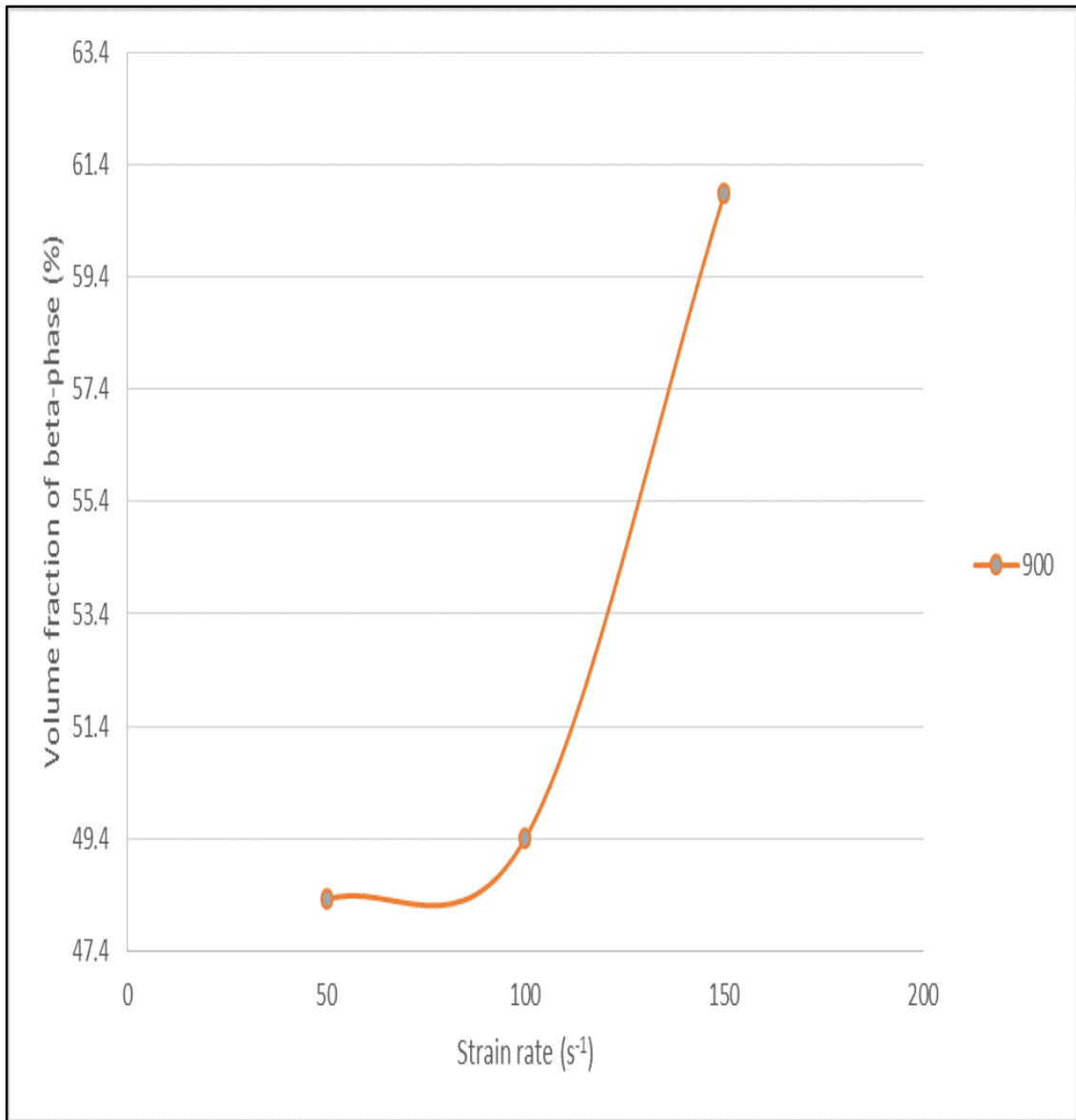


Figure 5.38: SEM micrographs at 900°C and strain rate of 150s<sup>-1</sup>

The microstructure of the deformed samples for all strain rates for the temperature of 900°C is similar to the microstructure at 850°C, consisting of primary alpha grains ( $\alpha_p$ -dark),  $\alpha$  laths between the grains ( $\alpha$ -dark), and martensite and  $\beta$  matrix in between (light).

The analysis of the volume fraction of beta phase in the centre of the samples is presented in Figure 5.39.



**Figure 5.39: Volume fraction of beta phase in the centre of the deformed sample at 900°C and strain rates of 50s<sup>-1</sup>, 100s<sup>-1</sup> and 150s<sup>-1</sup>**

The increase of the volume fraction of the beta phase at this temperature did not follow a linear trend. The change in volume fraction of beta phase for strain rates of 50 s<sup>-1</sup> and 100 s<sup>-1</sup> is similar to that seen at a temperature of 850°C but at the higher strain rate the change in volume fraction was more pronounced. The increase was 12% from a strain rate of 50 s<sup>-1</sup> to a strain rate of 150 s<sup>-1</sup>. The

morphology of the microstructure changes significantly at the higher strain rate, with primary alpha being less than 40%.

The SEM micrographs for the 950°C hot isothermal compression tests are presented in Figure 5.40, Figure 5.41 and Figure 5.42.

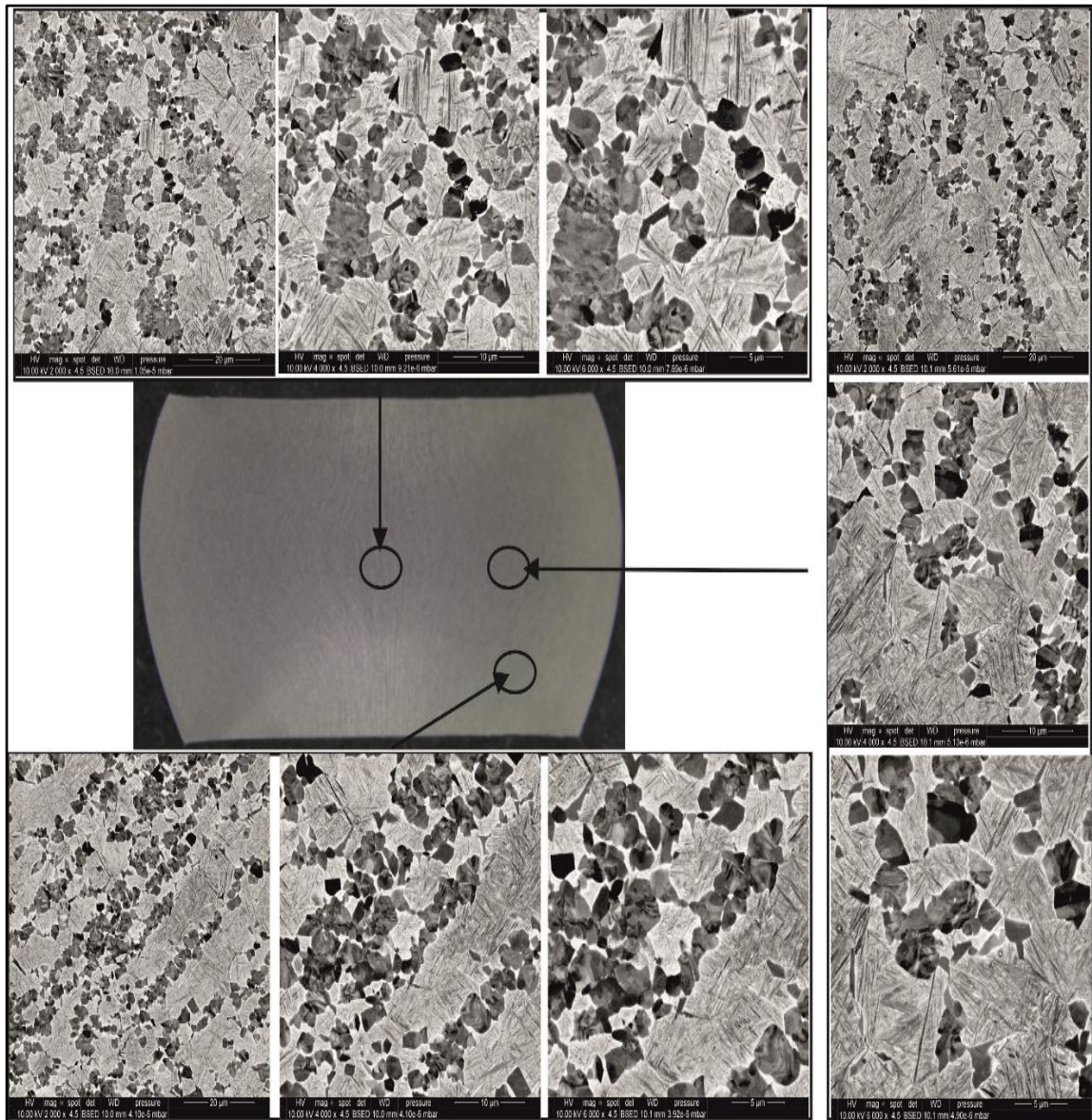


Figure 5.40: SEM micrographs at 950°C and strain rate of 50s<sup>-1</sup>

## Results and Evaluation of As-Received Microstructure

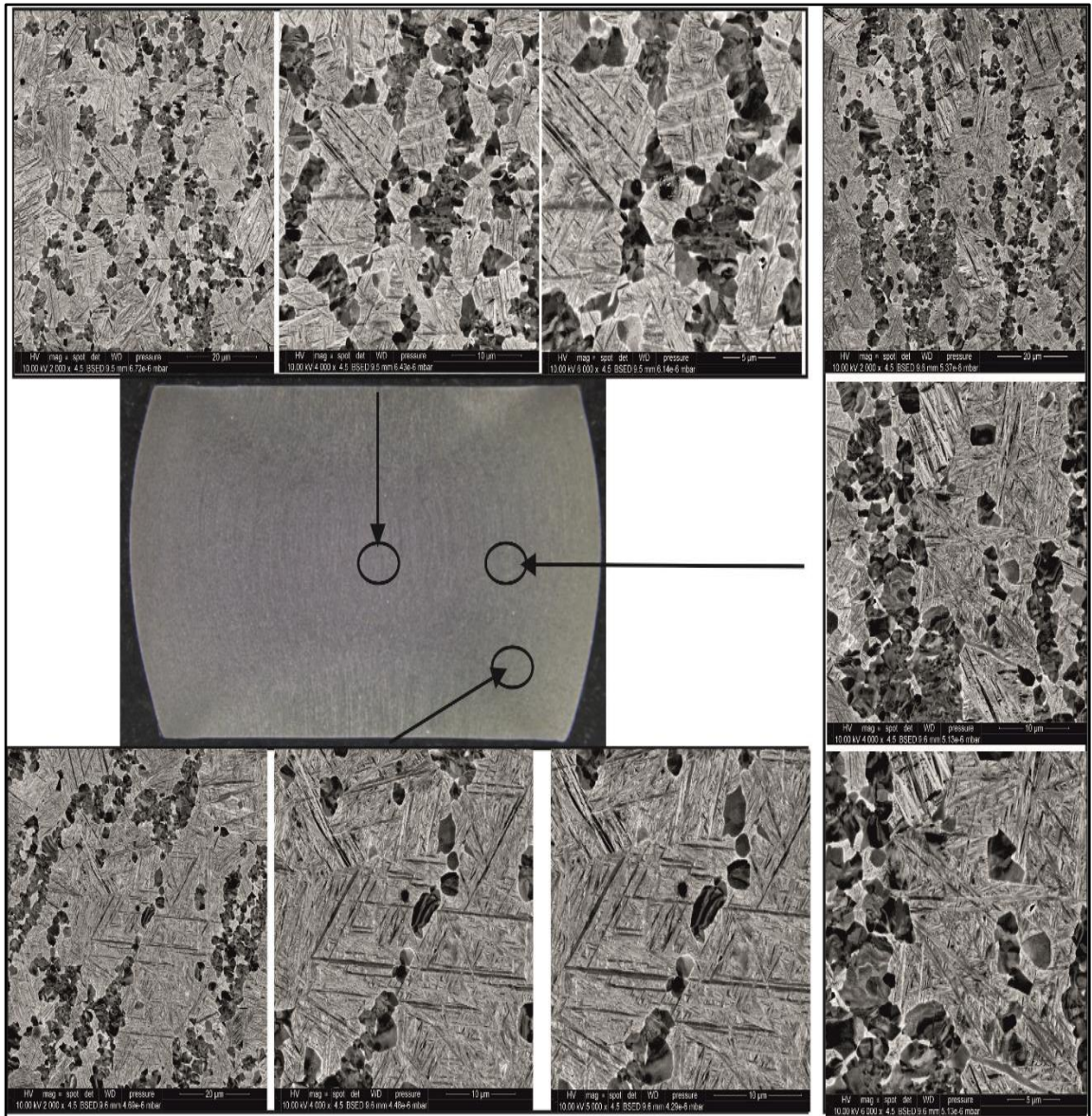


Figure 5.41: SEM micrographs at 950°C and strain rate of  $100\text{s}^{-1}$

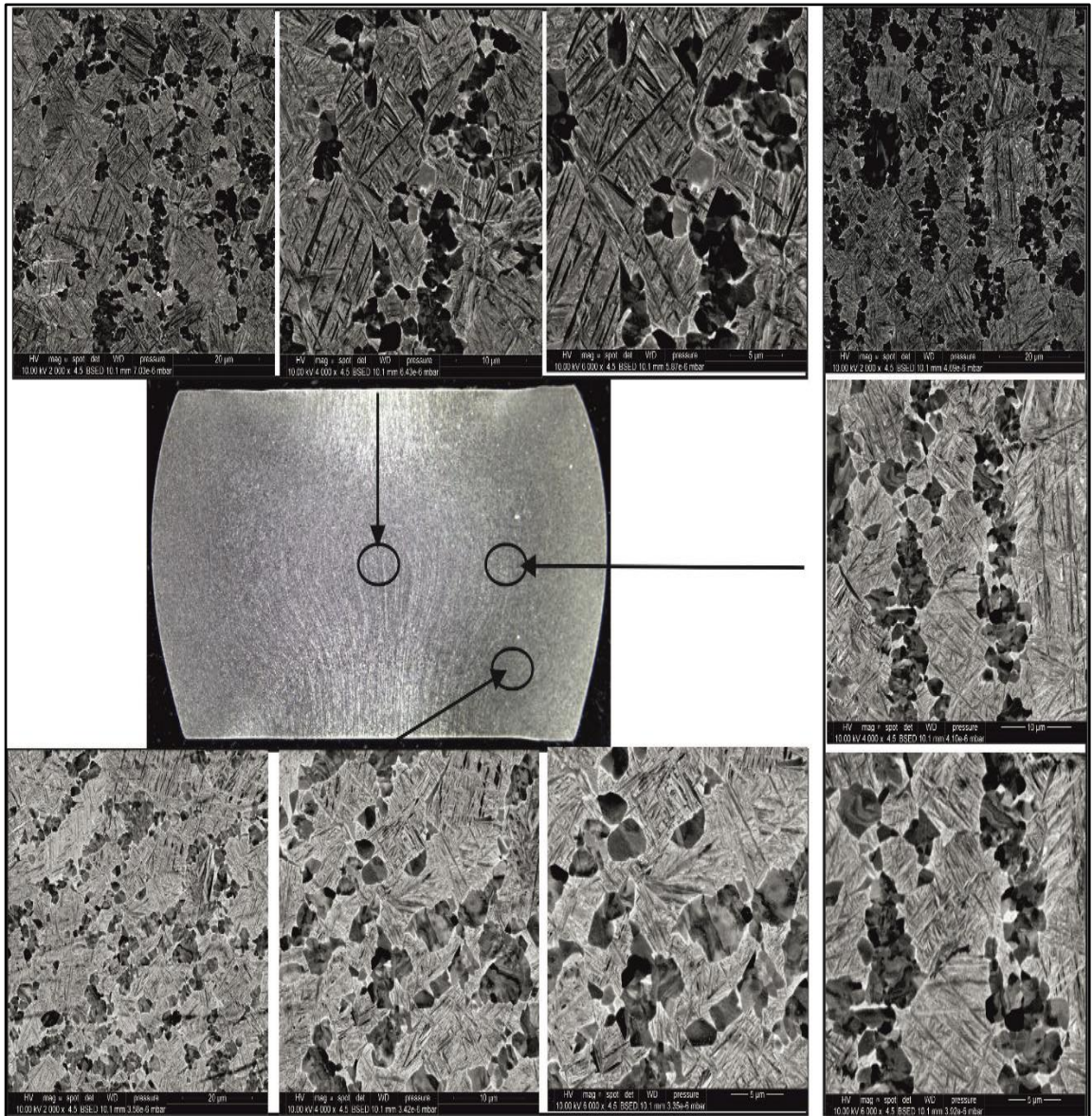
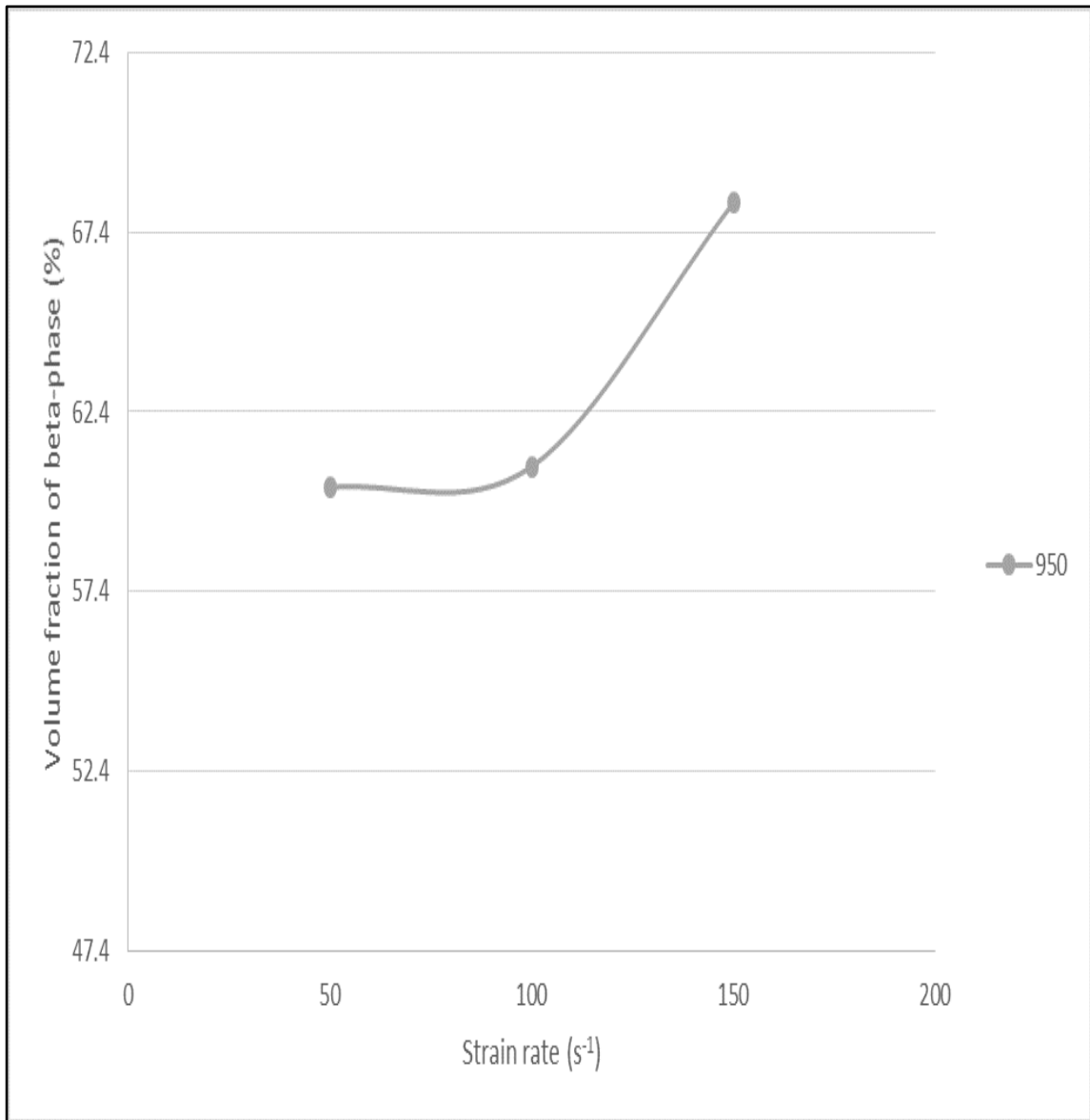


Figure 5.42: SEM micrographs at 950°C and strain rate of 150s<sup>-1</sup>

The analysis of the volume fraction of beta phase in the centre of the samples is presented in Figure 5.43.



**Figure 5.43:** Volume fraction of beta phase in the centre of the deformed sample at 950°C and strain rates of 50s<sup>-1</sup>, 100s<sup>-1</sup> and 150s<sup>-1</sup>

The volume fraction for 950°C follows a similar trend to the previous temperatures, indicating that the strain rate is not significantly affecting the percentage of beta volume fraction up to strain rate of 100 s<sup>-1</sup>. On the other hand the temperature increase has a pronounced effect on the percentage of the volume fraction, up to 12%, for strain rate of 150s<sup>-1</sup>. Substantial increase of the beta volume fraction was

noted at the high strain rate, indicating that strain rates higher than  $100 \text{ s}^{-1}$  could play a major role on the microstructural morphology.

Under high strain rate deformation at elevated temperatures, the stress–strain curves for Ti-6Al-4V with various beta-phase volume fractions decreased with increased beta-phase volume fraction, although the overall form of the curves is similar despite the volume fraction of beta-phase. The strain softening rate of Ti-6Al-4V significantly varies, suggesting that the beta-phase volume fraction does affect the strain softening rate of this alloy. The result was expected and has been reported in the literature [165].

## 6 Results and Evaluation Lamellar Microstructure

### 6.1 Flow behaviour at high strain rates

The high strain rate flow stress behaviour of Ti-6Al-4V was explored based on the experimental plan detailed on chapter 4 and presented in Table 4.8. The results of the 18 isothermal compression tests are presented in Appendix D. An example of the flow curve and the corrected curves for friction and adiabatic heating, as well as the flow curve fitted with H&S rheological law for both the experiments conducted at 900°C and strain rate of 100s<sup>-1</sup> is presented in Figure 6.1 and Figure 6.2.

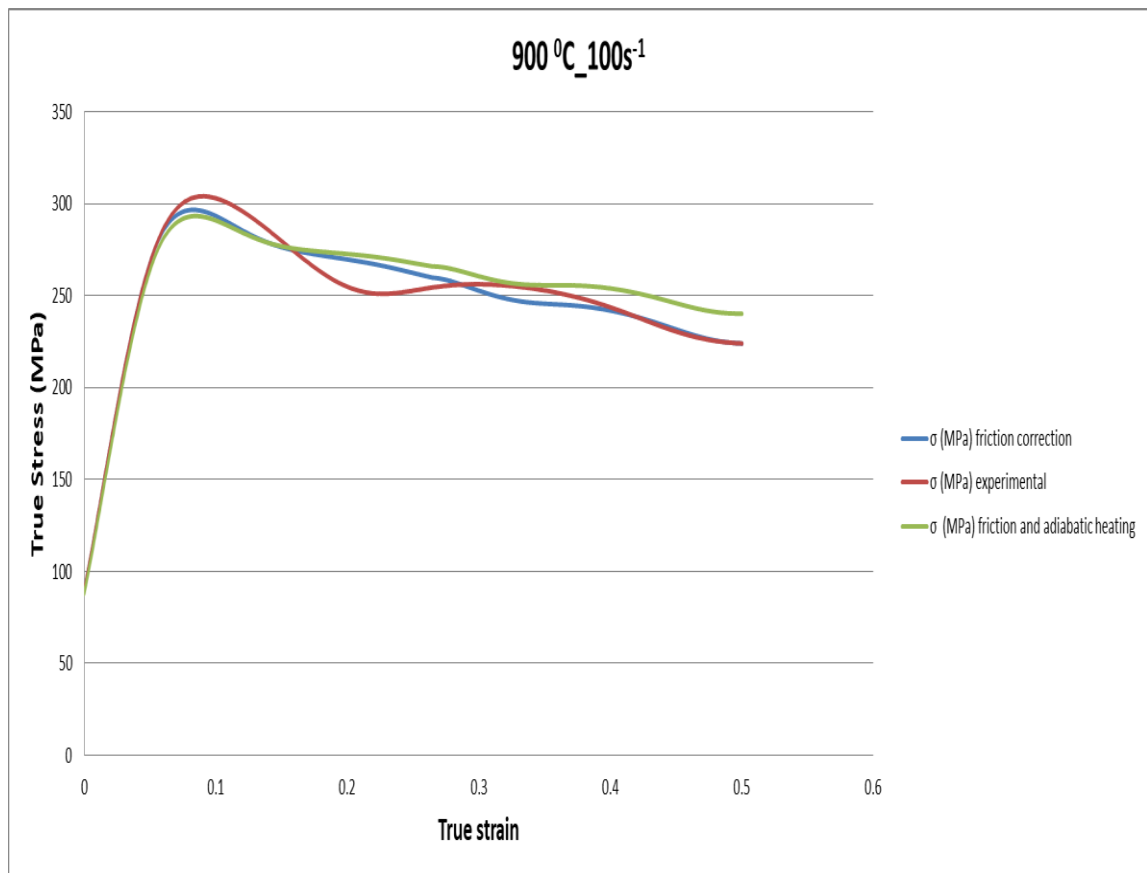


Figure 6.1: Flow stress at 900°C and 100s<sup>-1</sup>, experimental, with friction correction and adiabatic heating.

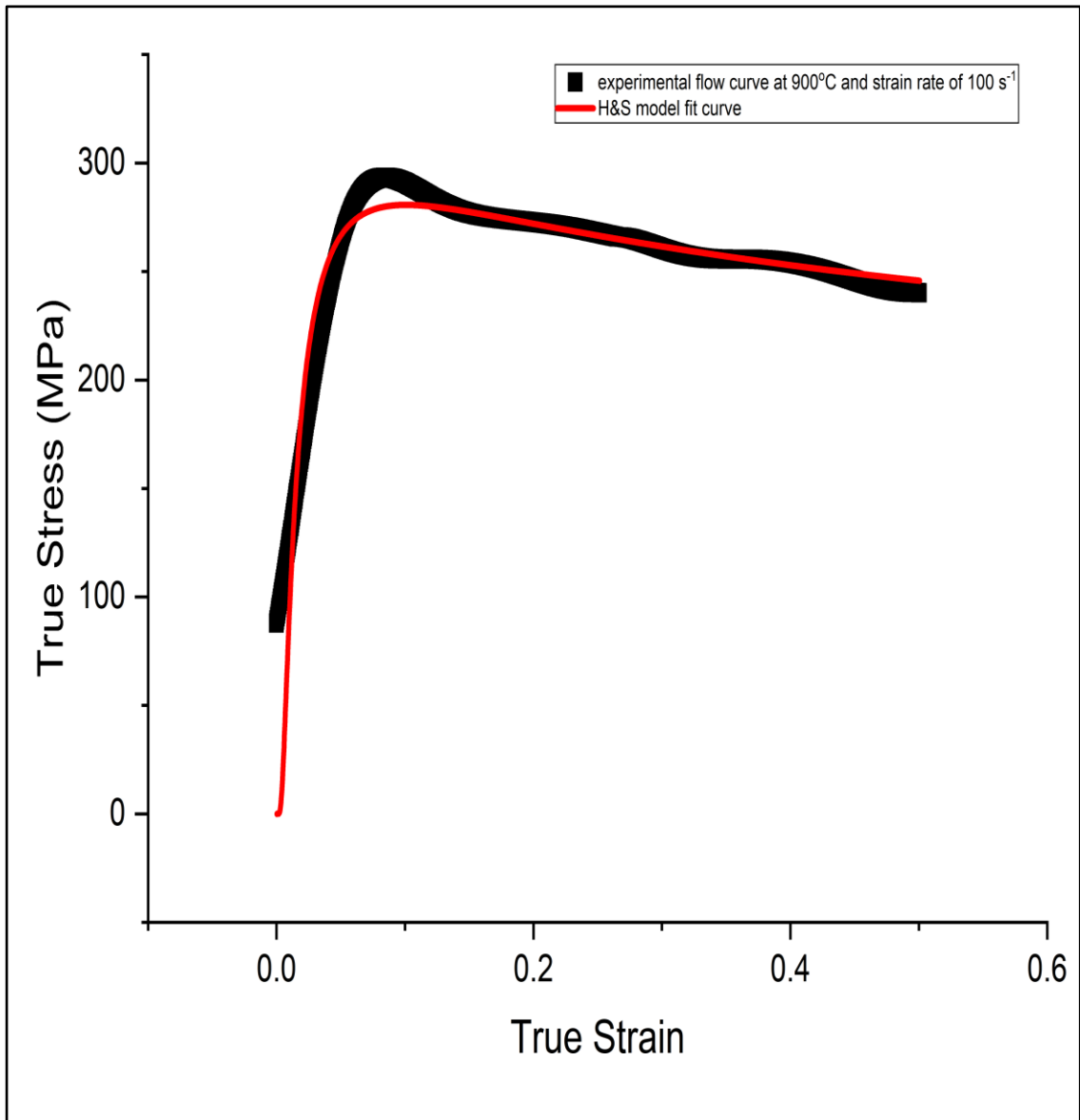


Figure 6.2: Flow stress at 900°C and 100s<sup>-1</sup>, after smoothing and fitting with H&S

The curves for the as received microstructure derived from hot isothermal compression tests at three strain rates (50s<sup>-1</sup>, 100s<sup>-1</sup> and 150s<sup>-1</sup>), at a strain level of 55% and three temperatures (850°C, 900°C and 950°C) are presented in Figure 6.3, Figure 6.4 and Figure 6.5.

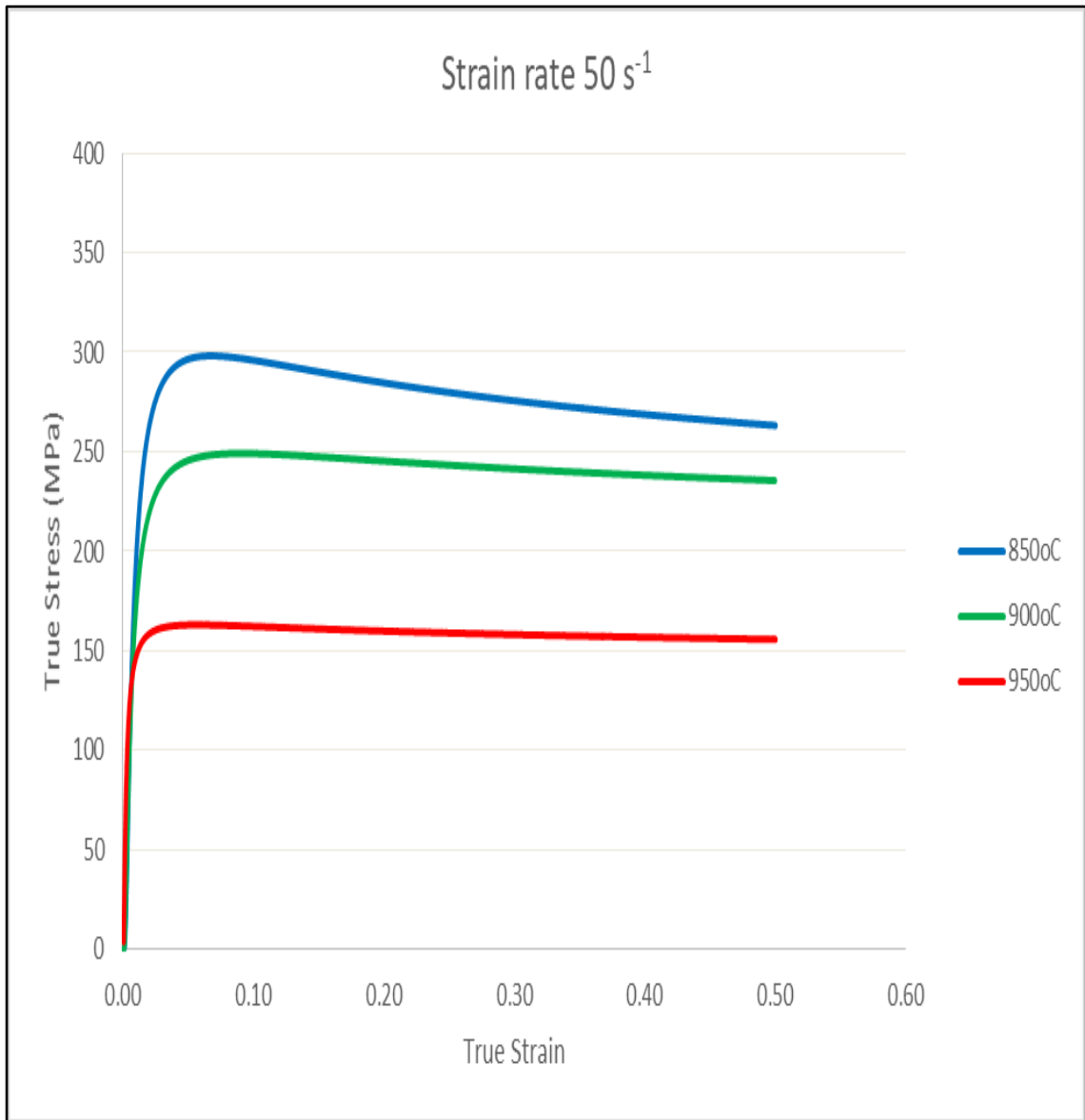


Figure 6.3: Flow stress behaviour of Ti-6Al-4V at  $50 \text{ s}^{-1}$  and three temperatures (850°C, 900°C and 950°C)

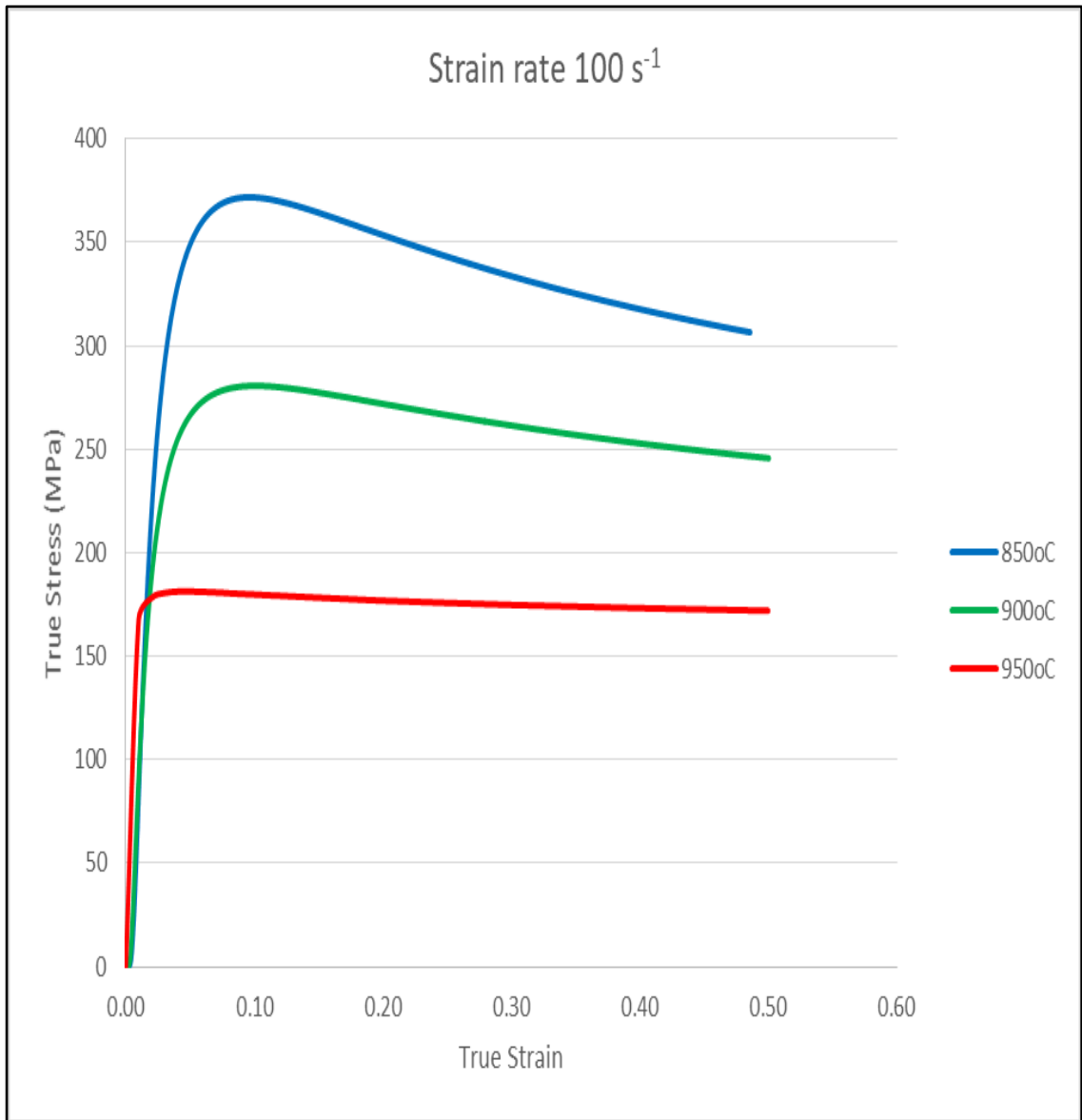


Figure 6.4: Flow stress behaviour of Ti-6Al-4V at  $100 \text{ s}^{-1}$  and three temperatures (850°C, 900°C and 950°C)

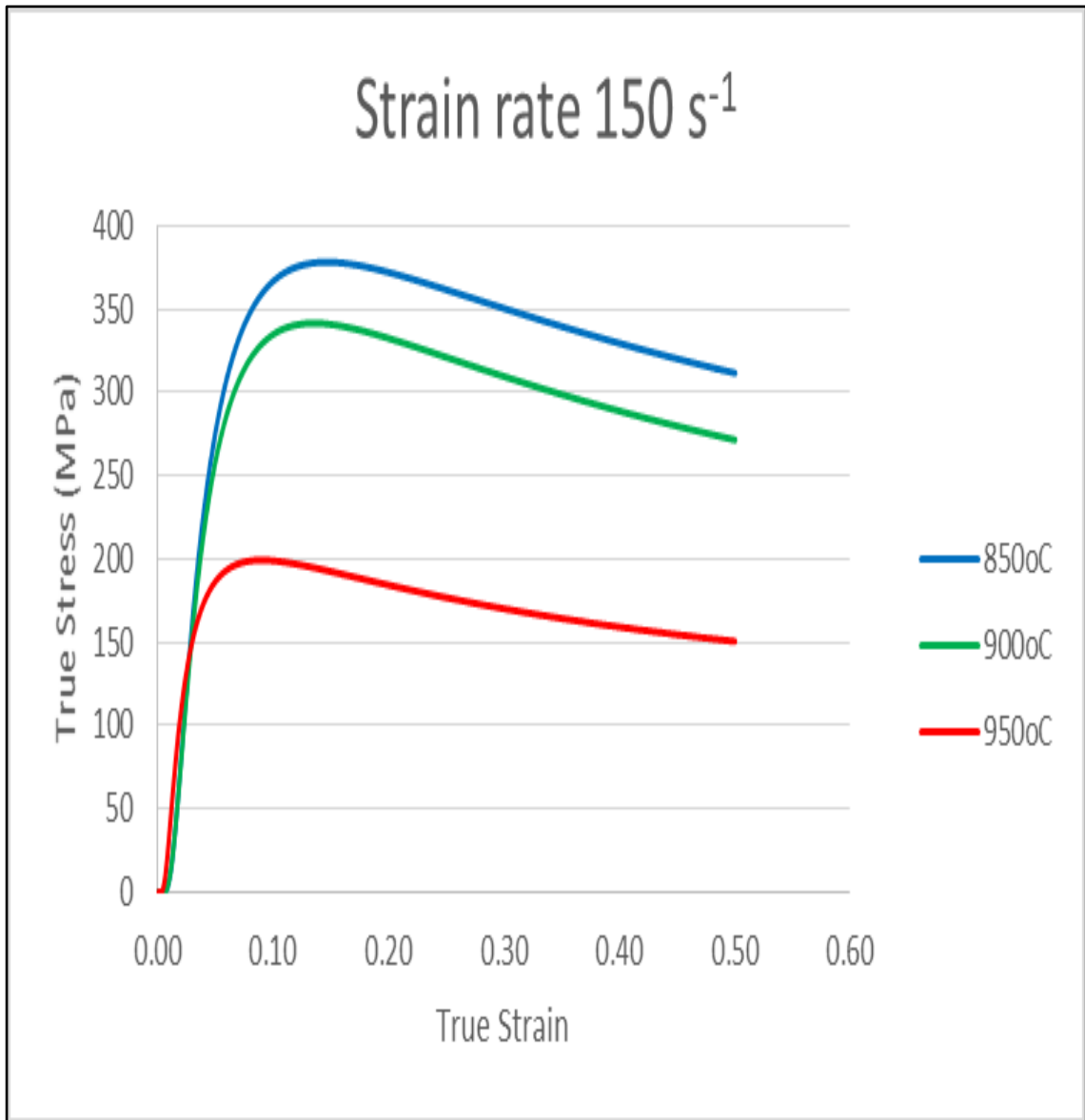


Figure 6.5: Flow stress behaviour of Ti-6Al-4V at 150 s<sup>-1</sup> and three temperatures (850°C, 900°C and 950°C)

The flow behaviour of the curves for the three strain rates is strongly dependent on the temperature. The flow stress curves initially present strain hardening with no peak at all strain rates and temperatures, followed by moderate flow softening for all temperatures (850°C, 900°C and 950°C). Similar type of flow behaviour have been also reported in the literature [49][64].

## 6.2 H&S modelling of flow behaviour

As has been mentioned in section 5.4 the flow behaviour of the lamellar microstructure, similar to as-received microstructure, has been modelled with the H&S rheological law. The flow curves and the material constants, as well as the percentage of confidence for the three temperatures and three strain rates are presented in this section.

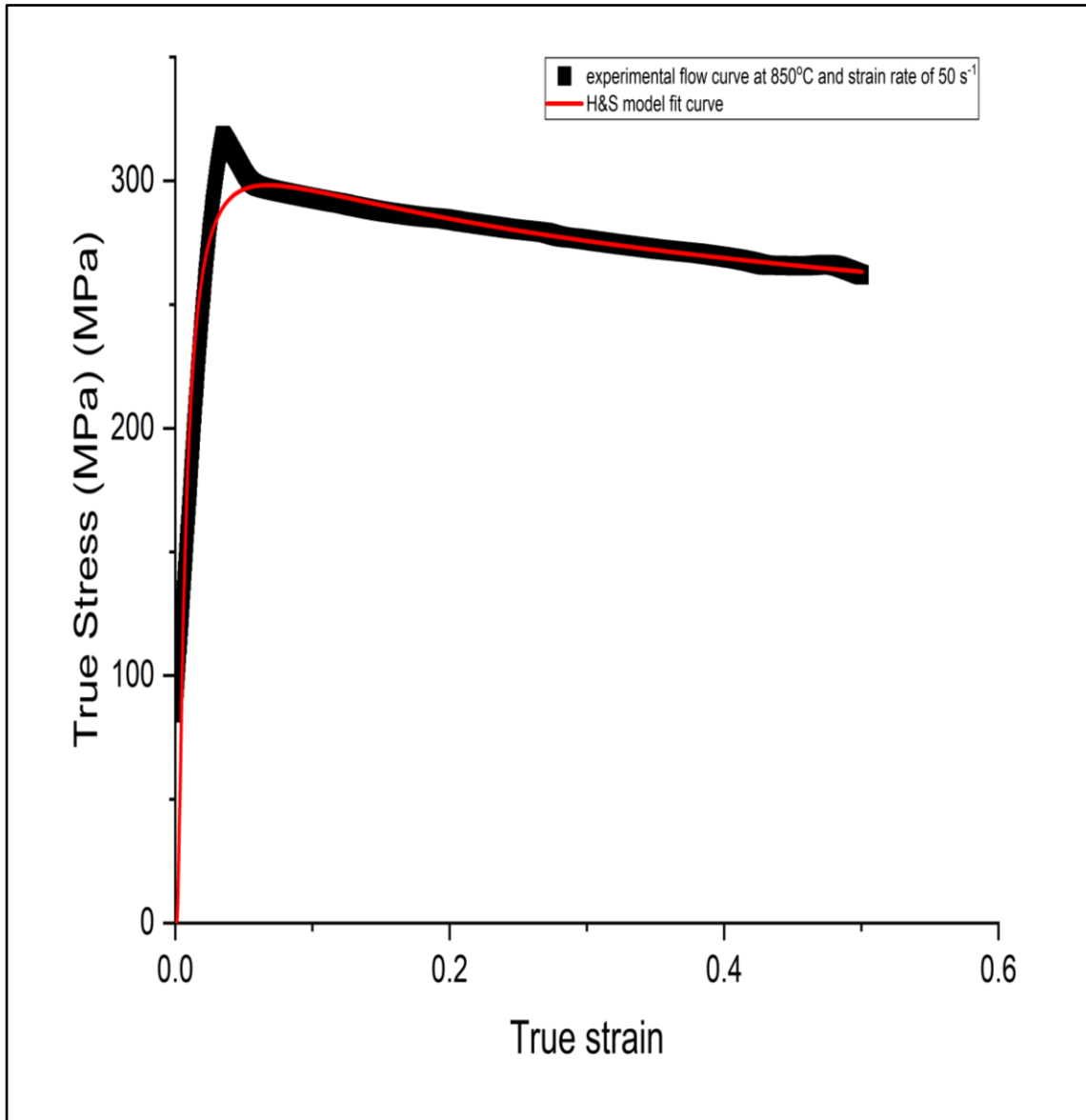


Figure 6.6: Experimental and modelled flow curves for 850°C and strain rate 50s<sup>-1</sup>

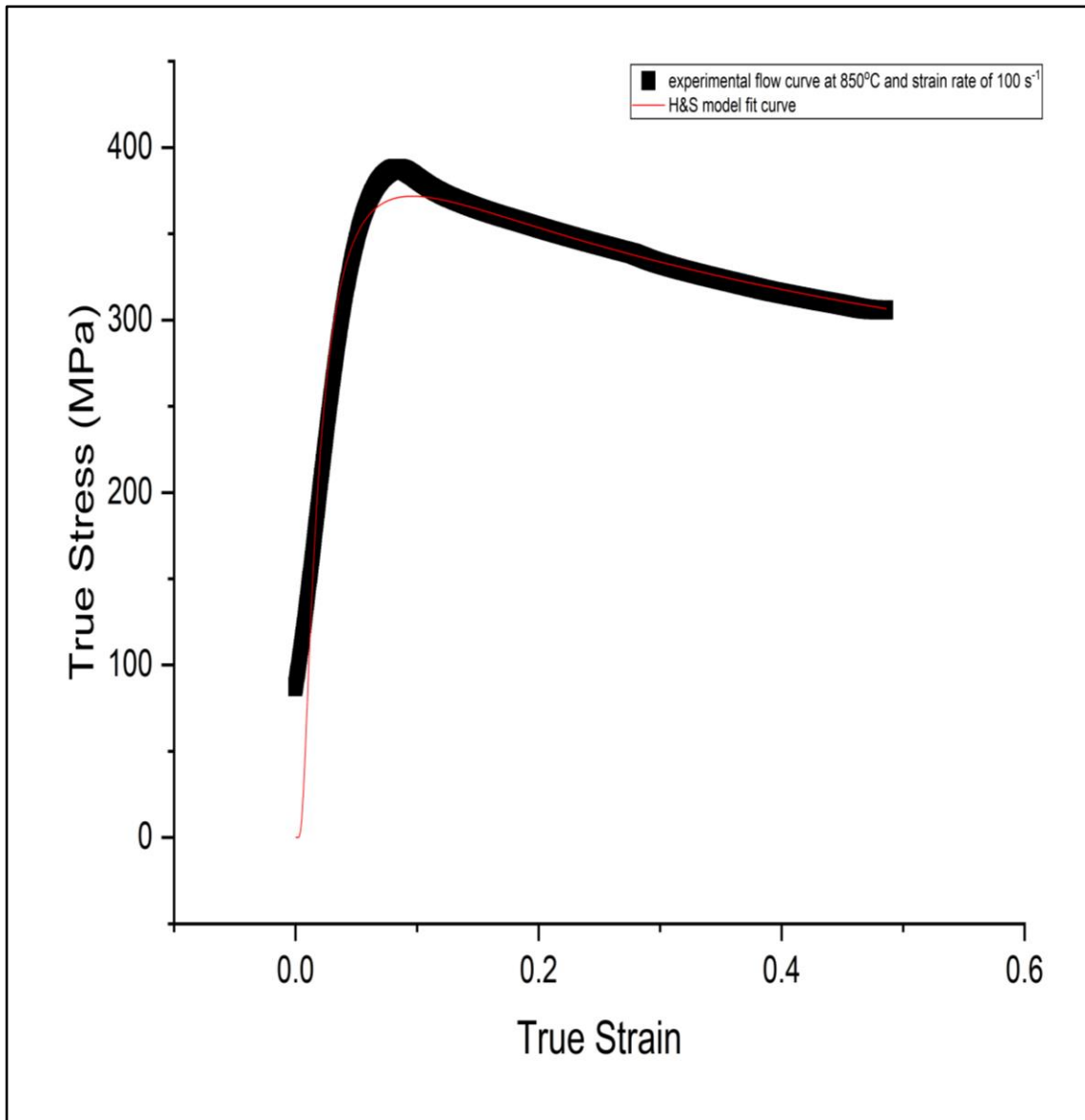


Figure 6.7: Experimental and modelled flow curves for 850°C and strain rate 100s<sup>-1</sup>

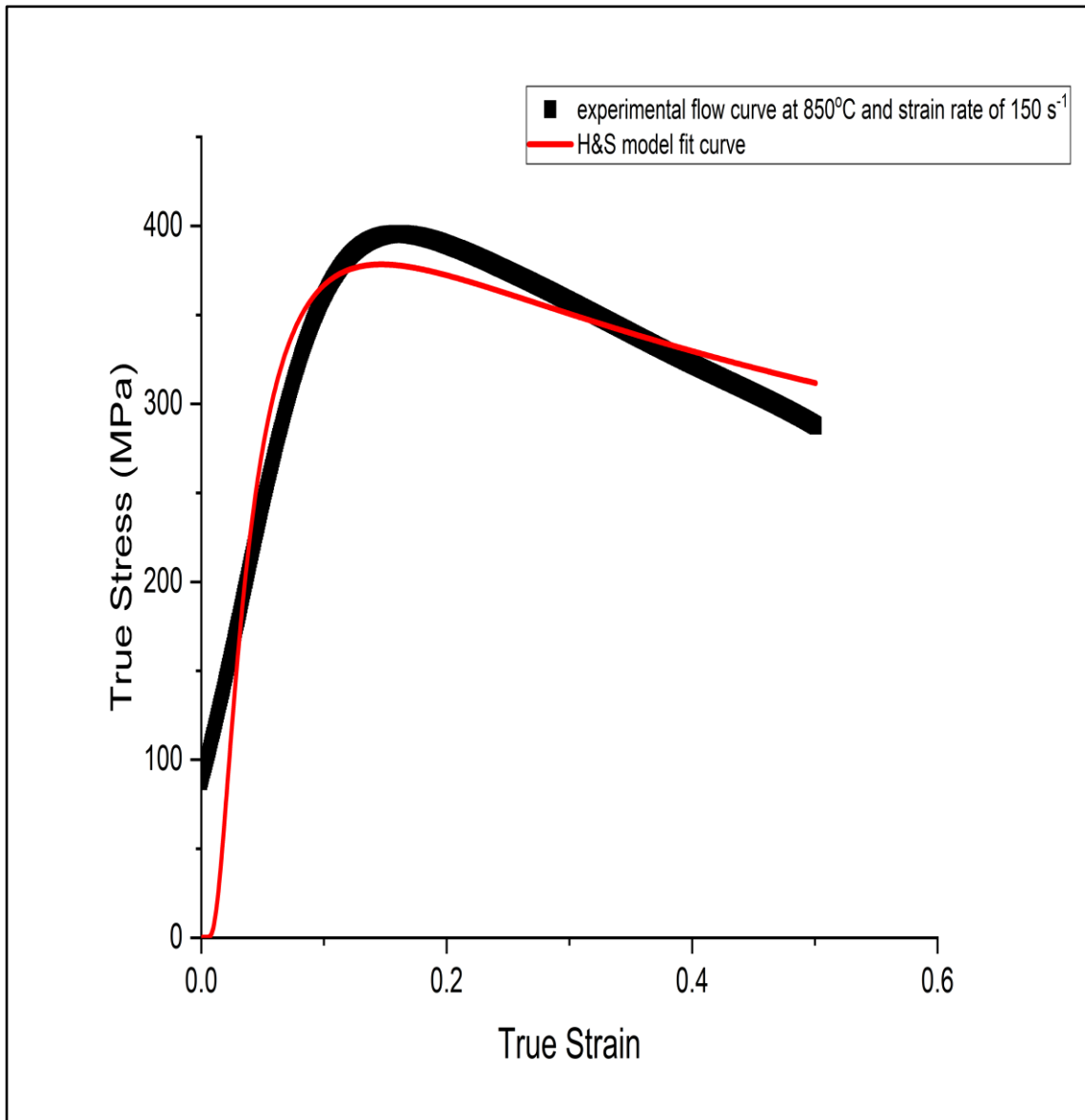


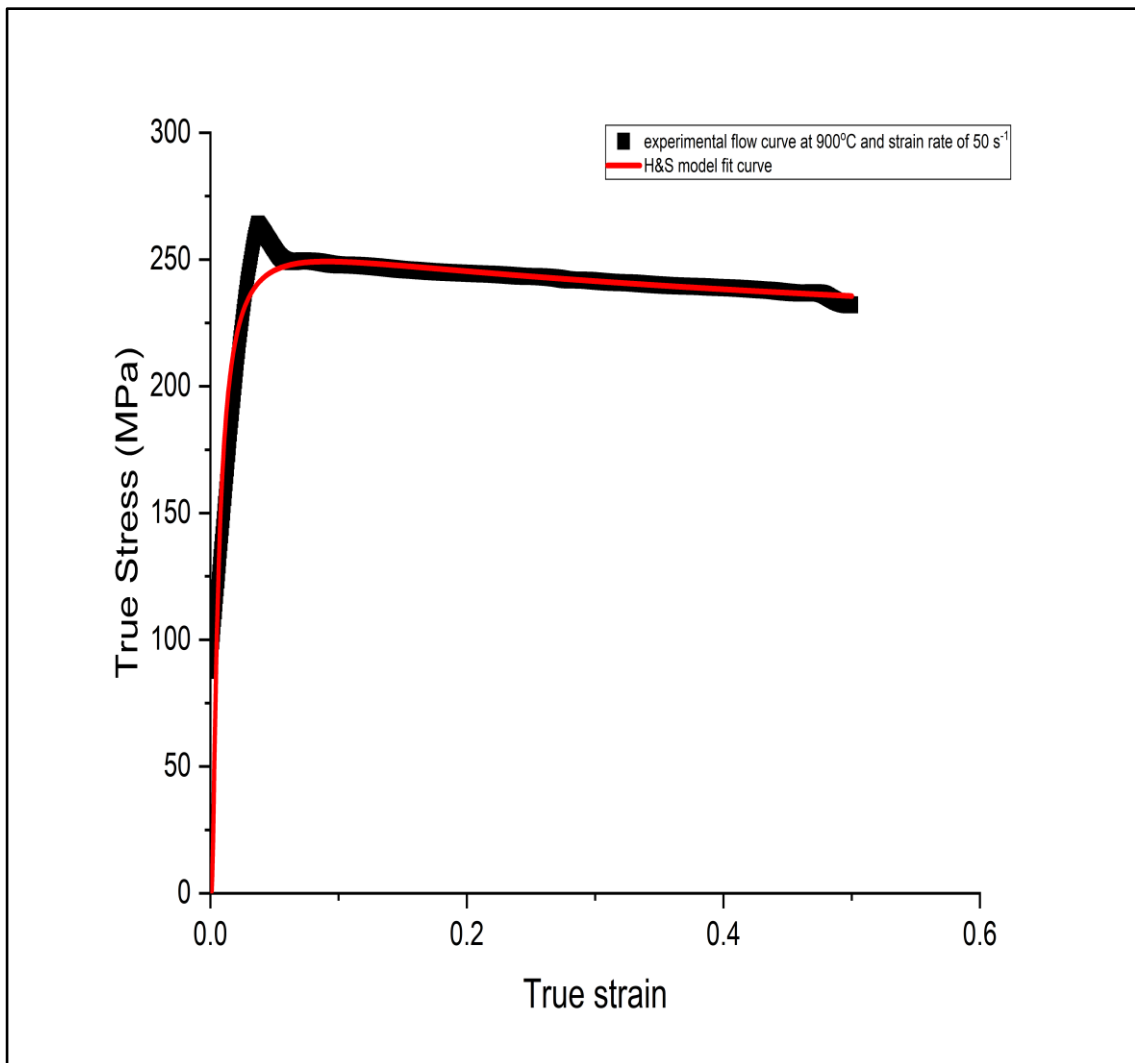
Figure 6.8: Experimental and modelled flow curves for 850°C and strain rate 150s<sup>-1</sup>

For the temperature of 850°C the confidence level and the H&S material constants are presented in Table 6.1. From the results it is clear that the model demonstrated a good response for all strain rates; with a similar percentage of confidence.

Table 6.1: H&amp;S material constants and level of confidence for 850°C

Strain rate (s <sup>-1</sup> )	A	m1	m2	m3	m4	Confidence (%)
50	16898.51683	-0.00254	-0.10964	-0.53752	-0.00741	87.0
100	16897.3217	-0.0024	-0.23584	-0.47231	-0.02269	89.9
150	17054.04884	-0.00256	-0.37247	-0.39562	-0.05468	85.3

For the temperature of 900°C the flow curves, the fitted curve, the confidence level and the H&S material constants are presented below.

Figure 6.9: Experimental and modelled flow curves for 900°C and strain rate 50s<sup>-1</sup>

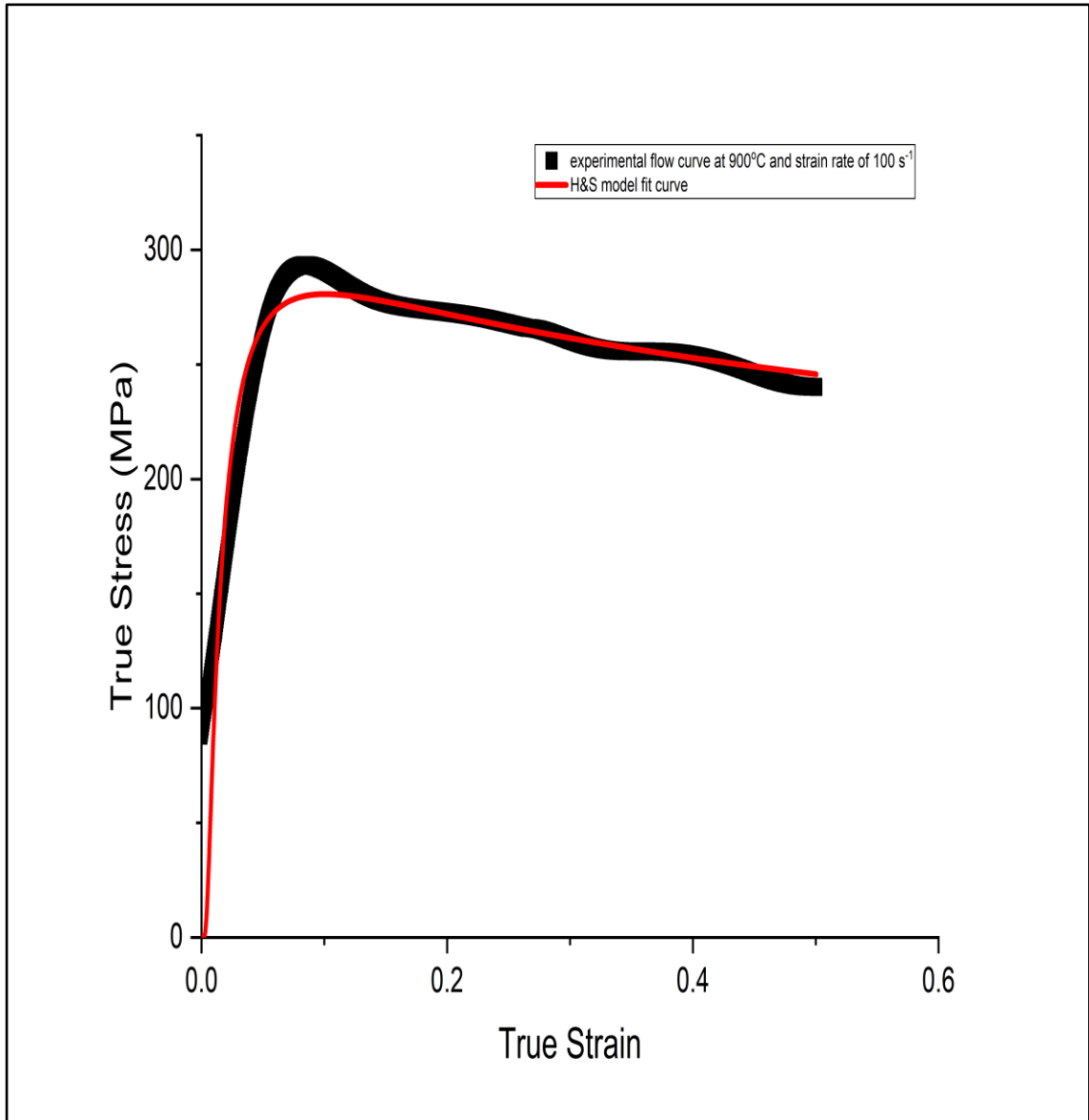


Figure 6.10: Experimental and modelled flow curves for 900°C and strain rate 100s<sup>-1</sup>

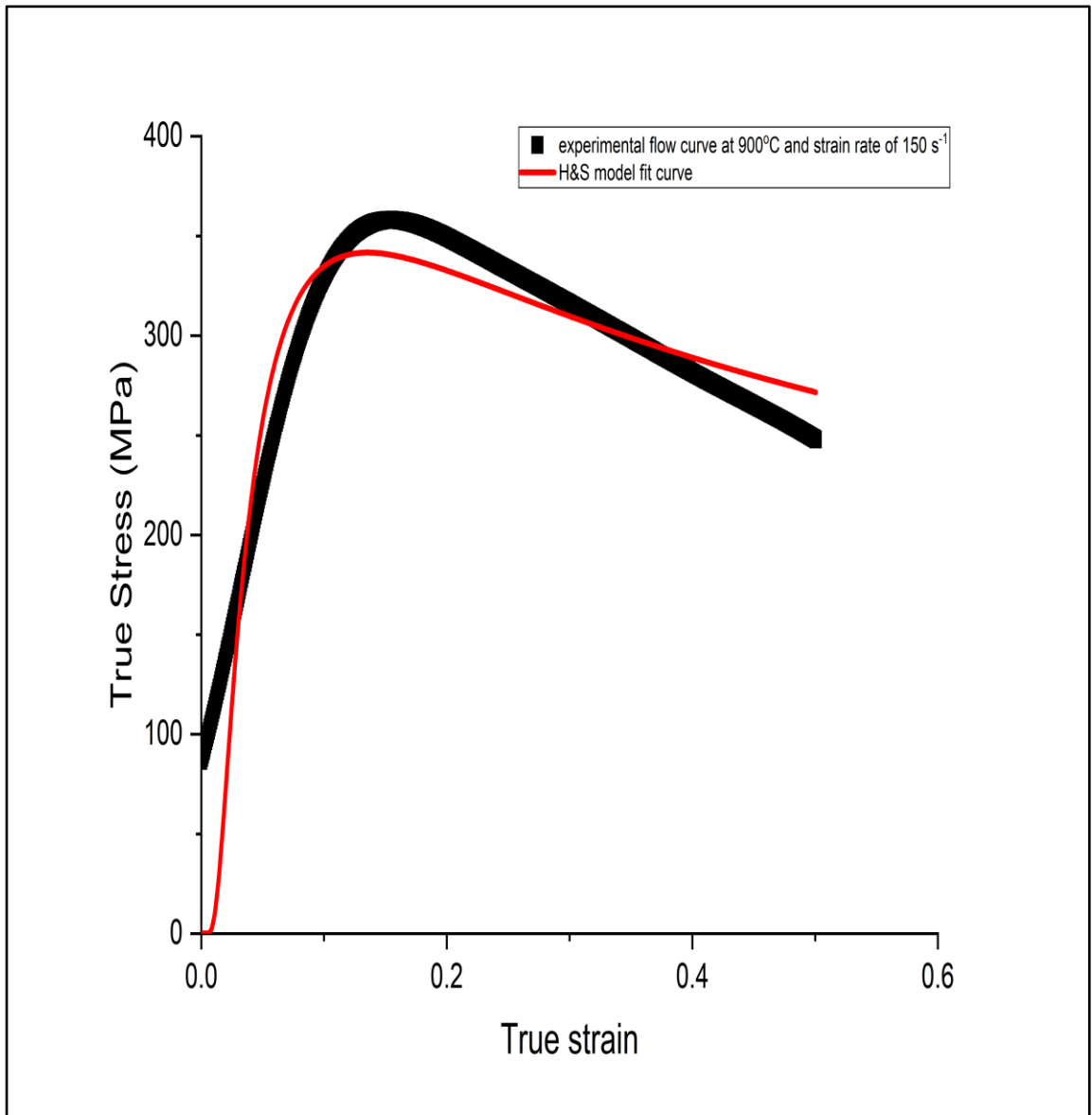


Figure 6.11: Experimental and modelled flow curves for 900°C and strain rate 150s<sup>-1</sup>

Table 6.2: H&amp;S material constants and level of confidence for 900°C

Strain rate (s <sup>-1</sup> )	A	m1	m2	m3	m4	Confidence (%)
50	16473.24131	-0.0024	-0.06329	-0.54853	-0.00575	82.2
100	15382.03421	-0.00262	-0.16533	-0.41919	-0.01666	83.2
150	17989.26234	-0.00255	-0.3971	-0.4101	-0.05381	82.2

From the percentage of confidence we can conclude that the model maintains a good and stable response. Even though, the values are slightly lower than those at 850°C, they are above 80%. As previously the modelling of the elastic region was responsible for the lower values. The initiation of the experimental flow curve was at 10kN whereas the initiation of the modelled curve was at the zero load. The 10KN load as the first valid experimental value was selected to avoid any noise created during the commencement of the test and the impact phenomena created during high strain rates.

The flow modelling curves and material constants at a temperature of 950°C and the three strain rates are presented Figure 6.12, Figure 6.13 and Figure 6.14.

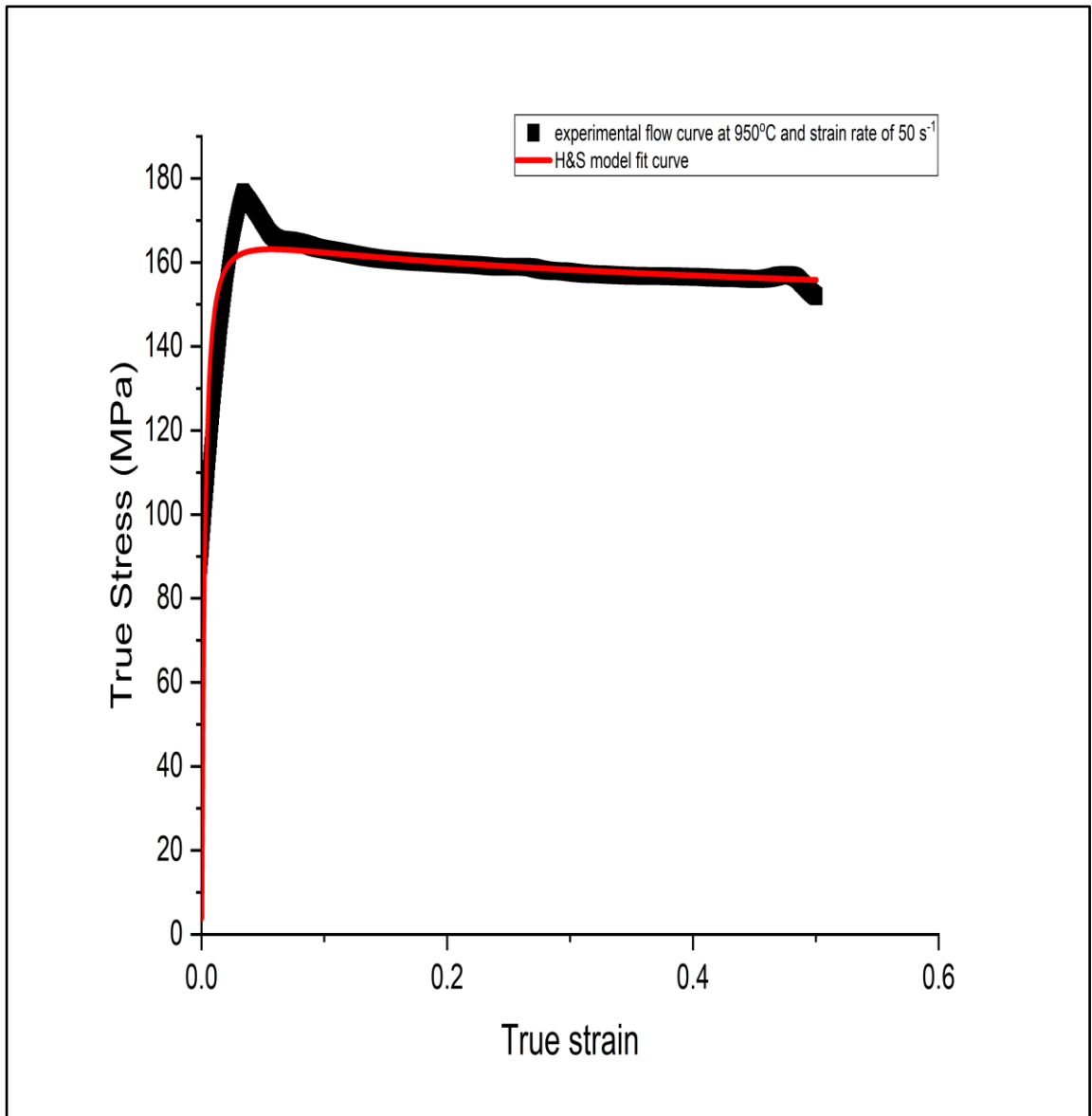


Figure 6.12: Experimental and modelled flow curves for 950°C and strain rate 50s<sup>-1</sup>

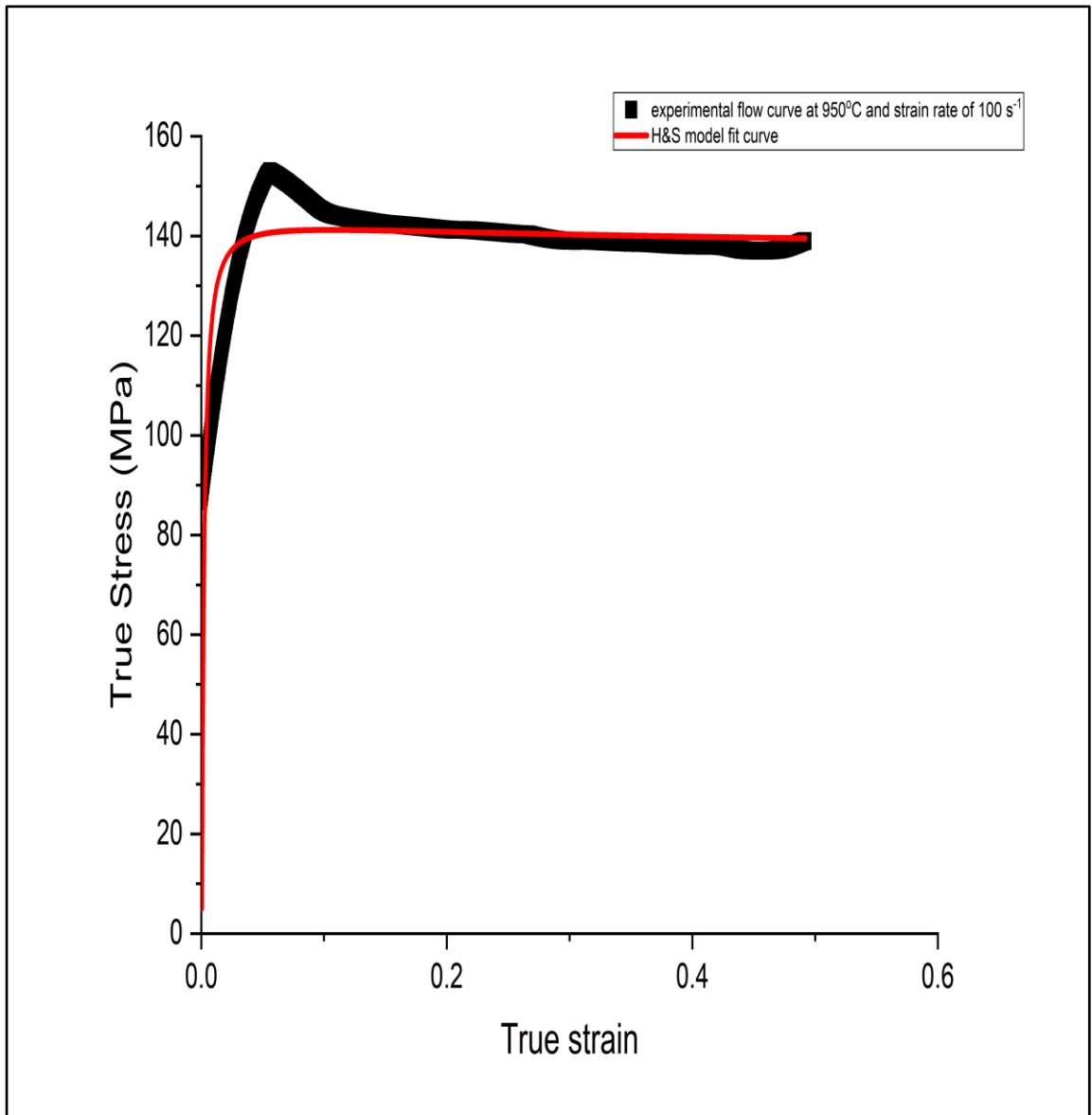


Figure 6.13: Experimental and modelled flow curves for 950°C and strain rate 100s<sup>-1</sup>

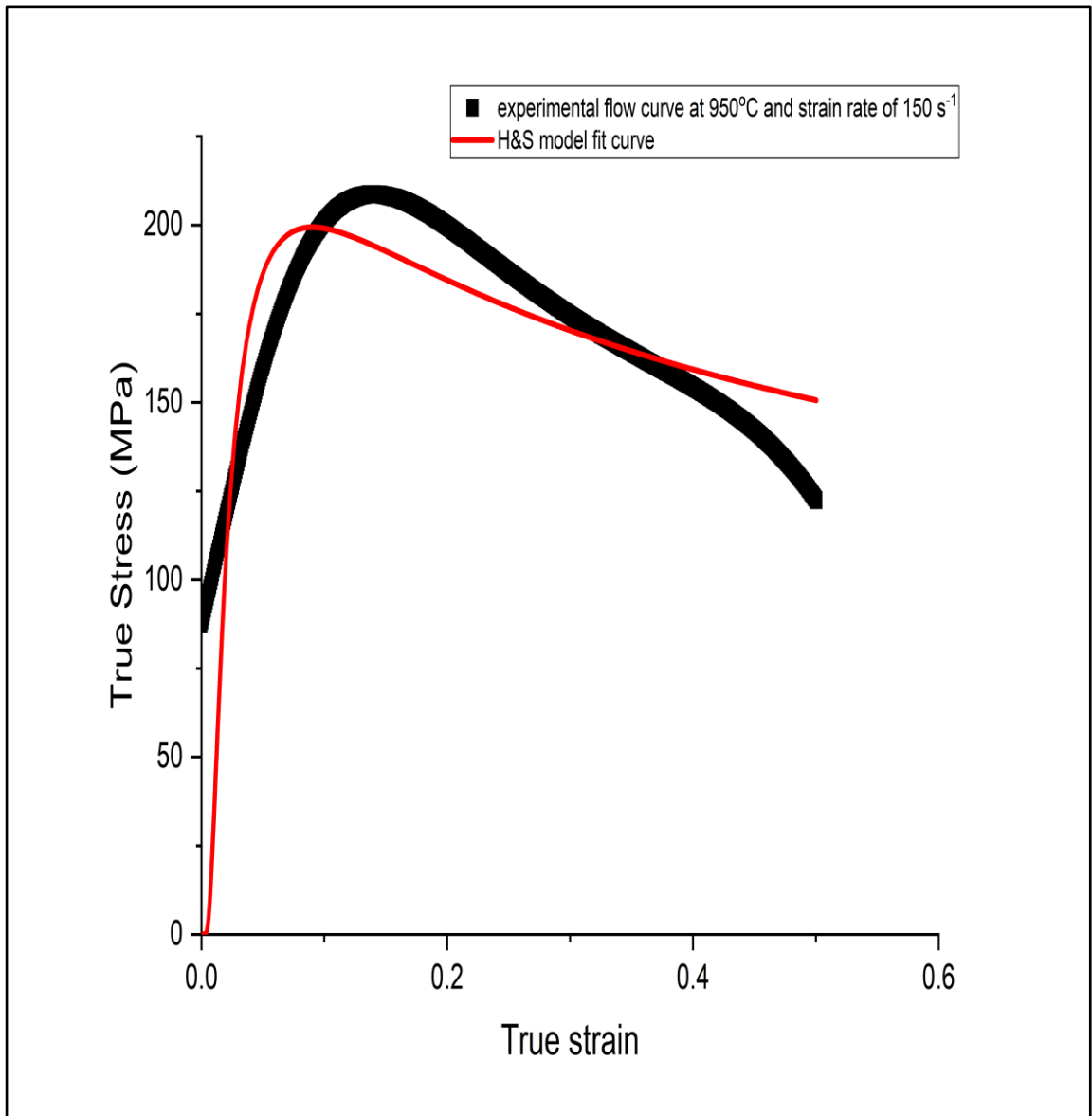


Figure 6.14: Experimental and modelled flow curves for 950°C and strain rate 150s<sup>-1</sup>

Table 6.3 presents the confidence level and the H&S material constants for 950°C.

Table 6.3: H&amp;S material constants and level of confidence for 950°C

Strain rate (s <sup>-1</sup> )	A	m1	m2	m3	m4	Confidence (%)
50	14146.98108	-0.00238	-0.03547	-0.58066	-0.00201	84.3
100	13007.82312	-0.00229	-0.01598	-0.52982	-0.00168	82.1
150	12623.13467	-0.0022	-0.31426	-0.49817	-0.02838	74.7

The percentage of confidence at this temperature is maintained high, close to 80%, the lower value at high strain rate of 150 s<sup>-1</sup> is the result of modelling the elastic region of the flow stress curve. Furthermore, at this temperature and strain rate the dynamic phenomena are more pronounced, which leads to lower values of confidence.

For all temperatures and strain rates we can see a flow softening behaviour which varies from low to high. The model describes the flow softening and the variation of the softening behaviour efficient; by maintaining an average 80% confidence.

From the Table 6.3 is clear that the model can reliably describe the flow behaviour up to strain rate of 100 s<sup>-1</sup> with more than 80% confidence and above the strain rate of 100 s<sup>-1</sup> the confidence drops to almost 75%.

### 6.3 Strain rate effect

The variation of the flow stress with the strain rate is presented in Figure 6.15 and Figure 6.16 for peak stress and 0.5 of true strain respectively. It can be seen that for all temperatures at peak stress the curves show a linear increase of the flow stress with the increase of strain rate. Similarly, the flow stress values are increasing with decreased temperature. Similar behaviour has been documented for the Ti-6Al-4V at lower strain rates [142][162]. On the other hand, at 0.5 true strain the material shows initially for 850°C and 900°C an increase of flow stress

with temperature, but at a temperature of 950°C the material demonstrates a steady state flow stress.

The effect of strain rate on the flow stress of the material quantified by the strain rate sensitivity ( $m$ ) has been described in section 5.5.5.

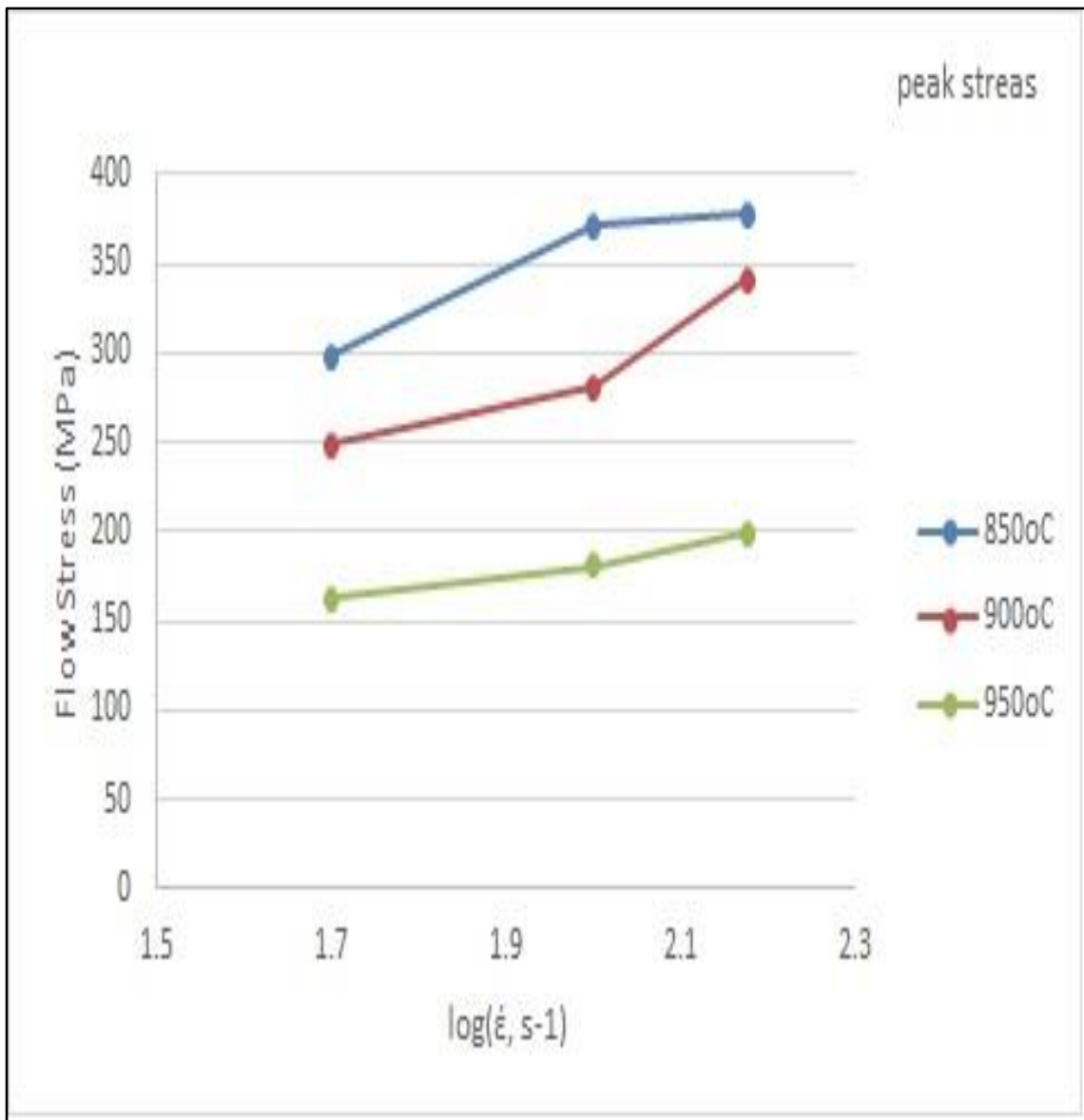


Figure 6.15: Influence of strain rate on flow stress at peak stress, as a function of temperature.

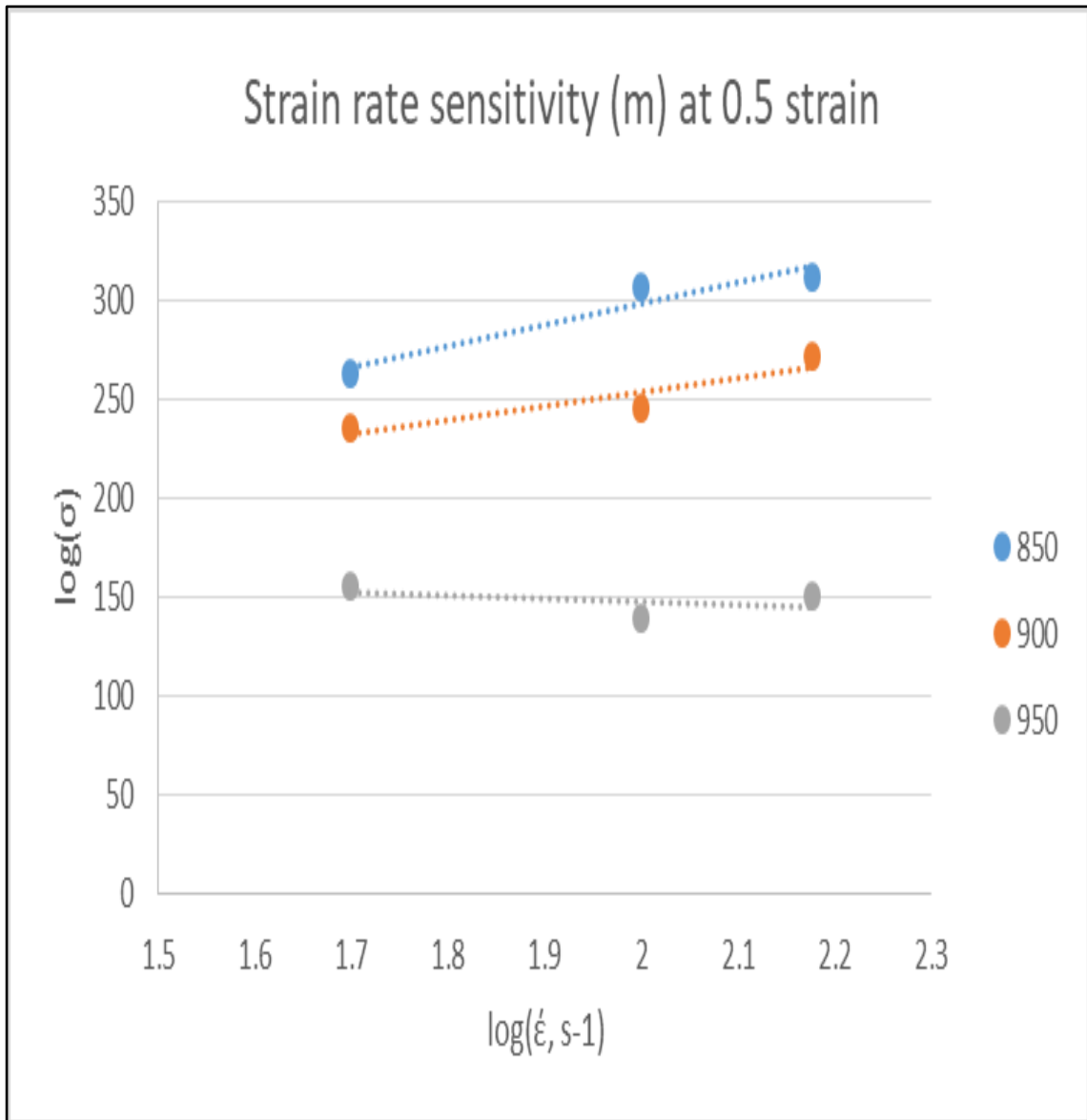


Figure 6.16: Influence of strain rate on flow stress at 0.5 of true stress, as a function of temperature.

The strain rate sensitivity ( $m$ ) values at peak stress and 0.5 of true strain are presented in Table 6.4. The values of strain rate sensitivity are below 0.3, indicating that the deformation mode is by dislocation glide/climb; Semiatin has also reported similar results investigating the effect of alpha platelet thickness on plastic flow during hot working of Ti6Al4V [163].

**Table 6.4: Strain rate sensitivity (m) and different temperatures peak stress.**

<b>Temperature</b>	<b>Strain rate sensitivity (m) at peak stress</b>	<b>Strain rate sensitivity (m) at 0.5 of true strain</b>
850°C	0.22	0.16
900°C	0.27	0.12
950°C	0.17	0

The calculated m values presented above at peak stress demonstrate an increase of strain rate sensitivity from 850°C to 900°C, and a decrease at 950°C. The m value dropped at 950°C to almost half the value seen at 900°C. The flow stress at the highest temperature is substantially affected by the temperature and is less strain rate sensitive. The fluctuation of the strain rate sensitivity values may come from the microstructure or the temperature, two factors documented in the literature which influence the strain rate sensitivity values [26][142]. For a true strain of 0.5 the strain rate sensitivity shows a decrease with the increase of temperature.

#### 6.4 Temperature effect

Figure 6.17 illustrates the temperature effect on the flow behaviour of Ti-6Al-4V, the plot of the peak flow stress as a function of the temperature for the three strain rates demonstrates the influence of temperature on deformation stress of Ti-6Al-4V.

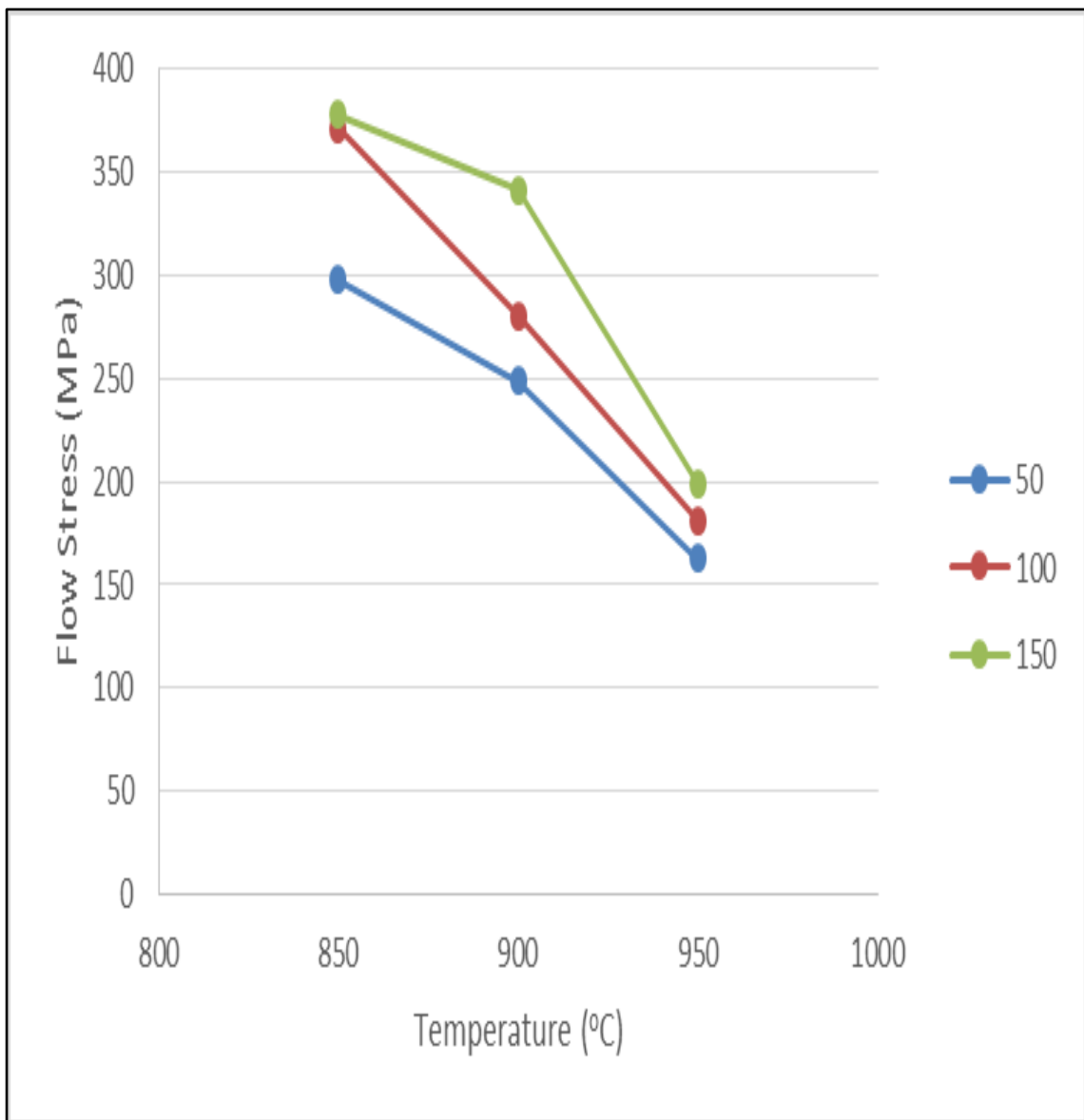


Figure 6.17: Effect of temperature on the peak flow stress as a function of strain rate

It is noted that the flow stress decreases almost linearly with the temperature increase. The rate of decrease is higher for a strain rate of  $100 \text{ s}^{-1}$  and lower for strain rate of  $50 \text{ s}^{-1}$ . For strain rate of  $150 \text{ s}^{-1}$  the rate of decrease is close to strain rate of  $100 \text{ s}^{-1}$  though slightly reduced which may reflect the influence of the microstructure changes at this temperature.

## 6.5 Microstructure evolution during hot isothermal compression

This section presents and discusses the evolution and changes in the lamellar microstructure due to hot isothermal compression under a range of temperatures and strain rates.

In this work flow softening is observed in all isothermal compression tests. It is important to understand the flow softening of Ti-6Al-4V, which is commonly observed in titanium alloys, in order to control the properties and microstructure. From the literature the flow softening behaviour is attributed to the adiabatic heating or changes to microstructure. At low temperatures and high strain rates (above  $1 \text{ s}^{-1}$ ) the adiabatic heating is mainly responsible for the microstructure changes and the majority of the flow softening behaviour.

Because in this work the adiabatic heating effect has been corrected for all conditions, the flow softening effect must be related to microstructure changes during deformation. Two parameters effect the peak stress of the isothermal deformed Ti-6Al-4V; the temperature and the strain rate. From the results it is clear that, with decreased strain rate and increased temperature the peak flow stress is decreased. The two main mechanisms are documented in the literature, as being responsible for the flow softening in the lamellar morphology: dynamic globularization of the lath structure and micro buckling [166].

In the literature it has been reported that dynamic globularization takes place at strains in excess of those at which flow softening initiates in Ti-6Al-4V; it was suggested that it is buckling of the alpha plates which leads to the softening. Since at low strain the volume fraction of globularized alpha is small, micro buckling is the main mechanism that controls the flow softening . Figure 6.18 presents a schematic illustration representing the microstructural evolution during dynamic globularization [167].

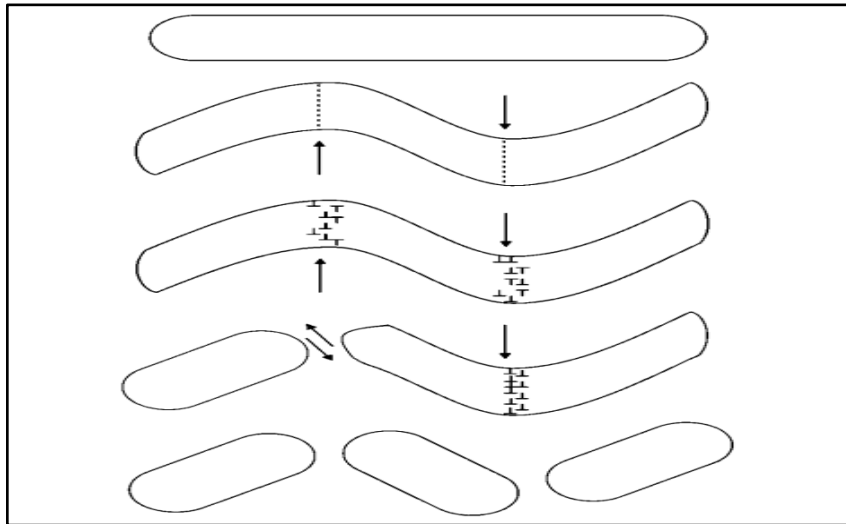


Figure 6.18: Schematic illustration representing microstructural evolution during dynamic globularization [167]

The micrographs obtained by SEM at 850°C at the centre of the sample are presented below. The compression axis is vertical to the micrographs, different magnification have been used to accurately represent the microstructure morphology.

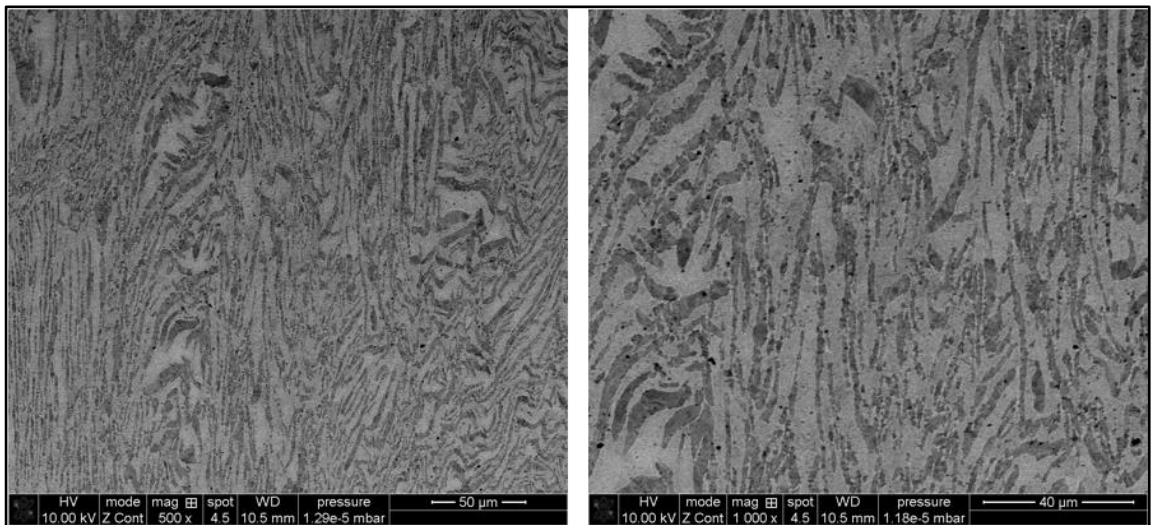


Figure 6.19: SEM micrographs at 850°C and strain rate of  $50s^{-1}$  (left 500x and right 1000x)

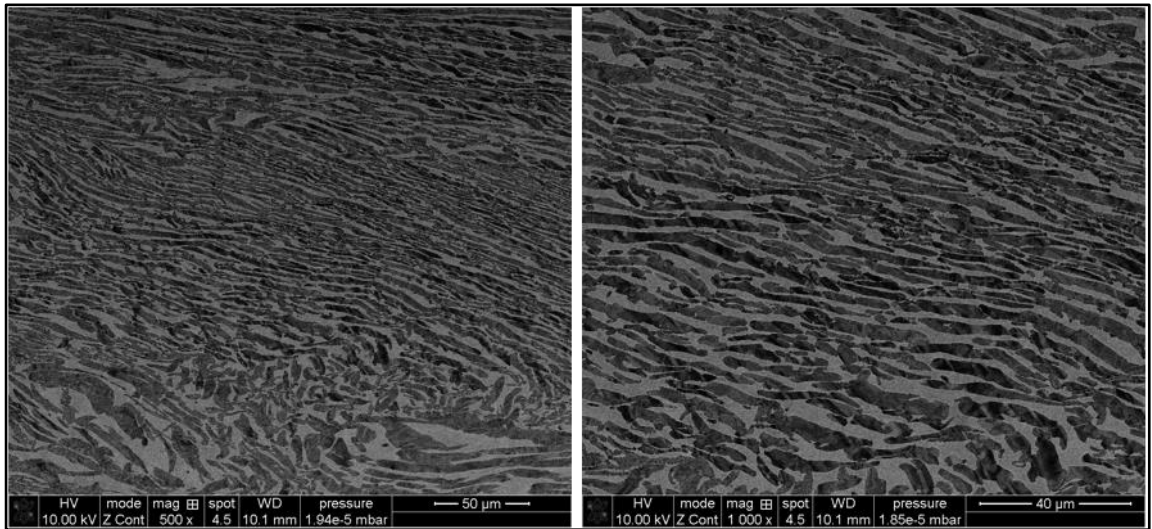


Figure 6.20: SEM micrographs at 850°C and strain rate of  $100\text{s}^{-1}$  (left 500x and right 1000x)

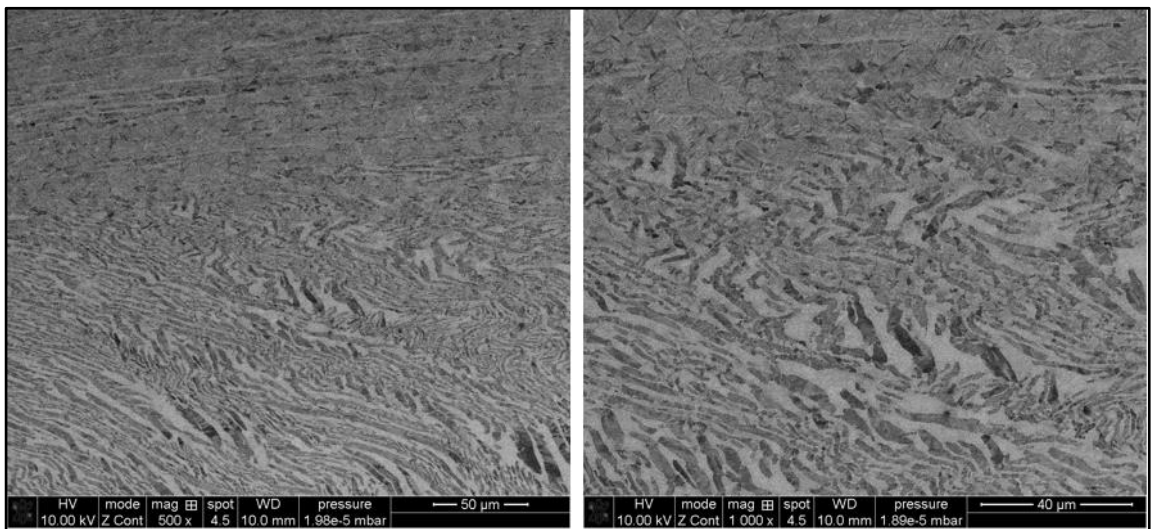


Figure 6.21: SEM micrographs at 850°C and strain rate of  $150\text{s}^{-1}$  (left 500x and right 1000x)

The microstructure observation at 850°C indicates significant distortion of the initial lath structure including kinking and bending. The laths initially morphology is following the direction of the bar. At strain rates above  $100\text{ s}^{-1}$  the laths are almost vertical to the compression direction. In the literature this deformation mode is well documented [167][142][168]. At this strain no evidence of

globularization is presented for any strain rates and the main mechanism of flow softening is the buckling.

The volume fraction of the alpha phase is presented in Figure 6.22. It is clear that at 850°C the strain rate has a substantial influence on the alpha phase volume fraction. The increase of strain rate leads to reduction of alpha phase.

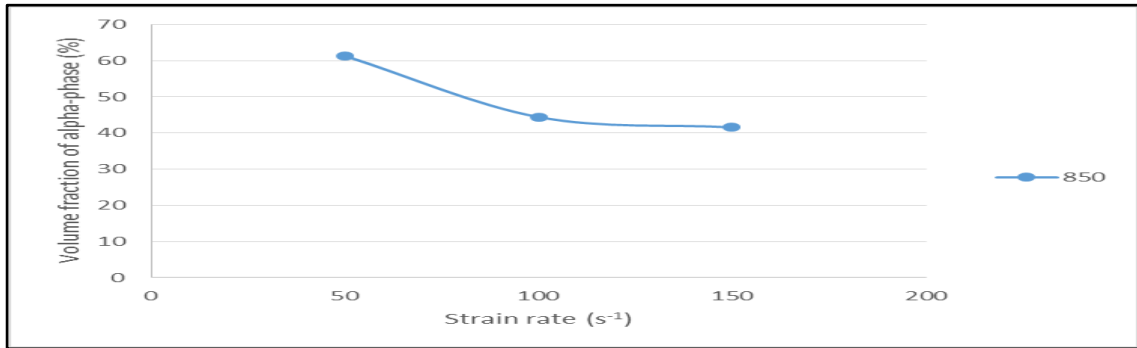


Figure 6.22: Volume fraction of alpha phase in the centre of the deformed sample at 850°C and strain rates of  $50s^{-1}$ ,  $100s^{-1}$  and  $150s^{-1}$

The micrographs obtained from the SEM at 900°C are presented in Figure 6.23, Figure 6.24 and Figure 6.25. The compression axis is vertical to the micrographs, different magnifications have been used to accurately represent the microstructure morphology.

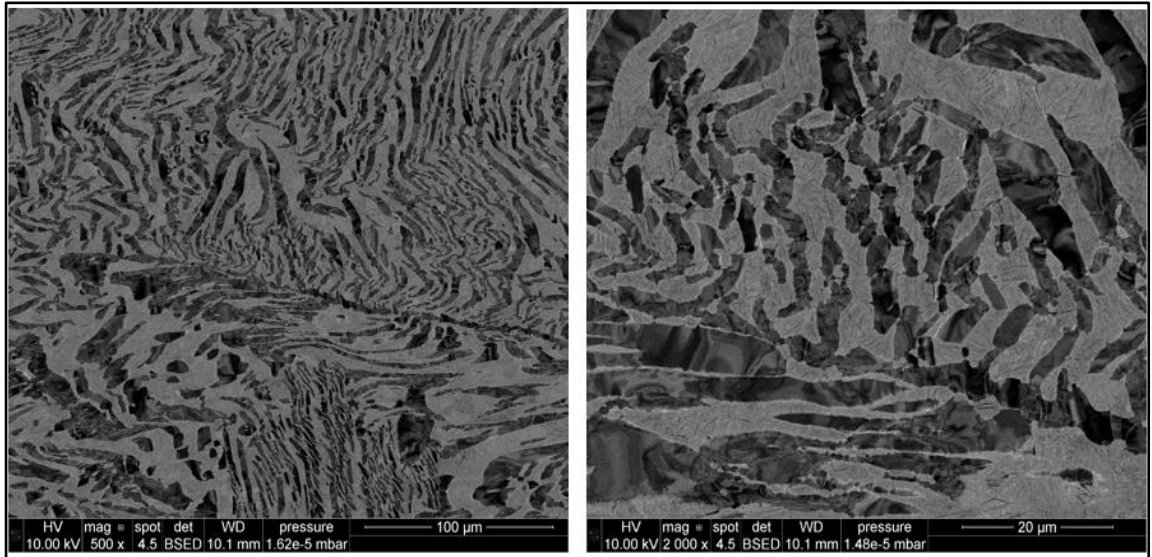


Figure 6.23: SEM micrographs at 900°C and strain rate of 50s<sup>-1</sup> (left 500x and right 1000x)

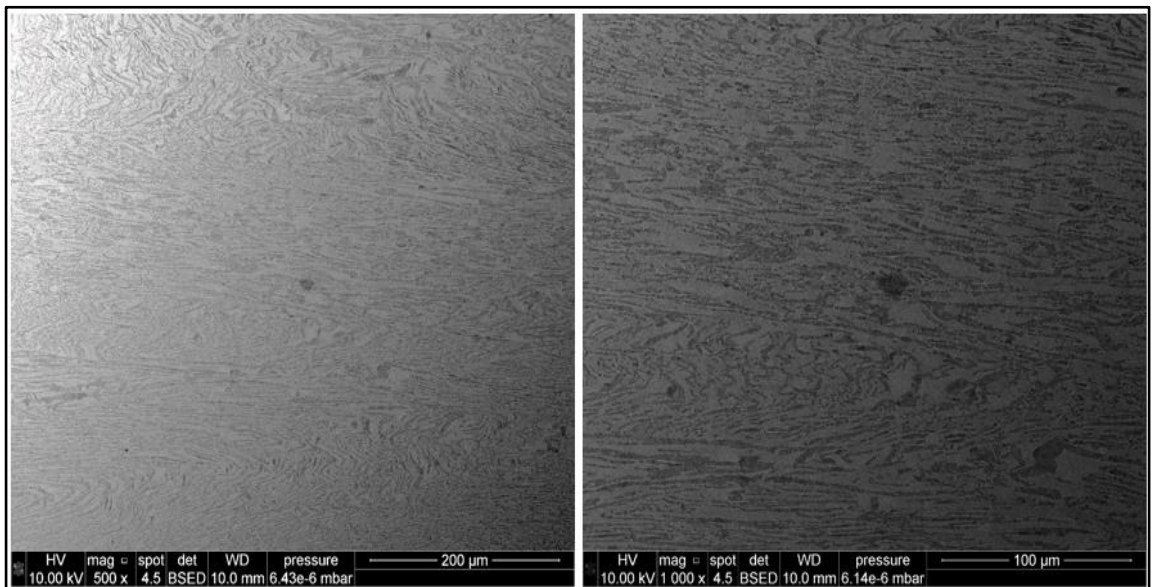


Figure 6.24: SEM micrographs at 900°C and strain rate of 100s<sup>-1</sup> (left 500x and right 1000x)

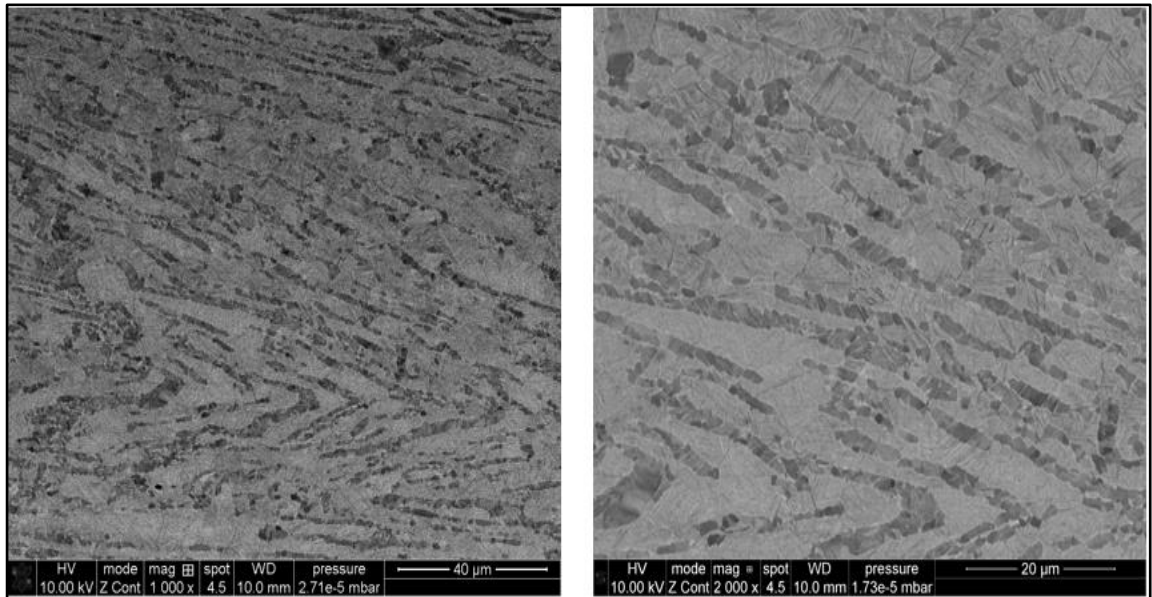
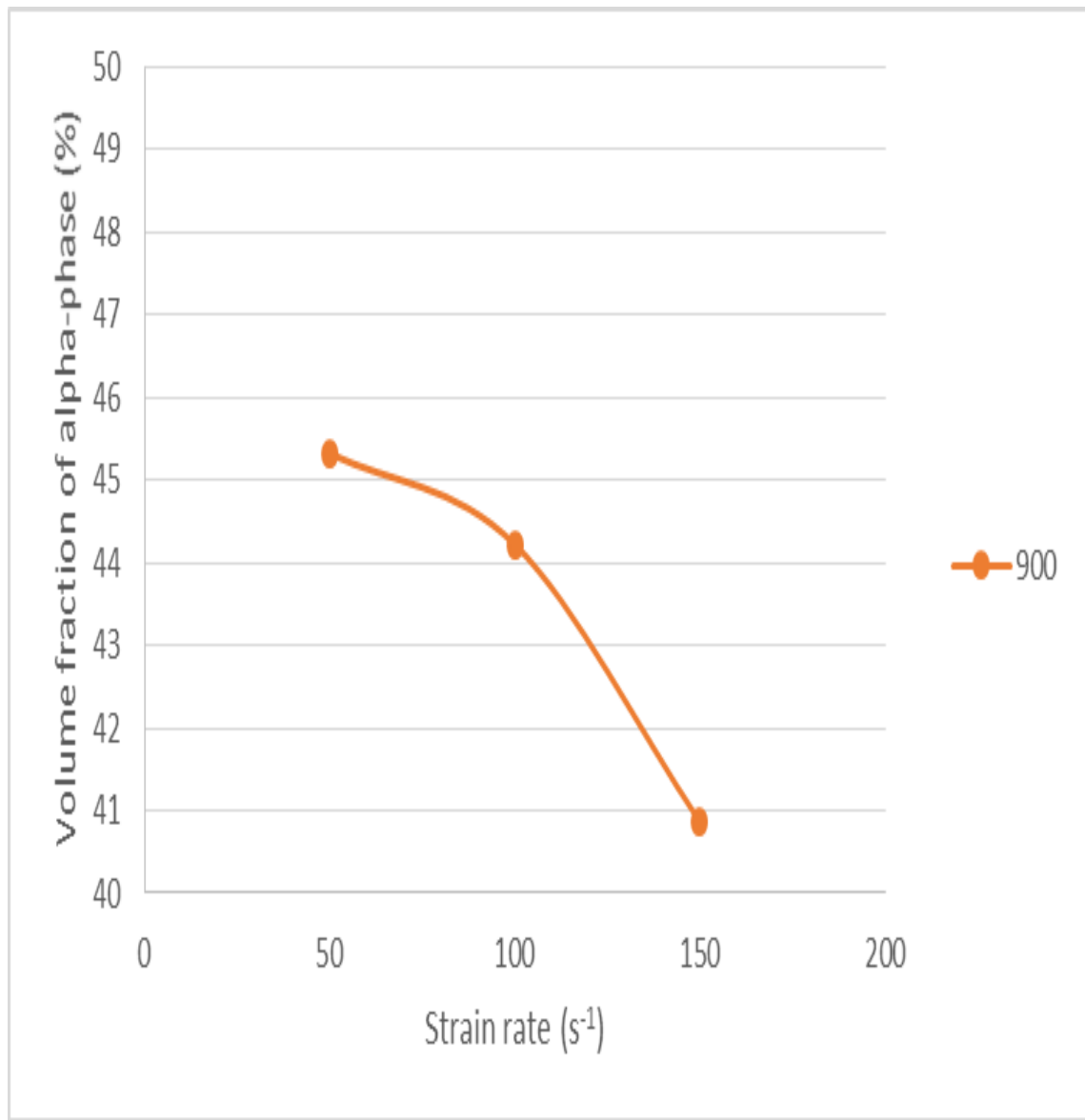


Figure 6.25: SEM micrographs at 900°C and strain rate of 150s<sup>-1</sup> (left 1000x and right 2000x)

Similar to the microstructure reported at 850°C, significant distortion of the initial lath structure including kinking and bending is observed for 900°C. Furthermore, at strain rates above 100 s<sup>-1</sup> the laths are almost vertical to the compression direction similar to 850°C. The volume fraction of the alpha phase is presented in Figure 6.26. At 900°C the strain rate shows significant variance in the alpha phase volume fraction similar to 850°C. The increase of strain rate leads to reduction of alpha phase. The change in volume fraction at this temperature is only 5% in comparison with the lower temperature where the volume fraction of the alpha phase was reduced by almost 20%.



**Figure 6.26: Volume fraction of alpha phase in the centre of the deformed sample at 900°C and strain rates of 50s<sup>-1</sup>, 100s<sup>-1</sup> and 150s<sup>-1</sup>**

The micrographs obtained from the SEM at 950°C are presented below. The compression axis is vertical to the micrographs, as before different magnifications have been used to accurately represent the microstructure morphology.

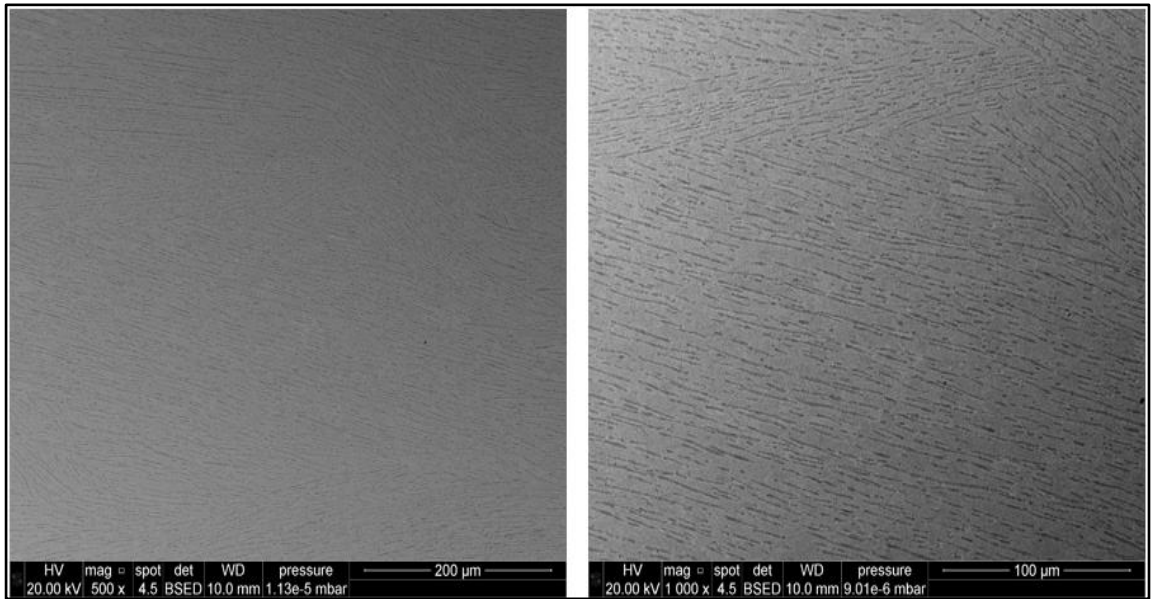


Figure 6.27: SEM micrographs at 950°C and strain rate of 50s<sup>-1</sup> (left 500x and right 1000x)

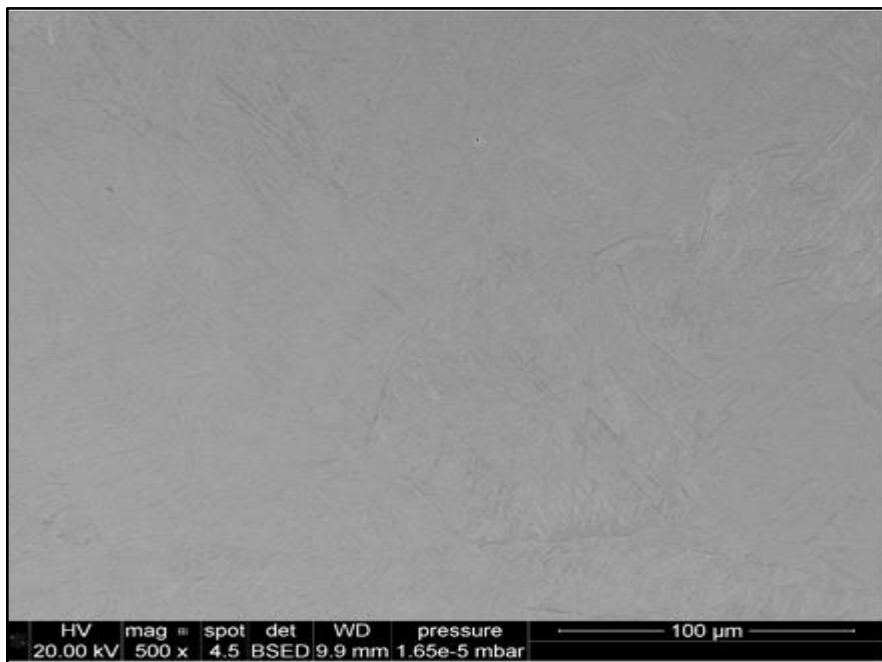


Figure 6.28: SEM micrographs at 950°C and strain rate of 100s<sup>-1</sup> magnification 500x

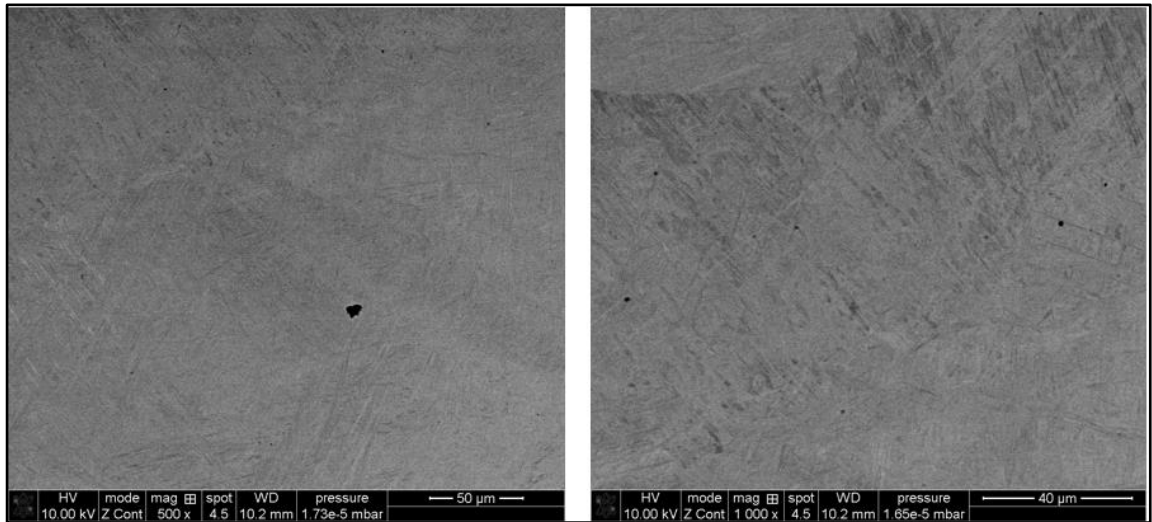


Figure 6.29: SEM micrographs at 950°C and strain rate of 150s<sup>-1</sup> (left 500x and right 1000x)

At 950°C significant changes occur to the microstructure. At 50 s<sup>-1</sup> strain rate the lath structure is almost vertical to the compression axis. Furthermore, the lath thickness is reduced significantly from the lower temperatures. At strain rates above 100 s<sup>-1</sup> the lamellar structure is transformed 100% to martensitic. Significant micro-pores were observed at strain rate of 150 s<sup>-1</sup>. The strain induced pores can be observed in Figure 6.29.

The two microstructures of the Ti-6Al-4V were investigated in terms of instability, efficiency of power dissipation and processing map in the next chapter. The process map for the examined strain rates (0.1s<sup>-1</sup>, 1s<sup>-1</sup>, 10 s<sup>-1</sup>, 50s<sup>-1</sup>, 100 s<sup>-1</sup> and 150 s<sup>-1</sup>) for the equiaxed microstructure, and 50s<sup>-1</sup>, 100 s<sup>-1</sup> and 150 s<sup>-1</sup> for the lamellar microstructure for all temperatures (850°C, 900°C and 950°C) have been constructed.

## 7 Process map and instability

Based on the methodology proposed by Prasad et al. described in section 4.8 the instability map, the efficiency of power dissipation map and the processing map for the two microstructures are presented in this chapter. A large number of maps have been proposed by many researches based on the different characteristics of the initial materials such as grain size, total deformation strain or thermomechanical history [78][169][74][170][171]. A generalised representation of the microstructure mechanisms expected for the Ti-6Al-4V based on the deformation temperature and strain rate for different starting microstructures is presented in Figure 7.1. Two sections are included in this chapter, the first section consists of the analysis for the as-received microstructure (equiaxed) and the second section the lamellar microstructure.

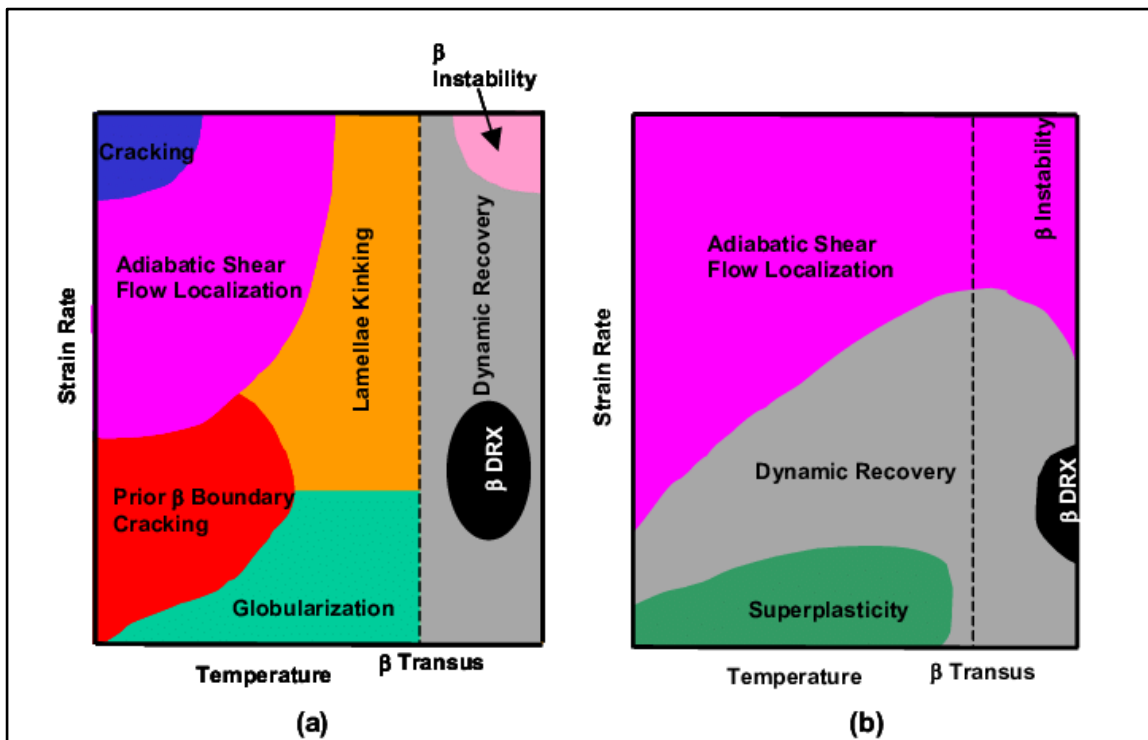


Figure 7.1: Processing maps. Ti-6Al-4V. (a) Starting microstructure: equiaxed  $\alpha + \beta$ . (b) Starting microstructure: lamellar  $\alpha + \beta$ [172].

### 7.1 Processing map As-received (equiaxed) microstructure

The analysis for the processing map is based on the results from 0.5 true strain. The values of the stress for each temperature and strain rate are presented at Table 7.1 and, the efficiency of power dissipation map, the instability map and the processing map at Figure 7.2, respectively.

Table 7.1: Flow stress of the isothermally compressed Ti-6Al-4V with equiaxed microstructure at 0.5 true strain.

True Strain	Strain rate ( $s^{-1}$ )	Temperature( $^{\circ}C$ )		
		850	900	950
0.5	0.1	138.2	87.1	47.0
	1	204.6	138.8	76.7
	10	247.4	199.8	121.8
	50	339.1	272.4	170.4
	100	295.6	244.5	171.5
	150	320.4	225.8	157.8

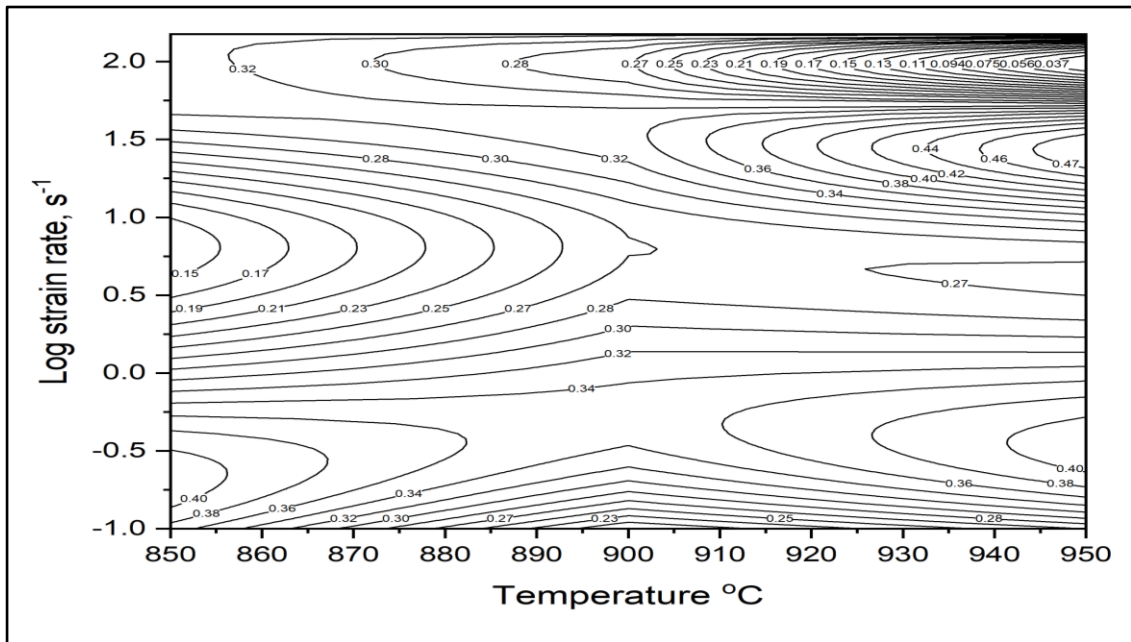


Figure 7.2: Power dissipation efficiency ( $\eta$ ) contour map, as-received microstructure at 0.5 strain

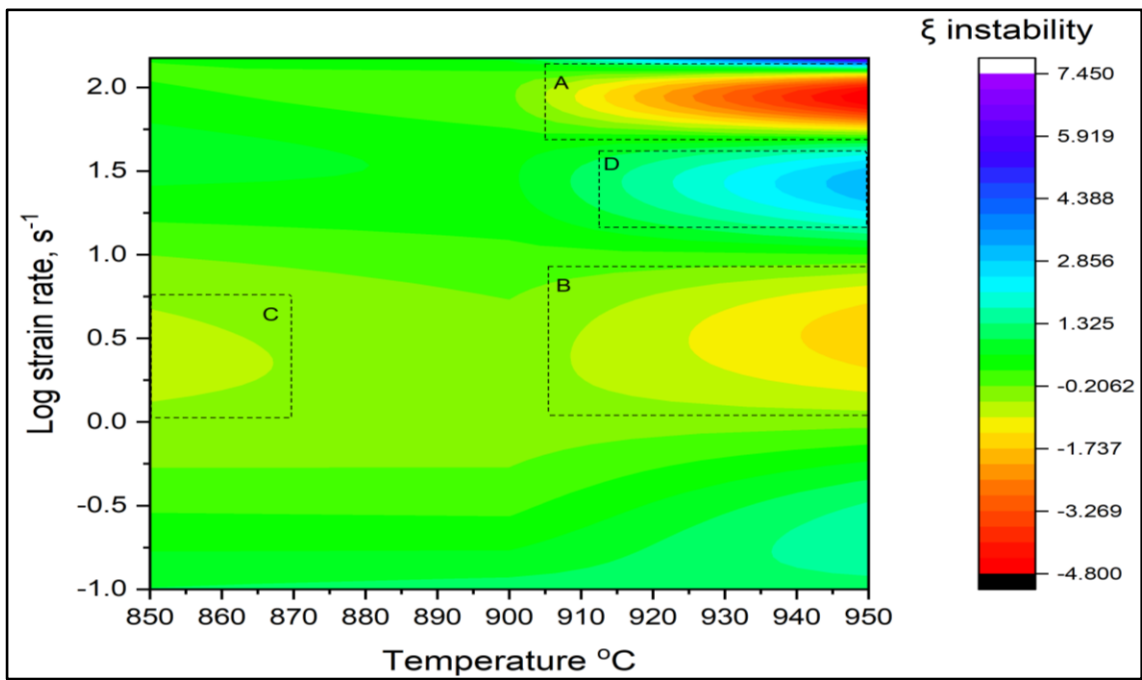


Figure 7.3: Instability ( $\xi$ ) map as-received microstructure at 0.5 strain, A, B, C instability regions and D stable region.

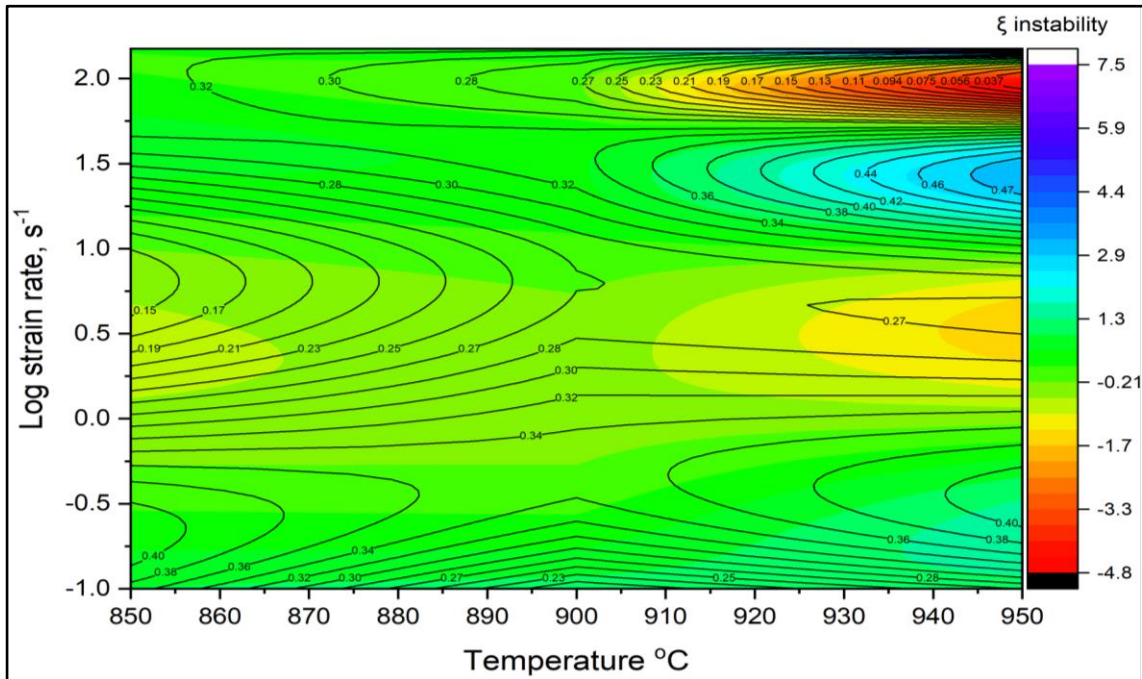


Figure 7.4: Processing map for Ti-6Al-4V as-received microstructure, contour lines represent Power dissipation efficiency ( $\eta$ ) and coloured area the instability ( $\xi$ ).

The power dissipation efficiency  $\eta$  is relevant to the material dynamic softening that operated in a given regime of temperature and strain rate [173]. When the range of the  $\eta$  value between 0.1 and 0.3 then DRV occurs, when the value is between 0.35 – 0.55 then DRX takes place and values above 0.60 indicate a superplastic deformation process since the strain rate sensitivities associated with this efficiency range are about 0.4–0.5 [62][80][174].

From the Figure 7.2 is clear that the value of  $\eta$  is temperature and strain rate sensitive. As the temperature increases at the same strain rate the  $\eta$  value decreased. The same can be observed also for the effect of the strain rate. Three regions are between 0.35 and 0.55, for strain rate of  $0.1\text{s}^{-1}$  and temperature between  $850^{\circ}\text{C}$ - $870^{\circ}\text{C}$  and  $910^{\circ}\text{C}$ - $950^{\circ}\text{C}$  and for strain rate of  $50\text{s}^{-1}$  and temperature between  $910^{\circ}\text{C}$ - $950^{\circ}\text{C}$ . These three regions indicate DRX as the main microstructure evolution mechanism and in the rest of the area DRV takes place. The DRX at high strain rate can be attributed to the fact that the combination of strain rate and strain provide sufficient time and energy for dynamic softening.

The variation of the flow instability parameter at different deformation temperatures and strain rates is shown in Figure 7.3. Three instability areas were identified A, B and C and one very stable area D. The unstable area C is at low strain rates between  $1\text{s}^{-1}$  and  $10\text{s}^{-1}$  and temperature from  $850^{\circ}\text{C}$  to  $870^{\circ}\text{C}$ . At the same strain rates but at higher temperatures we can locate the unstable area B for temperatures between  $910^{\circ}\text{C}$  - $950^{\circ}\text{C}$ . At very high strain rates ( $90\text{s}^{-1}$ - $150\text{s}^{-1}$ ) and temperatures ranging between  $910^{\circ}\text{C}$  and  $950^{\circ}\text{C}$  the flow instability area A can be observed.

For the processing map (see Figure 7.4) stable areas for forming and forging can be identified. For strain rates under  $1\text{s}^{-1}$  and for all temperatures, as well as for strain rates above  $10\text{s}^{-1}$  and for temperatures between  $850^{\circ}\text{C}$  and  $900^{\circ}\text{C}$ . Another

stable area can be found at strain rate of  $30\text{s}^{-1}$  and temperatures from  $910^{\circ}\text{C}$  to  $950^{\circ}\text{C}$ .

### 7.2 Processing map lamellar microstructure

In this section the efficiency of power dissipation map, the instability map and the processing map for the lamellar microstructure at 0.5 of strain are presented at Figure 7.5, Figure 7.6 and Figure 7.7 respectively. The values of the stress for each temperature and strain rate is presented in Table 7.2.

Table 7.2: Flow stress of the isothermally compressed Ti-6Al-4V with lamellar microstructure at 0.5 true strain.

True Strain	Strain rate ( $\text{s}^{-1}$ )	Temperature( $^{\circ}\text{C}$ )		
		850	900	950
0.5	50	263.2	235.5	155.8
	100	306.5	245.7	139.4
	150	311.7	271.6	150.6

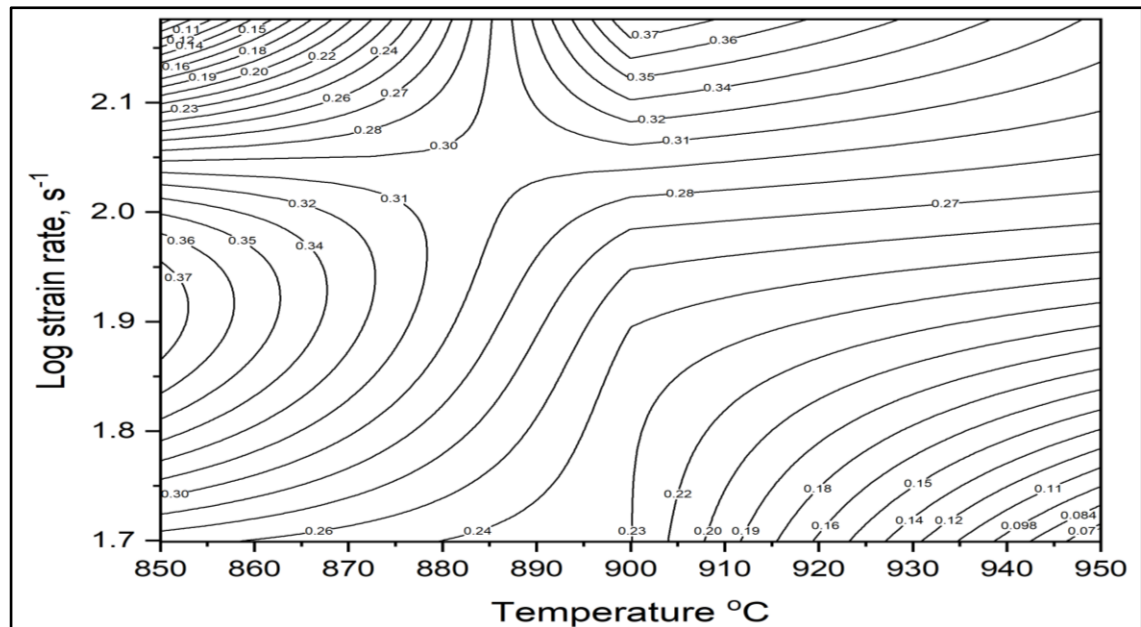


Figure 7.5: Power dissipation efficiency ( $\eta$ ) contour map, lamellar microstructure at 0.5 strain

Process map and instability

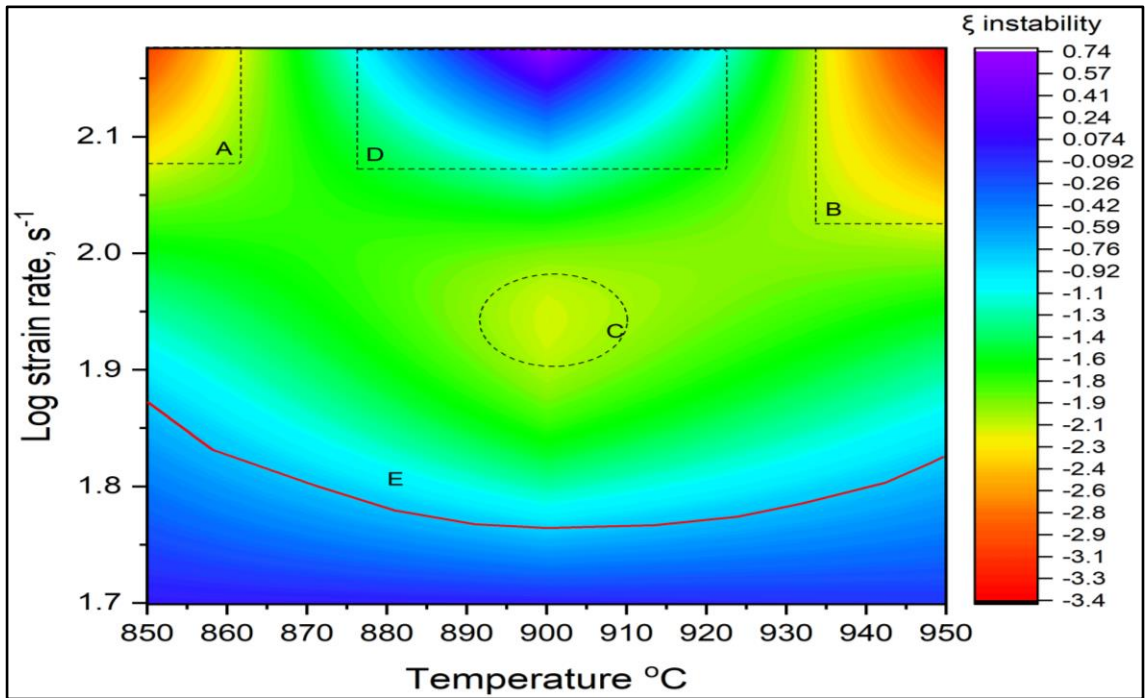


Figure 7.6: Flow instability ( $\xi$ ) map for lamellar microstructure at 0.5 strain; A, B, C are instability regions and D a stable region. The area above E would also tend to instability.

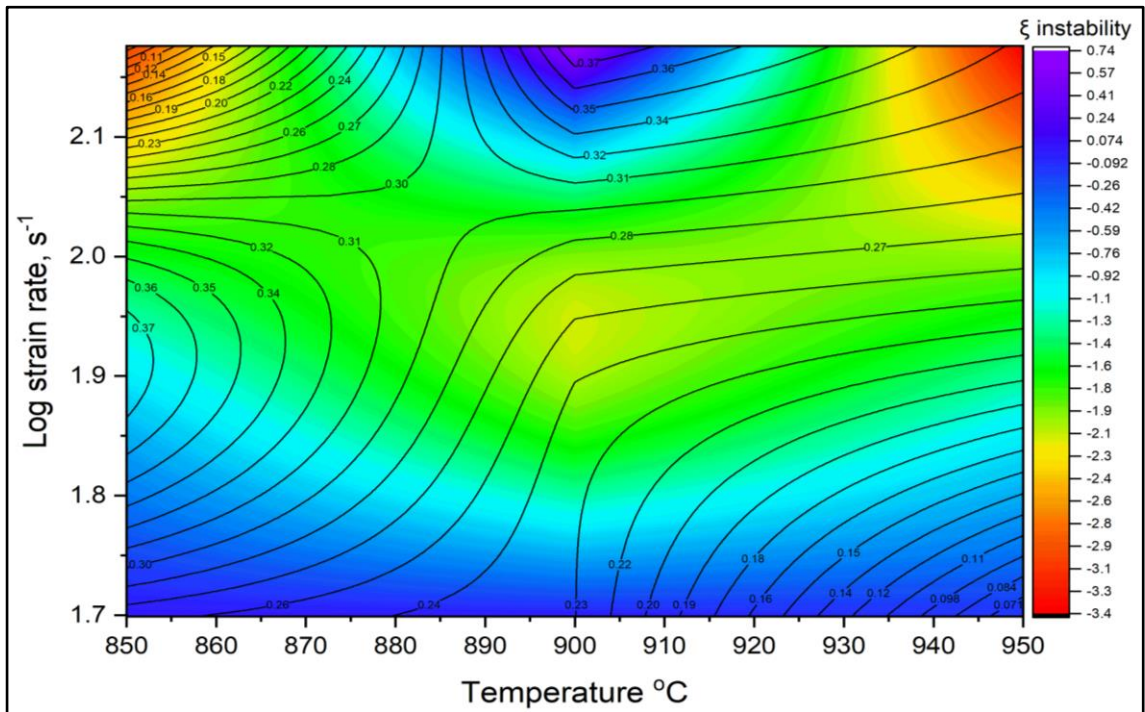


Figure 7.7: Processing map for Ti-6Al-4V lamellar microstructure, contour lines represent Power dissipation efficiency ( $\eta$ ) and coloured area the instability ( $\xi$ ).

From the power dissipation efficiency map (see Figure 7.7) only two regions present DRX as the microstructure evolution mechanism, in contrast to the rest of the map where DRV is the predominant microstructure evolution mechanism. The first area is located at 850°C and strain rate between 70s<sup>-1</sup> and 100s<sup>-1</sup>. Where the second area can be found at much higher strain rate and temperature (150s<sup>-1</sup> and 900°C).

The lamellar microstructure shows high flow instability for all temperatures. The instability area can be observed above the curve (E) with three areas A, B, and C presenting very high  $\xi$  value. The flow instability area for all temperatures (850°C-900°C) can be observed above a strain rate of 65s<sup>-1</sup>. From the flow instability map only one safe area can be identified at high strain rates and is for a temperature of 900°C.

Taking into consideration the power dissipation efficiency map and the flow instability map, the processing map for the Ti-6Al-4V with a lamellar microstructure is presented in Figure 7.7. Two safe areas can be easily identified, at low strain rates below 65s<sup>-1</sup> for all temperatures and at 900°C and 150s<sup>-1</sup>.

## 8 Further Discussion

The process optimization of the Phoenix high strain rate simulator was a significant part of this work. Bespoke equipment was optimized in terms of experimental procedure and noise minimization. The identification of the main parameters influencing any process is very important. From the comparison with the experiment conducted in a Gleeble 3800 (see section 9) the results saw significant similarity making the optimization process successful and adding a level of confidence from the result produced from hot isothermal compression tests with Phoenix high strain rate tester. Strain rate and temperature control are crucial for factors and the variations have been minimized.

As this work is driven by the forging community, the modelling of the flow behaviour is extremely important. The selection of the H&S model was dictated by the industrial partners of the AFRC as it is the most commonly used model for high speed forging. The results show that the model describes well the flow behaviour of both microstructures. For the as-received (equiaxed) microstructure at high temperatures and high strain rates the confidence level is reduced which may occur due to the dynamic phenomenon in the elastic region of the flow curve. Similar but not so intense reduction was noted for the lamellar microstructure. In general the model presents an 80% confidence level describing the flow behaviour.

The trend of the H&S parameters correlated with the flow stress obtained from the flow curves at 0.5 true strain for strain rates above  $50\text{s}^{-1}$  to  $150\text{s}^{-1}$  can be summarised in Table 8.1. For the  $m_1$  parameter, which is related to the effect of temperature, for the equiaxed microstructure at low temperature ( $850^\circ\text{C}$ ) the increase of the strain rate has as a result the increase of the flow stress. As the temperature increases the flow stress decreases with the increase strain rate. That it can be connected with the DRV softening (see Figure 7.4) and the increase

of the volume fraction of the  $\beta$  phase (see Figure 5.35, Figure 5.39, Figure 5.43) similar results were reported in the literature [175]. For the lamellar microstructure the  $m_1$  parameter presents the same trend as for the globular microstructure. The explanation for this can be also the DRV softening through the change of the  $\beta$  volume fraction (see Figure 6.22, Figure 6.26).

The  $m_3$  parameter of the equation is related to the strain rate effect. For both microstructures the values increased with the increase of the strain rate for all temperatures indicating that the strain rate have a profound effect on the flow stress. That can be verified also from the flow curves (see Figure 5.16, Figure 5.17, Figure 5.18, Figure 6.3, Figure 6.4 and Figure 6.5) and the strain rate sensitivity values (see Figure 5.29 and Figure 6.16).

**Table 8.1: Tendency of the H&S parameters values obtained from the flow curves modelling, correlation with the flow stress at 0.5 of true strain.**

		A	$m_1$	$m_2$	$m_3$	$m_4$
Equiaxed	850	↓	↑	↓	↑	↓
	900	↓	↓	↓	↑	↓
	950	↓	↓	↔	↑	↓
Lamellar	850	↑	↑	↓	↑	↓
	900	↑	↓	↓	↑	↓
	950	↓	↓	↓	↑	↓

The strain rate effect on the as-received microstructure becomes stronger at higher strain rates; above  $100\text{s}^{-1}$  the as-received microstructure showed a significant increase of the volume fraction of the beta-phase. At strain rates up to  $100\text{s}^{-1}$  the volume fraction of beta phase was increased. It can be concluded that there is more time for diffusion-controlled processes to take place at strain rates below  $100\text{s}^{-1}$ , which has as a result a greater dissolution of the alpha phase to the beta matrix [176]. The strain softening rate of Ti-6Al-4V significantly varies, suggesting that the beta-phase volume fraction does affect the strain softening

rate of this alloy. The strain rate sensitivity values are below the value of 0.3 which indicates that the deformation is controlled by dislocation glide has been reported by Semiatin [142].

For the equiaxed microstructure the process map was presented in section 7.1. Three instabilities have been identified, at 850°C for strain rate  $10\text{s}^{-1}$  and at 950°C for strain rates  $10\text{s}^{-1}$  and  $100\text{s}^{-1}$ . From microstructure observations (see Appendix E and F as well Figure 5.41) the instabilities in this areas are verified. At 850°C for strain rate  $10\text{s}^{-1}$  as well as the other locations the instability can be unidentified as adiabatic shear banding, these flow localization bands formed at an angle of about  $45^\circ$  to the compression axis, similar results have been reported in the literature for the same region from Seshacharyulu et al. [49].

The processing map of the lamellar microstructure have mainly revealed instability areas for strain rate above  $70\text{s}^{-1}$ . For the lower temperature (850°C) the microstructure observations have shown an instability in the form of buckling for all temperatures in contrast with the process map that strain rate of  $50\text{s}^{-1}$  is safe (see Figure 6.5). The microstructures exhibited kinking of lamellae. Micrograph of a specimen deformed at 850°C and  $50\text{s}^{-1}$ ,  $100\text{s}^{-1}$  and  $150\text{s}^{-1}$  are presented in section 6.5 in which coordinated arrays of primary kinking can be observed. It is likely that kinking is simply due to mechanical instability (e.g. buckling) of the lamellae under compressive strains and can form in the colonies inclined up to  $45^\circ$  to the compression axis. Similar behaviour have been reported in the literature for lower strain rates but higher temperatures [62].

At 950°C micro-cracking has been observed at  $150\text{s}^{-1}$ . The mechanism of cracking may be rationalized by considering the differences in the deformation behaviour of individual constituents of the microstructure. The structure consists of three micro constituents: lamellar  $\alpha+\beta$  colonies, grain boundary  $\alpha$  layer, and  $\alpha$  thin  $\beta$  layer in between the colony side-plates and grain boundary  $\alpha$ . Among these three, the colonies have the highest strength due to specific crystallographic

orientation (Burgers) relationships, while the  $\beta$  layer is inherently soft at the deformation temperature. During uniaxial compression at elevated temperatures, prior  $\beta$  boundaries oriented at  $\approx 45^\circ$  with respect to the compression axis will slide under a resolved shear stress, due to which stress concentrations develop at the triple junctions/boundaries[62].

The strain rate also effects the lamellar microstructure, the strain rate sensitivity values for this microstructure is below 0.3, indicating the same deformation mechanism, i.e. deformation by dislocation glide[142]. For the lamellar microstructure the strain rate effect is stronger as demonstrated in Figure 6.15, in comparison with the as received microstructure. Also the volume fraction of the alpha laths is reduced significantly with the increased strain rate, showing significant dependence of the microstructure to the strain rate.

The deformation temperature is another factor influenced the flow stress and the microstructure. In Figure 5.30 and Figure 6.17 documented the effect of temperature on flow stress for the as received and lamellar microstructure respectively. For both microstructures the effect is strong, with the increased temperature the flow stress is almost linear decreased. Furthermore, the deformation temperature have also significant influence on the microstructure. Below the  $\beta$  transus, the deformation is a thermal activated process, and the rise of the adiabatic temperature has a significant effect on the volume fraction of the beta-phase. The volume fraction of beta phase is increased with increased deformation temperature for both the microstructures.

At a temperature of  $950^\circ\text{C}$  and strain rates above  $100\text{s}^{-1}$  the lamellar microstructure is transformed to 100% martensitic. This indicates significant rise of the adiabatic heating which may take the actual temperature of the test above the beta transus.

Comparing the two microstructures in terms of processing window, the equiaxed microstructure at high strain rates shows more stable behaviour. The safe

processing window for the equiaxed microstructure is extended from 850°C to 900°C and from strain rates above 10s<sup>-1</sup>. Furthermore, at 950°C and strain rate of 50s<sup>-1</sup> a safe processing region can be identified. In contrast, the lamellar microstructure shows extensive instability for a wide range of strain rates (above 70s<sup>-1</sup>) for all temperatures. From microstructure observations (see Figure 6.19, Figure 6.20 and Figure 6.21) the instability is extended even in the stable areas suggested by the processing map.

In the next chapter is presented the conclusions from this research project for all the individual challenges addressed in this work.

## **9 CASE STUDY: Comparison Phoenix high strain rate tester with Gleeble 3800**

Another way to verify the results from Phoenix high strain rate tester is to compare the experimental results with an established equipment capable for similar strain rates. The Gleeble 3800 is one of the few testing machines capable for achieving similar strain rates at elevated temperatures. For that reason a number of hot isothermal compression tests have conducted and compared between the two pieces of equipment. Because of the limitations of the Gleeble 3800, two temperatures (900°C and 950°C) and two strain rates have been compared ( $50\text{s}^{-1}$  and  $100\text{s}^{-1}$ ). The results of the hot isothermal compression test are presented in Figure 9.1 and Figure 9.2.

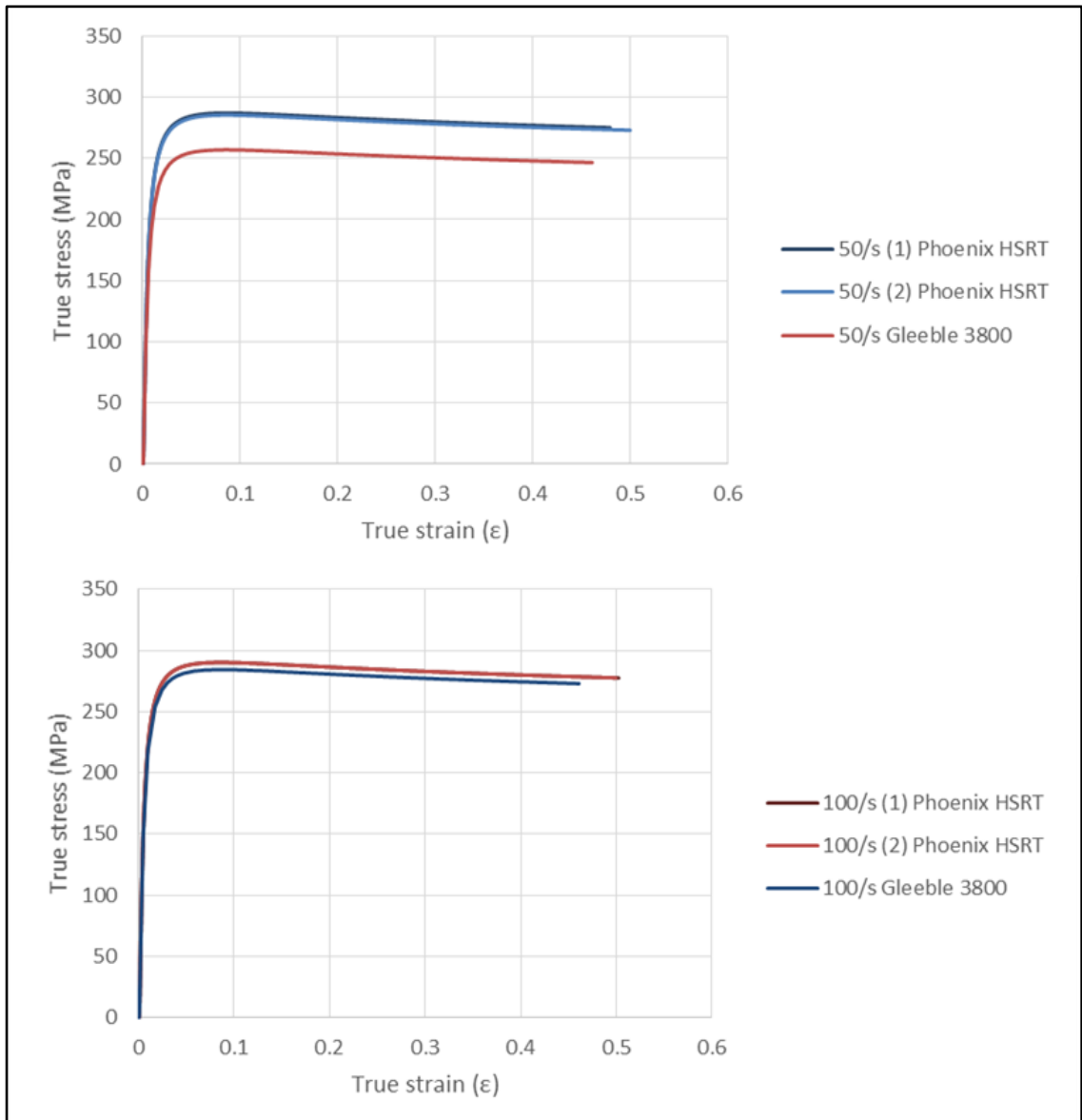


Figure 9.1: A comparisons between Phoenix and Gleeble 3800 at 900°C and strain rates of 50s<sup>-1</sup> and 100s<sup>-1</sup>

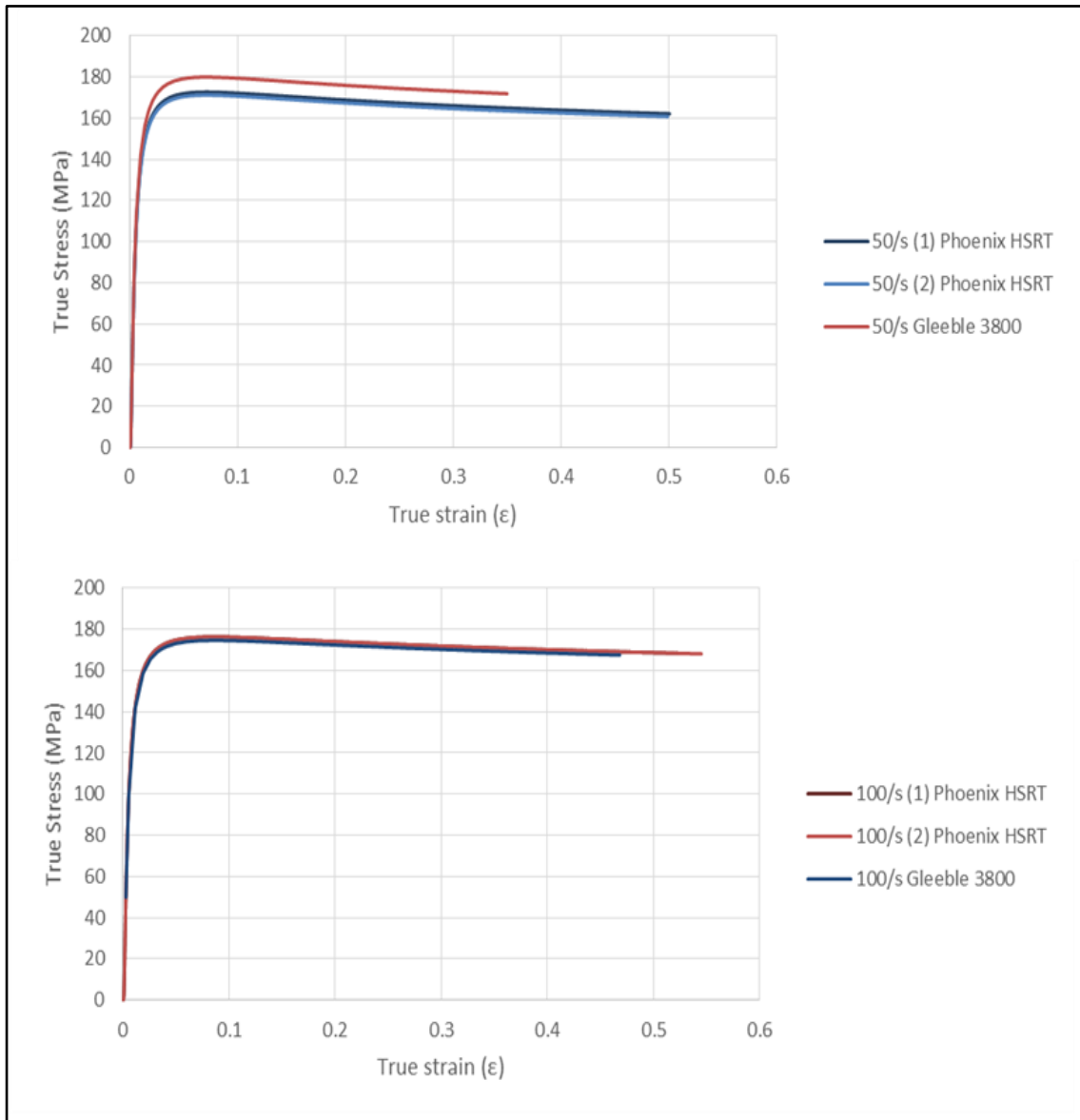


Figure 9.2: A comparisons between Phoenix and Gleeble 3800 at 950°C and strain rates of 50s<sup>-1</sup> and 100s<sup>-1</sup>

It can be seen that the Hansel-Spittle fitting of the flow stress curves generated from both compression test machines for the Ti-6AL-4V material tested at 100s<sup>-1</sup> practically overlap. This finding is encouraging given the level of intermediate processing involved. However, the coincidence of the two sets of tests held across

a reasonable range of temperatures and strain rates gives some level of confidence in the results generated. There is however, less commonality between both machines at the lower strain rate of  $50\text{s}^{-1}$ . This could be due to the fact that the strain rate range at  $100\text{s}^{-1}$  is a domain in which stress wave-propagation is more relevant and cannot be easily accounted for, making it one of the most difficult areas of study due to the great care that must be exercised in interpreting the data due to the coupling between impact-induced wave-propagation and machine vibrations. It is the authors opinion that 3 factors can potentially result in the fluctuations in the generated flow stress curves; (1) Impact induced, inelastic wave-propagation (2) Load cell ringing, as a result of machine vibration that can be mitigated by the use of a piezoelectric load cell (3) Strain rate control of a hydraulic system (i.e. tuning the PID to mitigate waves in the applied strain rate). All three of these factors can be more or less closely coupled and result in waves appearing in the measured flow stress curves.

In the case of the Phoenix HSR forge simulator results the tests performed at  $50\text{ s}^{-1}$  displayed the highest amplitude “waves” in the respective flow stress curves. It could be assumed that as a piezoelectric load cell is used to mitigate the effect of load cell ringing from machine vibration and that the PID settings have been optimised to result in the best possible control of the hydraulic strain rate, that this is an effect of inelastic, impact induced wave-propagation. Additionally, as this is the slowest of the strain rates it could be expected that more inelastic waves will be observed providing/assuming the frequency of the inelastic wave generated is

primarily a function of the load train geometry and properties at the test temperature together with the material properties. The Gleeble 3800 results required a lot of smoothing where operator judgment was required to determine the best curve fitting. This may account for why the Gleeble 3800 results at 950°C show the 50s<sup>-1</sup> flow stress curve to have a marginally higher flow stress than the results from the 100s<sup>-1</sup> test. From these results it can be determined that the Phoenix HSR forge simulator's piezoelectric load cell enables easier interpretation of wave-propagation on the flow stress by mitigating a potentially contributing variable. However, it must be considered that a piezoelectric load cell does not completely eliminate the effect of wave-propagation by load cell ringing and it may be that the frequency of the dynamic stress waves associated with the 50s<sup>-1</sup> tests happen to correlate with the natural frequency of the cell and hence a stronger effect is observed. This would be as a result of a combination of factors e.g. temperature, material and strain rate in addition to the dynamics of the cell.

The next chapter included the project methodology used for this research, the machine selection, the mechanical testing, the mechanical and microstructure analysis are described.

## 10 Summary

One of the aims of the research project was to address the challenges of a new bespoke high strain rate forging simulation machine and to test the capabilities and optimise the experimental procedure. Even though, the process optimisation is a challenging and time consuming process, finally the process optimisation of the forming simulation machine has been achieved in terms of temperature control to conform to existing standards, and strain rate stability. This work created an experimental procedure adopted and used by the AFRC for high strain rate compression tests. Additionally, the results of the bespoke equipment were verified through comparison experiments and proved reliable.

Furthermore, through the project a methodology based on the H&S model has been created for the analysis of the flow behaviour at elevated temperatures. The analysis was driven by the needs of the forging industry. As a result of this project the H&S modelling of the high strain rate curves have been evaluated through experimental methods and proved to describe adequately the flow behaviour of Ti-6Al-4V at isothermal high strain rate deformation.

The flow behaviour of the equiaxed microstructure was investigated in terms of strain rate sensitivity, temperature sensitivity and general flow behaviour. The results used for the creation of a processing map. Based on microstructure observations the processing map were validated, safe and unstable regions were identified as well as the instability mechanism. The equiaxed microstructure demonstrates better stability than the lamellar microstructure offering a safe forming region from 850°C to 900°C and strain rates above  $10\text{s}^{-1}$ , along with 950°C and strain rate of  $50\text{s}^{-1}$ . Main instability observed in the equiaxed microstructure is adiabatic shear banding and flow localisation.

In addition to the equiaxed microstructure, a lamellar microstructure was also investigated in this research. The flow behaviour, the strain rate sensitivity and

microstructure observations were used to identify a safe process window. The lamellar microstructure demonstrates more unstable behaviour in comparison with the equiaxed microstructure. Even though, the processing map demonstrates safe regions for strain rates below  $70\text{s}^{-1}$ , the microstructure observations revealed significant instabilities for all temperatures and strain rates with one exemption at  $900^\circ\text{C}$  and a strain rate of  $100\text{s}^{-1}$  where the microstructure had totally transformed to martensitic. The main mechanism of instability is likely buckling of the lamellae under compressive strains and can form in the colonies inclined up to  $45^\circ$  to the compression axis. At high temperature ( $950^\circ\text{C}$ ) and strain rates (above  $100\text{s}^{-1}$ ) micro cracking was observed as the instability mechanism.

For both microstructures DRV softening is the predominant microstructure evolution mechanism through the change of the  $\beta$  volume fraction. The volume fraction for both microstructures increases with strain rate and temperature.

### 10.1 Further work

The capabilities of the Phoenix high strain rate simulator must be investigated further. The author believe that the multistep deformation factor must be further investigated. The result from such an experimental investigation will be very useful for the forming and forging industry as a significant number of industrially forged parts use multi-step forging. Furthermore such data will be incredibly interesting for the simulation and optimisation of manufacturing processes.

The investigation at higher strain rates (above  $150\text{s}^{-1}$ ) will be attractive. Up to this point a significant gap of experimental data exist at the range of  $10\text{s}^{-1}$  to  $300\text{s}^{-1}$ . Data at this region will be very valuable to the process optimisation of high speed forging.

The author also believes that the validation of the experimental data obtained from this work through real parts will be very interesting. The comparison between real

size forging part and small experimental samples will be very interesting to reveal correlations and differences.

Finally, the process modelling based on the mechanical results obtained through this work combined with microstructure modelling will be a very fascinating future work to reveal the full scale interaction at high strain rates.

## 10.2 Industrial benefits

The research presented in the thesis can have a significant impact in the manufacturing community, especial at forging of aerospace components. The climate change demands less CO<sub>2</sub> emission from manufacturing and at the same time better final products at better prices.

The high speed forming and forging of such components may be the answer at during this challenging years. The instability maps presented in this thesis can be used as a reference and can further evaluated to increase the deformation speed, and reduce the energy spend during manufacturing.

Furthermore, through the thesis the engineer community can be benefit by understanding that high strain rate deformation data are available and doesn't need to extrapolate the data for simulations. That will benefit the future of manufacturing by simulating the processes more accurate.

## Appendix A – Temperature distribution experimental photos

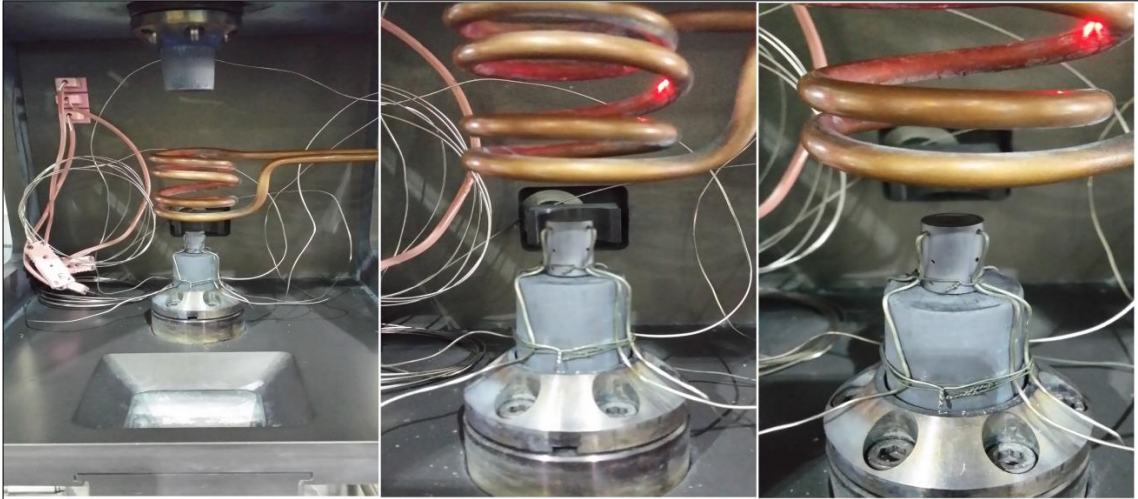


Figure A.1: Experimental set up of temperature distribution monitoring



Figure A.2: Phoenix machine during heating

## Appendix B – Compression test photos

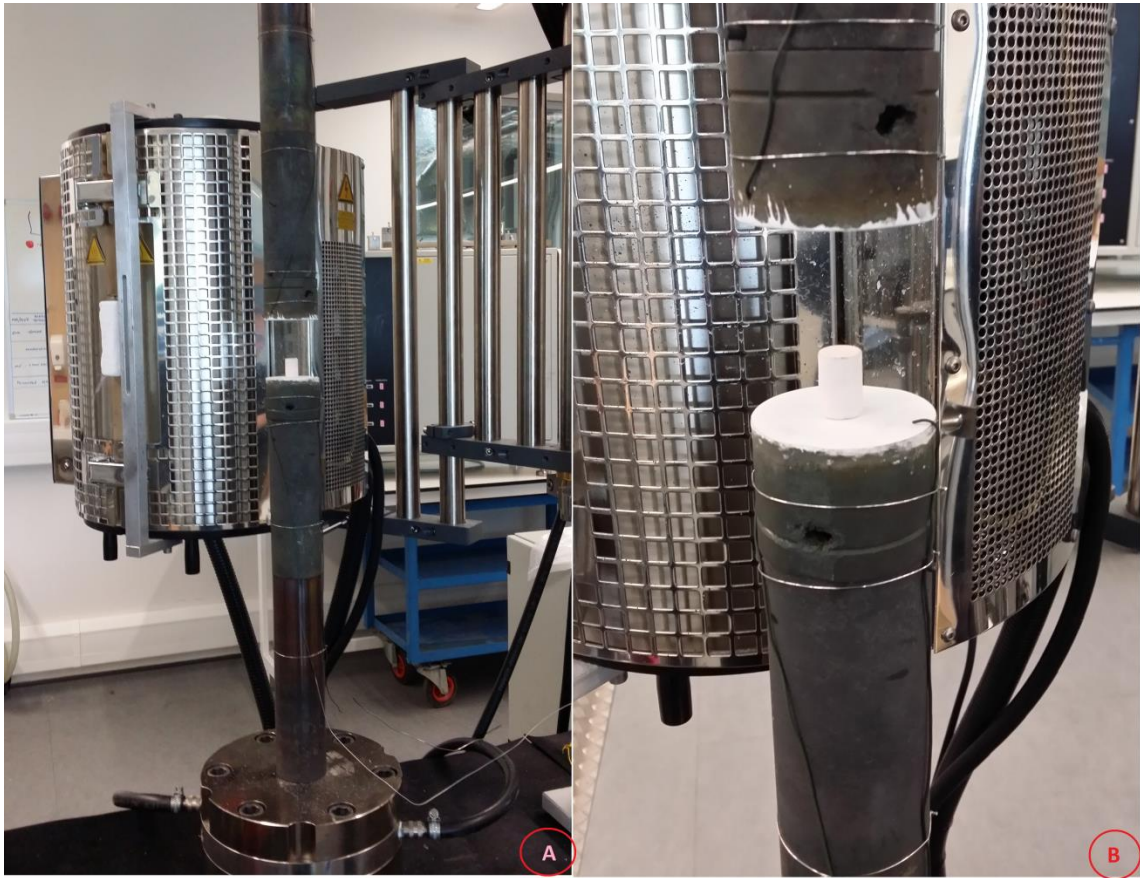


Figure B.1: A) Sample position before insert in the furnace B) Sample position on the bottom die of HA250

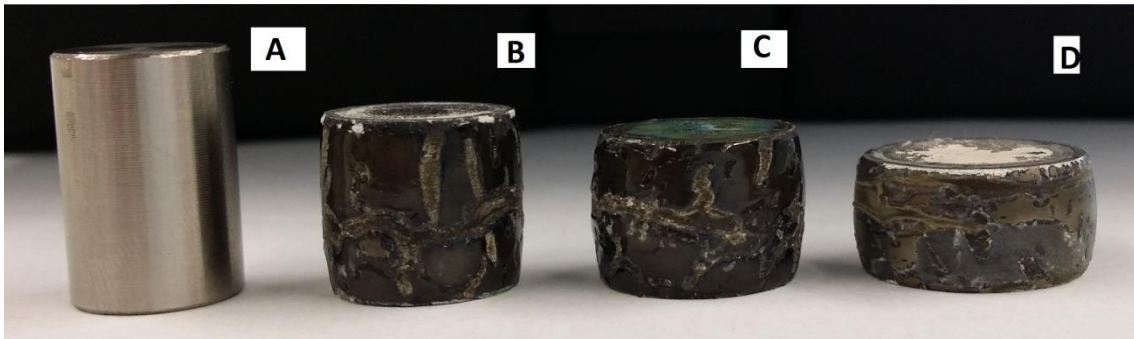
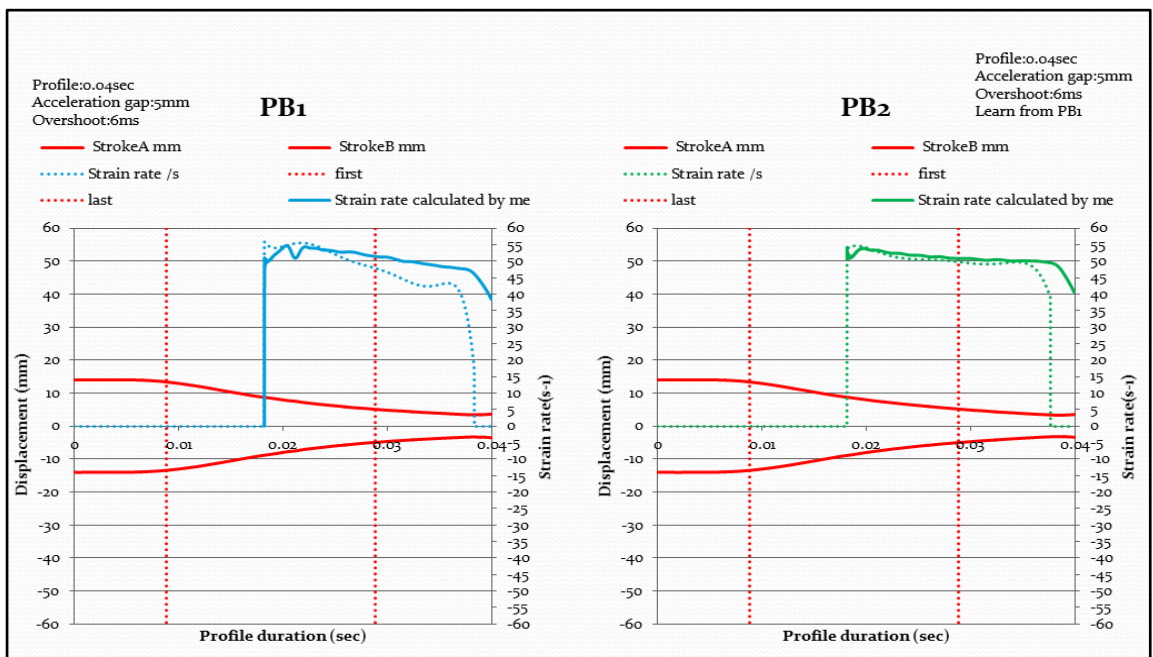
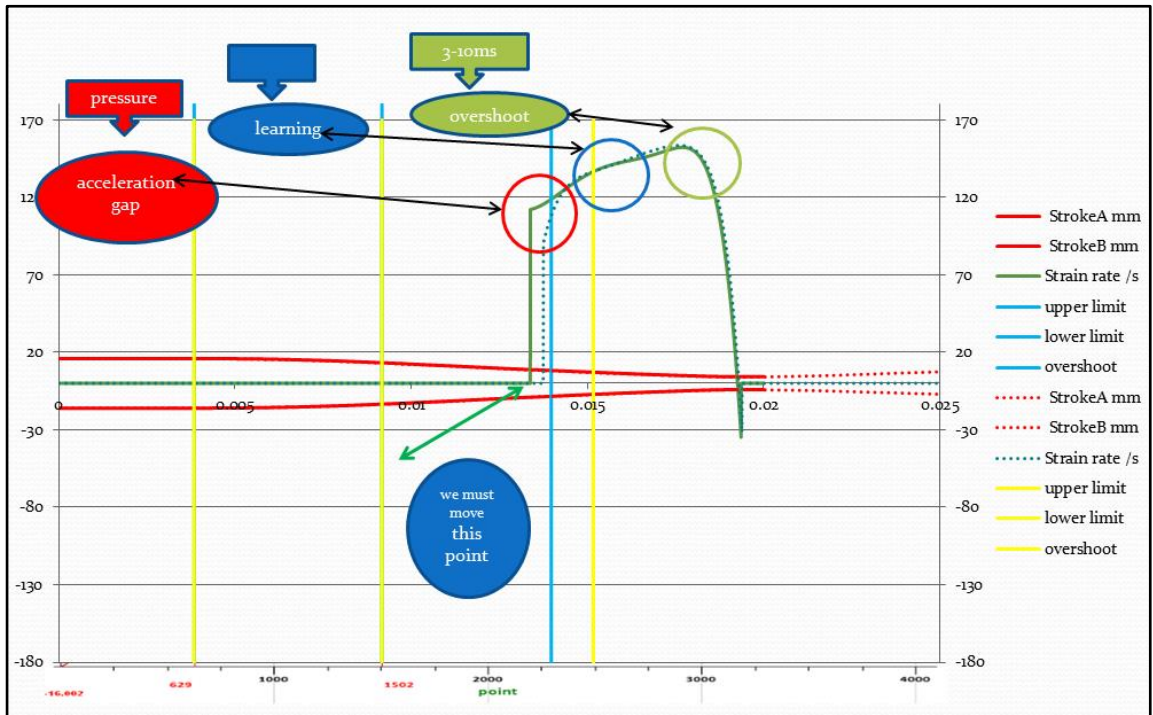


Figure B.2: Sample A) initial dimensions, B) 25% compressed, C) 40% compressed, D) 55% compressed

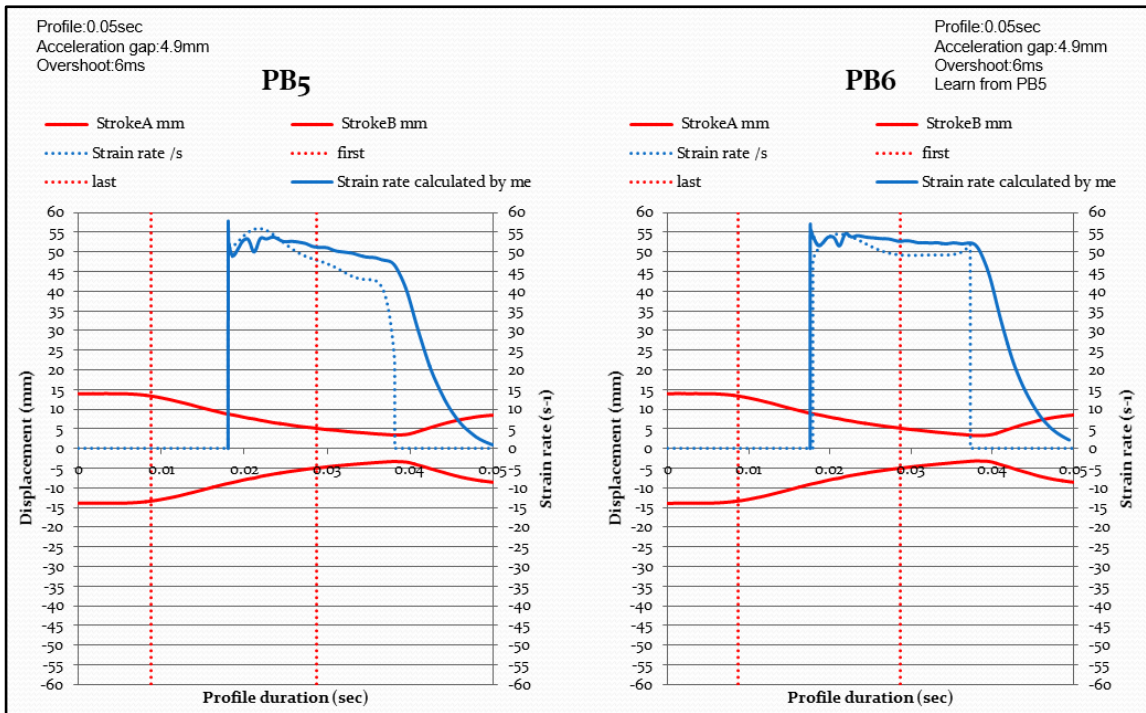
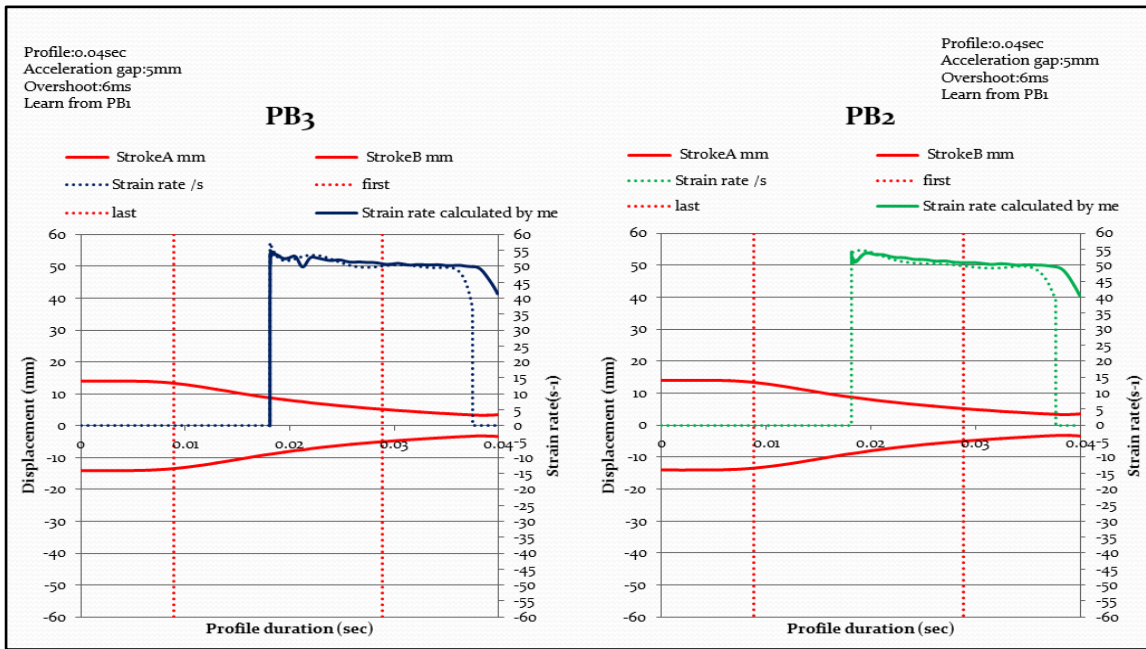


Figure B.3: Sample during heating inside Phoenix tester before compression

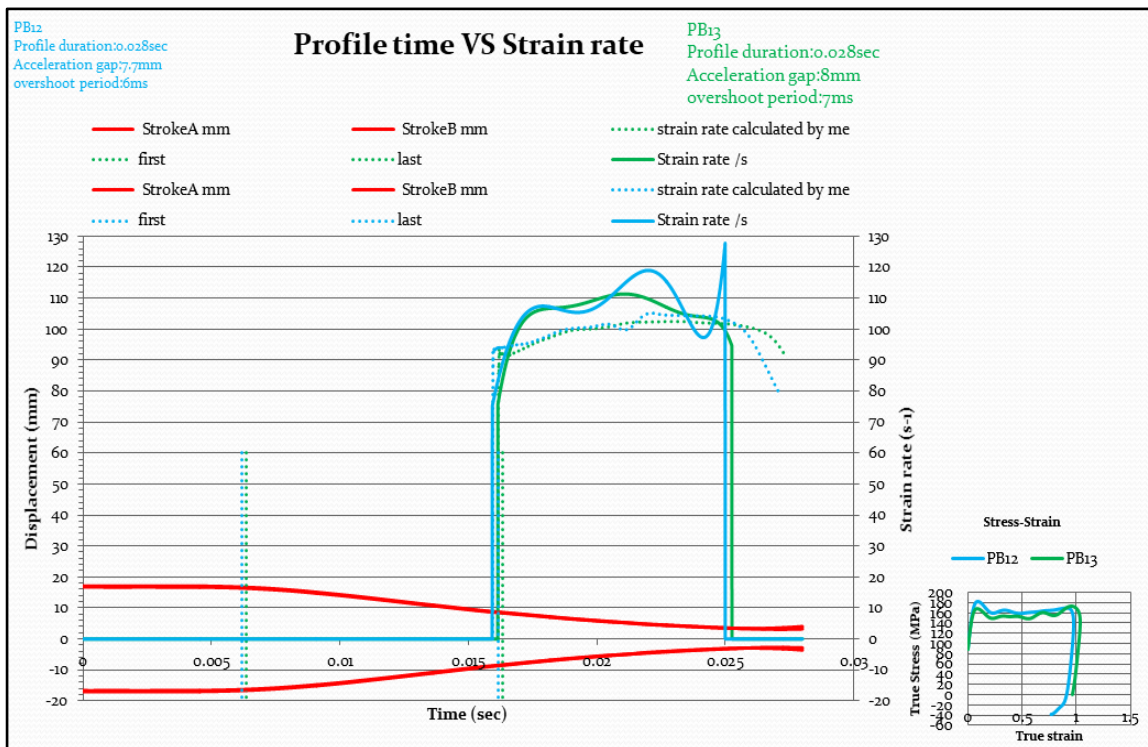
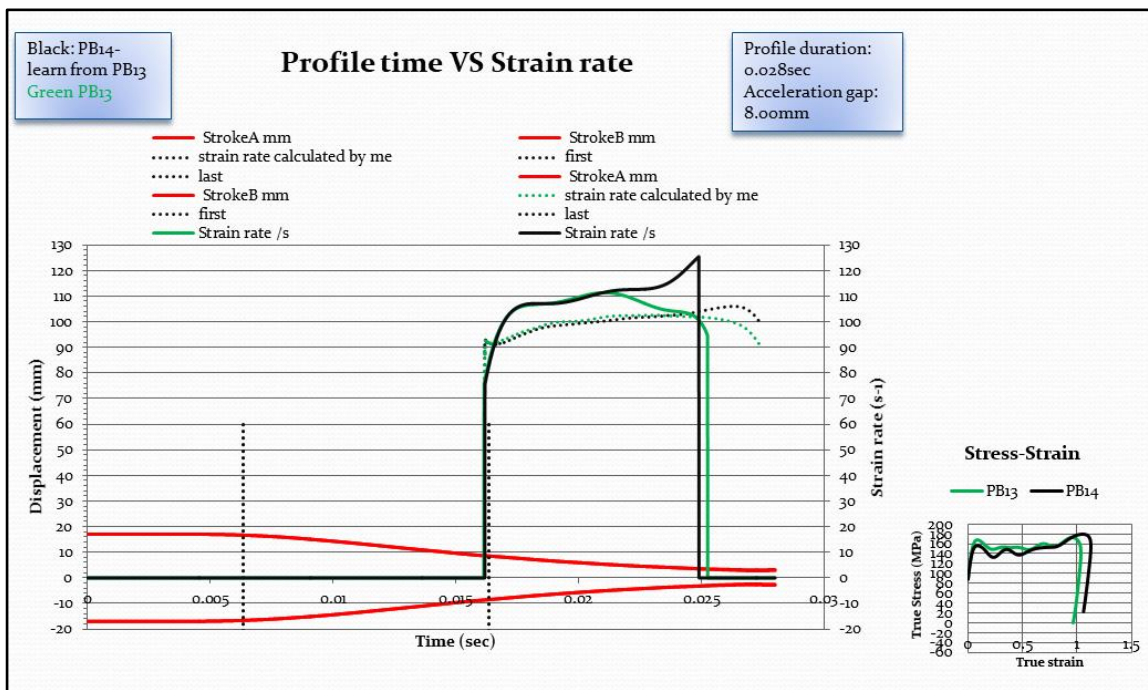
# Appendix C – Strain rate optimization



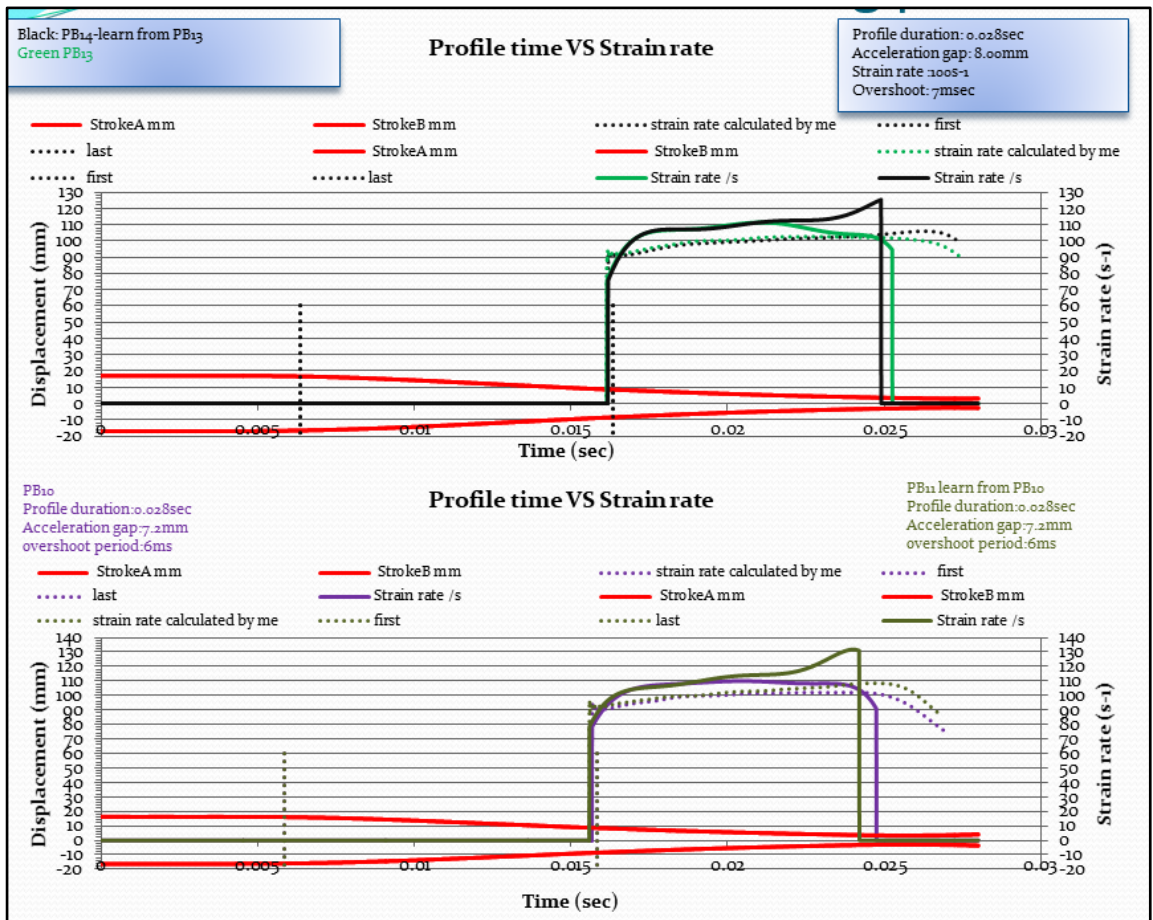
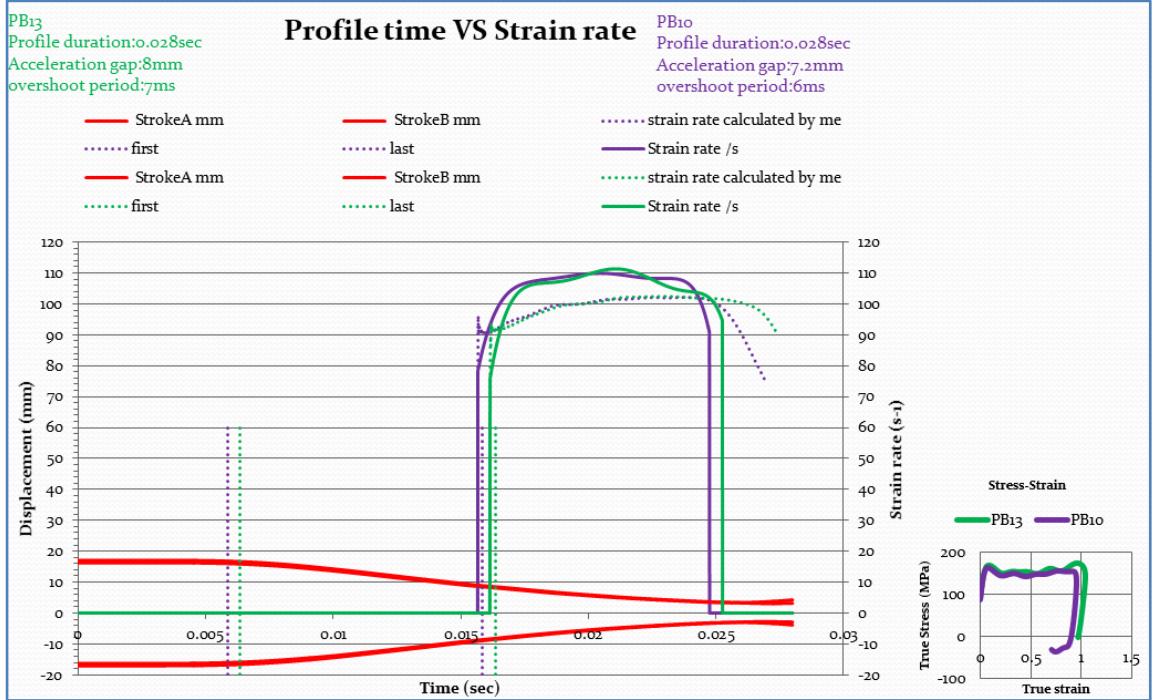
## Appendix C – Strain rate optimization



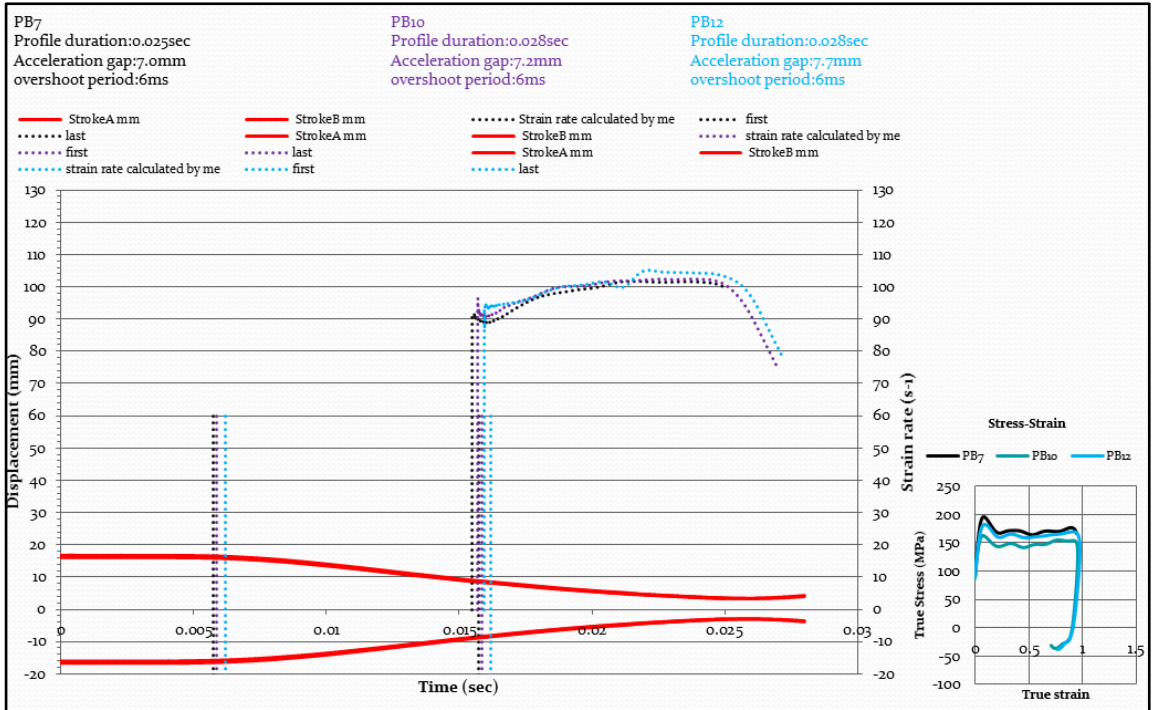
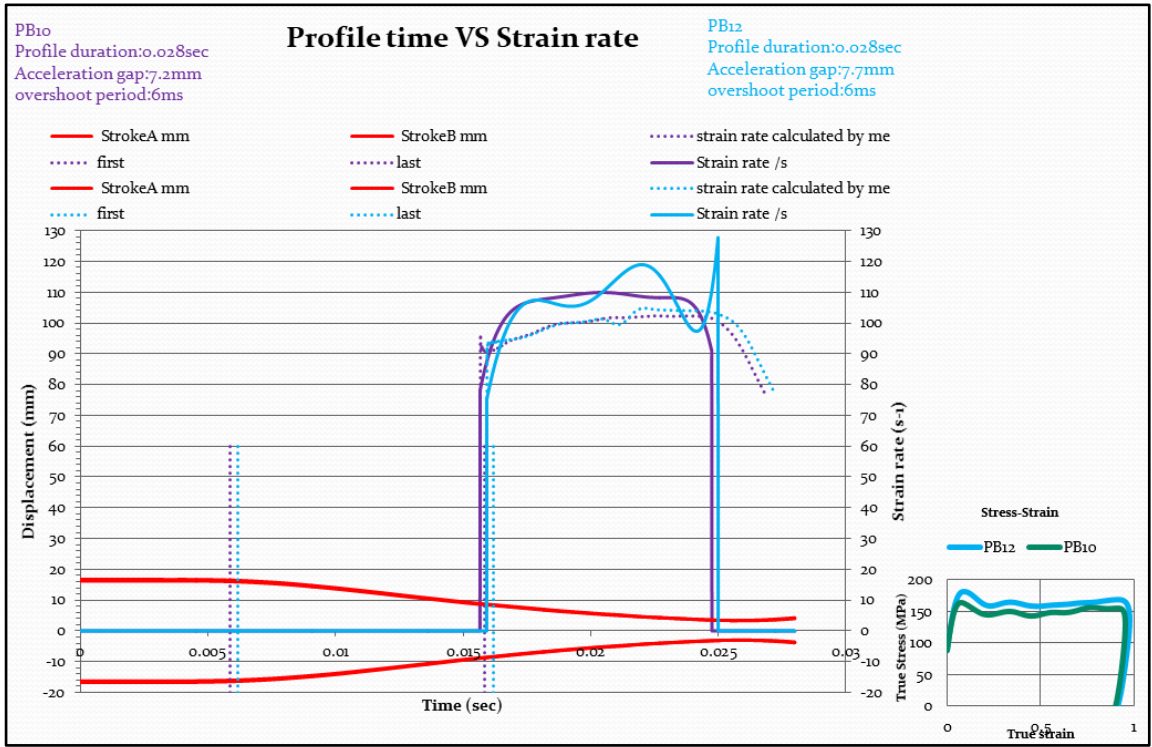
Appendix C – Strain rate optimization



Appendix C – Strain rate optimization



Appendix C – Strain rate optimization



# Appendix D – True stress vs. True Strain Curves

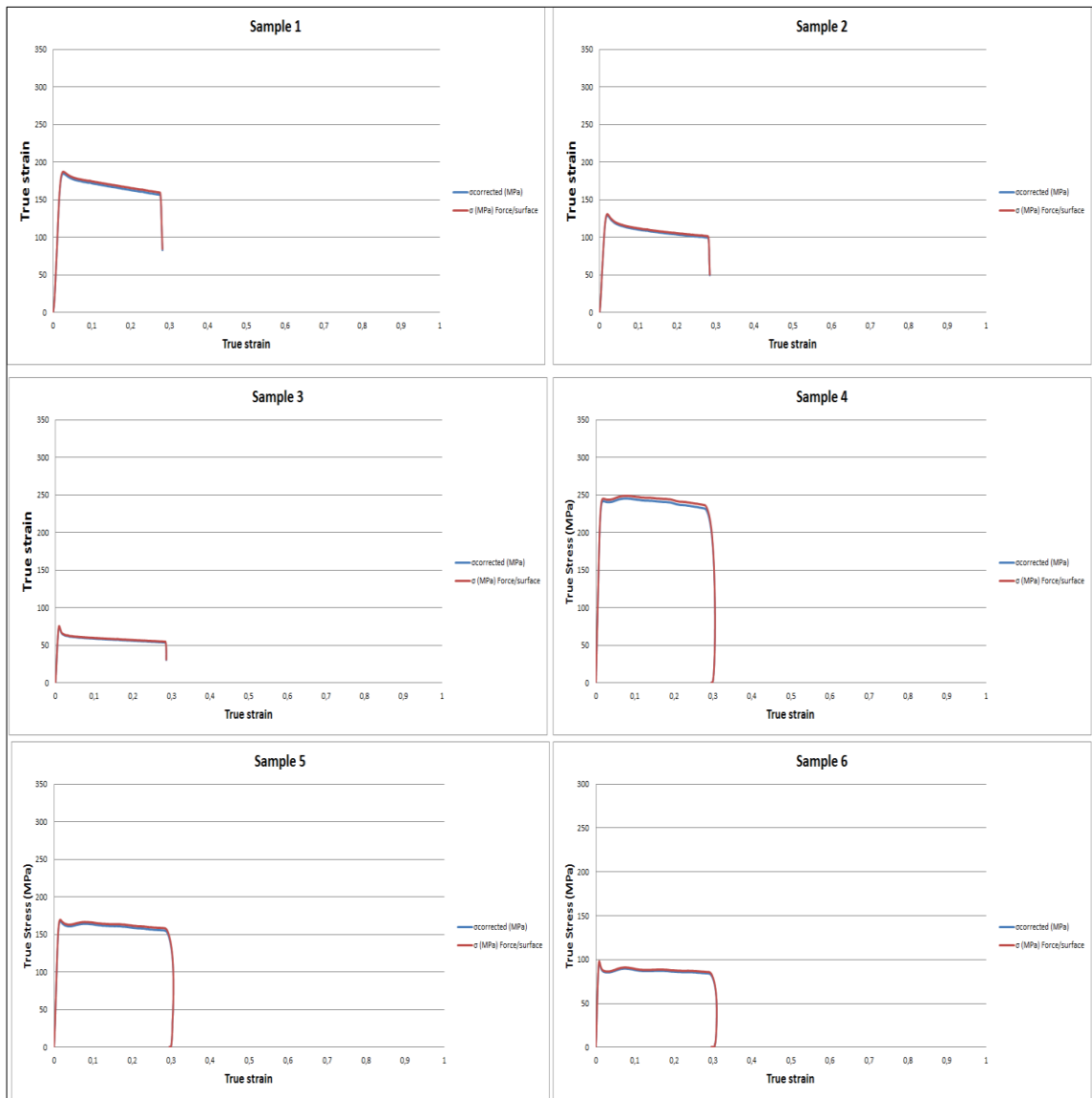


Figure D.1: Sample 1 to 6 true stress vs. true strain curves, sample 1 (0.1 S<sup>-1</sup>, 850°C and 25% strain), sample 2 (0.1 S<sup>-1</sup>, 900°C and 25% strain), sample 3 (0.1 S<sup>-1</sup>, 950°C and 25% strain), sample 4 (1 S<sup>-1</sup>, 850°C and 25% strain), sample 5 (1 S<sup>-1</sup>, 900°C and 25% strain) and sample 6 (0.1 S<sup>-1</sup>, 950°C and 25% strain)

Appendix D – True stress vs. True Strain Curves

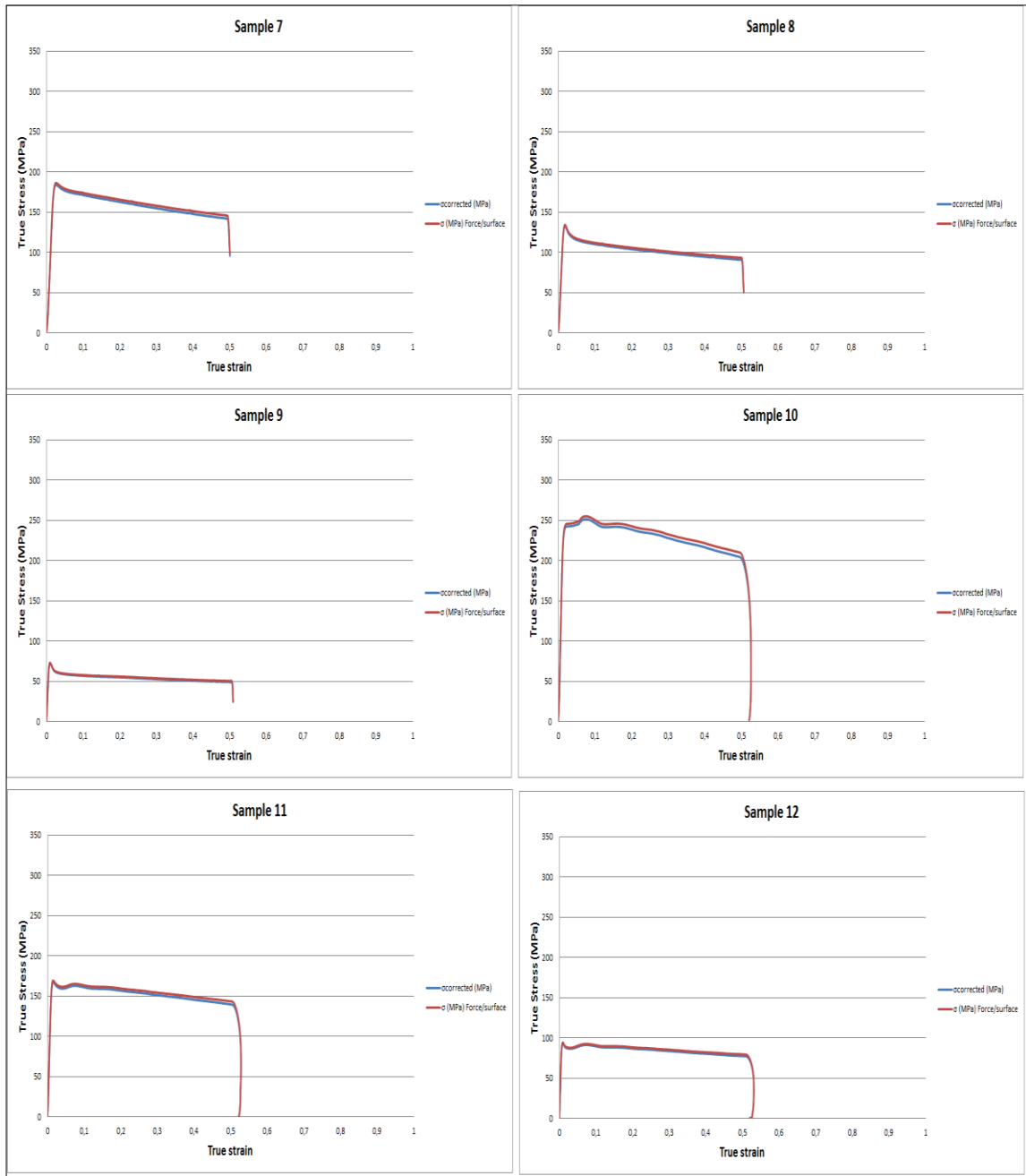
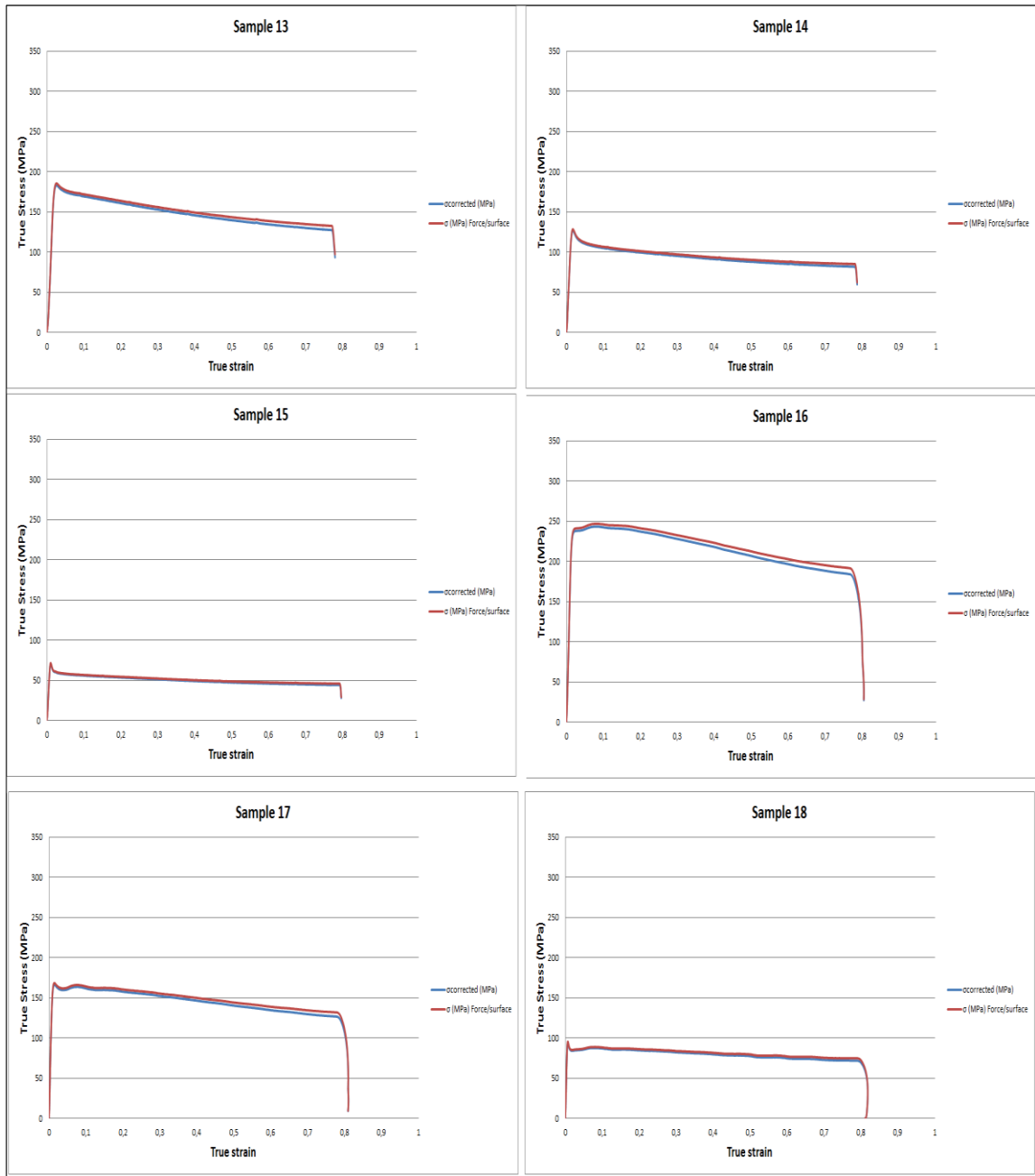


Figure D.2: Sample 7 to 12 true stress vs. true strain curves, sample 7 ( $0.1 \text{ S}^{-1}$ ,  $850^\circ\text{C}$  and 40% strain), sample 8 ( $0.1 \text{ S}^{-1}$ ,  $900^\circ\text{C}$  and 40% strain), sample 9 ( $0.1 \text{ S}^{-1}$ ,  $950^\circ\text{C}$  and 40% strain), sample 10 ( $1 \text{ S}^{-1}$ ,  $850^\circ\text{C}$  and 40% strain), sample 11 ( $1 \text{ S}^{-1}$ ,  $900^\circ\text{C}$  and 40% strain) and sample 12 ( $0.1 \text{ S}^{-1}$ ,  $950^\circ\text{C}$  and 40% strain)

Appendix D – True stress vs. True Strain Curves



**Figure D.3: Sample 13 to 18 true stress vs. true strain curves sample 13 (0.1 S<sup>-1</sup>, 850°C and 55% strain), sample 14 (0.1 S<sup>-1</sup>, 900°C and 55% strain), sample 15 (0.1 S<sup>-1</sup>, 950°C and 55% strain), sample 16 (1 S<sup>-1</sup>, 850°C and 55% strain), sample 17 (1 S<sup>-1</sup>, 900°C and 55% strain) and sample 18 (1 S<sup>-1</sup>, 950°C and 55% strain)**

## Appendix D – True stress vs. True Strain Curves

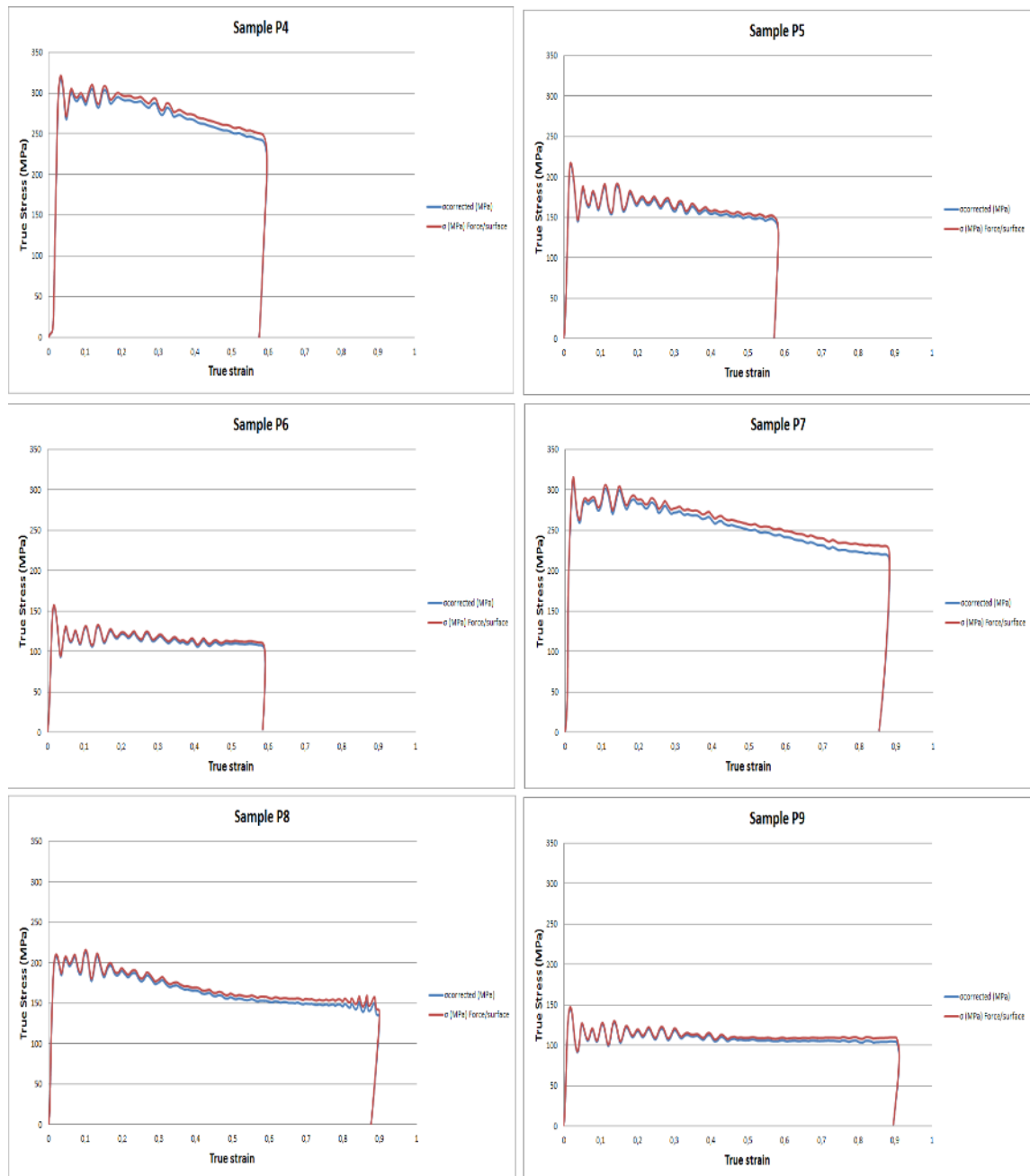


**Figure D.4: Sample P4 to P9 true stress vs. true strain curves, sample P4 ( $10 \text{ S}^{-1}$ ,  $850^\circ\text{C}$  and 40% strain), sample P5 ( $10 \text{ S}^{-1}$ ,  $900^\circ\text{C}$  and 40% strain), sample P6 ( $10 \text{ S}^{-1}$ ,  $950^\circ\text{C}$  and 40% strain), sample P7 ( $10 \text{ S}^{-1}$ ,  $850^\circ\text{C}$  and 55% strain), sample P8 ( $10 \text{ S}^{-1}$ ,  $900^\circ\text{C}$  and 55% strain) and sample P9 ( $10 \text{ S}^{-1}$ ,  $950^\circ\text{C}$  and 55% strain)**

Appendix D – True stress vs. True Strain Curves

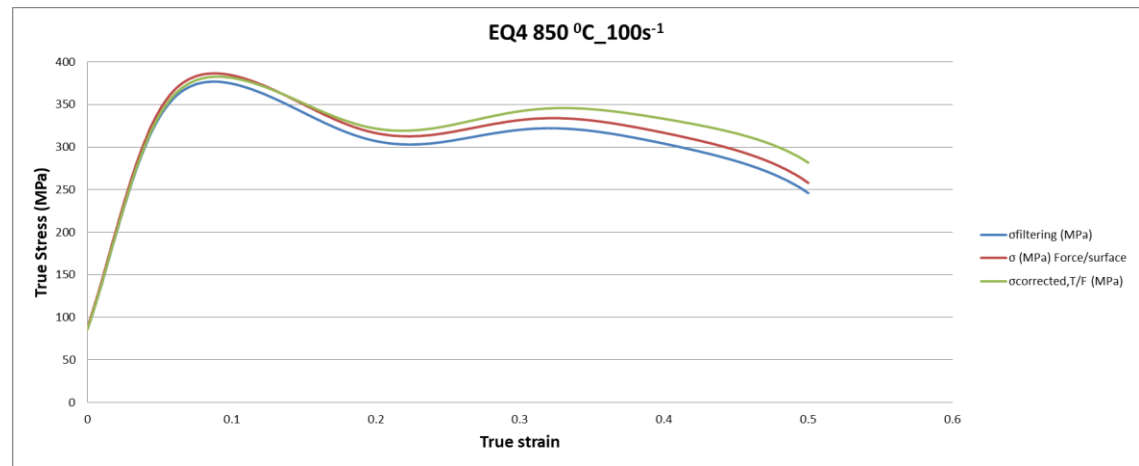
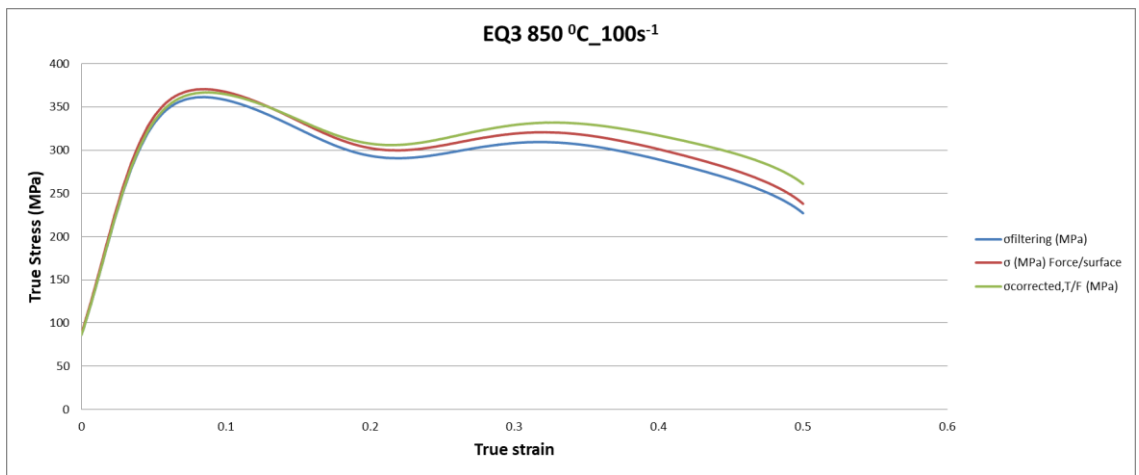
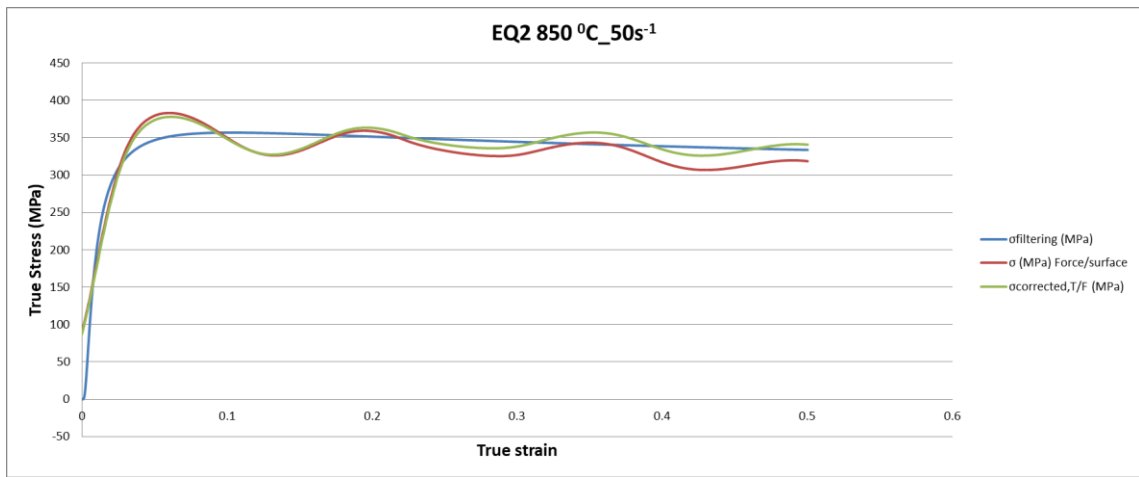


Figure D.5: Sample EQ2 to EQ4 true stress vs. true strain curves sample EQ2 (50 S<sup>-1</sup>, 850°C and 55% strain), sample EQ3 (100 S<sup>-1</sup>, 850°C and 55% strain), sample EQ4 (100 S<sup>-1</sup>, 850°C and 55% strain)

Appendix D – True stress vs. True Strain Curves

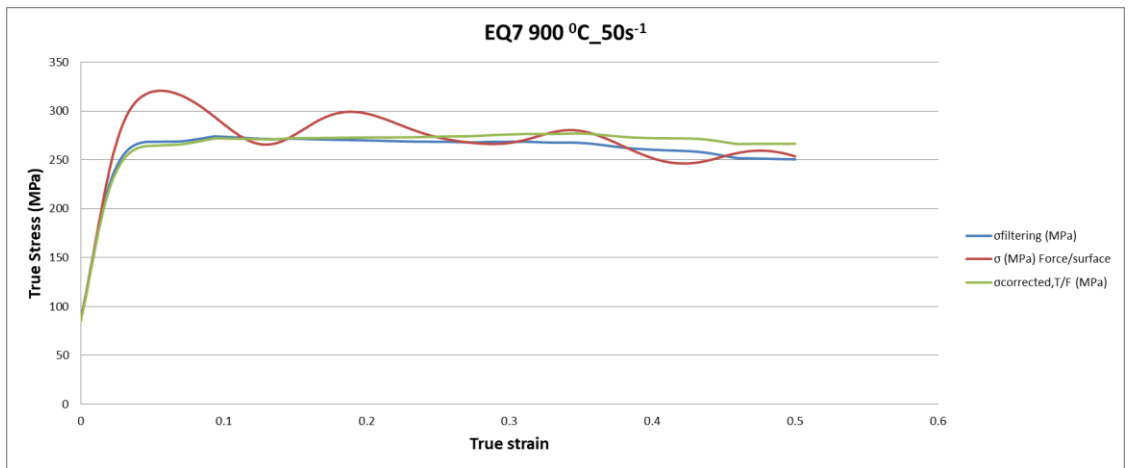
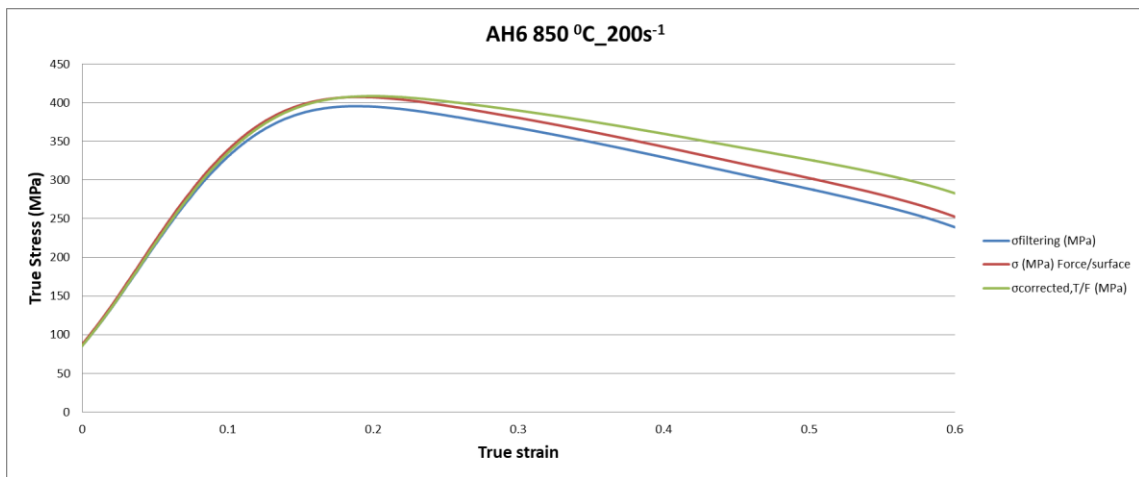
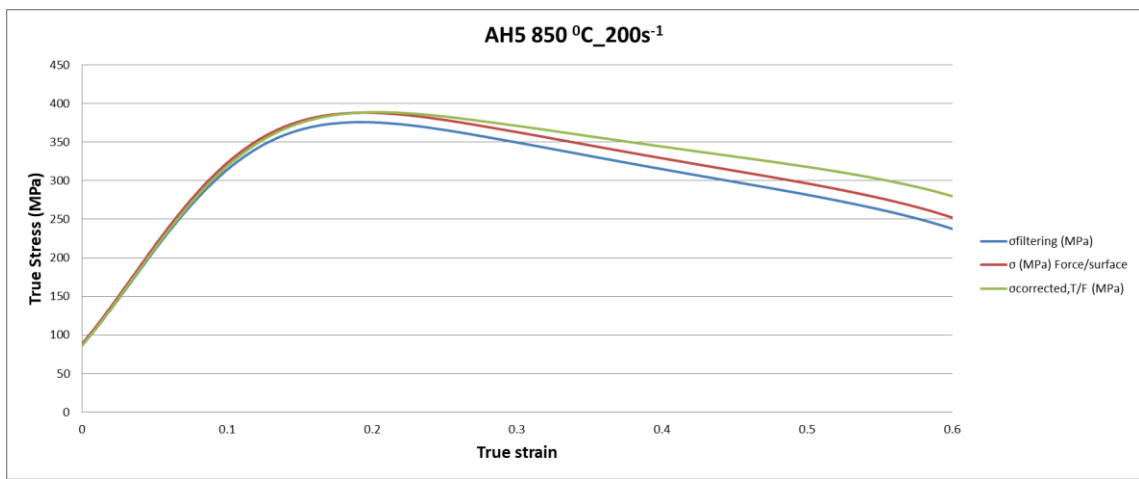


Figure D.6: Sample AH5 to EQ7 true stress vs. true strain curves sample AH5 (200 S<sup>-1</sup>, 850°C and 55% strain), sample AH6 (200 S<sup>-1</sup>, 850°C and 55% strain), sample EQ7 (50 S<sup>-1</sup>, 900°C and 55% strain)

Appendix D – True stress vs. True Strain Curves

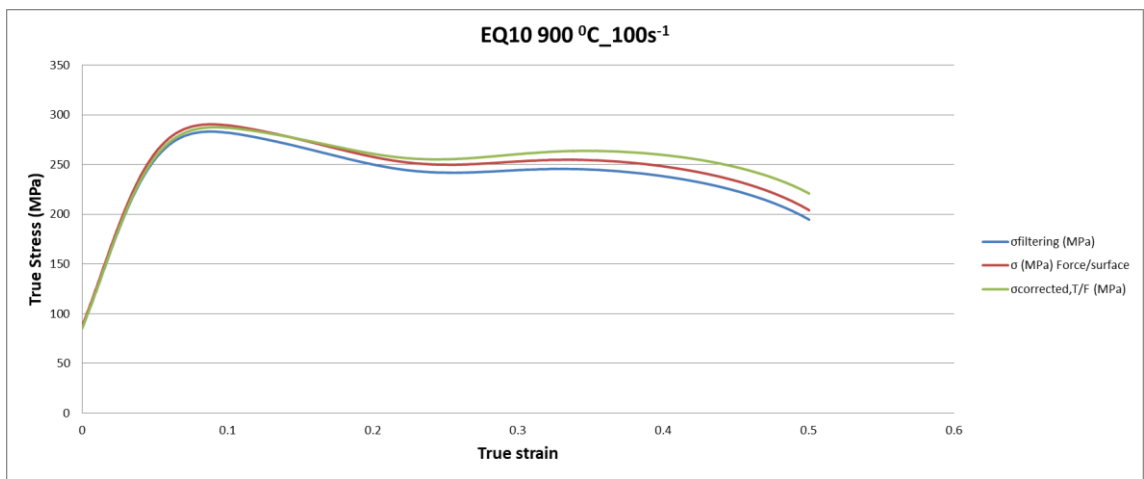
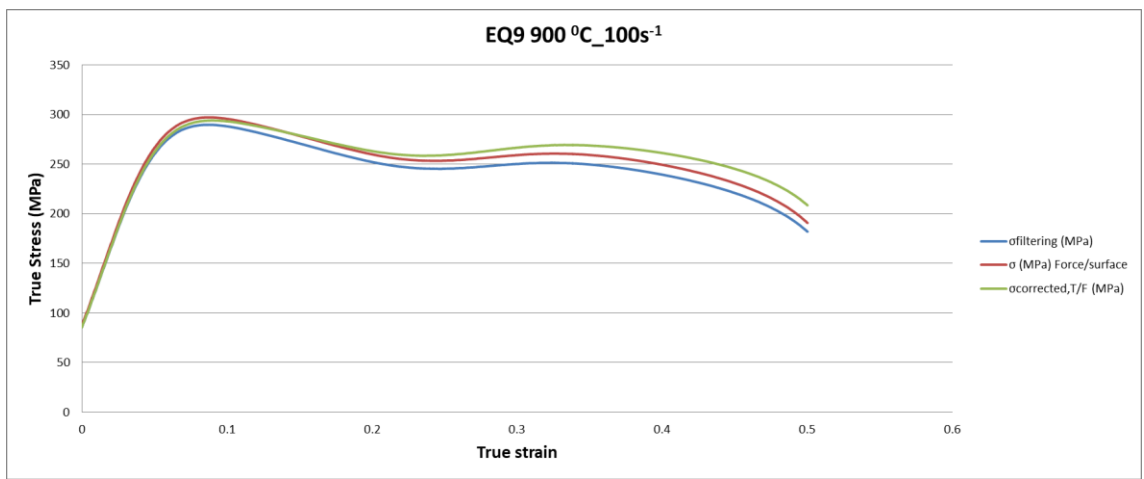
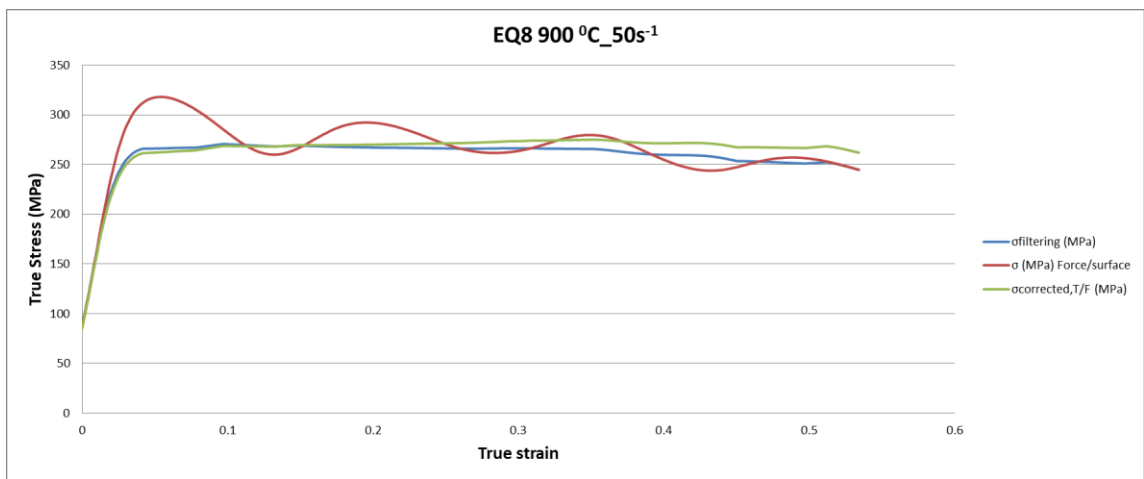


Figure D.7: Sample EQ8 to EQ10 true stress vs. true strain curves sample EQ8 (50 S<sup>-1</sup>, 900°C and 55% strain), sample EQ9 (100 S<sup>-1</sup>, 900°C and 55% strain), sample EQ10 (50 S<sup>-1</sup>, 900°C and 55% strain)

## Appendix D – True stress vs. True Strain Curves

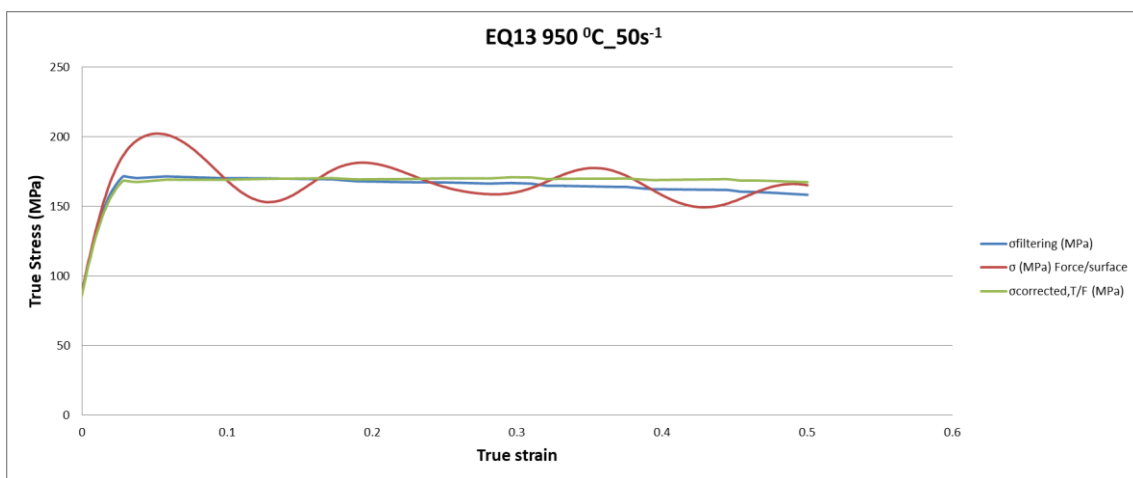
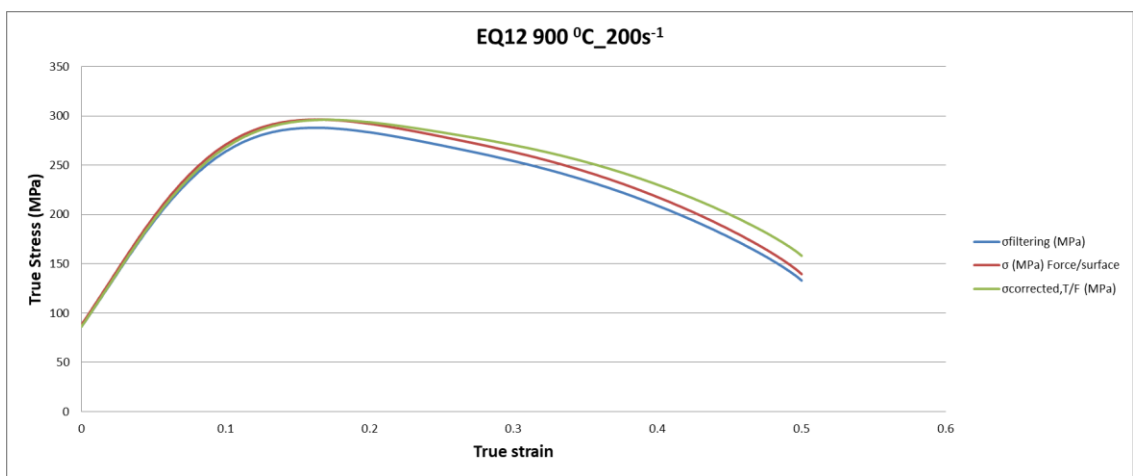
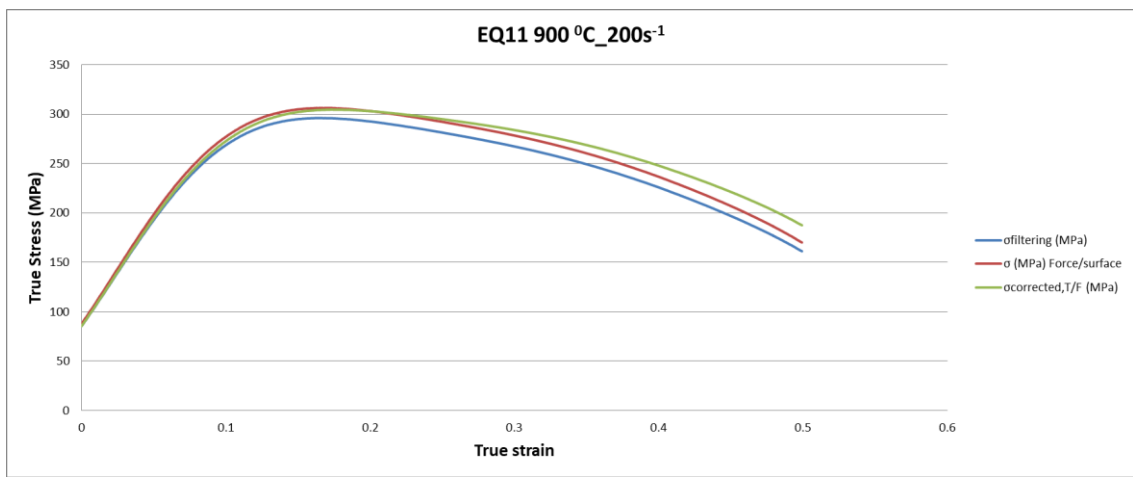


Figure D.8: Sample EQ11 to EQ13 true stress vs. true strain curves sample EQ 11 (200 S<sup>-1</sup>, 900°C and 55% strain), sample EQ12 (200 S<sup>-1</sup>, 900°C and 55% strain), sample EQ13 (50 S<sup>-1</sup>, 900°C and 55% strain)

Appendix D – True stress vs. True Strain Curves

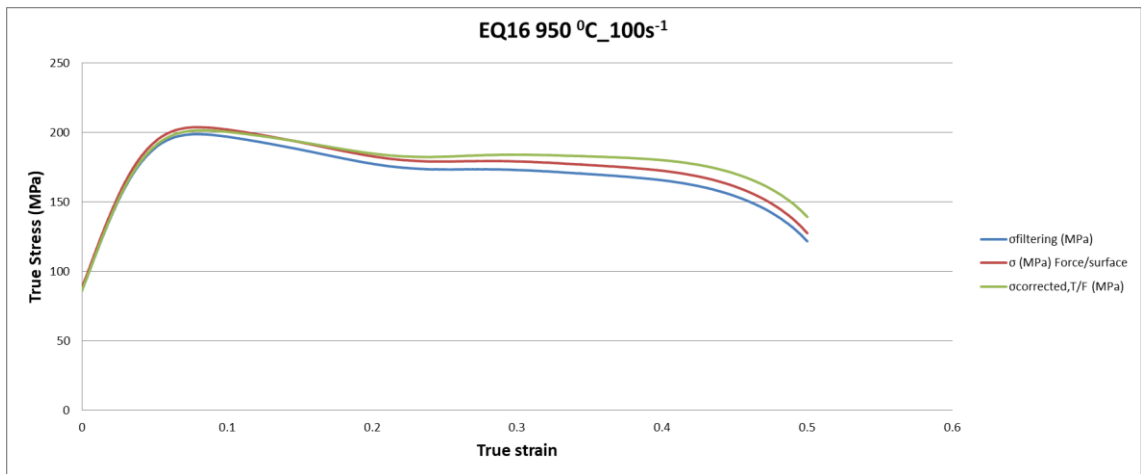
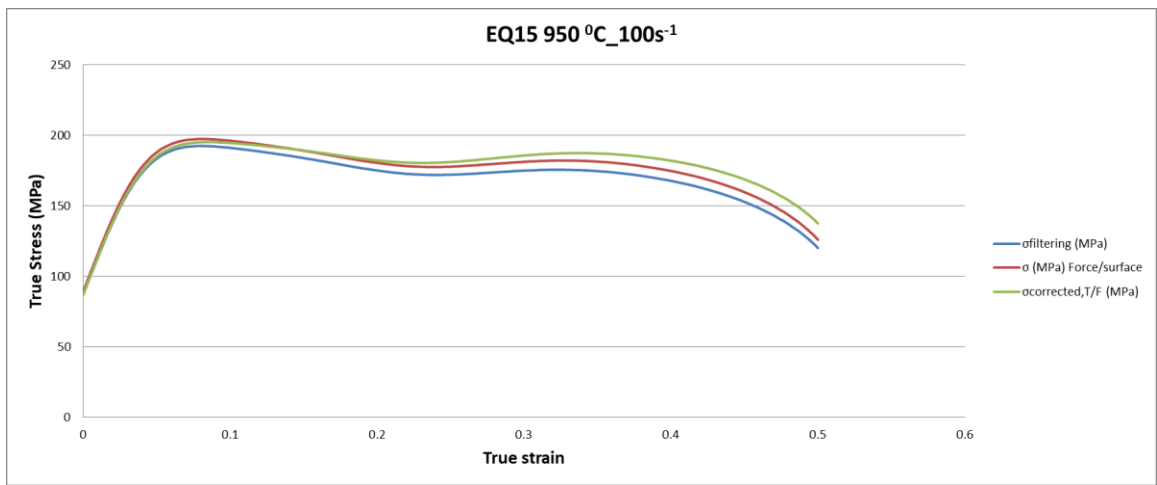
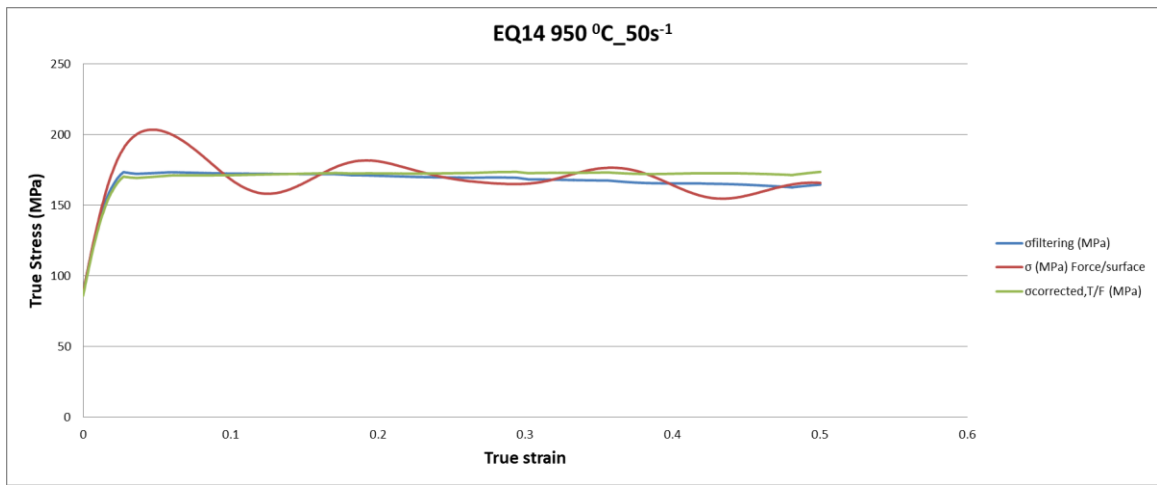


Figure D.9: Sample EQ14 to EQ16 true stress vs. true strain curves sample EQ 14 (50 S<sup>-1</sup>, 950°C and 55% strain), sample EQ15 (100 S<sup>-1</sup>, 950°C and 55% strain), sample EQ13 (100 S<sup>-1</sup>, 950°C and 55% strain)

Appendix D – True stress vs. True Strain Curves

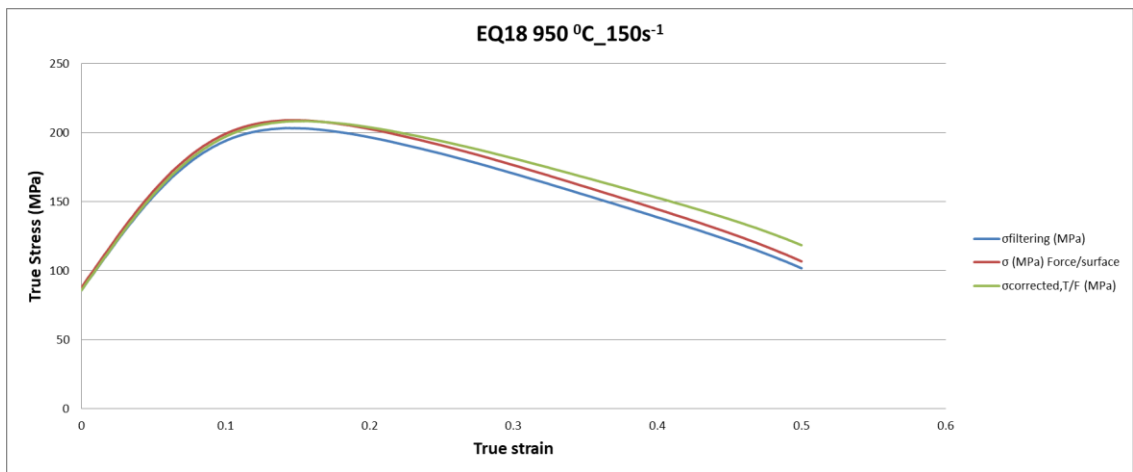
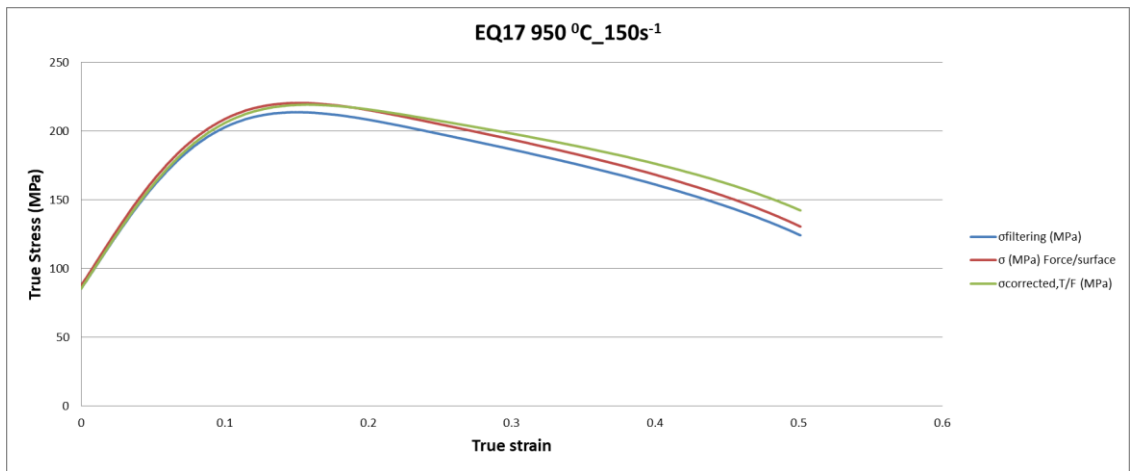


Figure D.10: Sample EQ17 to EQ18 true stress vs. true strain curves sample EQ 17 (150 S<sup>-1</sup>, 950°C and 55% strain), sample EQ18 (150 S<sup>-1</sup>, 950°C and 55% strain)

## Appendix E – Microstructure low strain rates

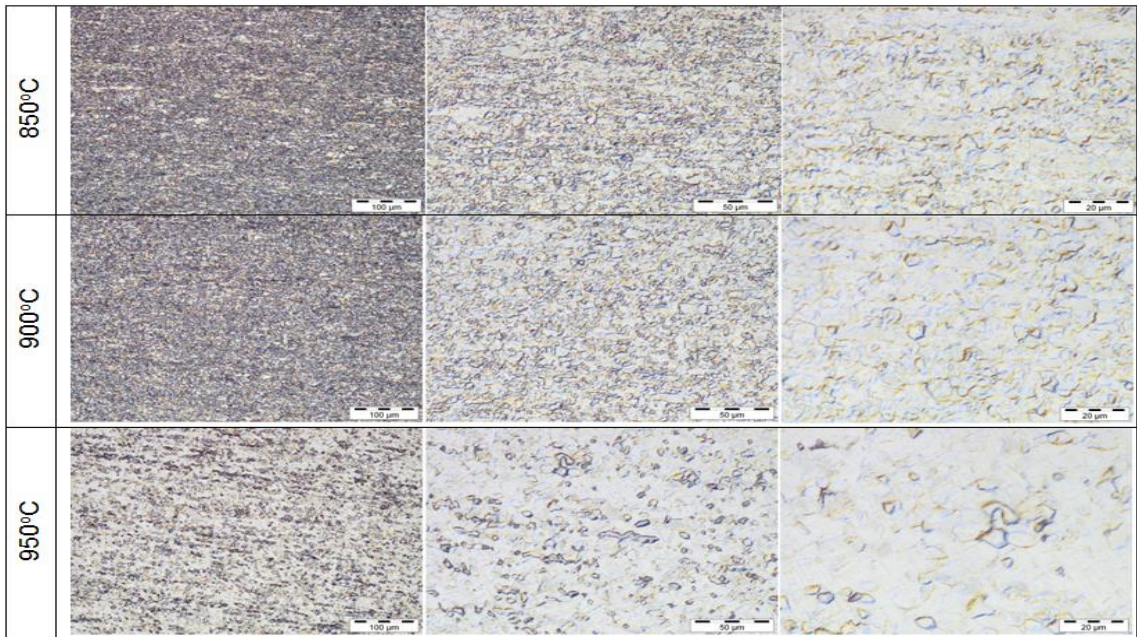


Figure E.1: Equiaxed Microstructure at 25% deformation and  $0.1\text{s}^{-1}$  strain rate at different temperatures

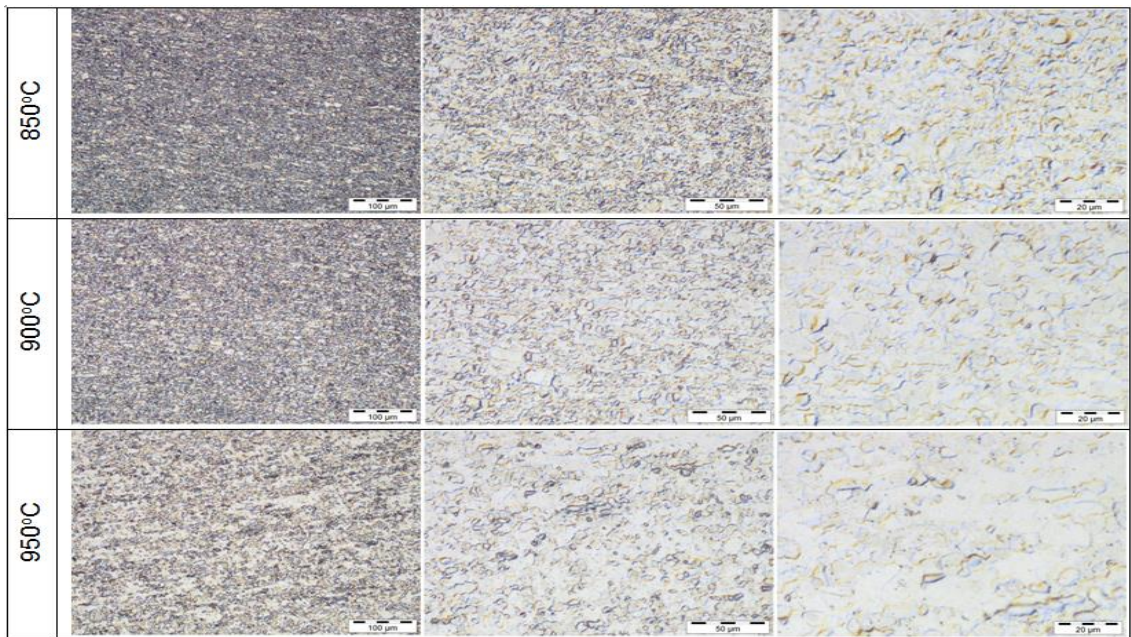


Figure E.2: Equiaxed Microstructure at 25% deformation and  $1\text{s}^{-1}$  strain rate at different temperatures

Appendix E – Microstructure low strain rates

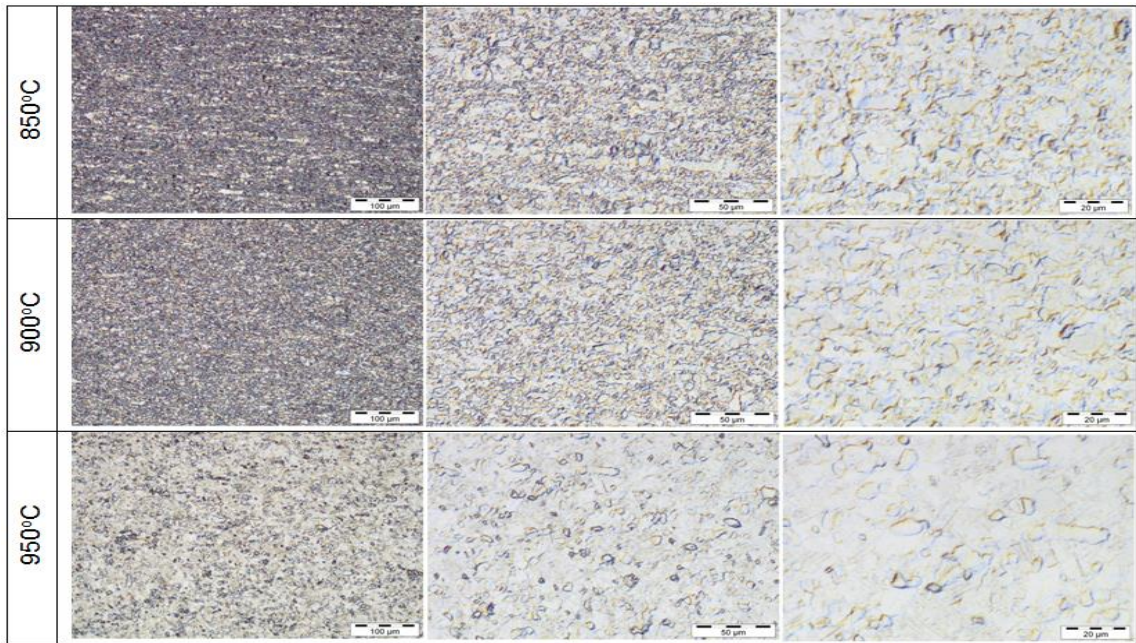


Figure E.3: Equiaxed Microstructure at 40% deformation and  $0.1\text{s}^{-1}$  strain rate at different temperatures

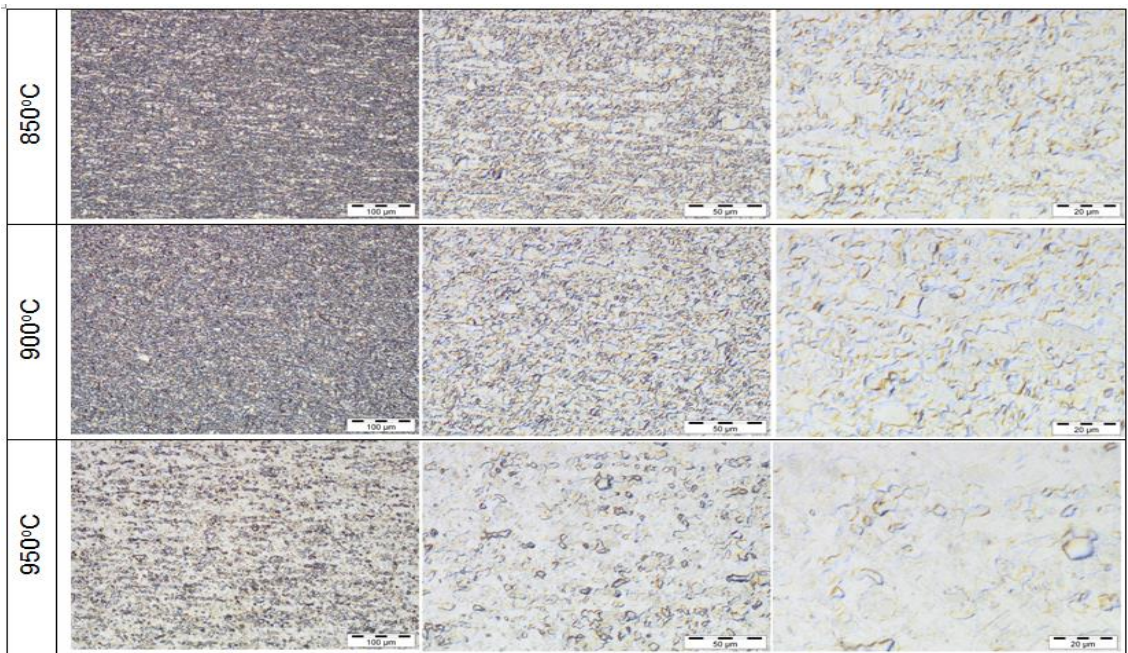


Figure E. 4: Equiaxed Microstructure at 40% deformation and  $1\text{s}^{-1}$  strain rate at different temperatures

Appendix E – Microstructure low strain rates

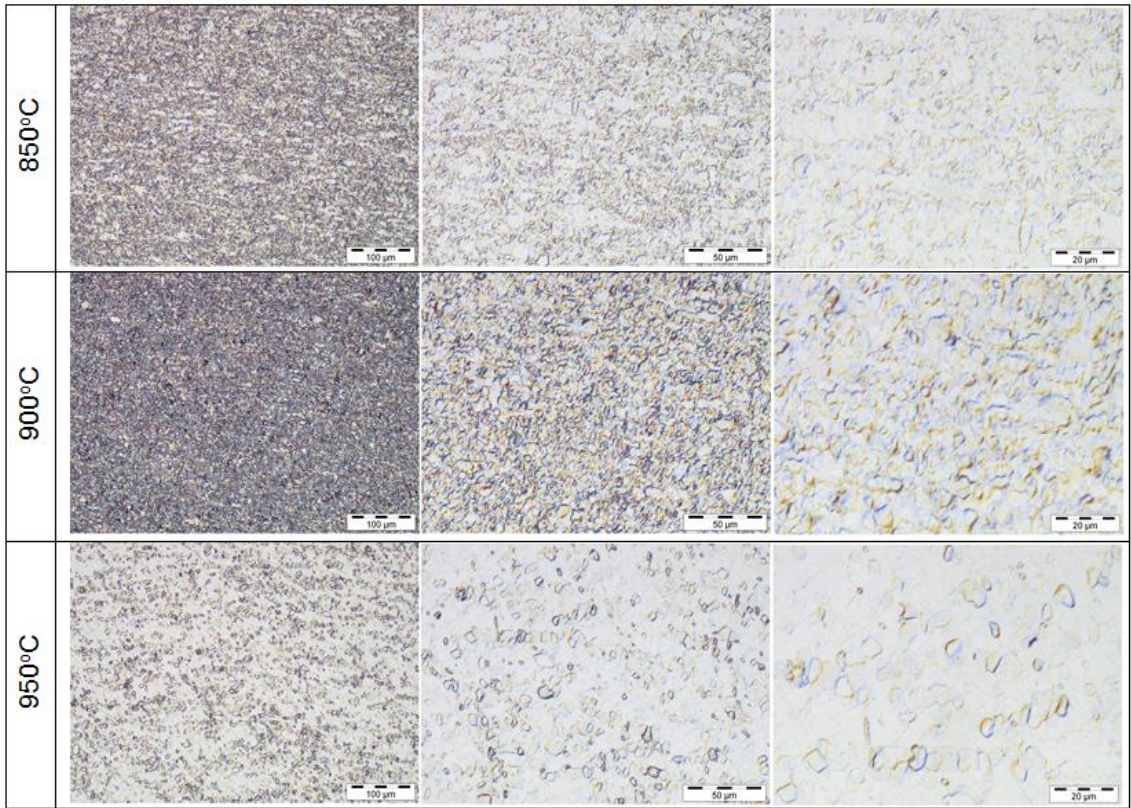


Figure E5: Equiaxed Microstructure at 55% deformation and  $0.1\text{s}^{-1}$  strain rate at different temperatures

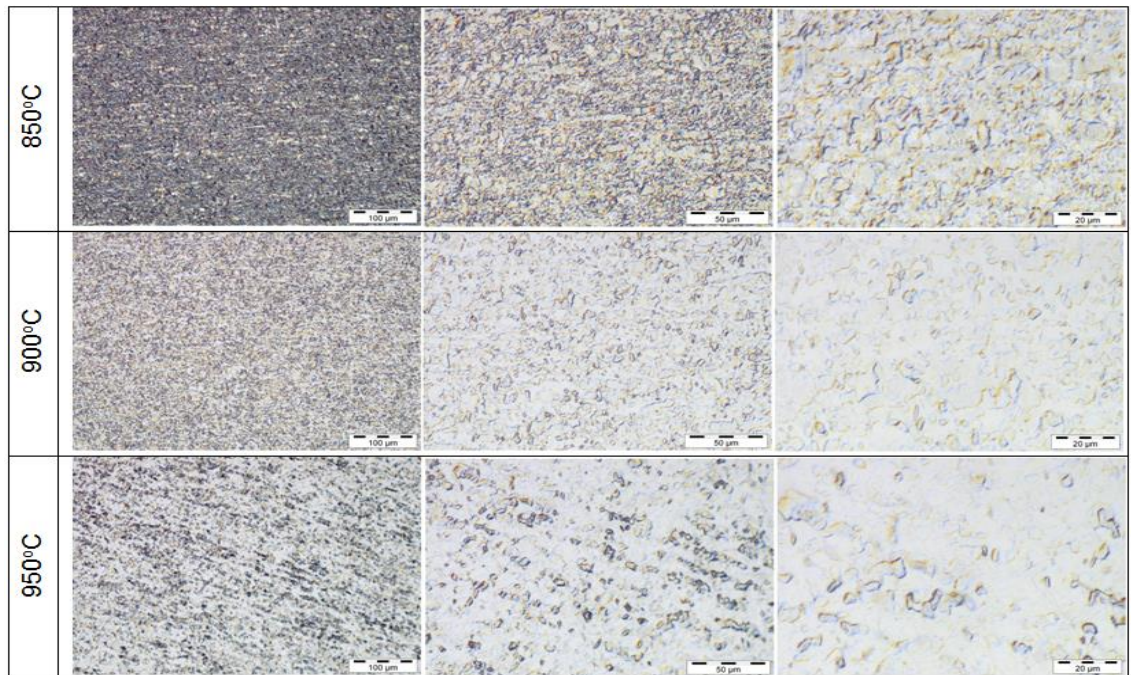


Figure E6: Equiaxed Microstructure at 55% deformation and  $1\text{s}^{-1}$  strain rate at different temperatures

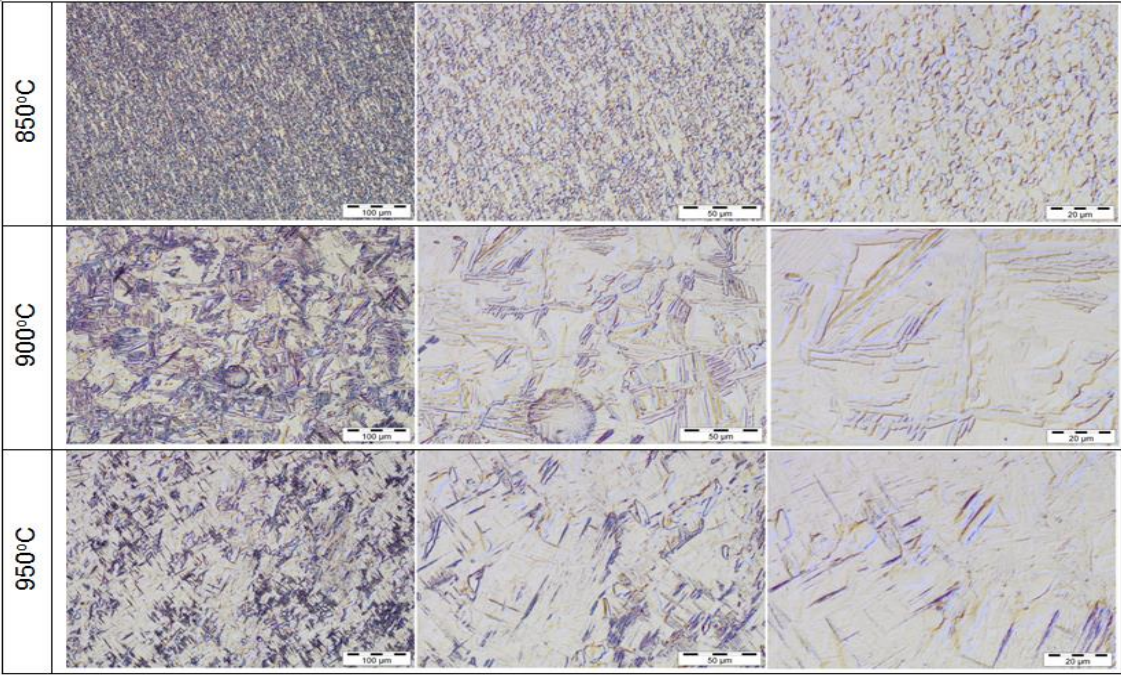


Figure E7: Equiaxed Microstructure at 55% deformation and  $10s^{-1}$  strain rate at different temperatures

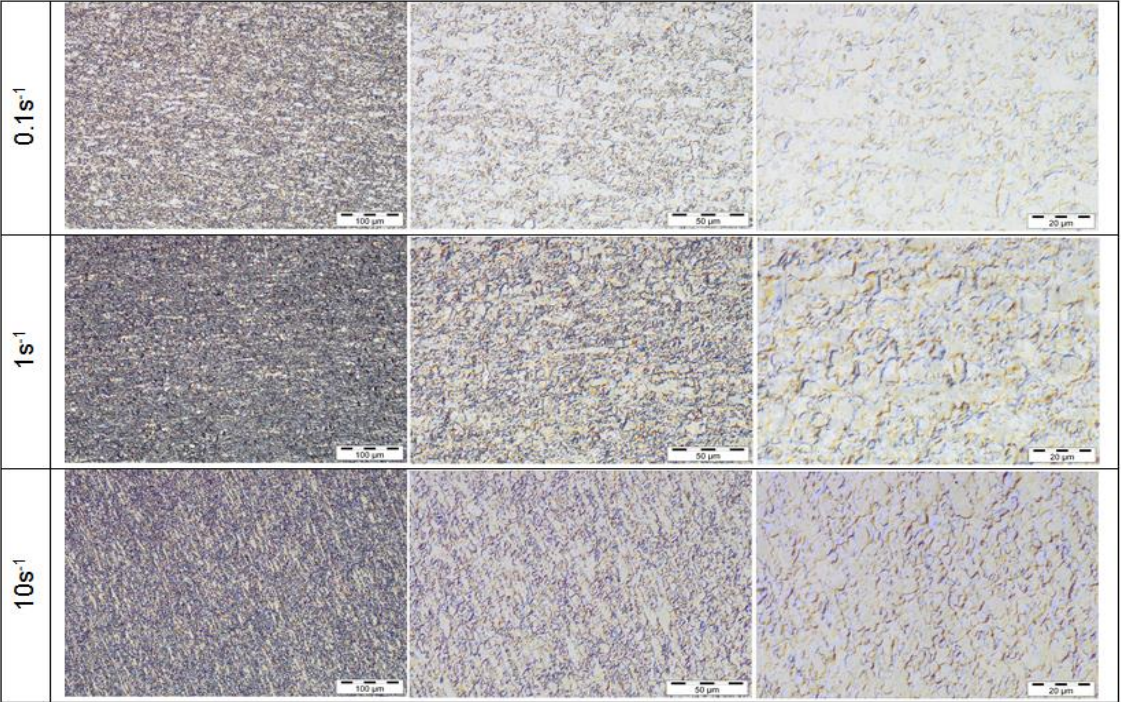


Figure E8: Equiaxed Microstructure at 55% deformation and 850°C temperature at different strain rates

Appendix E – Microstructure low strain rates

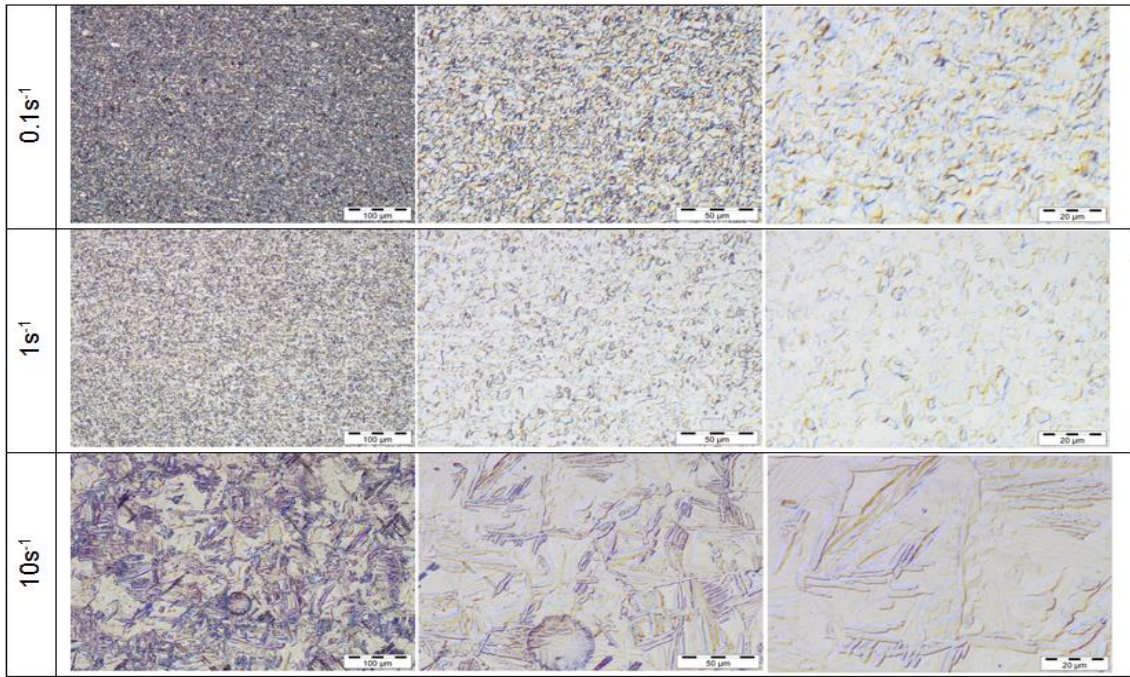


Figure E9: Equiaxed Microstructure at 55% deformation and 900°C temperature at different strain rates

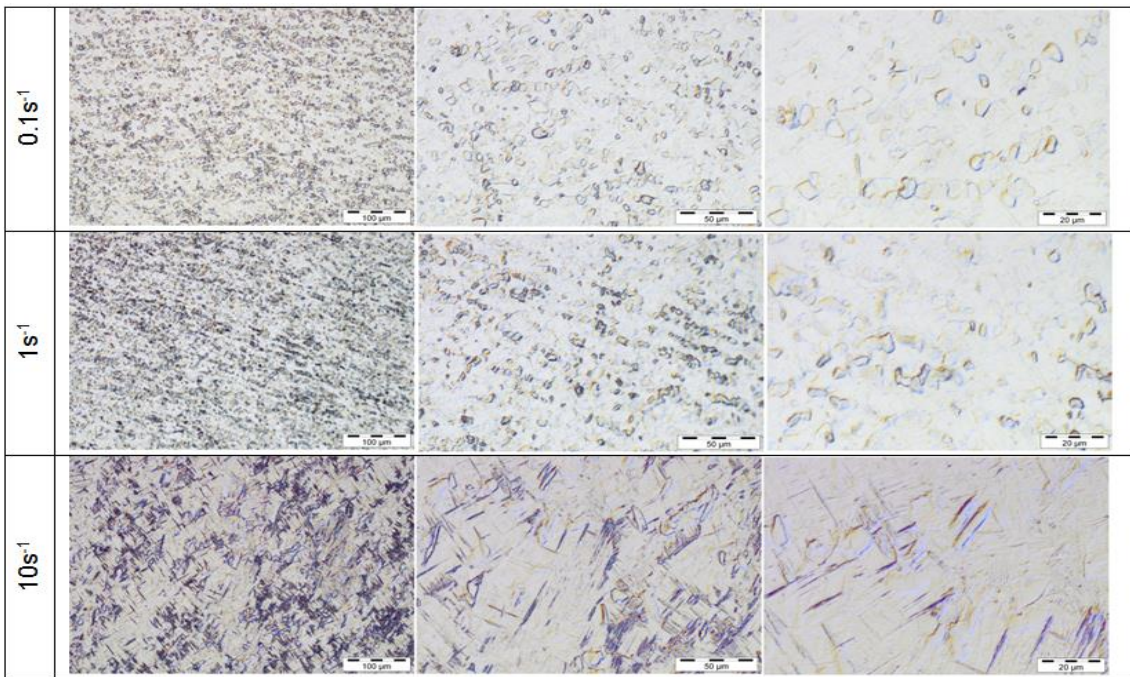


Figure E10: Equiaxed Microstructure at 55% deformation and 950°C temperature at different strain rates

# Appendix F - Flow patterns

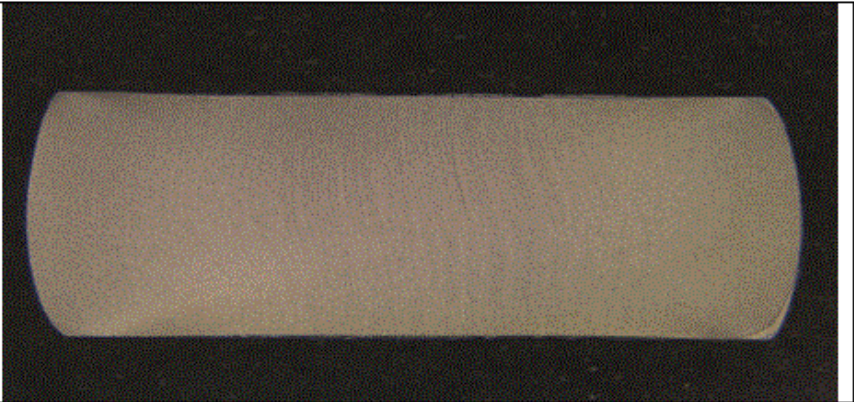
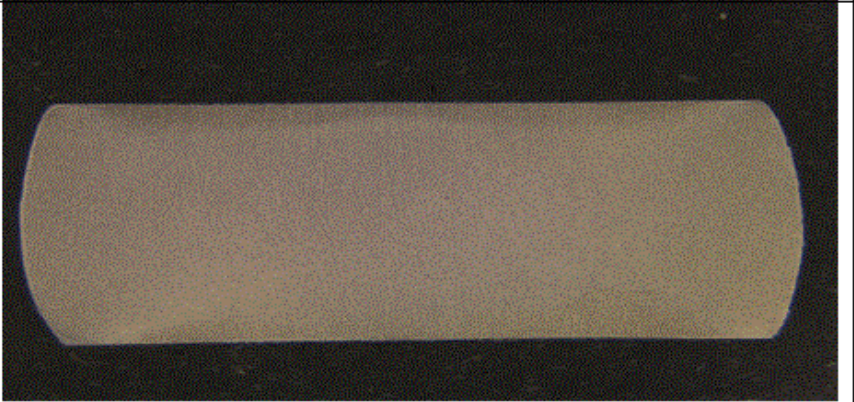
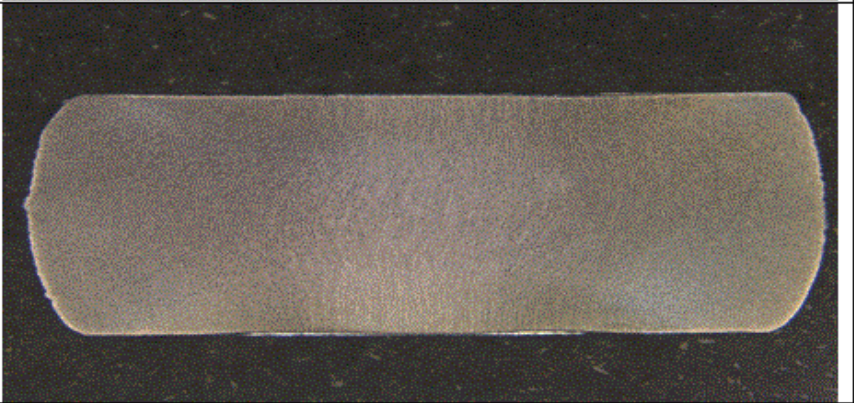
Strain rate $0.1s^{-1}$	850°C	
	900°C	
	950°C	

Figure F.1: Flow patterns at 55% deformation and  $0.1s^{-1}$  strain rate at different temperatures (Equiaxed microstructure)

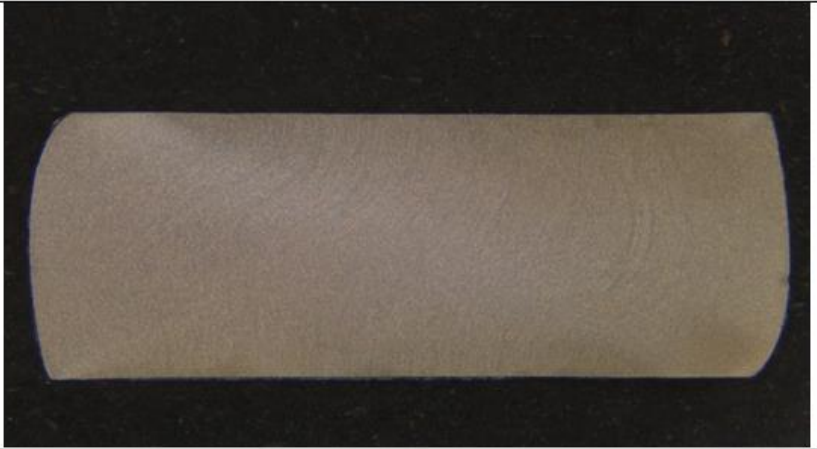
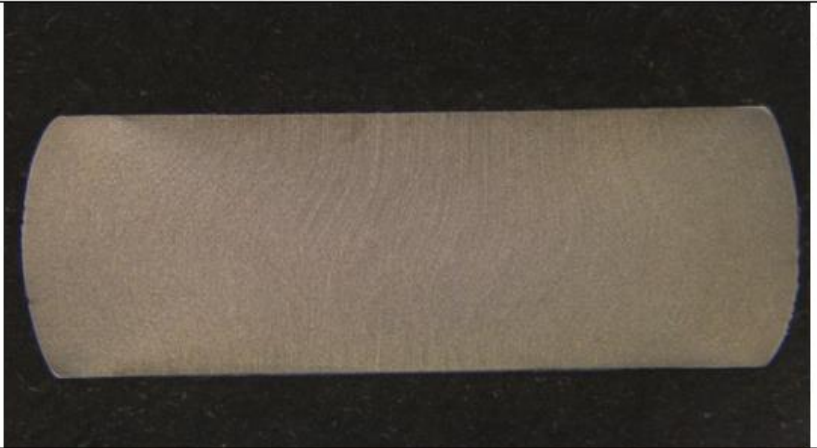
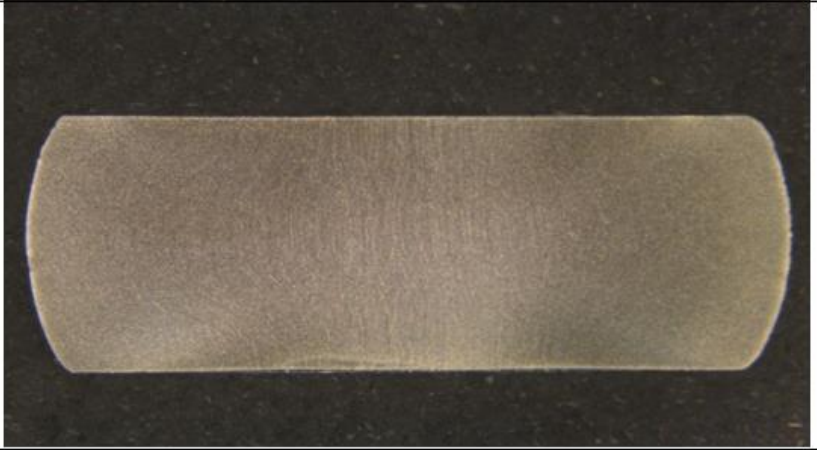
Strain rate $1\text{ s}^{-1}$	850°C	
	900°C	
	950°C	

Figure F.2: Flow patterns at 55% deformation and  $1\text{ s}^{-1}$  strain rate at different temperatures (Equiaxed microstructure)

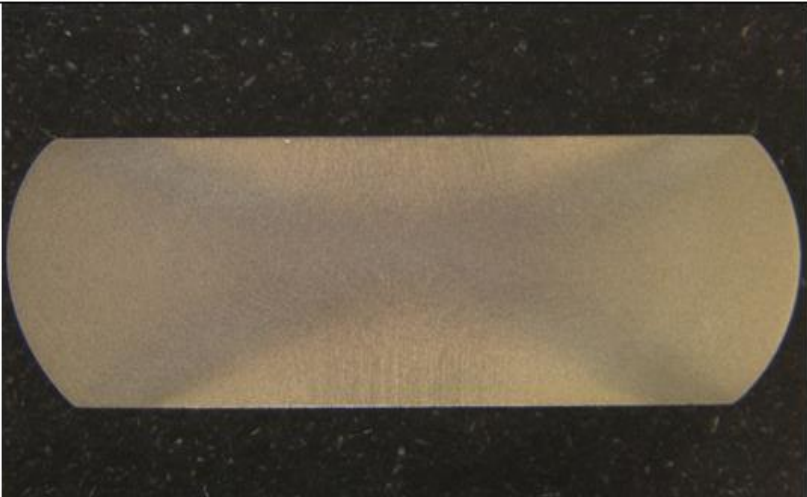
Strain rate $10s^{-1}$	850°C	
	900°C	
	950°C	

Figure F.3: Flow patterns at 55% deformation and  $10s^{-1}$  strain rate at different temperatures (Equiaxed microstructure)

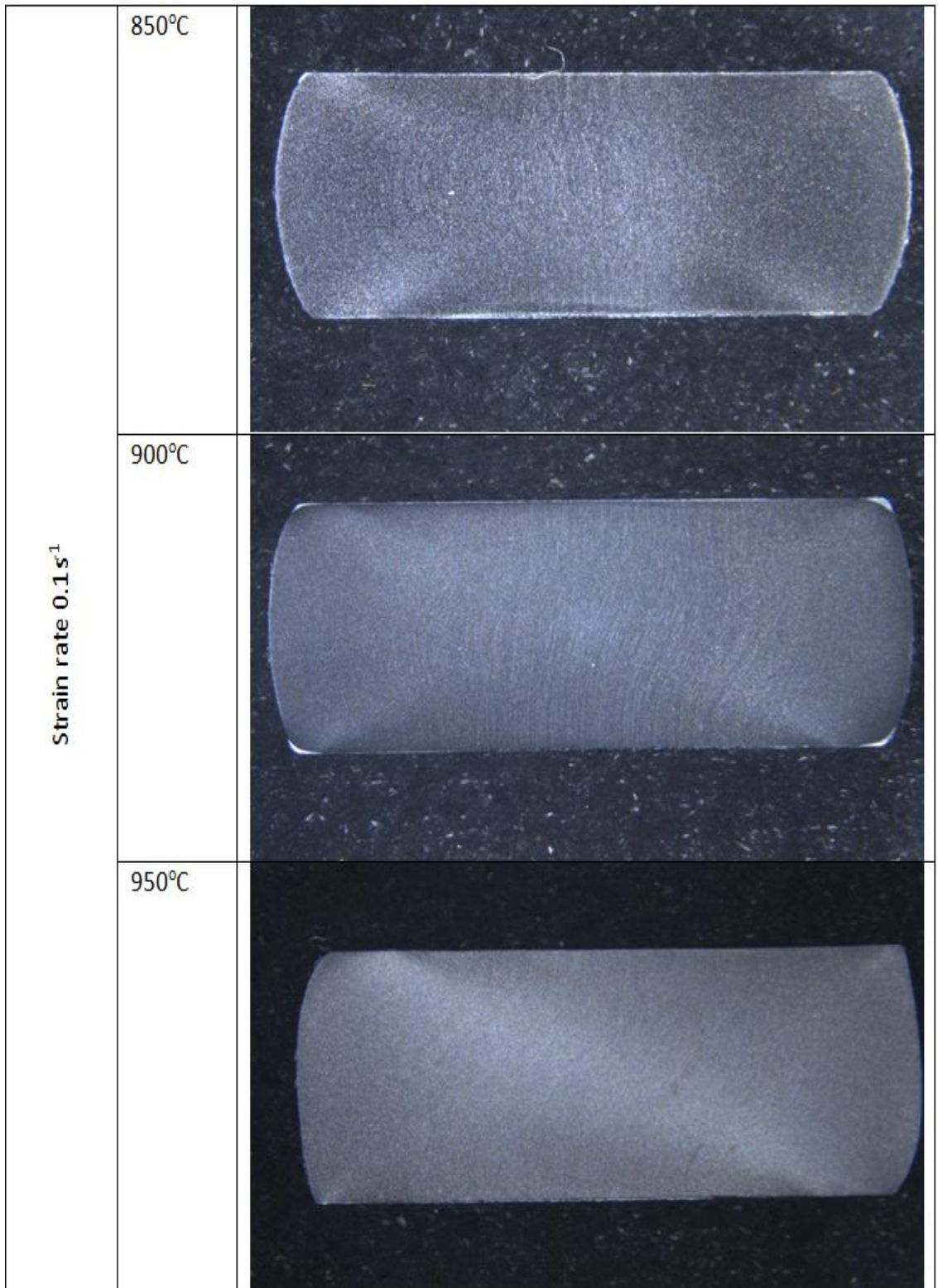


Figure F.4: Adiabatic shear band formation at 55% deformation and  $0.1\text{ s}^{-1}$  strain rate at different temperatures (Equiaxed microstructure)

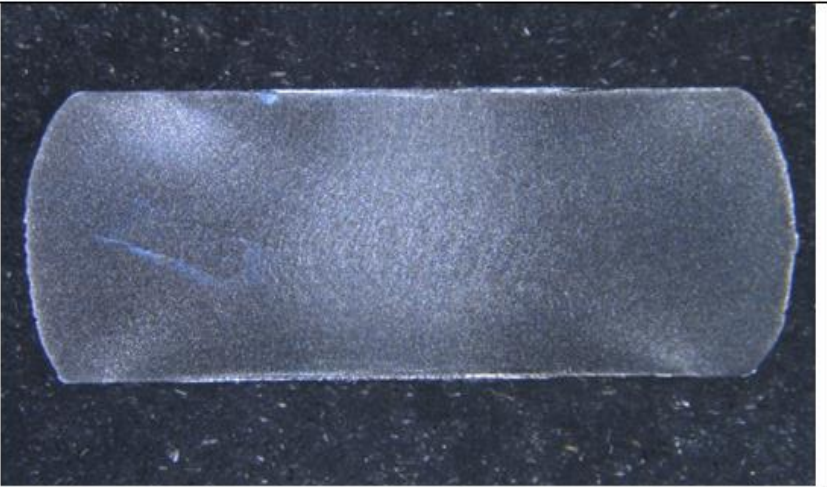
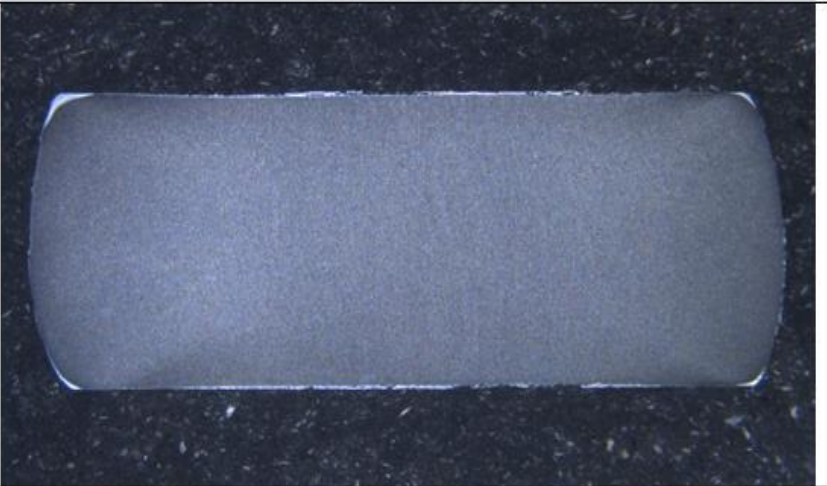
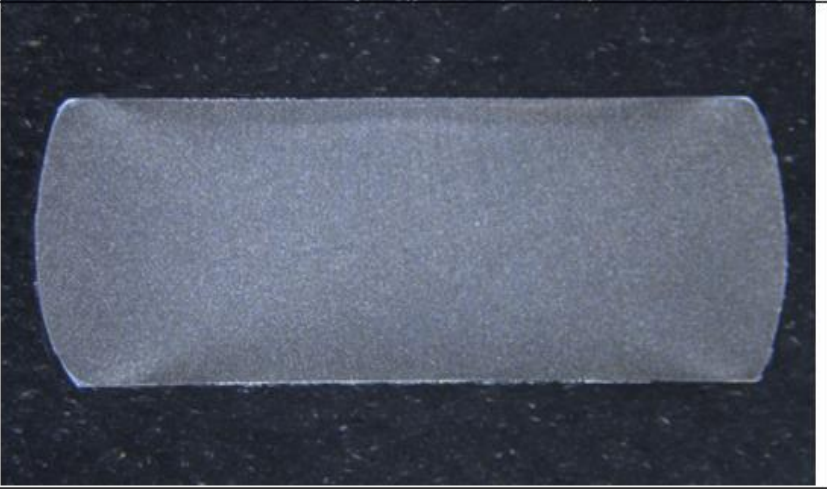
<b>Strain rate <math>1\text{ s}^{-1}</math></b>	850°C	
	900°C	
	950°C	

Figure F.5: Adiabatic shear band formation at 55% deformation and  $1\text{ s}^{-1}$  strain rate at different temperatures (Equiaxed microstructure)

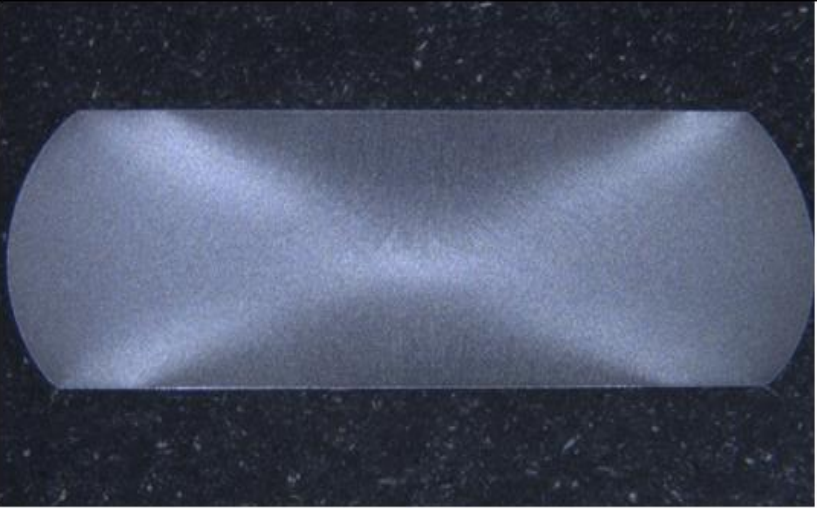
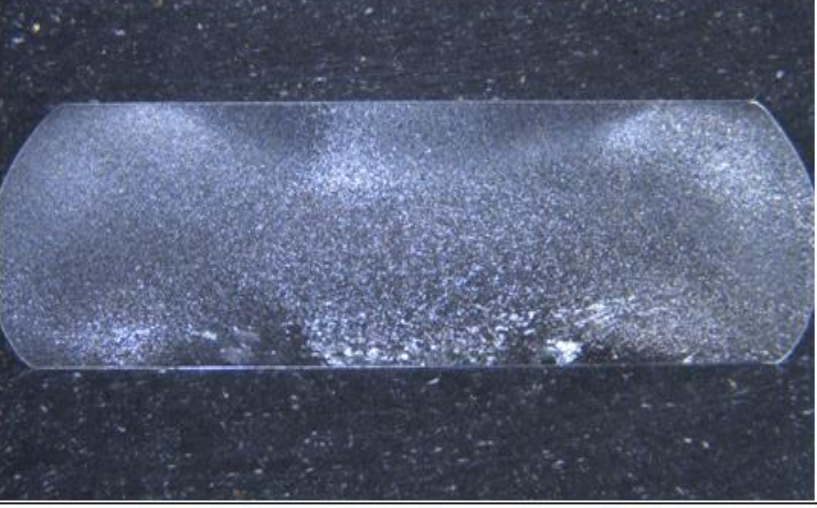
<b>Strain rate <math>10\text{ s}^{-1}</math></b>	850°C	
	900°C	
	950°C	

Figure F.6: Adiabatic shear band formation at 55% deformation and  $10\text{ s}^{-1}$  strain rate at different temperatures (Equiaxed microstructure)

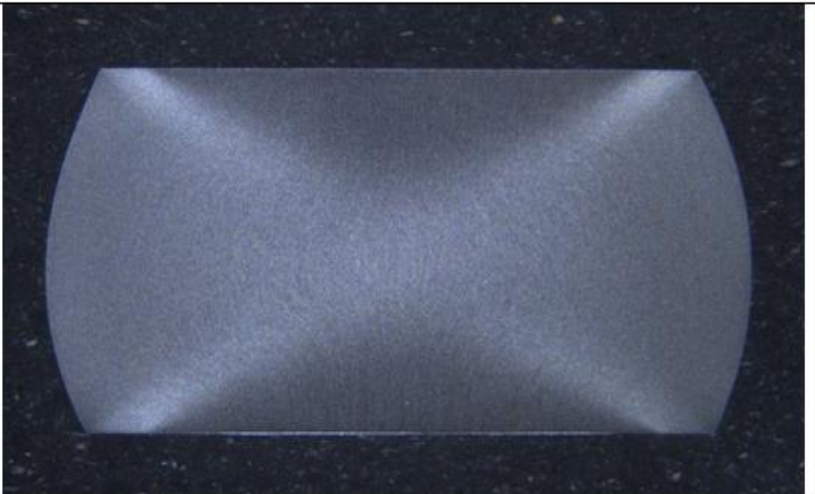
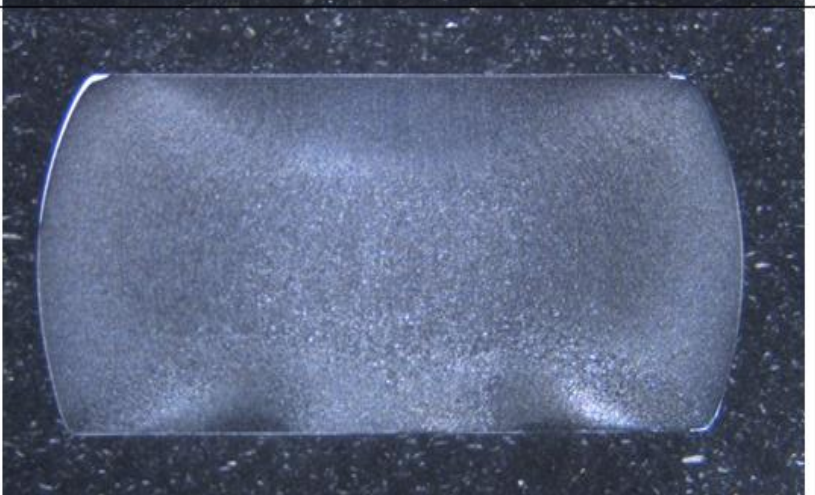
Strain rate $10s^{-1}$	850°C	
	900°C	
	950°C	

Figure F.7: Adiabatic shear band formation at 40% deformation and  $10s^{-1}$  strain rate at different temperatures (Equiaxed microstructure)

---

## Reference

- [1] H. Rosenberg K. H. J., "Titanium Production and Refining." pp. 9381–9384, 2001.
- [2] M. Peters, J. Hemptenmacher, J. Kumpfert, and C. Leyens, "Structure and Properties of Titanium and Titanium Alloys," in *Titanium and Titanium Alloys*, Wiley-VCH Verlag GmbH & Co. KGaA, 2003, pp. 1–36.
- [3] W. Callister, *Materials Science and Engineering*. Hoboken, NJ : Wiley, 2000.
- [4] G. Lütjering, *Titanium [internet resource]*. Berlin ; New York : Springer, 2007.
- [5] E. W. Collings, R. Boyer, and G. Welsch, Eds., *Materials properties handbook : titanium alloys*. Materials Park, OH : ASM International, 1994.
- [6] C. Leyens and M. Peters, *Titanium and Titanium Alloys*. Weinheim, FRG: Wiley-VCH Verlag GmbH & Co. KGaA, 2003.
- [7] M. J. Donachie, *Titanium: a technical guide*. ASM International, 1988.
- [8] I. J. Polmear, *Light Alloys : From Traditional Alloys to Nanocrystals*. 2005.
- [9] M. Cervenka, "The Rolls-Royce Trent Engine," *Rolls Royce PLC*, 2000. [Online]. Available: <https://www.phase-trans.msm.cam.ac.uk/mphil/Trent1/sld024.htm>.
- [10] Zion Market Research, "Forging Market (Rolled Rings, Open Die, and Impression Die) for Automotive, Aerospace, Oil & Gas, and Other Applications – Global Industry Perspective, Comprehensive Analysis, Size, Share, Growth, Segment, Trends and Forecast, 2015 – 2021".
- [11] A. Forcellese, E. Mancini, M. Sasso, and M. Simoncini, "Evaluation of Friction at High Strain Rate using the Split Hopkinson Bar," *Key Eng. Mater.*, vol. 651–653, pp. 108–113, 2015.
- [12] J. Luo, B. Wu, and M. Li, "3D finite element simulation of microstructure evolution in blade forging of Ti-6Al-4V alloy based on the internal state variable models," *Int. J. Miner. Metall. Mater.*, vol. 19, no. 2, pp. 122–130, Jan. 2012.
- [13] A. K. M. N. Amin, *Titanium Alloys - Towards Achieving Enhanced Properties for Diversified Applications*. InTech, 2012.
- [14] Z. M. Hu, J. W. Brooks, and T. a Dean, "The interfacial heat transfer coefficient in hot die forging of titanium alloy," *Proc. Inst. Mech. Eng. Part C J. Mech. Eng. Sci.*, vol. 212, no. February 1998, pp. 485–496, 1998.
- [15] M. Qiu, Y.-Z. Zhang, B. Shangguan, S.-M. Du, and Z.-W. Yan, "The relationships between tribological behaviour and heat-transfer capability of

- Ti6Al4V alloys,” *Wear*, vol. 263, no. 1–6, pp. 653–657, 2007.
- [16] J.-T. Yeom *et al.*, “Characterization of the interface heat transfer coefficient during non-isothermal bulk forming of Ti-6Al-4 V alloy,” *Proc. Inst. Mech. Eng. Part B J. Eng. Manuf.*, vol. 225, no. 9, pp. 1703–1712, 2011.
- [17] Y. Zhu, W. Zeng, X. Ma, Q. Tai, Z. Li, and X. Li, “Determination of the friction factor of Ti-6Al-4V titanium alloy in hot forging by means of ring-compression test using FEM,” *Tribol. Int.*, vol. 44, no. 12, pp. 2074–2080, 2011.
- [18] R. Ebrahimi and a. Najafizadeh, “A new method for evaluation of friction in bulk metal forming,” *J. Mater. Process. Technol.*, vol. 152, no. 2, pp. 136–143, Oct. 2004.
- [19] S. J. Mirahmadi, M. Hamed, and M. Cheraghzadeh, “Investigating Friction Factor in Forging of Ti-6Al-4V through Isothermal Ring Compression Test,” *Tribol. Trans.*, vol. 58, no. 5, pp. 778–785, 2015.
- [20] L. W. Meyer, a Weise, and F. Hahn, “Comparison of Constitutive Flow Curve Relations in Cold and Hot Forming,” *J. Phys IV Fr. Colloq. C3*, vol. 7, pp. 13–20, 1997.
- [21] G. T. Gray, “High-Strain-Rate Deformation: Mechanical Behavior and Deformation Substructures Induced,” *Annu. Rev. Mater. Res.*, vol. 42, no. 1, pp. 285–303, Aug. 2012.
- [22] J. E. Field, S. M. Walley, N. K. Bourne, and J. M. Huntley, “Experimental methods at high rates of strain,” *Le J. Phys. IV*, vol. 04, no. C8, pp. C8-3-C8-22, Sep. 1994.
- [23] J. E. Field, S. M. Walley, W. G. Proud, H. T. Goldrein, and C. R. Siviour, *Review of experimental techniques for high rate deformation and shock studies*, IJIE, vol. 30, no. 7. 2004.
- [24] K. Zweymüller, “Concept and material properties of a cementless hip prosthesis system with Al<sub>2</sub>O<sub>3</sub> ceramic ball heads and wrought Ti-6Al-4V stems,” *Arch. Orthop. Trauma. Surg.*, vol. 100, no. 4, pp. 229–236, 1982.
- [25] R. Wanhill and S. Barter, *Fatigue of Beta Processed and Beta Heat-treated Titanium Alloys*. Dordrecht: Springer Netherlands, 2012.
- [26] H. Flower, “Microstructural development in relation to hot working of titanium alloys,” *Mater. Sci. Technol.*, vol. 6, no. November, pp. 1082–1092, 1990.
- [27] C. Zhong *et al.*, “Laser metal deposition of Ti6Al4V-A brief review,” *Appl. Sci.*, vol. 10, no. 3, pp. 1–12, 2020.
- [28] TIMET, “Properties and processing of TIMETAL 6-4.” Brochure/Online
- [29] M. McCann and J. Fanning, “Designing with Titanium Alloys,” in *Handbook*

- of Mechanical Alloy Design*, CRC Press, 2003, pp. 539–583.
- [30] F. Froes, C. Suryanarayana, and D. Eliezer, “Synthesis, properties and applications of titanium aluminides,” *J. Mater. Sci.*, vol. 27, pp. 5113–5140, 1992.
- [31] I. Katzarov, S. Malinov, and W. Sha, “Finite element modeling of the morphology of  $\beta$  to  $\alpha$  phase transformation in Ti-6Al-4V alloy,” *Metall. Mater. Trans. A*, vol. 33, no. 4, pp. 1027–1040, Apr. 2002.
- [32] C. R. de Farias Azevedo and H. M. Flower, “Resulting morphologies on quenching of titanium aluminide alloys,” *Mater. Sci. Technol.*, vol. 15, no. 5, pp. 510–517, May 1999.
- [33] V. A. Joshi, *Titanium Alloys: An Atlas of Structures and Fracture Features*. Taylor & Francis, 2006.
- [34] B. B. Rath, “Kinetics of nucleation and growth processes,” *Mater. Sci. Eng. B*, vol. 32, no. 3, pp. 101–106, Jul. 1995.
- [35] E. Menon and H. I. Aaronson, “Overview no. 57 Morphology, crystallography and kinetics of sympathetic nucleation,” *Acta Metall.*, vol. 35, no. 3, pp. 549–563, 1987.
- [36] T. S. and J. T. and A. T. and R. W. and B. R. and E. L. and S. K. and R. B. and H. L. Fraser, “Rapid characterization of titanium microstructural features for specific modelling of mechanical properties,” *Meas. Sci. Technol.*, vol. 16, no. 1, p. 60, 2005.
- [37] G. Lütjering, “Influence of processing on microstructure and mechanical properties of ( $\alpha$ + $\beta$ ) titanium alloys,” *Mater. Sci. Eng. A*, vol. 243, pp. 32–45, 1998.
- [38] T. Materials and E. L. Langer, “The Materials Information Company,” *Technology*, p. 2173, 1991.
- [39] P. S. Follansbee and G. T. Gray III, “An analysis of the low temperature, low and high strain-rate deformation of Ti-6Al-4V,” *Met. Trans A*, vol. 20A, no. May, pp. 863–874, 1989.
- [40] M. A. Meyers, *Dynamic Behavior of Materials*. Wiley, 1994.
- [41] D. Hull and D. J. Bacon, *Introduction to Dislocations*. Elsevier Science, 2011.
- [42] M. A. Meyers, V. A. Lubarda, and O. Vo, “The onset of twinning in metals: a constitutive,” *Acta Materialia*, vol. 49, pp. 4025–4039, 2001.
- [43] G. H. Xiao, N. R. Tao, and K. Lu, “Effects of strain, strain rate and temperature on deformation twinning in a Cu–Zn alloy,” *Scr. Mater.*, vol. 59, no. 9, pp. 975–978, Nov. 2008.
- [44] F. J. Humphreys and M. Hatherly, *Recrystallization and Related Annealing Phenomena*. Elsevier Science, 1995.

- [45] G. Lütjering, J. Williams, and A. Gysler, "Microstructure and mechanical properties of titanium alloys," *Microstruct. Prop.*, 2000.
- [46] W.-S. Lee and C.-F. Lin, "High-temperature deformation behaviour of Ti6Al4V alloy evaluated by high strain-rate compression tests," *J. Mater. Process. Technol.*, vol. 75, no. 1–3, pp. 127–136, Mar. 1998.
- [47] W. Jia, W. Zeng, J. Liu, Y. Zhou, and Q. Wang, "On the influence of processing parameters on microstructural evolution of a near alpha titanium alloy," *Mater. Sci. Eng. A*, vol. 530, pp. 135–143, 2011.
- [48] Y. Qu *et al.*, "Behavior and modeling of high temperature deformation of an  $\alpha + \beta$  titanium alloy," *Mater. Sci. Eng. A*, vol. 555, pp. 99–105, 2012.
- [49] T. Seshacharyulu, S. C. Medeiros, W. G. Frazier, and Y. V. R. K. Prasad, "Hot working of commercial Ti–6Al–4V with an equiaxed  $\alpha$ – $\beta$  microstructure: materials modeling considerations," *Mater. Sci. Eng. A*, vol. 284, no. 1–2, pp. 184–194, May 2000.
- [50] R. Ding, Z. X. Guo, and a. Wilson, "Microstructural evolution of a Ti–6Al–4V alloy during thermomechanical processing," *Mater. Sci. Eng. A*, vol. 327, no. 2, pp. 233–245, Apr. 2002.
- [51] M. Edwards, "Properties of metals at high rates of strain," *Mater. Sci. Technol.*, vol. 22, no. 4, pp. 453–462, Apr. 2006.
- [52] W.-S. Lee, T.-H. Chen, C.-F. Lin, and G.-T. Lu, "Adiabatic Shearing Localisation in High Strain Rate Deformation of Al-Sc Alloy," *Mater. Trans.*, vol. 51, no. 7, pp. 1216–1221, 2010.
- [53] U. Lindholm, "Some experiments with the split hopkinson pressure bar\*," *J. Mech. Phys. Solids*, vol. 12, 1964.
- [54] A. Marchand and J. Duffy, "An experimental study of the formation process of adiabatic shear bands in a structural steel," *J. Mech. Phys. Solids*, vol. 36, no. 3, 1988.
- [55] S. Yadav and K. T. Ramesh, "The mechanical properties of tungsten-based composites at very high strain rates," *Mater. Sci. Eng. A*, vol. 203, no. 1–2, pp. 140–153, Nov. 1995.
- [56] W. Lee and M. Lin, "The effects of strain rate and temperature on the compressive deformation behaviour of Ti-6Al-4V alloy," *J. Mater. Process. Technol.*, pp. 235–246, 1997.
- [57] M. G. da Silva and K. T. Ramesh, "The rate-dependent deformation and localization of fully dense and porous Ti-6Al-4V," *Mater. Sci. Eng. A*, vol. 232, no. 1–2, pp. 11–22, Jul. 1997.
- [58] W.-S. Lee and C.-F. Lin, "Plastic deformation and fracture behaviour of Ti–6Al–4V alloy loaded with high strain rate under various temperatures," *Mater. Sci. Eng. A*, vol. 241, no. 1–2, pp. 48–59, Jan. 1998.

- [59] D. R. Chichili, K. T. Ramesh, and K. J. Hemker, "The high-strain-rate response of alpha-titanium: experiments, deformation mechanisms and modeling," *Acta Mater.*, vol. 46, no. 3, pp. 1025–1043, Jan. 1998.
- [60] I. Weiss and S. L. Semiatin, "Thermomechanical processing of beta titanium alloys—an overview," *Mater. Sci. Eng. A*, vol. 243, no. 1–2, pp. 46–65, Mar. 1998.
- [61] S. Nemat-Nasser, W. G. Guo, and J. Y. Cheng, "Mechanical properties and deformation mechanisms of a commercially pure titanium," *Acta Mater.*, vol. 47, no. 13, pp. 3705–3720, Oct. 1999.
- [62] T. Seshacharyulu, S. C. Medeiros, W. G. Frazier, and Y. V. R. K. Prasad, "Microstructural mechanisms during hot working of commercial grade Ti–6Al–4V with lamellar starting structure," *Mater. Sci. Eng. A*, vol. 325, no. 1–2, pp. 112–125, Feb. 2002.
- [63] H. Meyer and D. Kleponis, "Modeling the high strain rate behavior of titanium undergoing ballistic impact and penetration," *Int. J. Impact Eng.* Vol. 26, no. 1-10, pp. 509–521, 2001.
- [64] S. Bruschi, S. Poggio, F. Quadrini, and M. E. Tata, "Workability of Ti–6Al–4V alloy at high temperatures and strain rates," *Mater. Lett.*, vol. 58, no. 27–28, pp. 3622–3629, Nov. 2004.
- [65] A. S. Khan, R. Kazmi, and B. Farrokh, "Multiaxial and non-proportional loading responses, anisotropy and modeling of Ti–6Al–4V titanium alloy over wide ranges of strain rates and temperatures," *Int. J. Plast.*, vol. 23, no. 6, pp. 931–950, Jun. 2007.
- [66] A. S. Khan, Y. Sung Suh, and R. Kazmi, "Quasi-static and dynamic loading responses and constitutive modeling of titanium alloys," *Int. J. Plast.*, vol. 20, no. 12, pp. 2233–2248, Dec. 2004.
- [67] J. Peirs, P. Verleysen, J. Degrieck, and F. Coghe, "The use of hat-shaped specimens to study the high strain rate shear behaviour of Ti–6Al–4V," *Int. J. Impact Eng.*, vol. 37, no. 6, pp. 703–714, Jun. 2010.
- [68] S. V. S. Narayana Murty, B. Nageswara Rao, and B. P. Kashyap, "Instability criteria for hot deformation of materials," *Int. Mater. Rev.*, vol. 45, no. 1, pp. 15–26, 2000.
- [69] R. Raj, "Development of a Processing Map for Use in Warm-Forming and Hot-Forming Processes," *Metall. Trans. A*, vol. 12, no. 6, pp. 1089–1097, Jun. 1981.
- [70] Y. V. R. K. Prasad and T. Seshacharyulu, "Modelling of hot deformation for microstructural control," *Int. Mater. Rev.*, vol. 43, no. 6, pp. 243–258, 1998.
- [71] M. Xiong, Z. Yongqing, and W. Shaoli, "A Comparative Study of Various Flow Instability Criteria in Processing Map," *Rare Met. Mater. Eng.*, vol.

- 39, no. 5, pp. 756–761, 2010.
- [72] J. Cai, X. Zhang, K. Wang, Q. Wang, and W. Wang, “Development and Validation of Processing Maps for Ti-6Al-4V Alloy Using Various Flow Instability Criteria,” *J. Mater. Eng. Perform.*, vol. 25, no. 11, pp. 4750–4756, 2016.
- [73] S. V. S. Narayana Murty and B. Nageswara Rao, “On the development of instability criteria during hotworking with reference to IN 718,” *Mater. Sci. Eng. A*, vol. 254, no. 1–2, pp. 76–82, 1998.
- [74] Y. V. R. K. Prasad and T. Seshacharyulu, “Processing maps for hot working of titanium alloys,” *Mater. Sci. Eng. A*, vol. 243, no. 1–2, pp. 82–88, Mar. 1998.
- [75] S. L. Semiatin, M. R. Staker, and J. J. Jonas, “Plastic instability and flow localization in shear at high rates of deformation,” *Acta Metall.*, vol. 32, no. 9, pp. 1347–1354, Sep. 1984.
- [76] S. L. Semiatin and G. D. Lahoti, “The occurrence of shear bands in isothermal, hot forging,” *Metall. Trans. A*, vol. 13, no. 2, pp. 275–288, 1982.
- [77] J. C. Malas and V. Seetharaman, “Using material behavior models to develop process control strategies,” *JOM*, vol. 44, no. 6, pp. 8–13, 1992.
- [78] A. Lukaszek-Solek and J. Krawczyk, “Processing maps of the Ti-6Al-4V alloy in a forging process design,” *Key Eng. Mater.*, vol. 641, pp. 190–197, 2014.
- [79] J. Luo, M. Li, W. Yu, and H. Li, “Effect of the strain on processing maps of titanium alloys in isothermal compression,” *Mater. Sci. Eng. A*, pp. 90–98, 2009.
- [80] W. Zhang, H. Ding, J. Zhao, B. Yang, and W. Yang, “Hot deformation behavior and processing maps of Ti-6Al-4V alloy with starting fully lamellar structure,” *J. Mater. Res.*, vol. 33, no. 22, pp. 3677–3688, 2018.
- [81] W. S. Lee and C. F. Lin, “Adiabatic Shear Fracture of Titanium Alloy Subjected to High Strain Rate and high Temperature Loadings,” *J. Phys IV France*, vol. 7, no. 1 997, 1997.
- [82] H. C. Rogers, “Adiabatic Plastic Deformation,” *Annu. Rev. Mater. Sci.*, vol. 9, no. 1, pp. 283–311, Aug. 1979.
- [83] B. Dodd, B. Yilong, and Y. Bai, *Adiabatic Shear Localization*, 2nd ed. London: Elsevier Science Ltd, 2012.
- [84] Y. Me-Bar and D. Shechtman, “On the adiabatic shear of Ti- 6Al-4V ballistic targets,” *Mater. Sci. Eng.*, vol. 58, pp. 181–188, 1983.
- [85] S. Timothy and I. Hutchings, “The structure of adiabatic shear bands in a titanium alloy,” *Acta Metall.*, vol. 33, no. 4, pp. 667–676, 1985.

- [86] S. Timothy, "The structure of adiabatic shear bands in metals: a critical review," *Acta Metall.*, vol. 35, no. 2, pp. 301–306, 1987.
- [87] A. Shahan and A. Taheri, "Adiabatic shear bands in titanium and titanium alloys: a critical review," *Mater. Des.*, vol. 14, no. 4, 1993.
- [88] D. E. Grady, "Dissipation in adiabatic shear bands," *Mech. Mater.*, vol. 17, no. 2–3, pp. 289–293, Mar. 1994.
- [89] M. Meyers, G. Subhash, B. Kad, and L. Prasad, "Evolution of microstructure and shear-band formation in  $\alpha$ -hcp titanium," *Mech. Mater.*, vol. 17, pp. 175–193, 1994.
- [90] M. Zhou, A. Rosakis, and G. Ravichandran, "Dynamically propagating shear bands in impact-loaded prenotched plates—I. Experimental investigations of temperature signatures and propagation speed," *Mech. Phys.*, vol. 44, no. 6, pp. 981–1006, 1996.
- [91] Y. Yang, Z. Xinming, L. Zhenghua, and L. Qingyun, "Adiabatic shear band on the titanium side in the Ti/mild steel explosive cladding interface," *Acta Mater.*, vol. 44, no. 2, pp. 561–565, Feb. 1996.
- [92] A. Molinari, "Collective behavior and spacing of adiabatic shear bands," *J. Mech. Phys. Solids*, vol. 45, no. 9, pp. 1551–1575, 1997.
- [93] S. Liao and J. Duffy, "Adiabatic shear bands in a Ti-6Al-4V titanium alloy," *J. Mech. Phys. Solids*, vol. 46, no. 11, pp. 2201–2231, Oct. 1998.
- [94] S. Li, W. Liu, D. Qian, P. Guduru, and A. Rosakis, "Dynamic shear band propagation and micro-structure of adiabatic shear band," *Comput. Methods*, vol. 101, pp. 73-92, 2001.
- [95] a.-S. Bonnet-Lebouvier, a Molinari, and P. Lipinski, "Analysis of the dynamic propagation of adiabatic shear bands," *Int. J. Solids Struct.*, vol. 39, no. 16, pp. 4249–4269, Aug. 2002.
- [96] A. Molinari, C. Musquar, and G. Sutter, "Adiabatic shear banding in high speed machining of Ti-6Al-4V: experiments and modeling," *Int. J. Plast.*, vol. 18, no. 4, pp. 443–459, Apr. 2002.
- [97] T. J. Burns and M. A. Davies, "On repeated adiabatic shear band formation during high-speed machining," *Int. J. Plast.*, vol. 18, no. June 1999, pp. 487–506, 2002.
- [98] Q. Xue, M. a. Meyers, and V. F. Nesterenko, "Self-organization of shear bands in titanium and Ti-6Al-4V alloy," *Acta Mater.*, vol. 50, no. 3, pp. 575–596, Feb. 2002.
- [99] L. Qiang, X. Yongbo, and M. . Bassim, "Dynamic mechanical properties in relation to adiabatic shear band formation in titanium alloy-Ti17," *Mater. Sci. Eng. A*, vol. 358, no. 1–2, pp. 128–133, Oct. 2003.
- [100] M. Meyers, Y. B. Xu, Q. Xue, M. T. Pérez-Prado, and T. R. McNelley,

- “Microstructural evolution in adiabatic shear localization in stainless steel,” *Acta Mater.*, vol. 51, no. 5, pp. 1307–1325, Mar. 2003.
- [101] Q. Wei, L. Kecskes, T. Jiao, K. T. Hartwig, K. T. Ramesh, and E. Ma, “Adiabatic shear banding in ultrafine-grained Fe processed by severe plastic deformation,” *Acta Mater.*, vol. 52, no. 7, pp. 1859–1869, Apr. 2004.
- [102] J. F. C. Lins, H. R. Z. Sandim, H.-J. Kestenbach, D. Raabe, and K. S. Vecchio, “A microstructural investigation of adiabatic shear bands in an interstitial free steel,” *Mater. Sci. Eng. A*, vol. 457, no. 1–2, pp. 205–218, May 2007.
- [103] Y. Yang and B. F. Wang, “Dynamic recrystallization in adiabatic shear band in  $\alpha$ -titanium,” *Mater. Lett.*, vol. 60, no. 17–18, pp. 2198–2202, Aug. 2006.
- [104] X. Wang, “Quantitative calculation of local shear deformation in adiabatic shear band for Ti-6Al-4V,” *Trans. Nonferrous Met. Soc. China*, 2007.
- [105] X. Teng, T. Wierzbicki, and H. Couque, “On the transition from adiabatic shear banding to fracture,” *Mech. Mater.*, vol. 39, no. 2, pp. 107–125, Feb. 2007.
- [106] N. Ranc, L. Taravella, V. Pina, and P. Herve, “Temperature field measurement in titanium alloy during high strain rate loading—Adiabatic shear bands phenomenon,” *Mech. Mater.*, vol. 40, no. 4–5, pp. 255–270, Apr. 2008.
- [107] X. Liu *et al.*, “Influence of microstructure and strain rate on adiabatic shearing behavior in Ti-6Al-4V alloys,” *Mater. Sci. Eng. A*, vol. 501, no. 1–2, pp. 30–36, Feb. 2009.
- [108] L. E. Murr *et al.*, “Microstructure evolution associated with adiabatic shear bands and shear band failure in ballistic plug formation in Ti-6Al-4V targets,” *Mater. Sci. Eng. A*, vol. 516, no. 1–2, pp. 205–216, Aug. 2009.
- [109] X. Liu, C. Tan, J. Zhang, F. Wang, and H. Cai, “Correlation of adiabatic shearing behavior with fracture in Ti-6Al-4V alloys with different microstructures,” *Int. J. Impact Eng.*, vol. 36, no. 9, pp. 1143–1149, Sep. 2009.
- [110] Y. Yang, F. Jiang, B. M. Zhou, X. M. Li, H. G. Zheng, and Q. M. Zhang, “Microstructural characterization and evolution mechanism of adiabatic shear band in a near beta-Ti alloy,” *Mater. Sci. Eng. A*, vol. 528, no. 6, pp. 2787–2794, Mar. 2011.
- [111] Y. Yang, X. M. Li, X. L. Tong, Q. M. Zhang, and C. Y. Xu, “Effects of microstructure on the adiabatic shearing behaviors of titanium alloy,” *Mater. Sci. Eng. A*, vol. 528, no. 7–8, pp. 3130–3133, Mar. 2011.
- [112] Z. P. Wan, Y. E. Zhu, H. W. Liu, and Y. Tang, “Microstructure evolution of

- adiabatic shear bands and mechanisms of saw-tooth chip formation in machining Ti6Al4V," *Mater. Sci. Eng. A*, vol. 531, pp. 155–163, Jan. 2012.
- [113] G. G. Ye, S. F. Xue, M. Q. Jiang, X. H. Tong, and L. H. Dai, "Modeling periodic adiabatic shear band evolution during high speed machining Ti-6Al-4V alloy," *Int. J. Plast.*, vol. 40, pp. 39–55, Jan. 2013.
- [114] J. Peirs *et al.*, "Microstructure of adiabatic shear bands in Ti6Al4V," *Mater. Charact.*, vol. 75, pp. 79–92, Jan. 2013.
- [115] S. Osovski, D. Rittel, P. Landau, A. Venkert, "Microstructural effects on adiabatic shear band formation," *Scr. Mater.*, vol. 66, no. 1, pp. 9–12, Jan. 2012.
- [116] J. Zhang *et al.*, "Adiabatic shear fracture in Ti-6Al-4V alloy," *Trans. Nonferrous Met. Soc. China*, vol. 21, no. 11, pp. 2396–2401, Nov. 2011.
- [117] M. Ntovas and P. Blackwell, "A new high and moderate speed servo-hydraulic forging simulator capabilities and process optimization," *AIP Conf. Proc.*, vol. 1896, pp. 1–7, 2017.
- [118] B. Roebuck, J. D. Lord, M. Brooks, M. S. Loveday, C. M. Sellars, and E. R. W., "Measurement Good Practice Guide No 3: Measuring Flow Stress in Hot Axisymmetric Compression Tests," *Natl. Phys. Lab.*, no. 3, 2002.
- [119] B. Roebuck, J. D. Lord, M. Brooks, M. S. Loveday, C. M. Sellars, and R. W. Evans, "Measurement of flow stress in hot axisymmetric compression tests," *Mater. High Temp.*, vol. 23, no. 2, pp. 59–83, Jan. 2006.
- [120] "ASTM E209-18, Standard Practice for Compression Tests of Metallic Materials at Elevated Temperatures with Conventional or Rapid Heating Rates and Strain Rates," *ASTM Int.*, 2018.
- [121] B. Blocks, "Standard Practice for Compression Tests of Metallic Materials at Elevated Temperatures with Conventional or Rapid Heating Rates and Strain Rates 1," vol. 00, no. Reapproved 2010, pp. 1–7, 2014.
- [122] T. Machines, B. Blocks, and L. Adapters, "Standard Practice for Compression Tests of Metallic Materials at Elevated Temperatures with Conventional or Rapid Heating Rates and Strain Rates 1," vol. 03, pp. 1–7, 2018.
- [123] J. Antony, *Design of Experiments for Engineers and Scientists*, no. October. Oxford: Burlington, MA : Butterworth-Heinemann, 2003.
- [124] J. Antony, "Techniques Ten useful and practical tips for making your industrial experiments successful," *TQM Magazine*, vol. 11, no. 4, pp. 252–256, 1999.
- [125] D. C. Montgomery, "The use of statistical process control and design of experiments in product and process improvement," *IIE Trans.*, vol. 24, no. 5, pp. 4–17, Nov. 1992.

- [126] E. Science, G. Britain, and A. Youssef, "Comparison of a full factorial experiment to fractional and taguchi designs in a lathe dry turning operation 1 Introduction 3 Fractional Design Surface roughness measurement of work sample," *Computers and Industrial Engineering* vol. 27, no. 94, pp. 59–62, 1994.
- [127] A. Thomas and J. Antony, "Applying Shainin's variables search methodology in aerospace applications," *Assem. Autom.*, vol. 24, no. 2, pp. 184–191, 2004.
- [128] K. Tsui, "A critical look at Taguchi's modelling approach for robust design," *J. Appl. Stat.*, vol. 23, no. 1, 1996.
- [129] "SAE AMS 4928W : 2017 TITANIUM ALLOY BARS, WIRE, FORGINGS, RINGS, AND DRAWN SHAPES, 6AL - 4V, ANNEALED," *SAE International*. 2017.
- [130] B. Roebuck *et al.*, "Materials at High Temperatures Measurement of flow stress in hot axisymmetric compression tests Measurement of flow stress in hot axisymmetric compression tests," *Materials at High Temperatures*, vol. 3409, 2014.
- [131] G. E. Dieter, H. A. K. S. L. S. Edited by George E. Dieter, and G. E. Dieter, *Handbook of Workability and Process Design*. A S M International, 2003.
- [132] G. Dieter, *Handbook of workability and process design*. ASM International, 2003.
- [133] D. Jordan, "Study of alpha case formation heat treated Ti-6-4 alloy," *Heat Treat. Prog.*, vol. 8, no. 3, pp. 45–47, 2008.
- [134] H. Sofuoglu and H. Gedikli, "Determination of friction coefficient encountered in large deformation processes," *Tribol. Int.*, vol. 35, no. 1, pp. 27–34, 2002.
- [135] M. KUNOGI, *A New Method of Cold Extrusion*, *J. Sci. Res. Inst.*, vol. 50. 1957.
- [136] C. M. Male AT, "A method for the determination of the coefficient of friction of metals under condition of bulk plastic deformation," *J Inst Met.*, no. 93, pp. 38–46, 1965.
- [137] K. Zyguła, M. Wojtaszek, O. Lypchanskyi, T. Śleboda, G. Korpała, and U. Prahł, "The Investigation on Flow Behavior of Powder Metallurgy Ti-10V-2Fe-3Al Alloy Using the Prasad Stability Criterion," *Metall. Mater. Trans. A*, vol. 50, no. 11, pp. 5314–5323, 2019.
- [138] ASTM, "ASTM E112-13: Standard test methods for determining average grain size," *ASTM Int.*, vol. 96, pp. 1–28, 2013.
- [139] "ASTM E209-18, Standard Practice for Compression Tests of Metallic Materials at Elevated Temperatures with Conventional or Rapid Heating

- Rates and Strain Rates, ASTM International,” *ASTM Int.*, 2018.
- [140] Y. C. Lin and X.-M. Chen, “A critical review of experimental results and constitutive descriptions for metals and alloys in hot working,” *Mater. Des.*, vol. 32, no. 4, pp. 1733–1759, 2011.
- [141] S. L. Semiatin, F. Montheillet, G. Shen, and J. J. Jonas, “Self-Consistent Modeling of the Flow Behavior of Wrought Alpha / Beta Titanium Alloys under Isothermal and Nonisothermal Hot-Working Conditions,” *Mater. Trans Avol.* 33, no. August, pp. 2719–2727, 2002.
- [142] S. . Semiatin, V. Seetharaman, and I. Weiss, “Flow behavior and globularization kinetics during hot working of Ti–6Al–4V with a colony alpha microstructure,” *Mater. Sci. Eng. A*, vol. 263, pp. 257–271, 1999.
- [143] Blackwell Paul, “Private communication: AFRC ring compression test database,” 2014.
- [144] G. Dieter and D. Bacon, *Mechanical metallurgy*. 1986.
- [145] B. Roebuck, M. Brooks, and M. G. Gee, “Load Cell Ringing in High Rate Compression Tests,” *Appl. Mech. Mater.*, vol. 1–2, no. 1, pp. 205–210, 2004.
- [146] B. Roebuck, M. Brooks, and M. G. Gee, “Load Cell Ringing in High Rate Compression Tests,” *Appl. Mech. Mater.*, vol. 1–2, pp. 205–210, 2004.
- [147] A. M. Team, “Private communication: MathCAD routine IP protected,” 2014.
- [148] P. Rosakis, A. J. Rosakis, G. Ravichandran, and J. Hodowany, “Partition of plastic work into heat and stored energy in metals. 2: Theory,” *Experimental Mechanics* no. SM 98-8, pp. 113–123, 1998.
- [149] P. F. Bariani, T. Dal Negro, and S. Bruschi, “Testing and Modelling of Material Response to Deformation in Bulk Metal Forming,” *CIRP Ann. - Manuf. Technol.*, vol. 53, no. 2, pp. 573–595, 2004.
- [150] Q. Zhao, G. Wu, and W. Sha, “Deformation of titanium alloy Ti–6Al–4V under dynamic compression,” *Comput. Mater. Sci.*, vol. 50, no. 2, pp. 516–526, Dec. 2010.
- [151] G. Johnson and W. Cook, “A constitutive model and data for metals subjected to large strains, high strain rates and high temperatures,” *The 7th International Symposium of Ballistics*, 1983.
- [152] S. V. Sajadifar and G. G. Yapici, “Workability characteristics and mechanical behavior modeling of severely deformed pure titanium at high temperatures,” *Mater. Des.*, vol. 53, pp. 749–757, 2014.
- [153] C. Zener and J. H. Hollomon, “Effect of strain rate upon plastic flow of steel,” *J. Appl. Phys.*, vol. 15, no. 1, pp. 22–32, 1944.
- [154] P. F. Bariani, S. Bruschi, and T. Dal Negro, “Integrating physical and

- numerical simulation techniques to design the hot forging process of stainless steel turbine blades,” *Int. J. Mach. Tools Manuf.*, vol. 44, no. 9, pp. 945–951, 2004.
- [155] T. Bariani, P.F., Bruschi S., Dal Negro, “Accurate material behaviour representation: a prerequisite for accurate forging simulations,” in *Proc. of 14th ICAFT*, 2003.
- [156] A. Hensel, And, and T. Spittel, “Kraft-und Arbeitsbedarf bildsamer Formgebungsverfahren: mit 51 Tabellen.” 1978.
- [157] S. Marie, R. Ducloux, P. Lasne, J. Barlier, and L. Fourment, “Inverse Analysis of Forming Processes based on FORGE environment,” *Key Eng. Mater.*, vol. 612, pp. 1494–1502, 2014.
- [158] K. Chadha, D. Shahriari, and M. Jahazi, “Frontiers in Materials Processing, Applications, Research and Technology,” no. January, 2018.
- [159] M. El Mehtedi, F. Musharavati, and S. Spigarelli, “Modelling of the flow behaviour of wrought aluminium alloys at elevated temperatures by a new constitutive equation,” *Mater. Des.*, vol. 54, pp. 869–873, 2014.
- [160] K. Huang and R. E. Logé, “A review of dynamic recrystallization phenomena in metallic materials,” *JMADE*, vol. 111, pp. 548–574, 2016.
- [161] R. Ding and Z. X. Guo, “Microstructural evolution of a Ti-6Al-4V alloy during  $\beta$ -phase processing: Experimental and simulative investigations,” *Mater. Sci. Eng. A*, vol. 365, no. 1–2, pp. 172–179, 2004.
- [162] H. M. Flower, “Microstructural development in relation to hot working of titanium alloys,” *Mater. Sci. Technol.*, vol. 6, no. 11, pp. 1082–1092, Nov. 1990.
- [163] S. L. Semiatin and T. R. Bieler, “The effect of alpha platelet thickness on plastic flow during hot working of Ti-6Al-4V with a transformed microstructure,” *Acta Mater.*, vol. 49, no. 17, pp. 3565–3573, 2001.
- [164] S. L. Semiatin, V. Seetharaman, and A. K. Ghosh, “Plastic Flow , Microstructure Evolution , and Defect Formation during Primary Hot Working of Titanium and Titanium Aluminide Alloys with Lamellar Colony Microstructures [ and Discussion ] Author ( s ): S . L . Semiatin , V . Seetharaman , A . K . Ghosh ,” *Philos. Trans. Math. Phys. Eng. Sci.*, vol. 357, no. 1999, pp. 1487–1512, 2013.
- [165] Y. Ren, S. Zhou, W. Luo, Z. Xue, and Y. Zhang, “Influence of primary  $\alpha$ -phase volume fraction on the mechanical properties of Ti-6Al-4V alloy at different strain rates and temperatures,” *IOP Conf. Ser. Mater. Sci. Eng.*, vol. 322, no. 2, 2018.
- [166] F. J. Humphreys and M. Hatherly, “Chapter 9 - Recrystallization of Two-Phase Alloys,” F. J. Humphreys and M. B. T.-R. and R. A. P. (Second E. Hatherly, Eds. Oxford: Elsevier, 2004, pp. 285–319.

- [167] V. Seetharaman and S. L. Semiatin, "Influence of temperature transients on the hot workability of a two-phase gamma titanium aluminide alloy," *Metall. Mater. Trans. A*, vol. 27, no. 7, pp. 1987–2004, Jul. 1996.
- [168] T. R. Bieler, M. G. Glavicic, and S. L. Semiatin, "Using OIM to investigate the microstructural evolution of Ti-6Al-4V," *JoM*, vol. 54, no. 1, pp. 31–36, 2002.
- [169] Q. Liu, S. Hui, K. Tong, Y. Yu, W. Ye, and S. Yin Song, "Investigation of high temperature behavior and processing map of Ti-6Al-4V-0.11Ru titanium alloy," *J. Alloys Compd.*, vol. 787, pp. 527–536, 2019.
- [170] J. Klíber, "Dissipation of energy and instability process in various alloys based on plastometric tests," vol. 25, pp. 16–21, 2016.
- [171] A. A. Lakshmi and S. K. Singh, "ScienceDirect Review of Processing Maps and Development of Qualitative Processing Maps," vol. 4, pp. 946–956, 2017.
- [172] Terry Khaled, "An outsider looks at friction stir welding," 2015.
- [173] X. Peng, H. Guo, Z. Shi, C. Qin, Z. Zhao, and Z. Yao, "Study on the hot deformation behavior of TC4-DT alloy with equiaxed  $\alpha+\beta$  starting structure based on processing map," *Mater. Sci. Eng. A*, vol. 605, pp. 80–88, 2014.
- [174] Y. Liu, Y. Ning, Z. Yao, and H. Guo, "Hot deformation behavior of Ti-6.0Al-7.0Nb biomedical alloy by using processing map," *J. Alloys Compd.*, vol. 587, pp. 183–189, 2014.
- [175] P. M. Souza, H. Beladi, R. Singh, B. Rolfe, and P. D. Hodgson, "Constitutive analysis of hot deformation behavior of a Ti6Al4V alloy using physical based model," *Mater. Sci. Eng. A*, vol. 648, pp. 265–273, 2015.
- [176] M. Jackson, R. . Dashwood, L. Christodoulou, and H. . Flower, "Isothermal subtransus forging of Ti-6Al-2Sn-4Zr-6Mo," *J. Light Met.*, vol. 2, no. 3, pp. 185–195, 2003.